

**Satellite Versus GCM-Simulated Radiation Balance:
Comparisons and Implications for Climate Modeling**

by
Laura D. Smith

Department of Atmospheric Science
Colorado State University
Fort Collins, Colorado



**Department of
Atmospheric Science**

Paper No. 443

SATELLITE VERSUS GCM-SIMULATED RADIATION BALANCE:
COMPARISONS AND IMPLICATIONS FOR CLIMATE MODELING

by

Laura D. Smith

Research supported by NASA Contracts
NAS-1-16465 and NAG-1-865

Principal Investigator: Thomas H. Vonder Haar

Department of Atmospheric Science
Colorado State University
Fort Collins, Colorado 80523

Spring, 1989

Atmospheric Science Paper No. 443

This paper was also submitted in partial fulfillment of the
requirements for the Degree of Doctor of Philosophy.

ABSTRACT

SATELLITE VERSUS GCM-SIMULATED RADIATION BALANCE: COMPARISONS AND IMPLICATIONS FOR CLIMATE MODELING

Measurements of the earth radiation budget (ERB) from space-borne instruments and long-term simulations of climate with general circulation models (GCMs) make complementary contributions to improve our understanding of cloud-radiation-climate interactions and the role of clouds in the atmospheric general circulation. The first step of an increased use of three-dimensional climate models to study the forcing of clouds on climate is the validation against observations of GCM simulated climates, including their temporal and spatial variability. ERB measurements from satellites constitute one of the most suitable means for objective and easy comparisons with model outputs. In particular, they provide the necessary top-of-atmosphere boundary conditions that all climate models have to conform to. The infrared and solar components of the planetary radiation balance computed from long-term climate simulations with the NCAR Community Climate Model (NCAR CCM) are compared against those measured during the Nimbus-7 satellite mission. The latest version of the NCAR CCM, also known as version CCM1, is used. The model-generated radiative fields were obtained from a 15-year run including a seasonal cycle and a 1500-day run for perpetual January conditions. Daily broad-spectral-band narrow angle field-of-view (NFOV) ERB measurements were taken by the scanner radiometers on board Nimbus-7 during the period between May 1979 and June 1980. Estimates of cloud amounts derived from satellite radiance measurements and NFOV data of the outgoing infrared radiation taken by the scanners on-board the NOAA satellites were used to complete our observational data set.

Our comparison between the model-generated and satellite-observed radiation fields helped identify a major discrepancy in the simulation of climate with the NCAR CCM. The model reproduced successfully the mean steady state of the radiation budget components, especially at long wavelengths, but failed to simulate their temporal variability. Global maps of the time standard deviation of the model-simulated radiation fields resembled rather well those obtained from observations. However, the magnitude of the standard deviation was systematically two times larger than that computed from satellite data. Analyses of the model-generated cloudiness and its forcing on radiation demonstrated that the high frequency of occurrence of clouds explained most of the difference in the temporal variability between model and observations. It was showed that the prediction of clouds in term of the large-scale relative humidity field and the atmospheric stability, and the treatment of condensation as a complete rainout process, maintained a decoupling between clouds, radiation, and the hydrologic cycle. The impacts of the cloud prediction scheme and the parameterization of the interactions between clouds, and the radiative, dynamic, and thermodynamic processes were separately analyzed from two different climate experiments made with CCM1. Our results suggested that the inclusion of a prognostic equation of the liquid water and a more realistic partition between non-precipitating and precipitating condensed water in the atmosphere were the necessary ingredient to produce improved evolution times of clouds and, therefore, help lower the temporal variability of the model-generated planetary radiation budget.

Laura D. Smith
Department of Atmospheric Science
Colorado State University
Fort Collins, Colorado 80523
Spring 1989

ACKNOWLEDGEMENTS

This research was developed under the guidance of Pr. Thomas H. Vonder Haar. I would like to express my profound gratitude to Pr. Vonder Haar for having given me the opportunity to attend the Graduate Program of the Department of Atmospheric Science at CSU, supported and encouraged my research throughout my doctoral studies, and helped me develop numerous contacts within the scientific community in the United States. Pr. V. Ramanathan, from the Department of Geophysical Sciences at the University of Chicago, contributed a major part to the success of the modeling part of my dissertation. I would like to thank Pr. Ramanathan for his help in my understanding of the NCAR Community Climate Model and participation to my graduate committee. Prs. Graeme L. Stephens, Stephen K. Cox, and Hariharan K. Iyer accepted to be members of my advisory committee. I would like to thank them for their suggestions and critics up to the completion of my PhD. Finally, I would like to thank Pr. David A. Randall for his help using the CSU general circulation model and advices at the final stage of my research.

Several scientists at the National Center for Atmospheric Research¹ (NCAR) were very helpful in my learning of the NCAR Community Climate Model. I would like to thank Dr. Warren M. Washington, head of the Climate Global Division, for having provided me the computer-time necessary to run and analyze the general circulation model. Many thanks go to Mrs. Gloria S. Williamson and Mr. Richard J. Wolski for their assistance and constant availability in helping me use the NCAR CCM Modular Processor to analyze the model outputs.

¹The National Center for Atmospheric Research is sponsored by the National Science Foundation

David L. Randel and Dr. G. Garrett Campbell assisted me in learning how to access and analyze the various satellite data sets available at the Department of Atmospheric Sciences and used in this dissertation. I would like to address my special thanks to David for his help and patience at the beginning of my research in Fall 1983, friendship and support up to the defense of my PhD. Many thanks to all my friends at the Department of Atmospheric Science and Cooperative Institute for Research in the Atmosphere (CIRA). You are too many to be named individually in these acknowledgements but you all contributed to make my studies at CSU a very enjoyable american experience. In particular, thanks to David Randel, Shaze Naqvi, and Judy Dunn for the friendly atmosphere of Solar House II. I also would like to extend my appreciation and gratitude to Mrs. Joanne Williams and Loretta Wilson for their skillfull assistance. Thanks to Mrs. Judy Dunn for the drafting of some of the figures.

Before closing those acknowledgements, I would like to simply dedicate this dissertation to my parents, whose confidence and moral support from France contributed a major part to its successfull achievement.

This research was supported primarily by NASA contracts NAS-1-16465 (53-1984) and NAG-1-865 (53-1921).

TABLE OF CONTENTS

1 INTRODUCTION	1
1.1 Scientific contributions from earth radiation budget measurements	3
1.2 Scientific contributions from general circulation models	8
1.3 Objectives of the dissertation	11
1.4 Plan of the dissertation	14
2 NIMBUS-7 EARTH RADIATION BUDGET EXPERIMENT: TEM- PORAL AND SPATIAL VARIABILITY FROM NFOV DATA	17
2.1 Introduction	17
2.2 Overview of the Nimbus-7 ERB Experiment	17
2.3 Narrow angle field-of-view data set	18
2.3.1 Scanner instruments	18
2.3.2 Summary of the June 1979-May 1980 ERB data	20
2.4 Outgoing infrared radiation	20
2.4.1 Seasonal average	26
2.4.2 Standard deviation about the seasonal average	26
2.5 Planetary albedo	32
2.5.1 Seasonal average	32
2.5.2 Standard deviation about the seasonal average	32
2.6 Absorbed solar radiation	35
2.7 Outgoing infrared, absorbed solar radiation covariance	35
2.8 Cloud factor	42
2.8.1 Definition	42
2.8.2 Results	43
2.9 Sensitivity of the temporal variability	47
2.9.1 Discussion	47
2.9.2 Impact of the seasonal cycle	49
2.9.3 Impact of the diurnal sampling	49
2.9.4 Comparison against NOAA infrared data	59
2.9.5 Conclusion	67
2.10 Summary	67
3 DESCRIPTION OF THE NCAR COMMUNITY CLIMATE MODEL AND THE SIMULATIONS OF CLIMATE	72
3.1 Introduction	72
3.2 Model description	72
3.3 Radiative transfer scheme of short wavelengths	73
3.3.1 Shortwave spectral interval	73
3.3.2 Clear-sky fluxes	76

3.3.3	Cloud-radiation interactions	77
3.4	Radiative transfer of long wavelengths	78
3.4.1	Longwave spectral interval	78
3.4.2	Clear-sky fluxes	79
3.4.3	Cloud-radiation interactions	80
3.5	Cloud cover parameterization	80
3.5.1	Cloud fraction	81
3.5.2	Cloud emissivity	81
3.5.3	Cloud albedo	82
3.6	Simulations of climate with CCM1	82
3.6.1	Long-term simulations archived at NCAR	82
3.6.2	Stability of the simulated climate	84
3.7	Summary	85
4	RADIATION BUDGET STATISTICS FROM CLIMATE SIMULA-	
	TIONS WITH THE NCAR COMMUNITY CLIMATE MODEL	92
4.1	Introduction	92
4.2	Modeling of the atmospheric circulation	93
4.3	Outgoing infrared radiation	103
4.3.1	Seasonal average	103
4.3.2	Standard deviation about the seasonal average	104
4.4	Planetary albedo	105
4.4.1	Seasonal average	105
4.4.2	Standard deviation about the seasonal average	112
4.5	Absorbed solar radiation	112
4.6	Temporal correlation of the outgoing infrared radiation	119
4.6.1	Background	119
4.6.2	Satellite-derived correlation	126
4.6.3	Model-derived correlation	132
4.7	Discussion	133
4.8	Summary	141
5	INFLUENCE OF THE MODEL-GENERATED CLOUDINESS ON	
	THE TEMPORAL VARIABILITY OF THE RADIATION BUDGET	
	COMPONENTS	145
5.1	Introduction	145
5.2	Model-generated versus satellite-derived total cloudiness	146
5.2.1	Background	146
5.2.2	Seasonal average and standard deviation	148
5.2.3	Temporal correlation	150
5.2.4	Conclusion	160
5.3	Cloud radiative forcing	160
5.3.1	Definition	160
5.3.2	Longwave forcing	163
5.3.3	Shortwave forcing	165
5.3.4	Conclusion	170
5.4	Cloud-Atmosphere interactions	175
5.4.1	Origins of the interactions	175

5.4.2	Interactions in the NCAR CCM	178
5.5	Sensitivity experiments with the NCAR CCM	179
5.5.1	Impact of the cloud/no cloud threshold assumption	182
5.5.2	Impact of the rainout process assumption	182
5.6	Summary	183

6 INFLUENCE OF THE ECMWF CLOUD PREDICTION SCHEME ON THE MODEL-GENERATED RADIATION FIELDS 184

6.1	Introduction	184
6.2	Description of the ECMWF cloud prediction scheme	185
6.2.1	Convective clouds	186
6.2.2	High-level clouds	186
6.2.3	Middle-level clouds	187
6.2.4	Low-level clouds	187
6.2.5	Discussion	188
6.3	Distribution of the ECMWF cloud types	189
6.4	ECMWF versus CONTROL distribution of the cloud cover	196
6.4.1	Difference in the time series	196
6.4.2	Difference in the global distribution	197
6.4.3	Difference in the vertical distribution	201
6.5	ECMWF versus CONTROL temperature field	205
6.6	ECMWF versus CONTROL relative humidity field	213
6.7	ECMWF versus CONTROL cloud radiative forcing	218
6.7.1	Longwave forcing	218
6.7.2	Shortwave forcing	225
6.8	ECMWF versus CONTROL planetary radiation balance	228
6.8.1	Outgoing infrared radiation	231
6.8.2	Planetary albedo	232
6.9	Discussion	235
6.10	Summary	239

7 Influence of the large-scale precipitation rate on the model-generated climate 242

7.1	Introduction	242
7.2	Description of the large-scale condensation adjustment scheme	244
7.3	HYDRO versus CONTROL hydrologic cycle	246
7.3.1	Difference in the frequency of condensation	246
7.3.2	Difference in the moisture budget	251
7.3.3	Difference in the cloud cover	259
7.3.4	Conclusion	260
7.4	HYDRO versus CONTROL planetary radiation balance	261
7.4.1	Outgoing infrared radiation	261
7.4.2	Planetary albedo	266
7.4.3	Conclusion	266
7.5	HYDRO versus CONTROL atmospheric diabatic heating	271
7.5.1	Difference in the radiative heating	272
7.5.2	Difference in the condensational heating	273
7.5.3	Difference in the diabatic heating	276

7.5.4	Conclusion	277
7.6	HYDRO versus CONTROL atmospheric general circulation	277
7.6.1	Difference in the temperature field	281
7.6.2	Difference in the vertical velocity	281
7.6.3	Difference in the zonal wind	282
7.6.4	Conclusion	282
7.7	Discussion	282
7.8	Summary	284
8	SUMMARY AND CONCLUSION	290
8.1	Summary	292
8.1.1	Observed radiation balance	292
8.1.2	Simulated radiation balance	293
8.1.3	Impact of cloudiness	293
8.2	Contributions and future research	295
	REFERENCES	297
A	BASIC RADIOMETRIC CONVERSION ALGORITHMS	305
A.1	Introduction	305
A.2	Albedo derived from the NFOV channels	305
A.3	Outgoing longwave flux for the NFOV channels	307
A.4	Net radiation derived from the NFOV channels	308
A.5	Computation of the monthly mean values	308

LIST OF FIGURES

1.1 Schematic illustration of the processes commonly included in atmospheric general circulation models. The thickness of a particular arrow gives a qualitative indication of the importance of the interaction the arrow represents (from Simmons and Bengtsson, 1984).	12
2.1 ERB scan modes.	21
2.2 Time-latitude distribution derived from the ERB NFOV instruments: (a) outgoing infrared radiation, (b) planetary albedo.	22
2.2 Time-latitude distribution derived from the ERB NFOV instruments: (c) net radiation.	23
2.3 (a) Zonally-averaged distribution of the annually-averaged outgoing infrared radiation, planetary albedo, and net radiation.	23
2.3 Same as Figure 2.3 (a) but for: (b) June 79-July 79-August 79, and (c) September 79-October 79-November 79.	24
2.3 Same as Figure 2.3 (a) but for: (d) December 79-January 80-February 80; and (e) March 80-April 80-May 80.	25
2.4 Map of the outgoing infrared radiation for Northern Hemisphere winter (Wm^{-2}): (a) seasonal average, and (b) standard deviation.	28
2.5 Map of the outgoing infrared radiation for Northern Hemisphere summer (Wm^{-2}): (a) seasonal average, and (b) standard deviation.	29
2.6 Map of the planetary albedo for Northern Hemisphere winter (%): (a) seasonal average, and (b) standard deviation.	33
2.7 Map of the planetary albedo for Northern Hemisphere summer (%): (a) seasonal average, and (b) standard deviation.	34
2.8 Map of the absorbed solar radiation for Northern Hemisphere winter (Wm^{-2}): (a) seasonal average, and (b) standard deviation.	36
2.9 Map of the absorbed solar radiation for Northern Hemisphere summer (Wm^{-2}): (a) seasonal average, and (b) standard deviation.	37
2.10 Map of the covariance between the outgoing infrared radiation and the absorbed solar radiation for Northern Hemisphere (a) winter, and (b) summer (Wm^{-2}) ²	41
2.11 Map of the slope $\frac{\partial IR}{\partial \alpha}$ for Northern Hemisphere (a) winter, and (b) summer (Wm^{-2}).	45
2.12 Map of the cloud factor $[S_o(\frac{\partial IR}{\partial \alpha})^{-1} + 1]$ for Northern Hemisphere (a) winter, and (b) summer.	46
2.13 Map of the standard deviation of the outgoing infrared radiation (Wm^{-2}): (a) ERBE (January 1986), and Nimbus-7 (January 1980).	53
2.14 Map of the standard deviation of the outgoing infrared radiation (Wm^{-2}): (a) ERBE (July 1985), and Nimbus-7 (July 1979).	54

2.15	Zonally-averaged profile of the standard deviation of the outgoing infrared radiation (Wm^{-2}): (a) January, and (b) July.	55
2.16	Map of the standard deviation of the absorbed solar radiation (Wm^{-2}): (a) ERBE (January 1986), and (b) Nimbus-7 (January 1980).	56
2.17	Map of the standard deviation of the absorbed solar radiation (Wm^{-2}): (a) ERBE (July 1985), and (b) Nimbus-7 (July 1979).	57
2.18	Zonally-averaged profile of the standard deviation of the absorbed solar radiation (Wm^{-2}): (a) January, and (b) July.	58
2.19	Map of the normalized standard deviation of the outgoing infrared radiation for Northern Hemisphere winter (%): (a) NOAA, and (b) Nimbus-7.	63
2.20	Map of the normalized standard deviation of the outgoing infrared radiation for Northern Hemisphere summer (%): (a) NOAA, and (b) Nimbus-7.	64
2.21	Zonally-averaged profile of the normalized standard deviation of the outgoing infrared radiation (%): (a) Northern Hemisphere winter, and (b) summer.	65
2.22	Map of the difference between the standard deviation computed from the daily mean and the 12-hour observations of the outgoing infrared radiation for Northern Hemisphere winter (Wm^{-2}): (a) NOAA, and (b) Nimbus-7.	68
2.23	Map of the difference between the standard deviation computed from the daily mean and the 12-hour observations of the outgoing infrared radiation for Northern Hemisphere summer (Wm^{-2}): (a) NOAA, and (b) Nimbus-7.	69
3.1	Control of the model flow to compute the grid-data at time-step $n+1$, knowing the grid-data at time-steps n and $n-1$	74
3.2	Vertical discretization of the model atmosphere. K indices refer to full- σ levels, whereas $K \pm \frac{1}{2}$ indices refer to half- σ levels (from Williamson <i>et al.</i> , 1987).	75
3.3	Vertical distribution of large-scale condensation and convective clouds. Γ_e is the atmospheric adiabatic lapse rate (from Ramanathan <i>et al.</i> , 1983).	89
3.4	Map of (a) ensemble average of time average, and (b) ensemble standard deviation of the time average of the outgoing infrared radiation (Wm^{-2}).	90
3.5	Map of (a) ensemble average of the standard deviation, and (b) ensemble standard deviation of the standard deviation of the outgoing infrared radiation (Wm^{-2}).	91
4.1	Map of the seasonally-averaged sea-level pressure for Northern Hemisphere winter (mb): (a) computed distribution from the model, and (b) observed distribution compiled by Schutz and Gates (1971).	95
4.2	Map of the seasonally-averaged surface-air temperature for Northern Hemisphere winter (K): (a) computed distribution from the model, and (b) observed distribution compiled by Schutz and Gates (1971).	96
4.3	Latitude-height distribution of the seasonally-averaged zonal mean temperature for Northern Hemisphere winter (K): (a) computed distribution from the model, and (b) observed distribution compiled by Newell <i>et al.</i> (1972).	97
4.4	Map of the seasonally-averaged precipitation rate for Northern Hemisphere winter ($mm\ day^{-1}$): (a) computed distribution from the model, and (b) observed distribution compiled by Schutz and Gates (1972a).	99

4.5	Latitude-height distribution of the seasonal average of the zonal mean zonal-wind component for Northern Hemisphere winter (m s^{-1}): (a) computed distribution from the model, and (b) observed distribution compiled by Newell <i>et al.</i> (1972).	100
4.6	Latitude-height distribution of the seasonal average of the zonal mean meridional-wind component for Northern Hemisphere winter (m s^{-1}): (a) computed distribution from the model, and (b) observed distribution compiled by Newell <i>et al.</i> (1972).	101
4.7	Latitude-height distribution of the seasonal average of the zonal mean vertical velocity for Northern Hemisphere winter (10^{-4}mb s^{-1}): (a) computed distribution from the model, and (b) observed distribution compiled by Newell <i>et al.</i> (1972).	102
4.8	Map of the seasonal average of the outgoing infrared radiation for Northern Hemisphere winter (Wm^{-2}): (a) computed distribution from the model, and (b) observed distribution from Nimbus-7.	106
4.9	Map of the seasonal average of the outgoing infrared radiation for Northern Hemisphere summer (Wm^{-2}): (a) computed distribution from the model, and (b) observed distribution from Nimbus-7.	107
4.10	Zonally-averaged distribution of the seasonally-averaged outgoing infrared radiation (Wm^{-2}): (a) Northern Hemisphere winter, and (b) summer. . . .	108
4.11	Map of the standard deviation of the outgoing infrared radiation for Northern Hemisphere winter (Wm^{-2}): (a) computed distribution from the model, and (b) observed distribution from Nimbus-7.	109
4.12	Map of the standard deviation of the outgoing infrared radiation for Northern Hemisphere summer (Wm^{-2}): (a) computed distribution from the model, and (b) observed distribution from Nimbus-7.	110
4.13	Zonally-averaged distribution of the standard deviation of the outgoing infrared radiation (Wm^{-2}): (a) Northern Hemisphere winter, and (b) summer. . . .	111
4.14	Map of the seasonal average of the planetary albedo for Northern Hemisphere winter (%): (a) computed distribution from the model, and (b) observed distribution from Nimbus-7.	113
4.15	Map of the seasonal average of the planetary albedo for Northern Hemisphere summer (%): (a) computed distribution from the model, and (b) observed distribution from Nimbus-7.	114
4.16	Zonally-averaged distribution of the seasonal average of the planetary albedo (%): (a) Northern Hemisphere winter, and (b) summer.	115
4.17	Map of the standard deviation of the planetary albedo for Northern Hemisphere winter (%): (a) computed distribution from the model, and (b) observed distribution from Nimbus-7.	116
4.18	Map of the standard deviation of the planetary albedo for Northern Hemisphere summer (%): (a) computed distribution from the model, and (b) observed distribution from Nimbus-7.	117
4.19	Zonally-averaged distribution of the standard deviation of the planetary albedo (%): (a) Northern Hemisphere winter, and (b) summer.	118
4.20	Map of the seasonal average of the absorbed solar radiation for Northern Hemisphere winter (Wm^{-2}): (a) computed distribution from the model, and (b) observed distribution from Nimbus-7.	120

4.21	Map of the seasonal average of the absorbed solar radiation for Northern Hemisphere summer (Wm^{-2}): (a) computed distribution from the model, and (b) observed distribution from Nimbus-7	121
4.22	Zonally-averaged distribution of the seasonal average of the absorbed solar radiation (Wm^{-2}): (a) Northern Hemisphere winter, and (b) summer.	122
4.23	Map of the standard deviation of the absorbed solar radiation for Northern Hemisphere winter (Wm^{-2}): (a) computed distribution from the model, and (b) observed distribution from Nimbus-7.	123
4.24	Map of the standard deviation of the absorbed solar radiation for Northern Hemisphere summer (Wm^{-2}): (a) computed distribution from the model, and (b) observed distribution from Nimbus-7	124
4.25	Zonally-averaged distribution of the standard deviation of the absorbed solar radiation (Wm^{-2}): (a) Northern Hemisphere winter, and (b) summer.	125
4.26	Map of the autocorrelation coefficient of the outgoing infrared radiation, computed from NOAA IR data, for Northern Hemisphere winter (%): (a) 12-hour lag, and (b) 24-hour lag.	128
4.27	Map of the autocorrelation coefficient of the outgoing infrared radiation, computed from NOAA IR data, for Northern Hemisphere winter (%): (a) 36-hour lag, and (b) 48-hour lag.	129
4.28	Map of the autocorrelation coefficient of the outgoing infrared radiation, computed from NOAA IR data for Northern Hemisphere winter (%): (a) 60-hour lag, and (b) 72-hour lag.	130
4.29	Zonally-averaged distribution of the time-lagged autocorrelation coefficients of the outgoing infrared radiation (%): (a) in phase correlation, and (b) out of phase correlation.	131
4.30	Map of the 24-hour lag autocorrelation coefficient of the model-generated outgoing infrared radiation for Northern Hemisphere winter (%): (a) ensemble average, and (b) ensemble standard deviation.	134
4.31	Map of the 48-hour lag autocorrelation coefficient of the model-generated outgoing infrared radiation for Northern Hemisphere winter (%): (a) ensemble average, and (b) ensemble standard deviation.	135
4.32	Map of the 72-hour lag autocorrelation coefficient of the model-generated outgoing infrared radiation for Northern Hemisphere winter (%): (a) ensemble average, and (b) ensemble standard deviation.	136
4.33	Zonally-averaged distribution of the time-lagged autocorrelation coefficient of the outgoing infrared radiation at a 24-hour lag, 48-hour lag, and 72-hour lag (%), for Northern Hemisphere winter.	137
4.34	Zonally-averaged distribution of the time-lagged autocorrelation coefficient of the model-generated outgoing infrared radiation (%): (solid line) ensemble average, and (dashed line) ensemble standard deviation.	138
4.35	Map of the difference between the standard deviation of the outgoing infrared radiation computed from every 12-hour observations and daily mean values (Wm^{-2}): (a) Northern Hemisphere winter, and (b) summer.	142
4.36	Zonally-averaged distribution of the standard deviation of the outgoing infrared radiation produced with the CSU GCM (Wm^{-2}): (a) Northern Hemisphere winter, and (b) summer (Randall, private communication, 1988)	143

5.1	Map of the seasonal average of the total cloudiness for Northern Hemisphere winter (%): (a) computed distribution from the model, and (b) satellite-derived distribution from Nimbus-7 (CMATRIX).	151
5.2	Map of the standard deviation of the total cloudiness for Northern Hemisphere winter (%): (a) computed distribution from the model, and (b) satellite-derived distribution from Nimbus-7 (CMATRIX).	152
5.3	Zonally-averaged distribution of the total cloudiness for Northern Hemisphere winter (%): (a) seasonal average, and (b) standard deviation.	153
5.4	Zonally-averaged distribution of the time-lagged autocorrelation coefficients of the total cloud cover (CMATRIX) and outgoing infrared radiation (NOAA ERB) for Northern Hemisphere winter conditions (%): (a) 24-hour lag, (b) 48-hour lag, and (c) 72-hour lag.	155
5.5	Map of the 24-hour lag autocorrelation coefficient of the total cloudiness for Northern Hemisphere winter (%): (a) computed distribution from the model, and (b) satellite-derived distribution from Nimbus-7 (CMATRIX).	156
5.6	Map of the 48-hour lag autocorrelation coefficient of the total cloudiness for Northern Hemisphere winter (%): (a) computed distribution from the model, and (b) satellite-derived distribution from Nimbus-7 (CMATRIX).	157
5.7	Map of the 72-hour lag autocorrelation coefficient of the total cloudiness for Northern Hemisphere winter (%): (a) computed distribution from the model, and (b) satellite-derived distribution from Nimbus-7 (CMATRIX).	158
5.8	Zonally-averaged distribution of the time-lagged autocorrelation coefficient of the total cloudiness for Northern Hemisphere winter (%): (a) 24-hour lag, (b) 48-hour lag, and (c) 72-hour lag.	159
5.9	Map of the total cloud longwave radiative forcing for Northern Hemisphere winter (Wm^{-2}): (a) distribution of the seasonal average, and (b) distribution of the standard deviation.	166
5.10	Map of the cloud longwave radiative forcing of the surface for Northern Hemisphere winter (Wm^{-2}): (a) distribution of the seasonal average, and (b) distribution of the standard deviation.	167
5.11	Map of the cloud longwave radiative forcing of the atmosphere for Northern Hemisphere winter (Wm^{-2}): (a) distribution of the seasonal average, and (b) distribution of the standard deviation.	168
5.12	Zonally-averaged distribution of the cloud longwave radiative forcing for Northern Hemisphere winter (Wm^{-2}): (a) distribution of the seasonal average, and (b) distribution of the standard deviation.	169
5.13	Map of the total cloud shortwave radiative forcing for Northern Hemisphere winter (Wm^{-2}): (a) distribution of the seasonal average, and (b) distribution of the standard deviation.	171
5.14	Map of the cloud shortwave radiative forcing of the surface for Northern Hemisphere winter (Wm^{-2}): (a) distribution of the seasonal average, and (b) distribution of the standard deviation.	172
5.15	Map of the cloud shortwave radiative forcing of the atmosphere for Northern Hemisphere winter (Wm^{-2}): (a) distribution of the seasonal average, and (b) distribution of the standard deviation.	173

5.16	Zonally-averaged distribution of the cloud shortwave radiative forcing for Northern Hemisphere winter (Wm^{-2}): (a) distribution of the seasonal average, and (b) distribution of the standard deviation.	174
5.17	Time series of the total cloud cover at a single grid-point located at 2.2°N-150.0°W, for Northern Hemisphere winter (%): (a) predicted with the NCAR CCM and, (b) derived from satellite radiances (CMATRIX).	180
5.18	Time series of the total cloud cover at a single grid-point located at 46.7°N-150.0°W, for Northern Hemisphere winter (%): (a) predicted with the NCAR CCM, and (b) derived from satellite radiances (CMATRIX).	181
6.1	Schematic representation of the vertical distribution of clouds in the model and the division into high-, middle-, and low-level clouds (from Slingo, 1987).	190
6.2	Map of the ECMWF convective cloud cover (%): (a) monthly average, and (b) standard deviation.	191
6.3	Map of the ECMWF high-level cloud cover (%): (a) monthly average, and (b) standard deviation.	192
6.4	Map of the ECMWF middle-level cloud cover (%): (a) monthly average, and (b) standard deviation.	193
6.5	Map of the ECMWF low-level cloud cover (%): (a) monthly average, and (b) standard deviation.	194
6.6	Map of the ECMWF total cloud cover (%): (a) monthly average, and (b) standard deviation.	195
6.7	90-day time series of the total cloudiness at a single grid-point located at 2.2°N-150°W and 46.7°N-150°W obtained with (a) the CONTROL, and (b) the ECMWF cloud prediction schemes, for January conditions (%).	198
6.8	90-day time series of the outgoing infrared radiation at a single grid-point located at 2.2°N-150°W and 46.7°N-150°W obtained with (a) the CONTROL, and (b) the ECMWF cloud prediction schemes, for January conditions ($W m^{-2}$).	199
6.9	90-day time series of the planetary albedo at a single grid-point located at 2.2°N-150°W and 46.7°N-150°W obtained with (a) the CONTROL, and (b) the ECMWF cloud prediction schemes, for January conditions (%).	200
6.10	Map of the total cloud cover computed from the CONTROL simulation, for January conditions (%): (a) distribution of the monthly average, and (b) distribution of the standard deviation.	202
6.11	Map of the difference in the total cloud cover between the ECMWF and CONTROL simulations, for January conditions (%): (a) distribution of the monthly average, and (b) distribution of the standard deviation.	203
6.12	Latitude-height distribution of the cloud cover obtained from the CONTROL simulation (%): (a) monthly-average, and (b) standard deviation.	206
6.13	Latitude-height distribution of the difference in the cloud cover between the ECMWF and CONTROL simulations (%): (a) monthly average, and (b) standard deviation.	207
6.14	Vertical distribution of the cloudiness for single grid-points located at low latitudes (%).	208
6.15	Vertical distribution of the cloudiness for single grid-points located in the middle latitudes (%).	209

6.16	Latitude-height distribution of the temperature obtained from the CONTROL simulation (K): (a) monthly average, and (b) standard deviation.	211
6.17	Latitude-height distribution of the difference in the temperature between the ECMWF and CONTROL simulations (K): (a) monthly average, and (b) standard deviation.	212
6.18	Map of the 1-day lag autocorrelation coefficient of the temperature at $\sigma = .811$ (tenths): (a) CONTROL simulation, and (b) ECMWF simulation.	214
6.19	Map of the 2-day lag autocorrelation coefficient of the temperature at $\sigma = .811$ (tenths): (a) CONTROL simulation, and (b) ECMWF simulation.	215
6.20	Map of the 3-day lag autocorrelation coefficient of the temperature at $\sigma = .811$ (tenths): (a) CONTROL simulation, and (b) ECMWF simulation.	216
6.21	Latitude-height distribution of the relative humidity obtained from the CONTROL simulation (%): (a) monthly average, and (b) standard deviation.	219
6.22	Latitude-height distribution of the difference in the relative humidity between the ECMWF and CONTROL simulations (%): (a) monthly average, and (b) standard deviation.	220
6.23	Map of the 1-day lag autocorrelation coefficient of the relative humidity at $\sigma = .811$ (tenths): (a) CONTROL simulation, and (b) ECMWF simulation.	221
6.24	Map of the 2-day lag autocorrelation coefficient of the relative humidity at $\sigma = .811$ (tenths): (a) CONTROL simulation, and (b) ECMWF simulation.	222
6.25	Map of the 3-day lag autocorrelation coefficient of the relative humidity at $\sigma = .811$ (tenths): (a) CONTROL simulation, and (b) ECMWF simulation.	223
6.26	Monthly average of the cloud longwave radiative forcing (Wm^{-2}): (a) global distribution of the difference between the ECMWF and CONTROL simulations, and (b) zonally-averaged distribution.	226
6.27	Standard deviation of the cloud longwave radiative forcing (Wm^{-2}): (a) global distribution of the difference between the ECMWF and CONTROL simulations, and (b) zonally-averaged distribution.	227
6.28	Monthly average of the cloud shortwave radiative forcing (Wm^{-2}): (a) global distribution of the difference between the ECMWF and CONTROL simulations, and (b) zonally-averaged distribution.	229
6.29	Standard deviation of the cloud shortwave radiative forcing (Wm^{-2}): (a) global distribution of the difference between the ECMWF and CONTROL simulations, and (b) zonally-averaged distribution.	230
6.30	Monthly average of the outgoing infrared radiation (Wm^{-2}): (a) global distribution of the difference between the ECMWF and CONTROL simulations, and (b) zonally-averaged distribution.	233
6.31	Standard deviation of the outgoing infrared radiation (Wm^{-2}): (a) global distribution of the difference between the ECMWF and CONTROL simulations, and (b) zonally-averaged distribution.	234
6.32	Monthly average of the planetary albedo (%): (a) global distribution of the difference between the ECMWF and CONTROL simulations, and (b) zonally-averaged distribution.	236
6.33	Standard deviation of the planetary albedo (%): (a) global distribution of the difference between the ECMWF and CONTROL simulations, and (b) zonally-averaged distribution.	237

7.1	Time series of the total condensation rate obtained from the HYDRO and CONTROL simulations at a single grid-point located at 2.2°N-150.0°W ($10^2 \text{ g cm}^{-2} \text{ day}^{-1}$): (a) $\sigma = .245$, (b) $\sigma = .165$, and (c) $\sigma = .110$	247
7.2	Time series of the total condensation rate obtained from the HYDRO and CONTROL simulations at a single grid-point located at 46.7°N-150.0°W ($10^2 \text{ g cm}^{-2} \text{ day}^{-1}$): (a) $\sigma = .245$, (b) $\sigma = .165$, and (c) $\sigma = .110$	248
7.3	Time series of the total cloud cover (%) predicted with the HYDRO and CONTROL simulations at a single grid-point located at: (a) 2.2°N-150.0°W, and (b) 46.7°N-150.0°W.	249
7.4	Zonally-averaged distribution of the mostly cloudy sky frequency (total cloud cover greater than 80 %) for the HYDRO and CONTROL simulations (%).	250
7.5	30-day average of the large-scale precipitation rate (mm day^{-1}): (a) global distribution computed from the CONTROL simulation, and (b) zonally-averaged distribution.	253
7.6	30-day average of the convective precipitation rate (mm day^{-1}): (a) global distribution computed from the CONTROL simulation, and (b) zonally-averaged distribution.	254
7.7	30-day average of the total precipitation rate (mm day^{-1}): (a) global distribution computed from the CONTROL simulation, and (b) zonally-averaged distribution.	255
7.8	30-day average of the evaporation rate (mm day^{-1}): (a) global distribution computed from the CONTROL simulation, and (b) zonally-averaged distribution.	256
7.9	Latitude-height distribution of the 30-day average of the specific humidity (10^3 Kg Kg^{-1}): (a) distribution computed from the CONTROL simulation, and (b) difference between the HYDRO and CONTROL simulations.	257
7.10	Latitude-height distribution of the 30-day average of the relative humidity (%): (a) distribution computed from the CONTROL simulation, and (b) difference between the HYDRO and CONTROL simulations.	258
7.11	Map of the difference in the total cloud cover between the HYDRO and CONTROL simulations (%): (a) distribution of the 30-day average, and (b) distribution of the standard deviation.	262
7.12	Latitude-height distribution of the 30-day average of the cloud cover: (a) computed from the CONTROL simulation, and (b) difference between the HYDRO and CONTROL simulations.	263
7.13	Latitude-height distribution of the 30-day average of the effective cloud cover (%): (a) computed from the CONTROL simulation, and (b) difference between the HYDRO and CONTROL simulations.	264
7.14	Latitude-height distribution of the difference in the standard deviation of the cloudiness between the HYDRO and CONTROL simulations (%): (a) cloud cover, and (b) effective cloud cover.	265
7.15	30-day average of the outgoing infrared radiation (Wm^{-2}): (a) global distribution of the difference between the HYDRO and CONTROL simulations, and (b) zonally-averaged distribution.	267
7.16	Standard deviation of the outgoing infrared radiation (Wm^{-2}): (a) global distribution of the difference between the HYDRO and CONTROL simulations, and (b) zonally-averaged distribution.	268

7.17	30-day average of the planetary albedo (%): (a) global distribution of the difference between the HYDRO and CONTROL simulations, and (b) zonally-averaged distribution.	269
7.18	Standard deviation of the planetary albedo (%): (a) global distribution of the difference between the HYDRO and CONTROL simulations, and (b) zonally-averaged distribution.	270
7.19	Latitude-height distribution of the longwave radiative heating rate (K day^{-1}): (a) 30-day average computed from the CONTROL simulation, and (b) difference between the HYDRO and CONTROL simulations.	274
7.20	Latitude-height distribution of the shortwave radiative heating rate (K day^{-1}): (a) 30-day average computed from the CONTROL simulation, and (b) difference between the HYDRO and CONTROL simulations.	275
7.21	Latitude-height distribution of the latent heating (K day^{-1}): (a) 30-day average computed from the CONTROL simulation, and (b) difference between the HYDRO and CONTROL simulations.	278
7.22	Latitude-height distribution of the sum of the net radiative and latent heating rates (K day^{-1}): (a) 30-day average computed from the CONTROL simulation, and (b) difference between the HYDRO and CONTROL simulations.	279
7.23	Vertically-integrated global distribution of the sum of the net radiative and latent heating rates (K day^{-1}): (a) 30-day average computed from the CONTROL simulation, and (b) difference between the HYDRO and CONTROL simulations.	280
7.24	Latitude-height distribution of the atmospheric temperature (K): (a) 30-day average computed from the CONTROL simulation, and (b) difference between the HYDRO and CONTROL simulations.	286
7.25	Latitude-height distribution of the zonal wind (m s^{-1}): (a) 30-day average computed from the CONTROL simulation, and (b) difference between the HYDRO and CONTROL simulations.	287
7.26	Latitude-height distribution of the vertical velocity (10^4 m b s^{-1}): (a) 30-day average computed from the CONTROL simulation, and (b) difference between the HYDRO and CONTROL simulations.	288

LIST OF TABLES

2.1	Wavelength spectral interval of the ERB channels of the Nimbus-7 scanner radiometers (from Jacobowitz <i>et al.</i> , 1984).	30
2.2	Scanning radiometer target areas for the Nimbus-7 mission.	31
2.3	Radiative Budget Statistics for individual 4.5° grid-boxes.	40
2.4	Characteristics of the ERBE mission and scanner instruments (from Luther <i>et al.</i> , 1986, and Kopia, 1986).	51
2.5	Characteristics of the Nimbus-7 and NOAA satellites (from Gruber and Jacobowitz, 1985).	60
1		
3.1	Vertical σ -coordinate system. σ and σH^* refer to the full- and half-levels.	88
3.2	Initial atmospheric data set.	88
3.3	Global average of the ensemble average and ensemble standard deviation of the time average and time standard deviation (σ) of the temperature (T) and net radiation budget (NET) fields.	89
4.1	List of time-span realizations used to build the various climate ensembles.	93
4.2	Globally-averaged values of the seasonal average and standard deviation of the Nimbus-7 and model-generated radiation fields. All the fields are given in Wm^{-2} , except the planetary albedo which is in %.	144
5.1	Globally-averaged cloud radiative forcing at the top of the atmosphere (TOA), of the surface (SFC), and of the atmosphere (ATM), computed from the model-generated radiation fields for Northern Hemisphere winter.	176
6.1	List of time-span realizations used for comparison between the CONTROL and ECMWF climate simulations, for perpetual January conditions.	241
6.2	Globally-averaged values of the monthly average and standard deviation of the model-generated radiation fields. All the fields are given in $W m^{-2}$, except the planetary albedo and the total cloud cloudiness which are in %.	241
7.1	Globally-averaged values of the 30-day averaged components of the hydrologic budget. All the fields are in $mm day^{-1}$, except the total cloud cover which is %.	289
7.2	Globally-averaged values of the 30-day average and standard deviation of the planetary radiation budget components. All the fields are in Wm^{-2} , except the planetary albedo which is in %.	289

Chapter 1

INTRODUCTION

The only energy exchanges between the earth-atmosphere system and space take place through radiation. At the top of the atmosphere, the radiation balance is defined as the difference between the absorbed solar radiation, a unique source of energy, and the outgoing infrared radiation emitted to space by the earth's surface and atmosphere, a unique sink of energy. Mathematically, this difference, called the net radiation may be written as:

$$NET = S_o(1 - \alpha) - IR, \quad (1.1)$$

where S_o is the solar constant, α the planetary albedo, and IR the outgoing infrared radiation at the top of the atmosphere. On an annual average, the net radiation is positive at low latitudes, changes sign around 40° of latitude at which the maximum meridional energy transport takes place, then decreases monotonically poleward. The seasonal and geographical distributions of the regions of maximum radiative gain are mainly driven by the annual cycle and latitudinal variations of the incident solar radiation. In addition, the gradient of net radiation undergoes important zonal variations with the seasons because of the temperature contrast between land and ocean. The differential heating between different areas of the globe sets the local winds and drives the general circulation of the atmosphere and the oceans. The geographical distribution of the sources and sinks of net radiative energy plays, therefore, a major role in the maintenance of climate at both regional and global scales.

In the climate system, clouds are one of the key climate components to affect the dynamics of the atmosphere through complex couplings between radiative, thermodynamic,

and dynamic processes (Arakawa, 1975). Although the role of clouds in climate and the nature of the interactions between clouds and the large-scale circulation are not completely understood, it has been long recognized that clouds play a significant role in the redistribution of the total atmospheric diabatic heating. The change in the diabatic components, which in turn influences the large-scale atmospheric motions, may be partially attributed to interactions between clouds and radiation, and between clouds and the hydrologic cycle via evaporation, condensation and precipitation.

Clouds modify the vertical distribution of the radiative heating and cooling rates. At short wavelengths ($0.15\mu\text{ m} \leq \lambda \leq 4.0\mu\text{ m}$), clouds reflect radiation and contribute a major part to the planetary albedo. At long wavelengths ($4.0\mu\text{ m} \leq \lambda \leq 100\mu\text{ m}$), clouds absorb and reemit radiation, thus reducing the amount of infrared radiation lost to space and enhancing the greenhouse warming of the atmosphere. As a result, changes in cloudiness may critically modify the planetary radiation budget in two competing ways. However, the relative magnitude of the albedo effect versus the greenhouse effect of clouds also depends upon the cloud optical thickness and the cloud height, and a change in the global cloud cover is still the subject of some debate.

Our understanding of the role of clouds on the large-scale dynamics of the atmosphere is as important to improve as of the impact of clouds on radiation. Clouds modify the heat budget of the surrounding environment through latent heat release and indirectly affect the large-scale motions. For example, satellite observations show that in the first stage of its development, a convective cloud cluster consists of isolated precipitating towers (Leary and Houze, 1979). In its mature stage, the original cloud tops have horizontally spread into an extended upper tropospheric cloud shield connecting the isolated *hot towers*. Houze (1982) analyzes the variations of the sensible heat budget of a large-scale area containing an idealized cloud cluster. His theoretical study demonstrates that, as the cloud cluster extends into a widespread cloud shield, the net heating increases in the upper troposphere and decreases below. Accordingly, large-scale vertical motions increase aloft and decrease at lower levels in order to restore the balance of the heat budget against

the effects of the cluster. Hartmann *et al.* (1984) further emphasize the importance of the vertical distribution of the diabatic heating profile induced by a mature cloud cluster to the large-scale circulation. Although the impact of the cluster development on the large-scale vertical motion field is clearly established, both studies point out the need of additional observations to compare their results against observed heating profiles. Direct measurements of the earth radiation budget (ERB) from satellites, and parameterization of the interactions between clouds and the other components of the climate system in general circulation models (GCMs), present complementary capabilities to investigate further the role of clouds in climate.

1.1 Scientific contributions from earth radiation budget measurements

Over the last twenty years, measurements of the planetary radiation balance from space have considerably broadened our knowledge of the radiative exchanges between the earth-atmosphere system and space at both short and long radiative wavelengths. House *et al.* (1984) review the history of satellite missions and measurements of the earth radiation budget from the launch of the first American meteorological satellite in 1959 up until the present. Early ERB wide angle field-of-view (WFOV) observations from flat plate instruments produced the first estimates of the shortwave and longwave components of the earth's radiation budget. Vonder Haar and Suomi (1971) summarize 39 months of measurements of the earth's radiation budget from the first (TIROS-type) and second (Nimbus and ESSA) generation United States meteorological satellites taken during the time period 1962-1966. Aside from discussions of the distributions of the globally- and seasonally-averaged values of the radiation balance, they produce estimates of the mean annual and seasonal values of the equator-to-pole gradient of net radiation, and of the total poleward energy transport and its major components. Raschke and Bandeen (1970) provide global maps of the emitted longwave radiation, the reflected solar radiation, and the net radiation based on Nimbus-II satellite observations during the period 16 May-28 July 1966. Measurements of the same quantities taken from radiometers on board the satellite Nimbus-III during 10 semi-monthly periods between April 1969

and February 1970, yielded the first latitude versus time cross-sections of the planetary radiation balance components (Raschke *et al.*, 1973). Finally, Jacobowitz *et al.* (1979) give refined measurements of the annual mean planetary albedo (31 %) and of the longwave radiation flux (234 Wm^{-2}) based on the first 18 months of ERB observations from the Nimbus-6 experiment.

At the present time, the annual cycle of the solar and infrared radiation components is accurately understood over the whole globe. Annual and seasonal averages of the outgoing infrared radiation, the reflected solar radiation, and the net radiation as measured from various instrument packages have been archived, so that a climatology of the mean steady state of the planetary radiation balance is available for climate research and climate modeling (Stephens *et al.*, 1981; Gruber, 1985; Kyle *et al.*, 1985). In particular, the Nimbus-7 experiment is still adding to the first multi-year data set from the same array of instruments. Starting in November 1978 and extending through October 1985, seven years of broad-spectral-band WFOV measurements of the outgoing infrared radiation, the planetary albedo, and the net radiation have been consistently recalibrated and processed for studies of climate, including interannual variability (Smith *et al.*, 1986), and for research on potential climate changes. Ardanuy *et al.* (1986) demonstrate that the Nimbus-7 ERB data for the wide angle field-of-view can be successfully used to observe outgoing longwave anomalies induced by an El Niño/Southern Oscillation event. In their study, the outgoing longwave radiative response to the 1982/1983 El Niño is obtained from analyses of the resultant fields and anomalies with respect to a five-year climatology of WFOV outgoing infrared data. Kyle and Vasanth (1986) analyze the differences in the reflectance characteristics between land and ocean from WFOV near-ultraviolet and near-infrared reflected solar radiation measurements. On an annual average, the albedo of the Northern Hemisphere is found to be 2 or 3 % larger than that of the Southern Hemisphere, although the summer hemisphere is always the brightest. Most of the broad-spectral-band ERB measurements over the whole globe are WFOV measurements, with the exception of 20 months of infrared and solar radiation data taken by the relatively narrow angle field-of-view (NFOV) scanner radiometers on board the satellite Nimbus-7

during the time period between November 1978 and June 1980¹. Although WFOV observations are making important contributions in our quest of a better understanding of the global mean climate and of the meridional energy transport by the atmosphere and the oceans (Oort and Vonder Haar, 1976; Carissimo *et al.*, 1985), their spatial resolution of about 1000 km is too coarse for regional energy budget studies.

The role of Earth Radiation Budget data in climate and general circulation research at shorter temporal and spatial scales has been reemphasized since the beginning of the Earth Radiation Budget Experiment (ERBE) in November 1984. The implementation of the ERBE program and the scientific objectives are described in detail in Barkstrom and Smith (1986). In summary, this experiment consists of three satellites loaded with identical broad-spectral-band instruments, but with different orbital characteristics. NOAA-9 and NOAA-10 were launched into sun-synchronous orbits whereas the third satellite, the Earth Radiation Budget Satellite (ERBS), was positioned into a low inclination precessing orbit, so that ERB data at a given satellite sub-point can be taken at multiple local times. In addition to wide and medium angle field-of-view measurements, NFOV measurements taken by the ERBE scanners are becoming available for the entire globe on a 2.5° latitude by 2.5° longitude grid. These measurements are expected to be especially useful to study regional energy budgets and to determine the time and space correlations of the radiation balance components and their relationship with the life cycles of cloud systems. Hartmann *et al.* (1986) and Ramanathan (1987) describe how ERB measurements have been used in the past and stress the major contributions that ERB measurements, especially with the aid of ERBE scanner data, will continue to make in the near future. Two of these major contributions are an increased understanding of the role of clouds in climate and validation of long-term climate simulations carried out with atmospheric GCMs.

Most of the crucial but still unanswered questions about the role of clouds in climate are concerned with *cloud-radiation-climate* interactions, cloud radiative forcing, and cloud feedback processes. Some of these questions, taken from Ramanathan are listed below:

¹The scanning mechanisms ceased functioning in June 1980.

1. What is the net radiative effect (i.e., heating or cooling) of the present-day cloud distribution in climate?
2. What is the influence of cloud radiative forcing on the general circulation of the atmosphere and the oceans ?
3. How does one formulate the cloud-climate feedback problem within the context of ERB data ?
4. How does one use ERB data to verify radiation models of atmospheric longwave radiation and surface albedo ?

The sensitivity of the net radiation to a change in cloudiness has been extensively examined in the past from satellite observations (Cess, 1976; Ellis, 1978; Hartmann and Short, 1980; Ohring and Clapp, 1980; Cess *et al.*, 1982). The numerous methods developed to compute the sensitivity parameters to a change in the cloud cover can be found in an exhaustive review by Ohring and Gruber (1983). All of these studies, with the exception of Cess, conclude that clouds are more efficient in reducing the amount of absorbed solar radiation at the top of the atmosphere than in increasing the amount of infrared radiation emitted back to the surface, so that an overall increase in globally-averaged cloudiness would lead to an overall cooling of the earth-atmosphere system.

Hartmann and Short (1980) define a sensitivity parameter, the *cloud factor*, which is the simplest sensitivity parameter used in the different studies referenced above. It only requires measurements of the planetary albedo and of the total outgoing infrared radiation, whereas other sensitivity parameters require an additional data set of the global cloud distribution. They show that there are important geographical variations in the radiative effects of clouds, but that an increase in the fractional area of the current distribution of cloudiness would, overall, tend to cool the earth. However, they employed narrow-spectral-band satellite observations converted to broad-band values at both short and long wavelengths, and their results have to be, therefore, analyzed with caution.

Ramanathan (1987) introduces the concept of the cloud longwave and shortwave radiative forcings, simply defined as the difference between the clear-sky and total radiative

fluxes. The cloud forcing is comprised of the direct radiative effect of clouds plus the contribution of the embedded feedback mechanisms between clouds and the other components of the climate system. On the one hand, because NFOV observations necessary to obtain the clear-sky fluxes are scarce, few estimates of the cloud radiative forcing from space-based platforms are available. On the other hand, the forcing of clouds on long-wave and shortwave radiation is routinely computed from climate simulations with GCMs (Ramanathan, 1987; Slingo and Slingo, 1987). Slingo and Slingo find that the globally-averaged cloud forcing predicted by one GCM is equal to -21 Wm^{-2} , so that the net effect of clouds is to cool the climate system, a result in agreement with the earlier studies listed above.

A second contribution of ERB measurements is the validation of the top-of-atmosphere radiation balance obtained from long-term simulations with GCMs. The support of satellite or more conventional observations is required in climate modeling for (1) direct input for initialization and /or updating, (2) developing parameterizations for model processes, and (3) testing the validity of models. Because GCMs are greatly simplified representations of the real climate system and are tuned to represent today's climate, it is not obvious that they can successfully simulate climate fluctuations or climate forcings. Therefore, the validation of climate simulations made with GCMs, and especially the ability of these models to reproduce the different order climate statistics, has become a priority of the World Climate Research Program as discussed in Thiele and Schiffer (1985).

Observations of the earth's radiation budget from space-borne instruments are certainly one of the most suitable and convenient means for objective comparison with model outputs. Broad-spectral-band ERB measurements from polar-orbiting satellites possess several advantages over more conventional data. They provide the necessary boundary conditions that GCMs have to conform to. They are simply defined, spectrally distinct quantities and are easy to use. They cover the whole globe on a regular daily basis (twice daily at infrared wavelengths) for the narrow angle field-of-view, and on a weekly basis for the wide angle field-of-view. Finally, they are taken from the same array of carefully calibrated instruments over a long time period and are, therefore, consistent quantities.

Most validations of GCM climate simulations have been limited to a comparison with the time-averaged solar and infrared radiation fields (Geleyn *et al.*, 1982; Slingo, 1985), while few or no studies have actually dealt with the comparison of the second- and higher-order climate statistics.

1.2 Scientific contributions from general circulation models

General circulation models of the atmosphere constitute, at the present time, the top rank in the hierarchy of physically-based climate models. They are three-dimensional spectral numerical models which explicitly simulate the large-scale characteristics of the atmospheric circulation and which include the fundamental physical mechanisms involved in climate. The increasing complexity in the parameterizations of the numerous processes which GCMs take into account has closely followed the parallel development of our observational and theoretical knowledge of climate and the growing computational capability of successive generations of computers. Simmons and Bengtsson (1984) summarize the history of the development of three-dimensional atmospheric modeling from the first forecast experiments with baroclinic models (Charney and Phillips, 1953) until the present time. Early versions of GCMs (Phillips, 1956; Smagorinsky *et al.*, 1963) consisted of only two atmospheric layers and radiation was considered as an external thermal forcing to generate the atmospheric motions. The vertical distribution of the radiative heating and cooling rates was computed for prescribed atmospheric absorbers, clouds, and surface albedo, and only varied with latitude to maintain the temperature contrast between the equator and the poles. Successive developments in modeling techniques led to the inclusion of an interactive coupling between the radiative, temperature, and humidity fields, as well as moist processes (Manabe *et al.*, 1965; Manabe, 1969), while clouds were prescribed by climatological, zonally-averaged values. Finally, Figure 1.1 schematically illustrates the atmospheric processes and interactions between processes commonly included in the latest versions of three-dimensional climate models. In particular, GCMs now include dynamically-generated cloudiness, which is interactive with the radiation schemes of short and long wavelengths.

The ability of GCMs to reproduce the characteristic properties of the averaged climate, including its temporal and spatial variability, is limited by their treatment of the interactions between the various physical mechanisms which, in the real atmosphere, mostly take place at mesoscale resolution. The computational cost of long-term climate simulations has forced GCM's modellers to neglect detailed sub-grid scale features, and the reasonably satisfactory behavior of efficient low-spatial-resolution spectral models has led to them being adopted for multi-year integrations (Manabe and Hahn, 1981; Lau, 1981). Consequently, it has been assumed that most of the processes which take place at spatial scales unresolved by the model can be parameterized in terms of the large-scale variables. Prediction of the distribution of cloudiness is a good example of the limitations encountered in three-dimensional climate modeling.

Most GCMs typically distinguish between two kinds of clouds: convective and large-scale clouds (Rutledge and Schlesinger, 1985). For both types, the occurrence of clouds solely depends upon the thermodynamic state of the atmosphere, specifically static stability and relative humidity, and upon their large-scale tendencies. Although condensation usually starts in the real world before the relative humidity reaches 100 %, large-scale clouds in the models form whenever the relative humidity exceeds a prescribed saturation threshold. When saturation does occur, the model grid-box is either totally filled with clouds or the cloud fraction is defined as a simple function of the relative humidity. No prediction scheme currently used in GCMs explicitly takes into account the life cycle of convective cloud clusters, and cirrus shield and upper tropospheric cloud debris are usually included in the large-scale cloudiness parameterization. In addition, the optical properties of clouds (reflectivity, transmissivity, and absorptivity at long and short wavelengths) are prescribed separately.

The necessary ingredients of a realistic parameterization of clouds, i.e., a prognostic equation for condensed water and some memory of the history of the convection, are missing in most current GCMs. As a result, the misrepresentation of the time dependence between the horizontal cloud fraction and the cloud water results in a decoupling between clouds, radiation, and the hydrologic cycle in the atmosphere.

General circulation models are primarily designed to reproduce the steady state climate and its variability in time and space, and to study its sensitivity to external and internal forcings. The atmospheric circulation is primarily driven by the differential heating present between the equator and the poles, while direct atmospheric heating occurs through latent heat release. A model's response is, therefore, highly sensitive to the parameterization schemes of moist convection, radiation and clouds, and surface heating by radiation, as well as to the treatment of boundary-layer clouds and turbulence. The performance of different spectral general circulation models in reproducing the characteristic features of climate and the atmospheric circulation has been extensively discussed by several modeling groups (Schlesinger and Gates, 1980; Hansen *et al.*, 1983; Pitcher *et al.*, 1983; Rind *et al.*, 1988).

The response of a general circulation model to climate perturbations, such as a change of the solar constant (Wetherald and Manabe, 1975) or of the concentration of carbon dioxide (Wetherald and Manabe, 1975), has usually been using a prescribed distribution of cloudiness. Many studies have demonstrated the importance of the inclusion of an interactive cloud prediction scheme in sensitivity experiments and of the basic feedback mechanisms between clouds and the other climate components (Hunt, 1978; Hunt *et al.*, 1980; Wetherald and Manabe, 1980; Meleshko and Wetherald, 1981; Shukla and Sud, 1981, Wetherald and Manabe, 1988). The sensitivity of the solar and infrared radiation balance components to a change in the averaged cloudiness has led a variety of results, which are as inconclusive as those obtained from satellite observations.

Wetherald and Manabe (1980) test the sensitivity of the heat balance, the hydrologic cycle, and the atmospheric circulation to changes of the solar constant with a simplified three-dimensional model, in which either a fixed or a variable distribution of cloudiness is used. They show that the variations in the globally-averaged climate have the same amplitude in both experiments, and conclude that cloud feedback mechanisms have a minor effect on the sensitivity of climate. They attribute their results to a compensation mechanism between variations in the greenhouse and albedo effects resulting from a change in the distribution of the cloud cover. On the other hand, Wetherald and Manabe (1988)

find an opposite result of their earlier study. They show that the inclusion of cloud feedback processes in a GCM of the atmosphere coupled with a mixed layer model of the oceans actually enhances the sensitivity of the model climate to a doubling of the carbon dioxide concentration.

Shukla and Sud compare the impact of a fixed versus a dynamically predicted distribution of clouds on the climate of the general circulation model of the Goddard Laboratory for Atmospheric Sciences (GLAS). In the control run, clouds are internally generated and continuously interact with the radiative heating fields. In the fixed cloud run, clouds are specified on certain grid-points according to their mean frequency of occurrence in the control run and act as zonally asymmetric radiative heat sources. Shukla and Sud find significant changes in the large-scale dynamic circulation, the hydrological cycle, precipitation and evaporation, and in regional climate. Their results suggest that changes in the radiative forcing may yield substantial variations in the total thermal forcing and the dynamic circulation.

At the present time, the importance of dynamically-generated clouds in climate simulations with GCMs is well recognized and sensitivity studies are being performed with the aim to assess the performance of cloud prediction schemes (Hense and Heise, 1984; Slingo and Slingo, 1988).

1.3 Objectives of the dissertation

Considering the results listed above, it is clear that, despite numerous efforts using satellite observations and climate simulations with GCMs, our understanding of the role of clouds in climate and of the interactions between clouds and the other components of the climate system remains limited. Until recently, ERB research has lacked NFOV observations of the reflected solar radiation and of the outgoing infrared radiation which are required to measure the cloud radiative forcing and to relate the variability of the earth's radiation budget to a change in cloudiness. The 20 months of Nimbus-7 NFOV data is the only extended and archived data set of such broad-spectral-band observations and the ERBE NFOV data set will be available in the near future. Prediction of the

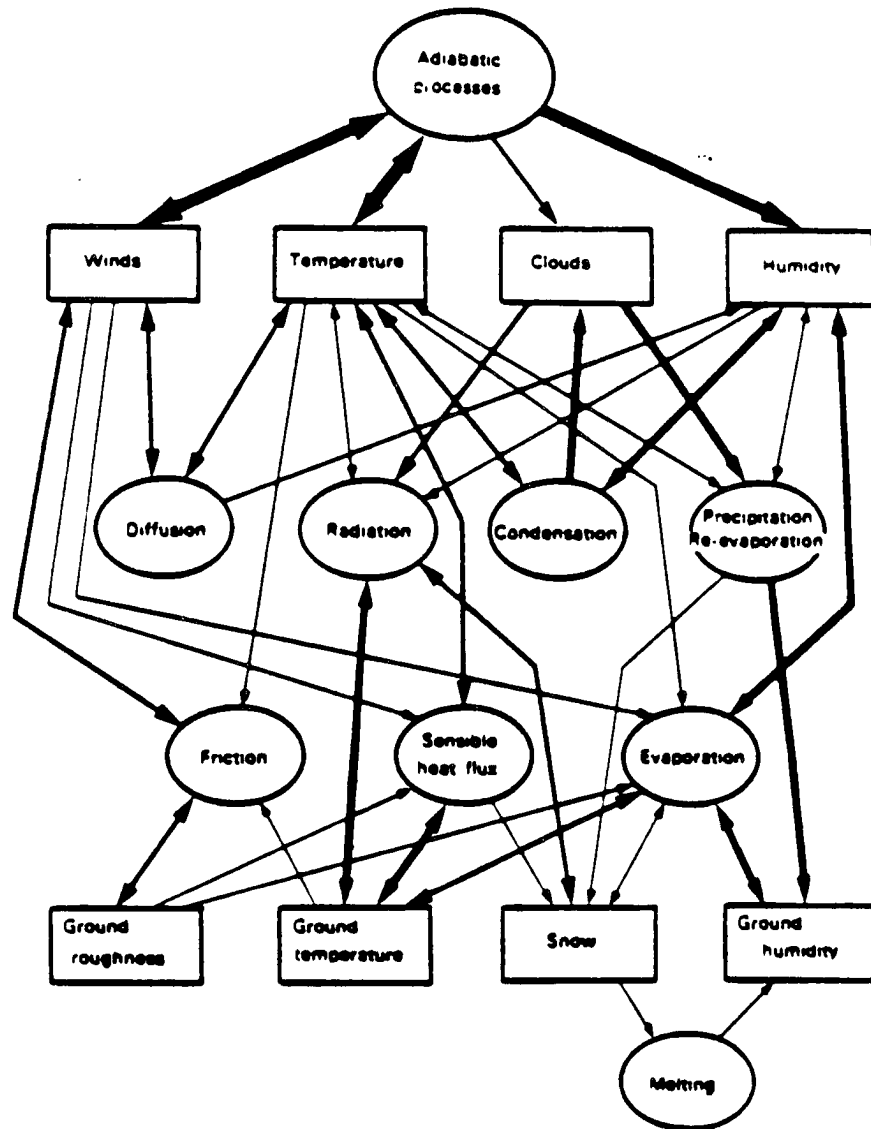


Figure 1.1: Schematic illustration of the processes commonly included in atmospheric general circulation models. The thickness of a particular arrow gives a qualitative indication of the importance of the interaction the arrow represents (from Simmons and Bengtsson, 1984).

distribution of clouds is one of the most difficult tasks in climate modeling. Low-spatial-resolution GCMs do not prognostically take into account the coupling between clouds and the condensed water. As a result, the response of the climate simulated with a GCM to cloud fluctuations does not contain the basic feedback processes between clouds, radiation, and the hydrologic cycle. Despite those negative remarks, several studies emphasize that GCMs are able to successfully reproduce the mean large-scale features of the atmospheric circulation and that their contributions to the understanding of the impact of clouds in climate are as important as these of satellite ERB observations. The first step of an increased role of GCMs to the knowledge of *cloud-radiation-climate* interactions and cloud feedback processes is to assess their ability to simulate the temporal and spatial variability of the earth climate system. In this regard, NFOV ERB measurements certainly constitute the best tool to help validate the top-of-atmosphere radiation balance of a GCM climate simulation.

Within this context, the chief objectives of this work are:

1. To describe the unique characteristics of the daily broad-spectral-band NFOV observations taken by the scanner radiometers on board the satellite Nimbus-7 and to use quantitatively these observations to estimate the temporal variability of the earth's radiation budget and its sensitivity to a change in cloudiness.
2. To use this satellite data set to help validate the top-of-atmosphere radiation budget produced in long-term climate simulations made with the NCAR Community Climate Model (or simply NCAR CCM) developed at the National Center for Atmospheric Research.
3. To demonstrate that the misrepresentation of the interactions between clouds and the hydrologic cycle can be held responsible for most of the differences in temporal variability found between satellite-observed and model-generated radiation balance components.

1.4 Plan of the dissertation

In the following chapter, daily NFOV measurements from the Nimbus-7 ERB experiment during the period between June 1979 and May 1980 are used to compute seasonal averages, and temporal standard deviations about the seasonal average of the longwave and shortwave components of the planetary radiation balance. This data set is the only compilation of simultaneous infrared and solar broad-spectral-band observations archived at present. Therefore, it represents an extremely valuable contribution to the understanding of *cloud-radiation-climate* interactions from space and reference for future research on the temporal and spatial variability of the earth's radiation budget from ERBE scanner data which are not yet available. In particular, new results on the simultaneous fluctuations of the daily mean outgoing infrared radiation and absorbed solar radiation are presented, along with improved maps of the geographical distribution of the *cloud factor* originally discussed by Hartmann and Short (1980).

The newest version of the NCAR Community Climate Model (or version CCM1) is described in the third chapter, with an emphasis on the parameterization of radiation at short and long wavelengths, and of the cloud prediction scheme. The strategy to statistically compare the various climatic fields computed from long-term simulations with CCM1 against real observations is described, and follows the method proposed by Chervin (1981). The simulated earth's radiation budget is obtained from a 15-year run including a seasonal cycle and from a 1500-day integration for perpetual January conditions.

In the fourth chapter, we discuss the performance of CCM1 to reproduce the longwave and shortwave components of the planetary radiation balance against satellite observations. Global maps of the first- and second-order moment climate statistics of the outgoing infrared radiation, the planetary albedo, and the absorbed solar radiation, are compared for Northern Hemisphere winter and summer seasons. The chief differences between the model-generated and satellite-derived radiation fields are outlined; these reveal a major deficiency in the representation of the temporal behavior of climate simulations with CCM1.

In Chapter Five, hypotheses on the origins of the discrepancies between model predictions and observations are formulated. In view of the limitations in the parameterization of the cloudiness, and of the interactions between clouds and the other physical processes in CCM1, it is shown that clouds are responsible for the *on* and *off* blinking of the simulated atmosphere. Comparison of the model-generated total cloud cover against cloud estimates from satellite radiance measurements shows that the model does not realistically simulate cloud life-cycles. Analyses of the cloud longwave and shortwave radiative forcings show that the temporal variability of the model-simulated radiation balance components is driven by the high frequency of occurrence of clouds in the model. Finally, two different climate simulations using CCM1 are proposed which are analyzed in the following two chapters.

In Chapter Six, the impact of the cloud prediction scheme on the model-generated radiation fields is studied. The parameterization of clouds currently used in CCM1 has been replaced by an adapted version of the scheme routinely used at the European Centre for Medium Range Weather Forecast (ECMWF), for perpetual January conditions. Analyses of the outgoing infrared radiation and planetary albedo fields show that there exist some differences in the magnitude of the standard deviation, especially at regional scales. However, both the CONTROL and ECMWF cloud prediction schemes yield identical discrepancies in the time variability between the simulated and observed radiation fields.

In Chapter Seven, a simple attempt is made to reduce the temporal variability of the radiation fields by forcing the model to produce clouds more frequently than in the CONTROL run. In contrast to the CONTROL run for which condensation is treated as a complete rainout process, the large-scale precipitation rate in the HYDRO experiment is strongly reduced while the condensed water remaining in the atmosphere is mixed back into the humidity field. More clouds form so that the normalized standard deviation of the total cloud cover decreases and comes into closer agreement with observations. The impact of an increased persistence in the total cloud cover on the model-generated radiation fields

and the general circulation is analyzed to infer the importance of correctly reproducing the temporal variability of the atmosphere in general circulation modeling.

Finally, Chapter Height summarizes the principal new results described in this dissertation and how they may be used as references for future research on the use of satellite radiation budget measurements to validate general circulation models.

Chapter 2

NIMBUS-7 EARTH RADIATION BUDGET EXPERIMENT: TEMPORAL AND SPATIAL VARIABILITY FROM NFOV DATA

2.1 Introduction

In this chapter, daily, NFOV observations taken by the scanner radiometers on board the satellite Nimbus-7 are used to compute the seasonal average and standard deviation about the seasonal average, of the outgoing infrared radiation, the planetary albedo, and the absorbed solar radiation, for Northern Hemisphere winter and summer seasons. The covariance between the outgoing infrared radiation and the absorbed solar radiation is also calculated to locate regions of the globe where simultaneous variability at short and long radiative wavelengths takes place. Analyses of the temporal variability of the shortwave and longwave components of the planetary radiation balance show that its magnitude is mostly driven by day-to-day fluctuations of the cloud cover. The geographical distribution of the sensitivity of the net radiation to a change in the cloud cover is discussed from computation of the sensitivity parameter known as the cloud factor. Our results indicate that the albedo effect of clouds dominates their greenhouse effect, so that an increase of the global cloudiness would certainly lead to an overall cooling of the earth's climate.

2.2 Overview of the Nimbus-7 ERB Experiment

In October 1978, the Nimbus-7 satellite was launched into a sun-synchronous, near-polar orbit, with equatorial crossing times close to local noon in its ascending node and local mid-night in its descending node. The ERB instrument package on board the spacecraft was divided into three separate groups of sensors which independently monitored the spectral and total solar irradiances, as well as the earth solar reflected and earth infrared

emitted radiation fluxes for both wide and narrow angle field-of-views. Descriptions and performances of the three instruments can be found in Jacobowitz *et al.* (1984). Table 2.1 summarizes the wavelength spectral interval of each ERB channel. The spectral solar irradiances were measured using ten different wavelength intervals whereas four flat plate, hemispheric sensors (or fixed WFOV channels) monitored the shortwave and longwave irradiances at the satellite altitude. A group of four identical broad-spectral-band, relatively NFOV scanner radiometers were used to record the angular dependence of the shortwave and longwave earth radiances, and to obtain synoptic and planetary scale observations of the earth-atmosphere radiation balance.

Solar irradiance data, WFOV and NFOV shortwave and longwave components of the planetary radiation balance were averaged into daily, weekly, and monthly values stored on the so-called Matrix tapes into 2070 target grids of approximately equal surface area of 500 km by 500 km. Table 2.2 gives the latitude and longitude coordinates of the target areas. Jacobowitz *et al.* (1984) discuss the first year of the Nimbus-7 ERB data set between November 1978 and October 1979, in which comparisons are made between WFOV and NFOV radiation budget data. Due to the unfortunate failure in the scanning mechanism, only twenty months of radiation budget measurements taken by the scanner radiometers are available between November 1978 and June 1980. On the other hand, seven years of both total solar irradiance and consistently well-calibrated WFOV observations of the outgoing infrared radiation, the planetary albedo, and the net radiation can be used for various studies of the earth-atmosphere climate system from space-borne instruments.

2.3 Narrow angle field-of-view data set

2.3.1 Scanner instruments

The ERB instrument package had four optical telescopes arranged in a fan shape, each of them containing a shortwave and a longwave optical system. The optical hardware was designed so that the telescope could focus collected radiation alternately on one of the two apertures via a chopping wheel with mirrored teeth. The scan head was on a gimbal mounted on the main frame of the radiometer unit. The gimbal arrangement allowed the

pointing direction of the scan head to be varied within a vertical plane by rotation of the scan head and within a horizontal plane by rotation of the gimbal. The field of views (FOVs) of the four telescopes were rectangular ($0.25^\circ \times 5.12^\circ$) and arranged so that, at the horizon, the upper corners of the FOV's lay along the earth's horizon, the narrow angle (0.25°) side of the FOV being in the direction of vertical motion.

The radiance recorded from various scenes, and over a wide range of incident and emerging angles, was obtained from the combination of five different scan modes, as schematically illustrated in Figure 2.1. Four patterns, repeated every 700 km, were a composite of long and short scans: a long scan in the forward direction was followed by a short scan in the cross-track direction and then concluded with a long scan in the aft direction. The fifth scan, repeated every 1400 km along the subpoint track, was a composite of scan pattern 3 immediately followed by scan pattern 4. The first four scan modes ensured the ability to obtain a maximum number of angular independent views of a given geographical area whereas scan mode 5 was the normal mode of operation yielding maximum earth coverage. This combination of scan patterns consequently gave a fairly complete picture of the angular distribution of radiation emerging from a given region in the scanning field-of-view.

The calibrated radiances and associated viewing angles were used to build models of the angular distribution of the reflected solar and emitted terrestrial radiation for use in processing the narrow-angle data (Taylor and Stowe, 1984). Angular reflectance models were derived for four surface types (land, snow or ice, and clouds) and for 10 ranges of solar zenith angle, while only two models of the emitted radiation were derived (one for latitudes greater than 70° and the second for latitudes less than 70°). Because of power budget requirements on board the satellite, NFOV observations were recorded on a 3-day on, 1-day off cycle. The narrow-angle data, with the aid of angular dependence models, were further converted into fluxes to yield daily, 6-day, and monthly-averaged values of the various radiation budget products (see Appendix A).

2.3.2 Summary of the June 1979-May 1980 ERB data

The annual cycle of the earth radiation budget obtained from NFOV observations over the time period between June 1979 and May 1980 is summarized in Figure 2.2. Latitude-time distributions of the monthly-averaged outgoing infrared radiation, planetary albedo, and net radiation show that the planetary radiation balance undergoes its largest month-to-month-variation in the middle and high latitudes, because of the strong latitudinal and seasonal dependence of the solar radiation incident at the top of the atmosphere. Figure 2.3 shows the characteristic zonally-averaged profiles of the annual and seasonal mean components of the planetary radiation budget. On an annual average, the globally-averaged net radiation is equal to -3.2 Wm^{-2} , which may result from uncertainties in the calibration of the NFOV channels or from the radiance to flux conversion using angular dependence models.

In the following sections, time series spanning between June 1979 to August 1979, and December 1979 to February 1980 of the daily mean outgoing infrared radiation, absorbed solar radiation, and planetary albedo are used for Northern Hemisphere summer and winter seasons (later simply referred as summer and winter). The seasonal averages and standard deviations computed from the seasonal average, are calculated for both seasons. The covariance between the outgoing infrared radiation and the absorbed solar radiation is also computed to demonstrate regions of the globe where simultaneous variability in the shortwave and longwave components of the radiation balance occurs. Finally, estimates of the sensitivity parameter, known as the cloud factor, are calculated to assess the relative importance of the albedo effect versus the greenhouse effect of clouds.

2.4 Outgoing infrared radiation

In the planetary radiation balance equation, the outgoing infrared radiation represents the amount of energy lost to space by the earth-atmosphere system. Its magnitude is a function of the thermal emission of the earth's surface, the tropospheric lapse rate, the vertical distribution of the major absorbing constituents (H_2O , CO_2 , O_3 , and other trace gases), and the cloud cover (cloud amount, cloud emissivity, and cloud-top temperature).

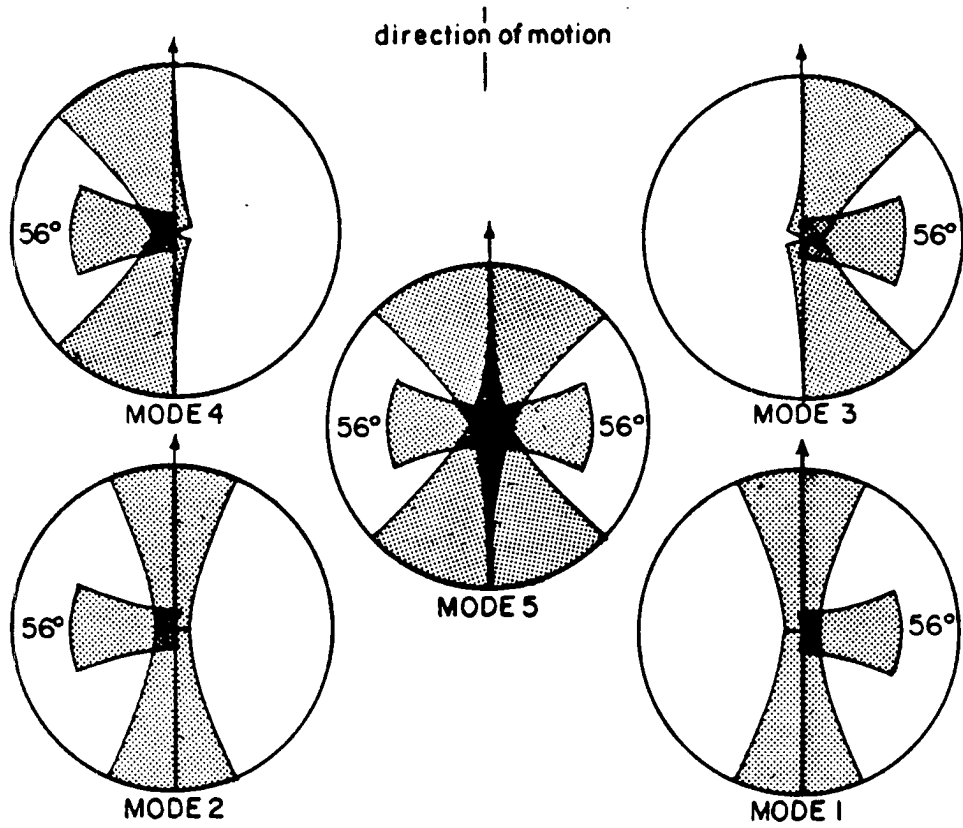


Figure 2.1: ERB scan modes.

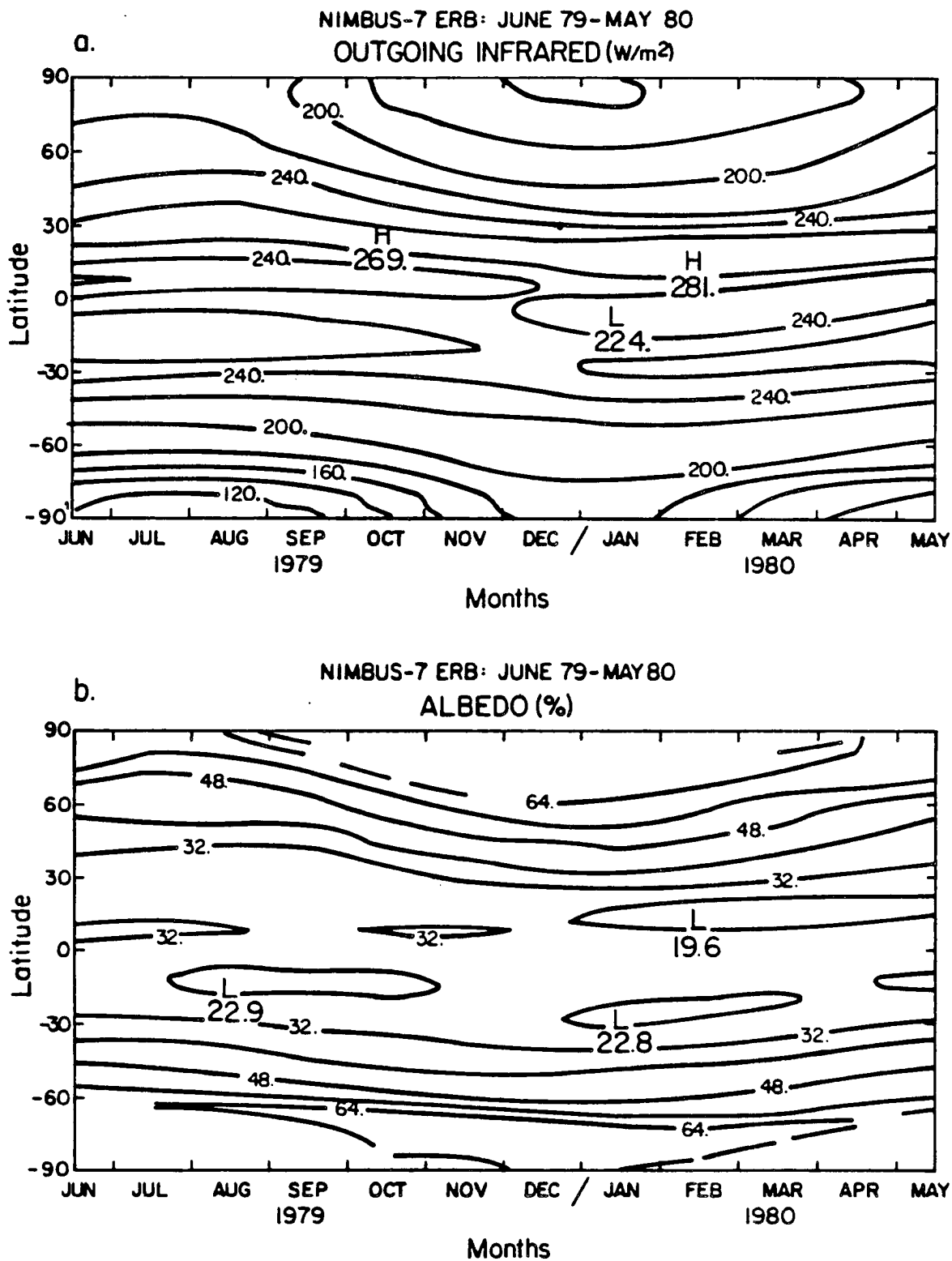


Figure 2.2: Time-latitude distribution derived from the ERB NFOV instruments: (a) outgoing infrared radiation, (b) planetary albedo.

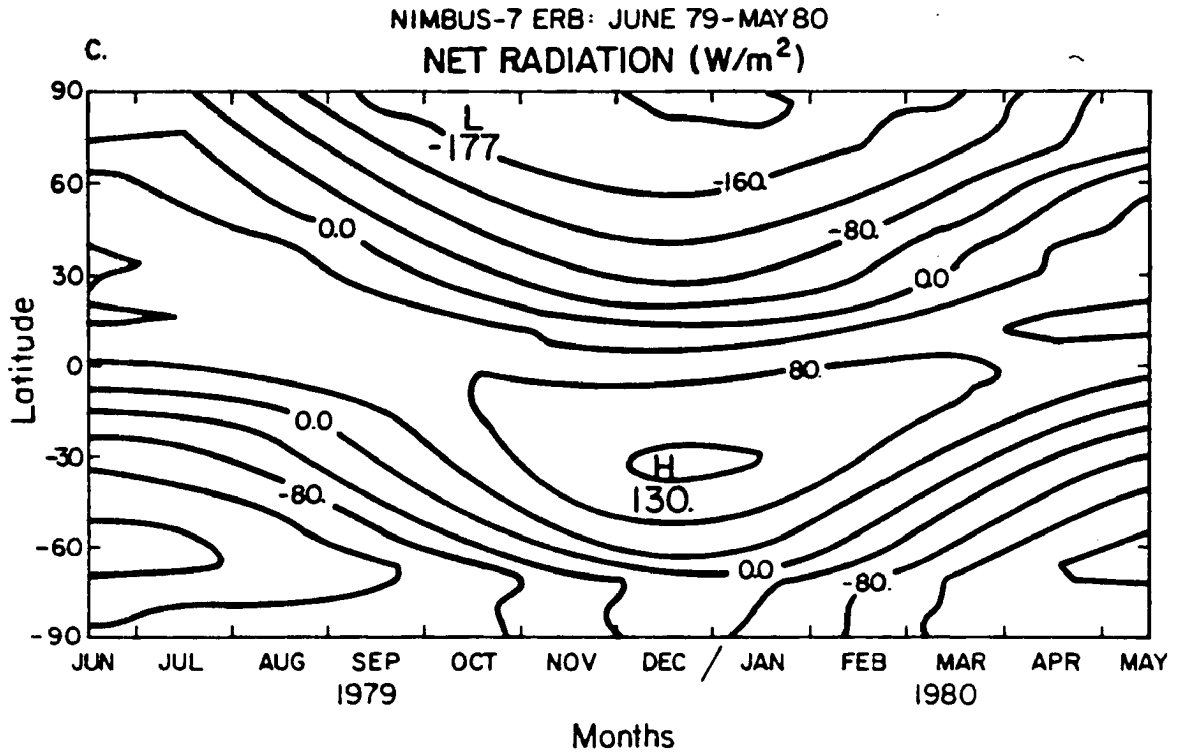


Figure 2.2: Time-latitude distribution derived from the ERB NFOV instruments: (c) net radiation.

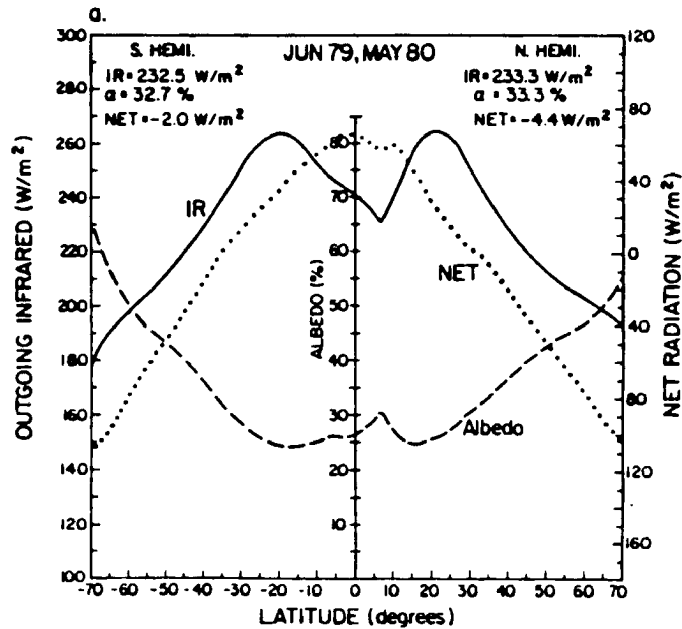


Figure 2.3: (a) Zonally-averaged distribution of the annually-averaged outgoing infrared radiation, planetary albedo, and net radiation.

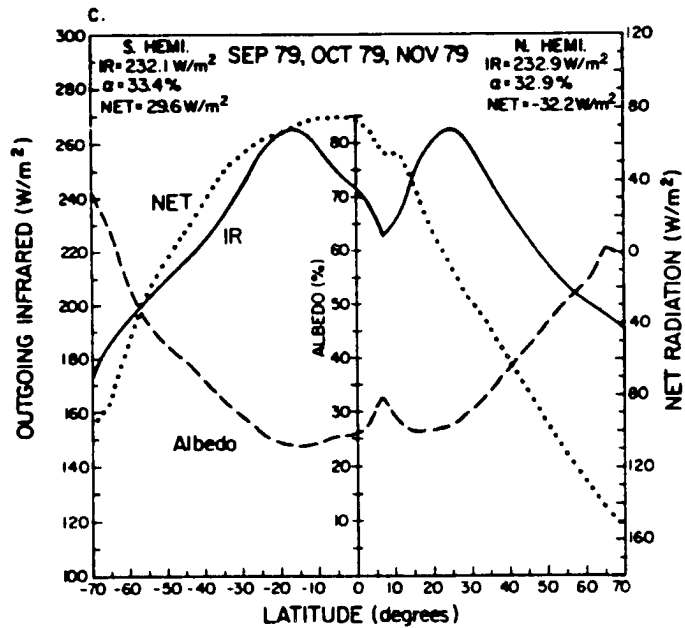
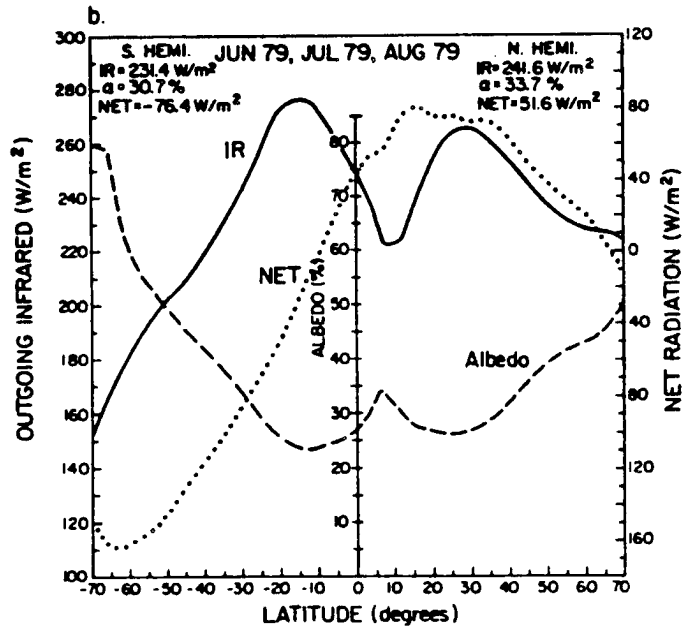


Figure 2.3: Same as Figure 2.3 (a) but for: (b) June 79-July 79-August 79, and (c) September 79-October 79-November 79.

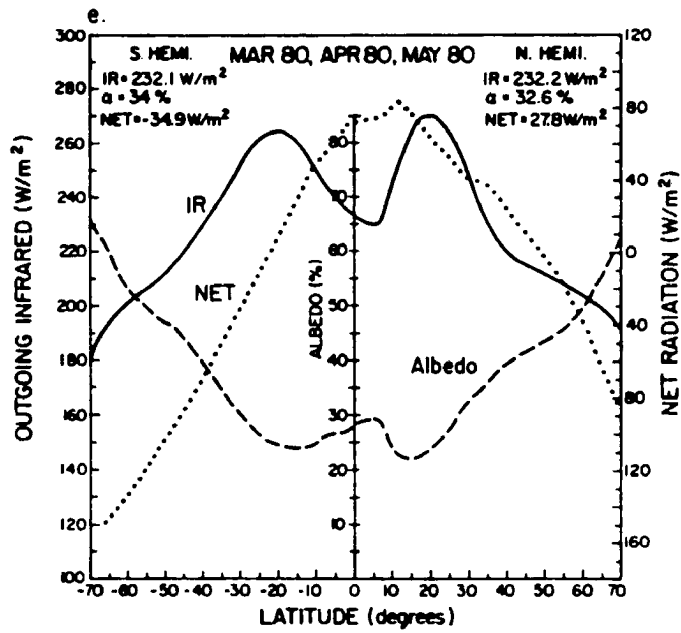
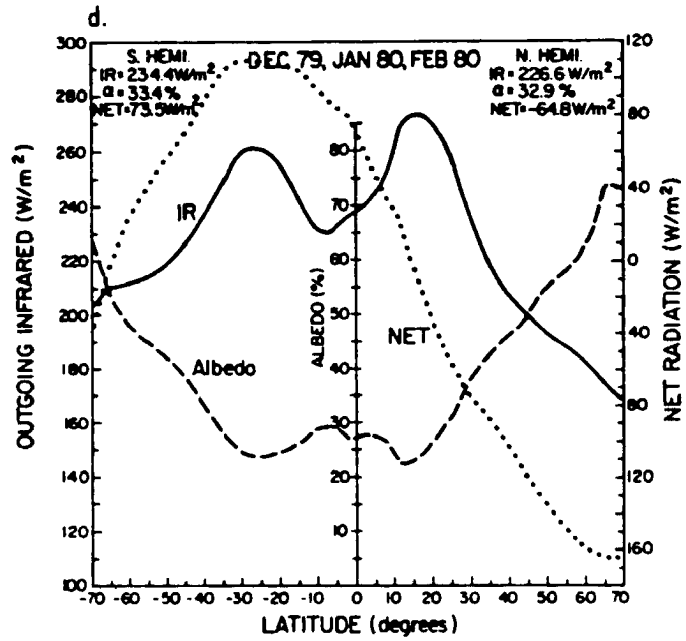


Figure 2.3: Same as Figure 2.3 (a) but for: (d) December 79-January 80-February 80, and (e) March 80-April 80-May 80.

As seen from satellite observations, clouds are the most significant factor in monitoring day-to-day fluctuations of the outgoing infrared radiation. Figures 2.4 and 2.5 show the geographical distributions of the seasonal average (IR) and standard deviation ($\sigma(\text{IR})$) of the daily mean outgoing infrared radiation for the winter and summer seasons.

2.4.1 Seasonal average

Poleward of 40° , the outgoing infrared radiation shows a predominant zonal structure. Its meridional gradient follows closely the northward decrease of the earth's surface and atmospheric temperatures, with tighter isolines located in the winter hemisphere. This feature is particularly well seen over the oceans in the Southern Hemisphere. At the top of the atmosphere, the subtropics are characterized by large areas of infrared emission greater than 280 Wm^{-2} : above the relatively cloud-free Pacific, Atlantic and Indian oceans, and above the major desert regions over the continents (Sahara, Australian and African deserts). In the tropics, the Intertropical Convergence Zone (ITCZ), along which intense upward atmospheric lifting develop into extended cumulus cloud systems, is defined as a relatively narrow band of infrared emission less than 240 Wm^{-2} across the Pacific and Atlantic oceans, as is very well seen in summer. Above the continents, areas of IR less than 240 Wm^{-2} , which are characterized by the development of convective clouds and heavy rainfall, are located above Central America and equatorial Africa in summer, and above South America and southern Africa in winter. Finally, the comparison between Figures 2.4 and 2.5 clearly shows the seasonal shift of the monsoon region. In winter, the monsoon extends between Malaysia and the dateline, and shifts to the northwest above India and the Indonesian peninsula in summer.

2.4.2 Standard deviation about the seasonal average

At poleward latitudes, $\sigma(\text{IR})$ is less than 20 Wm^{-2} because of the small seasonal cycle and low emission of outgoing longwave radiation. At low latitudes, for both winter and summer seasons, mostly clear-sky regions, as the subtropical oceans, and mostly overcast regions, as the deep tropical activity regions over South America, southern Africa, and the monsoon region, are characterized by low values of the standard deviation. On the

other hand, regions which are located at the boundary between mostly cloud-free and overcast regions are characterized by increased values of the standard deviation. Figures 2.4 and 2.5 show that, for both seasons, the variability of the outgoing infrared radiation emitted at the top of the atmosphere is primarily driven by day-to-day fluctuations of clouds, in particular high-level clouds. Tall, cold cloud-top temperature clouds have a strong signature at infrared wavelengths by significantly reducing the loss of thermal radiation at the top of the atmosphere. The generation and dissipation of deep convective clouds, associated with the development of extended cloud anvils and advection of cloud debris, strongly modify the daily magnitude of emitted infrared radiation, which explains high values of $\sigma(\text{IR})$ above those areas. In addition to convective activity regions, semi-permanent frontal regions in the Southern Hemisphere along the eastern coasts of South America and Madagascar are also identified as regions of high values of $\sigma(\text{IR})$.

The standard deviation fails to indicate the major storm track regions of the Northern Hemisphere in winter, above the northwestern Pacific and Atlantic oceans, and the areas of extended stratiform clouds along the western coasts of the continents. The spatial averaging of the satellite pixels into a 4.5° grid is too coarse to separate the thermal emission of the cloud top from that of the ocean surface, especially on a seasonal basis. The persistence of stratocumulus clouds over several days tends to lower $\sigma(\text{IR})$, so that the magnitude of the standard deviation is close to this computed for cloud-free areas. Analyses of Figures 2.4 and 2.5 indicate that the computation of $\sigma(\text{IR})$ helps to distinguish convective and cyclogenetic regions from regions that show a more stationary cloud pattern or are almost cloud-free on a seasonal basis, but that constraints on the time sampling and spatial averaging of the infrared daily data hinder the distinction between convective and stratiform cloud regimes.

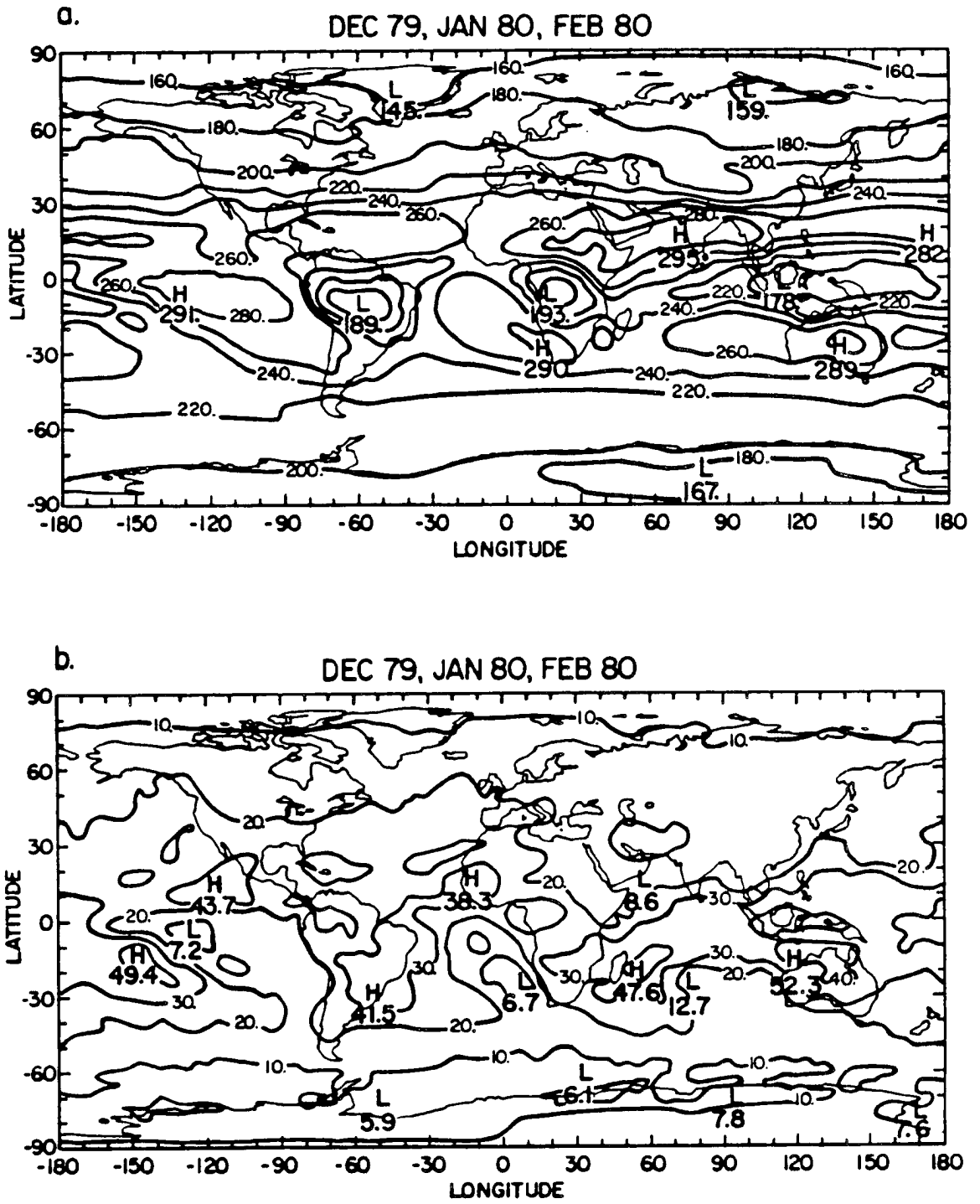


Figure 2.4: Map of the outgoing infrared radiation for Northern Hemisphere winter (Wm^{-2}): (a) seasonal average, and (b) standard deviation.

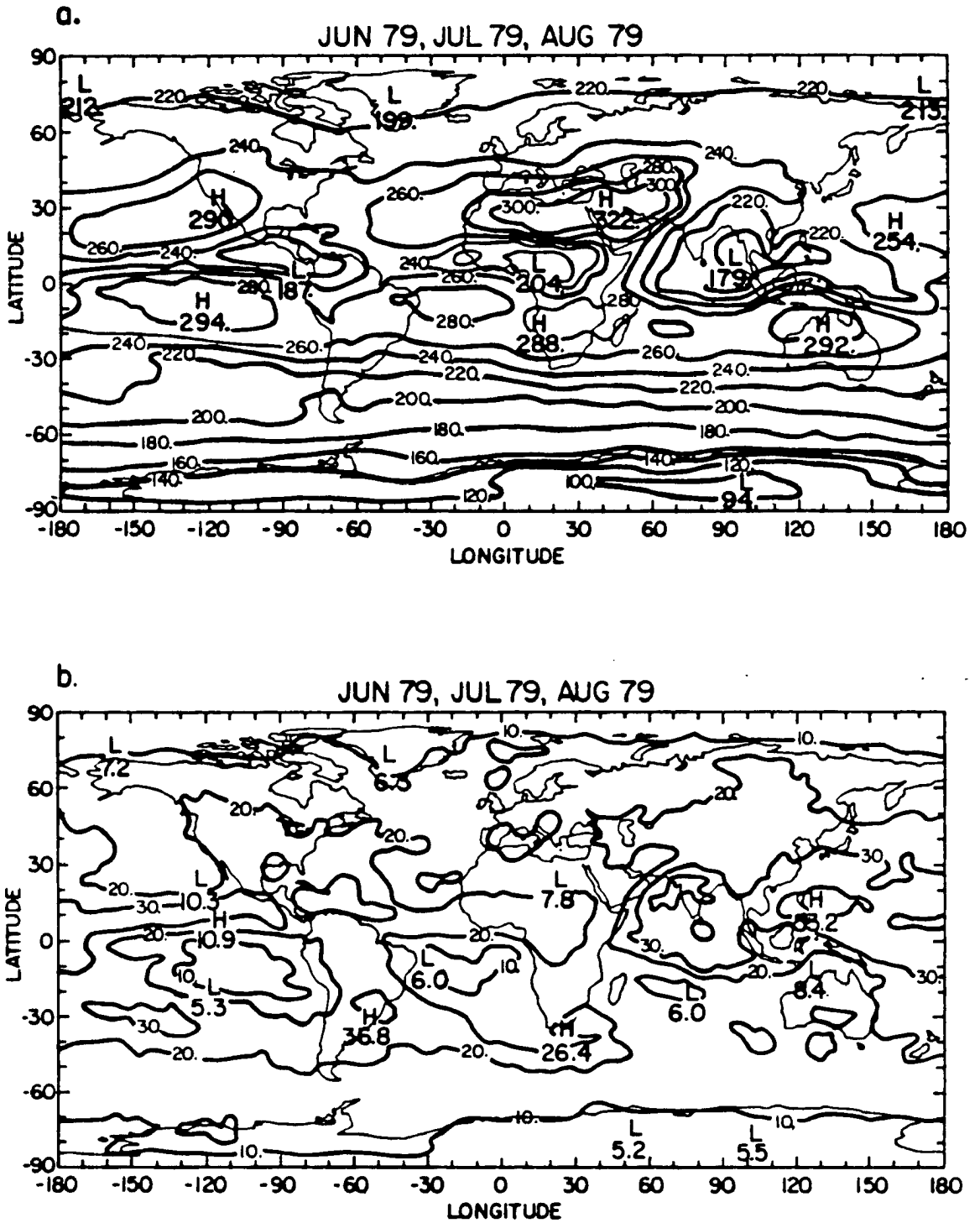


Figure 2.5: Map of the outgoing infrared radiation for Northern Hemisphere summer (Wm^{-2}): (a) seasonal average, and (b) standard deviation.

Table 2.1

Table 2.1: Wavelength spectral interval of the ERB channels of the Nimbus-7 scanner radiometers (from Jacobowitz *et al.*, 1984).

Wavelength limits (μm)	Solar	Wavelength limits(μm)	WFOV	NFOV
0.2 - 3.8	1	< 0.2 to > 50.	11	
0.2 - 3.8	2	< 0.2 to > 50.	12	
(0.2 to) 50.	3	0.2 to 3.8	13	
0.536 - 2.8	4	0.695 to 2.8	14	
0.698 - 2.8	5	0.2 - 4.8		15-18
0.395 - 0.508	6	4.5 - 50.		19-22
0.344 - 0.460	7			
0.300 - 0.410	8			
0.275 - 0.360	9			
(0.2 to) 50.	10			

Table 2.2

Table 2.2: Scanning radiometer target areas for the Nimbus-7 mission.

Latitude Lower limit ¹	Latitude Upper limit	Longitude interval ²
0.0	4.5	4.5
4.5	9.0	4.5
9.0	13.5	4.5
13.5	18.0	4.5
18.0	22.5	5.0
22.5	27.0	5.0
27.0	31.5	5.0
31.5	36.0	5.0
36.0	40.5	6.0
40.5	45.0	6.0
45.0	49.5	6.0
49.5	54.0	7.5
54.0	58.5	8.0
58.5	63.0	9.0
63.0	67.5	10.0
67.5	72.0	12.0
72.0	76.5	18.0
76.5	81.0	22.5
81.0	85.5	40.0
85.5	90.0	120.0

¹ For the Southern Hemisphere, the zone numbers range from 21 at the equator to 40 at the south pole.

² For each latitude band, the longitude intervals start at the 0° meridian and progress east by the increments listed.

2.5 Planetary albedo

As for the outgoing infrared radiation, the global distribution of the planetary albedo is very well known and has been extensively discussed in earlier studies. Because of the transparency of the atmosphere at solar wavelengths, the planetary albedo mainly depends upon the reflectance characteristics of the earth's surface and cloudiness. Figures 2.6 and 2.7 show the geographical distributions of the seasonal average (α) and standard deviation ($\sigma(\alpha)$) of the daily planetary albedo for the winter and summer seasons.

2.5.1 Seasonal average

The distribution of the albedo is practically zonal in the winter hemisphere, with increasing magnitude towards the poles and tight isolines at the snow/ice boundary. At low latitudes, clear-sky regions are characterized by α values less than 16 % above the subtropical oceans, and greater than 32 % above the desert regions because of the high land surface reflectivity. Areas of deep tropical convection are defined by α values greater than 40 % because of the large reflectivity of thick cumulus clouds. It is also interesting to note the increase of the planetary albedo along the western coast of the continents, due to the presence of persistent stratiform clouds, as is very well observed in the Southern Hemisphere.

2.5.2 Standard deviation about the seasonal average

In the subtropics, areas of low standard deviation, or $\sigma(\alpha)$ less than 4 %, superimpose well with areas of α smaller than 16 % above the cloud-free subtropical oceans, and α greater than 32 % above the desert regions. The position of the ITCZ clearly appears as a narrow zonal band of $\sigma(\alpha)$ values greater than 12 % across the Pacific and Atlantic oceans, as is very well observed in summer. Areas of intense cumulus activity and heavy rainfall above the continents are characterized by $\sigma(\alpha)$ greater than 16 %. There is a slight increase in the magnitude of the standard deviation above the stratocumulus regions located along the western coast of the continents. Finally, $\sigma(\alpha)$ increases towards the poles up to the snow/ice pack boundary and decreases at higher latitudes where snow/ice conditions are present during the all year.

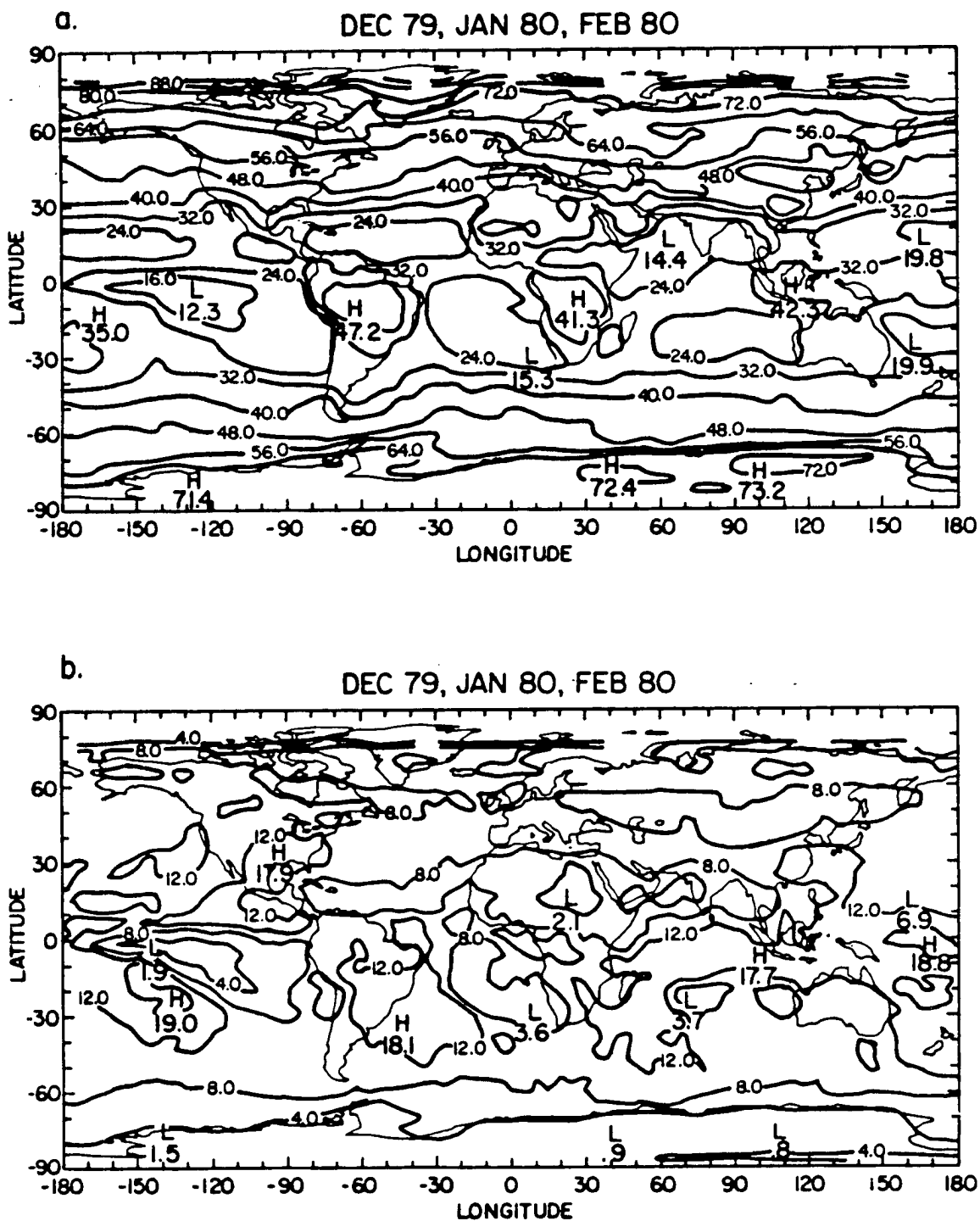


Figure 2.6: Map of the planetary albedo for Northern Hemisphere winter (%): (a) seasonal average, and (b) standard deviation.

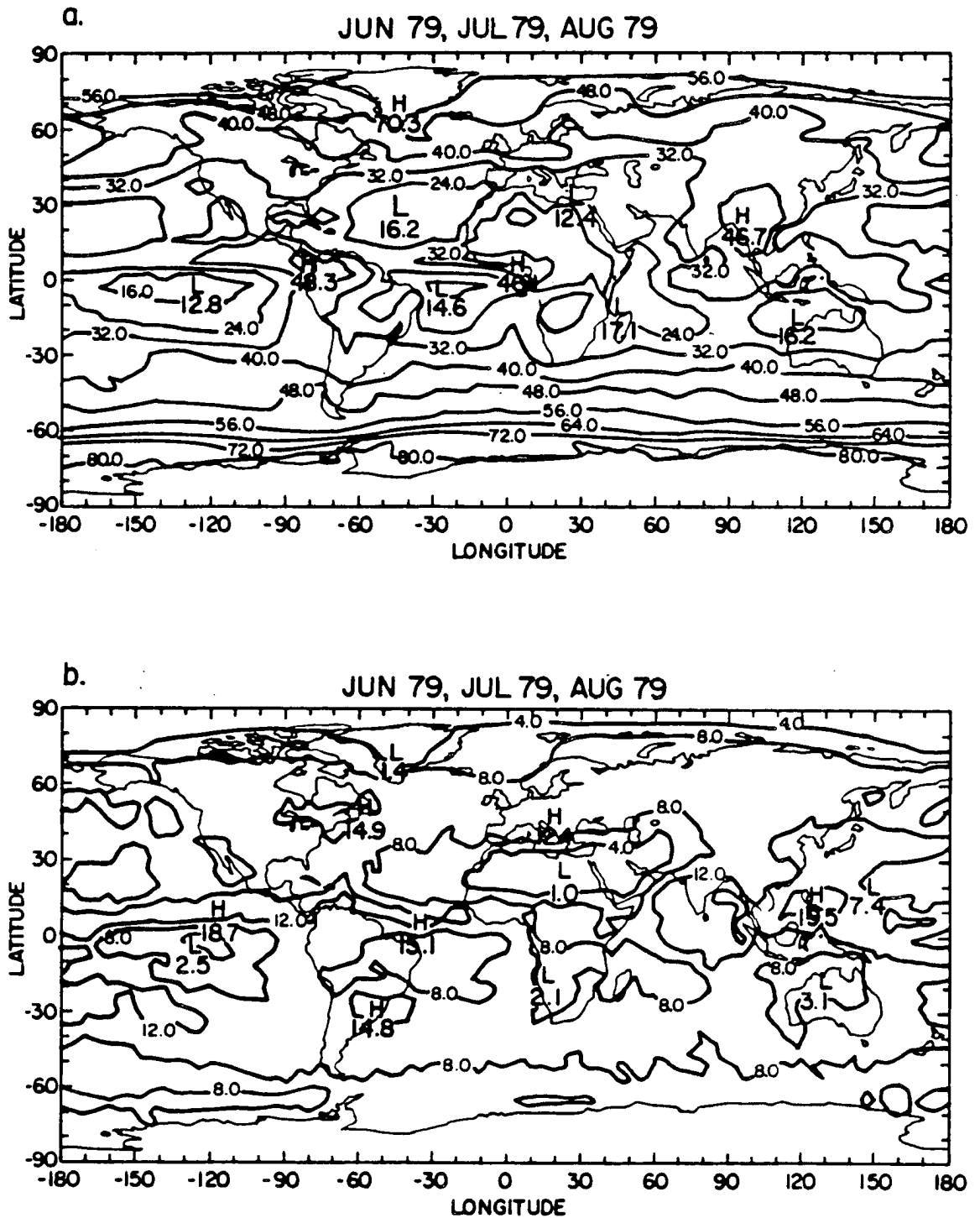


Figure 2.7: Map of the planetary albedo for Northern Hemisphere summer (%): (a) seasonal average, and (b) standard deviation.

2.6 Absorbed solar radiation

The absorbed solar radiation is equal to $S_0(1 - \alpha)$. The amount of solar radiation absorbed by the earth's surface and the atmosphere depends upon the magnitude of solar radiation incident at the top of the atmosphere, and is, therefore, a strong function of the latitude and the season. Figures 2.8 and 2.9 show the geographical distributions of the seasonal average (ABS) and standard deviation ($\sigma(\text{ABS})$) of the daily absorbed solar radiation for the winter and summer seasons.

In the winter hemisphere, the absorbed solar radiation has a predominantly zonal distribution and rapidly decreases towards the poles, because of the north-south gradient of the incident solar radiation. At lower latitudes, at which it does not show such a strong seasonal cycle, the amount of absorbed solar radiation is mainly driven by the magnitude of the planetary albedo, i.e., mainly the reflectivity of the cloud cover and the earth's surface. The comparison between Figures 2.4 and 2.8 for winter, and between Figures 2.5 and 2.9 for summer, shows that areas of absorbed solar radiation greater than 360 Wm^{-2} and $\sigma(\text{ABS})$ less than 40 Wm^{-2} superimpose well with areas of outgoing infrared radiation greater than 260 Wm^{-2} and $\sigma(\text{IR})$ less than 20 Wm^{-2} , as is well observed above the subtropical oceans and the desert regions. The ITCZ across the Pacific and Atlantic oceans, which is characterized by $\sigma(\text{IR})$ greater than 40 Wm^{-2} , is also defined by $\sigma(\text{ABS})$ greater than 60 Wm^{-2} . An identical correlation between the standard deviation of the outgoing infrared radiation and absorbed solar radiation is observed above the winter and summer monsoon regions, as well as above the semipermanent frontal regions in the Southern Hemisphere.

2.7 Outgoing infrared, absorbed solar radiation covariance

In the previous sections, the global distribution of the standard deviation of the longwave and shortwave components of the planetary radiation balance were discussed separately. It is shown that the temporal variability of the outgoing infrared radiation, the planetary albedo, and of the absorbed solar radiation is mainly driven by day-to-day

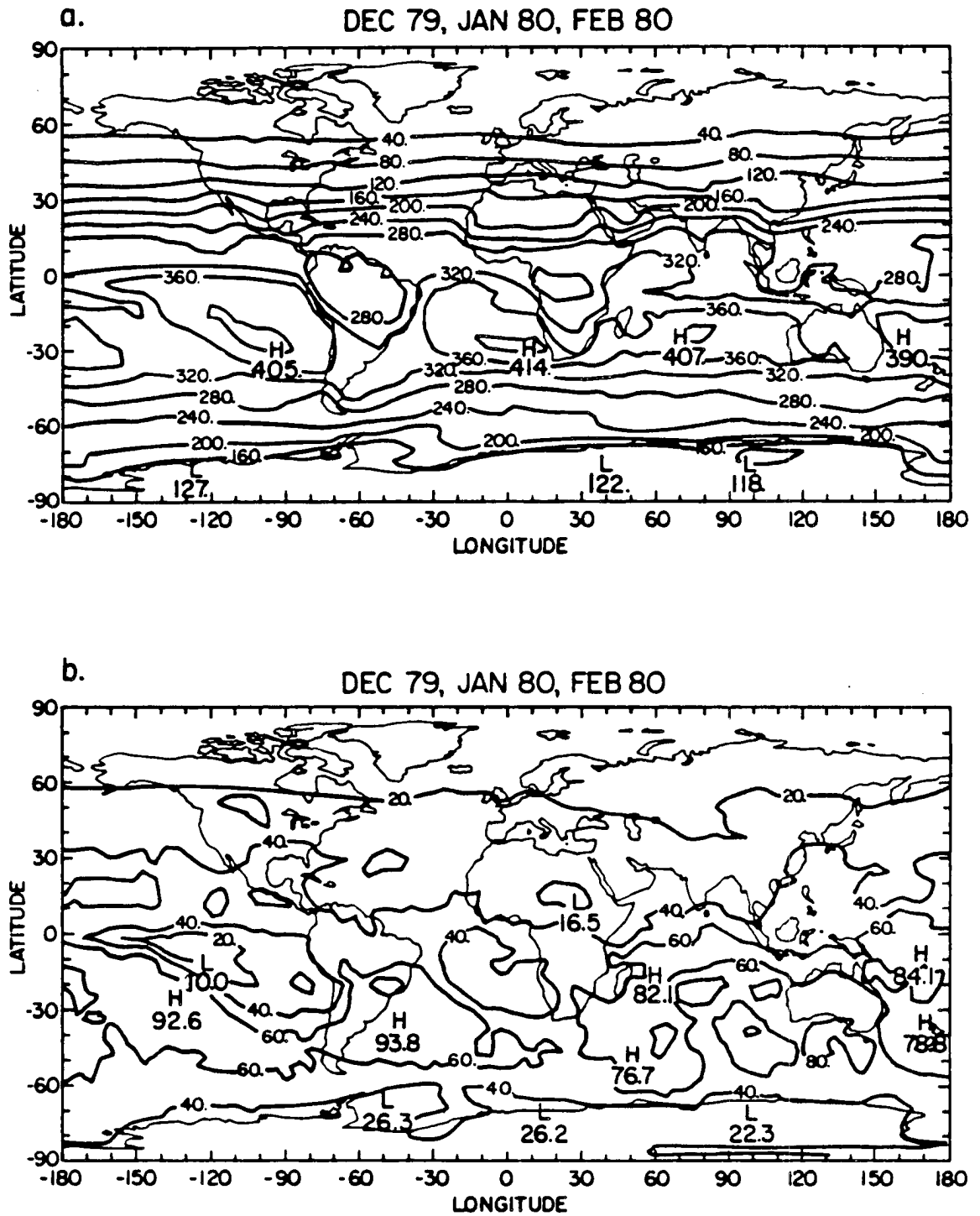


Figure 2.8: Map of the absorbed solar radiation for Northern Hemisphere winter (Wm^{-2}): (a) seasonal average, and (b) standard deviation.

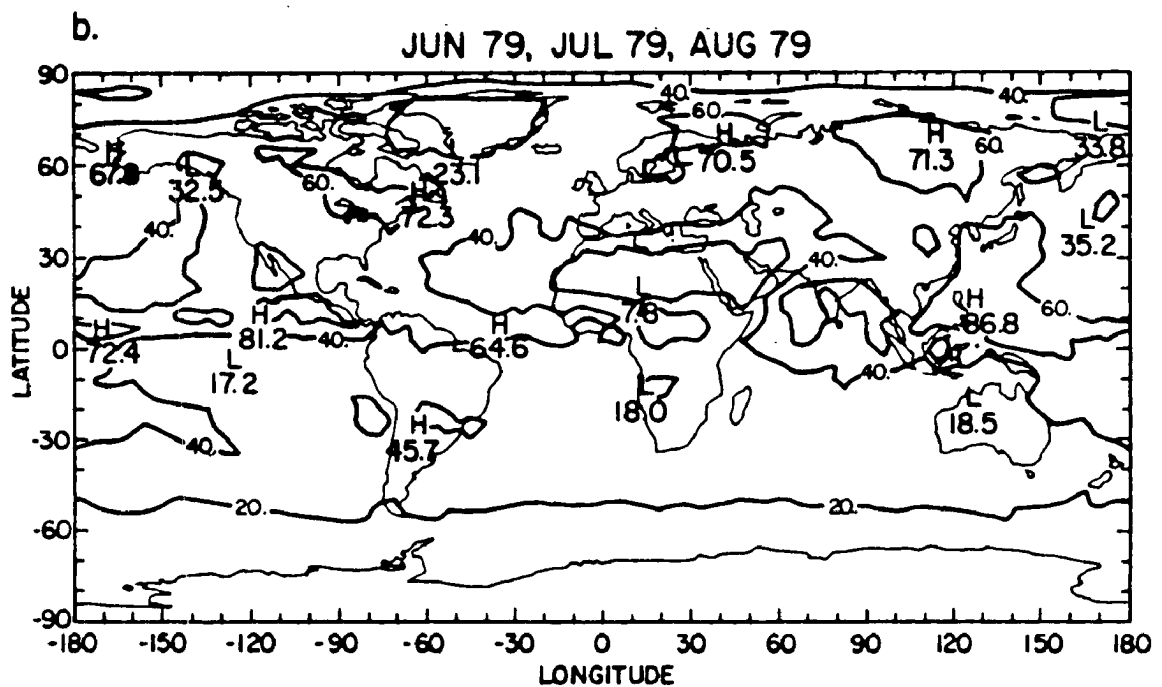
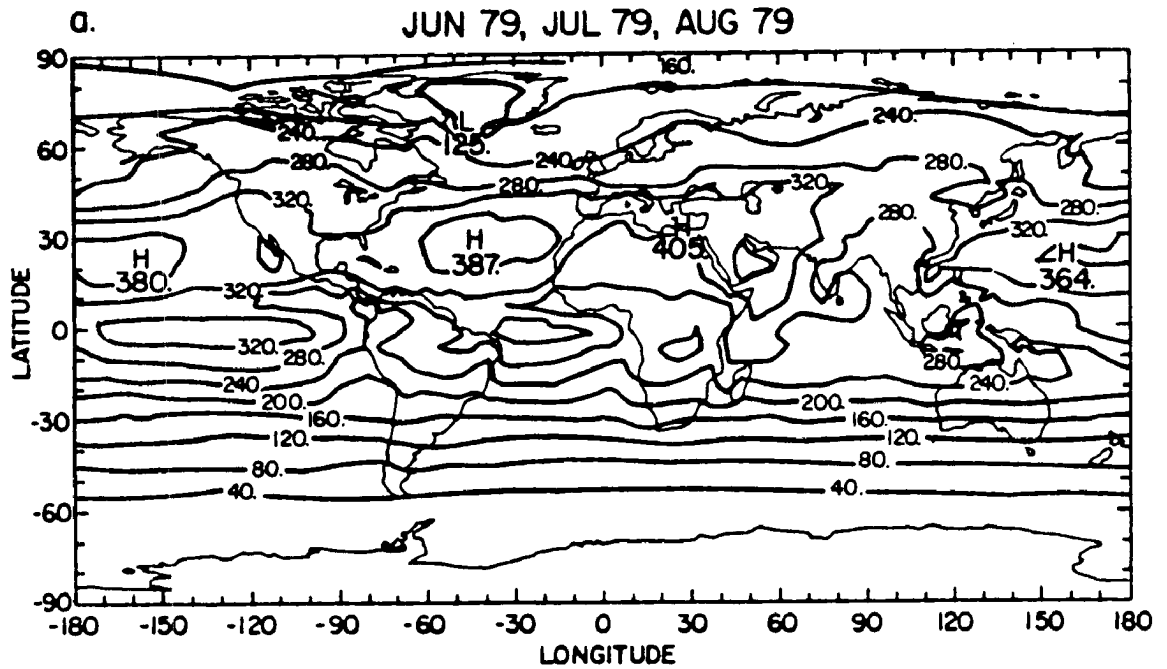


Figure 2.9: Map of the absorbed solar radiation for Northern Hemisphere summer (Wm^{-2}): (a) seasonal average, and (b) standard deviation.

fluctuations in the distribution of the cloud cover. Convective and stratiform clouds have different impacts on radiation. Low-level, optically thick stratiform clouds have a strong albedo effect. Because they are close to the ground, their greenhouse effect is small and they do not substantially affect the longwave radiation emitted at the surface. High-level convective clouds also have a large shortwave reflectivity and reduce more effectively the loss of infrared radiation to space. For optically thin cirrus clouds, the greenhouse effect dominates. Because of the coarse spatial resolution of the satellite data, relatively cloud-free regions over the oceans and regions dominated by the presence of stratiform clouds have an identical variability at long wavelengths. The computation of the covariance between the outgoing infrared radiation and the absorbed solar radiation helps identify regions of the globe which show a large variability at both short and long wavelengths. The covariance is expressed by the relation:

$$COV = \frac{1}{N} \sum_{i=1}^N (ABS_i - ABS)(IR_i - IR), \quad (2.1)$$

in which

$$ABS = \frac{1}{N} \sum_{i=1}^N ABS_i, \quad (2.2)$$

and

$$IR = \frac{1}{N} \sum_{i=1}^N IR_i. \quad (2.3)$$

N is the length of the time series, and ABS_i and IR_i are daily values of the absorbed solar and outgoing infrared radiation.

Figure 2.10 shows the geographical distribution of the covariance for the winter and summer seasons. The outgoing longwave, absorbed solar radiation covariance presents a sharp gradient at the boundaries between areas of low and high variability. Large positive values of the covariance are observed above regions which are simultaneously highly variable at short and long wavelengths, i.e., mainly regions of deep tropical convection. Low positive values of the covariance correspond to regions where both outgoing infrared and absorbed solar radiation undergo small day-to-day fluctuations, i.e. clear-sky regions

above the subtropical oceanic regions and desert regions over the continents. Finally, the covariance, computed on a seasonal basis, rapidly decreases north of 40° of latitude because of the small amplitude of the outgoing infrared and absorbed solar radiation. The comparison between the winter and summer seasons clearly shows the seasonal shift of the areas of intense cumulus convection above land and ocean. The position of the ITCZ, the major convective regions over the continents, and the semi-permanent frontal zones are very well delineated. There is a strong decrease, between Northern Hemisphere winter and summer, in the magnitude of the covariance above the cyclogenetic areas positioned along the eastern coast of South America and southern Africa, and in the South Pacific ocean. On the other hand, there is a relatively constant convective activity off the shore of Central America.

Table 2.3 summarizes the radiative budget statistics of individual 4.5° grid-boxes located above the oceans. The first set of target areas corresponds to regions characterized by large values of the standard deviation at short and long wavelengths, which are also regions of large covariance. The second set of target areas has been chosen for their small values of longwave and shortwave standard deviation, i.e. the relatively cloud-free subtropical Pacific, Atlantic and Indian oceans. For regions which are cloudless during most of the season, the lowest value of $\sigma(\text{IR})$ and $\sigma(\alpha)$ give an estimate of the variability of the atmosphere itself, resulting from the advection of the temperature and humidity fields, plus the advection of cloud debris. Because of the size of the target areas, the signal recorded at the satellite altitude by the scanning instruments represents an averaged value of the infrared emission and solar absorption from completely cloudless pixels, plus the contribution from some neighboring cloudy pixels. Therefore, at that spatial resolution, the smallest value of $\sigma(\text{IR})$ and $\sigma(\alpha)$ computed from the Nimbus-7 time series only represents an estimate of the noise induced by cloud contamination above relatively cloud free areas, instead of an estimate of the natural variability of the atmosphere itself. The last set of individual grid-points are located along the western coasts of the continents, where low-level stratiform clouds are likely to be observed. They are defined by low infrared standard deviation, but are distinguishable from cloudless areas areas by their higher standard deviation at short wavelengths.

Table 2.3

Table 2.3: Radiative Budget Statistics for individual 4.5° grid-boxes.

Location	IR Wm^{-2}	$\sigma(\text{IR})$ Wm^{-2}	α %	$\sigma(\alpha)$ %	ABS Wm^{-2}	$\sigma(\text{ABS})$ Wm^{-2}	COV $(\text{Wm}^{-2})^2$
A. Winter							
High $\sigma(\text{IR})$, high $\sigma(\alpha)$							
9.0S,148.5W	231.8	49.4	30.2	18.0	322.0	83.0	3729.5
18.0N,117.0W	250.5	43.7	29.3	17.2	248.1	67.0	2495.0
31.5S, 45.0W	241.2	35.2	30.0	18.1	343.2	93.8	2784.0
18.0S, 54.0E	240.3	47.6	25.7	16.7	356.4	80.2	3560.0
13.5S,117.0E	219.2	52.3	26.6	16.6	346.4	78.5	3619.1
4.5S,166.5E	192.4	43.6	37.5	18.7	280.4	84.1	3141.9
Low $\sigma(\text{IR})$, low $\sigma(\alpha)$							
4.5S,121.5W	290.9	7.8	12.8	2.0	391.1	10.3	27.9
4.5S, 13.5W	278.6	8.1	17.3	5.7	370.8	26.2	56.3
22.5S, 76.5E	274.6	12.7	16.4	4.3	405.7	27.0	98.6
Low $\sigma(\text{IR})$, higher $\sigma(\alpha)$							
18.0S,85.5W	275.7	12.4	20.6	9.6	380.1	44.4	222.1
9.0S, 0.0	268.2	13.5	24.9	9.4	346.3	43.1	57.0
B. Summer							
High $\sigma(\text{IR})$, high $\sigma(\alpha)$							
13.5N,117.0W	214.3	40.9	38.1	18.7	269.3	81.2	2912.0
13.5N,175.5E	237.9	37.5	24.3	13.0	329.5	56.6	1725.3
13.5N, 22.5W	222.3	27.8	33.3	13.3	290.1	58.0	1328.1
9.0N, 67.5E	210.0	39.4	31.7	16.6	288.9	71.1	2511.7
18.0N,126.0E	203.4	53.2	33.7	19.5	295.3	86.8	4168.4
Low $\sigma(\text{IR})$, low $\sigma(\alpha)$							
0.0 ,126.0W	290.6	7.0	12.8	2.6	340.1	17.2	26.6
4.5S, 27.0W	286.3	9.2	15.6	3.6	313.2	19.9	35.5
13.5S, 58.5E	281.3	7.3	19.7	5.2	262.7	29.1	89.8
Low $\sigma(\text{IR})$, higher $\sigma(\alpha)$							
36.0N,130.5W	267.1	12.2	25.7	11.3	343.8	51.8	99.8
13.5S, 85.5W	273.6	10.7	37.2	10.7	205.1	40.4	233.6
9.0S, 4.5E	279.7	11.4	33.0	11.5	234.1	37.1	129.2

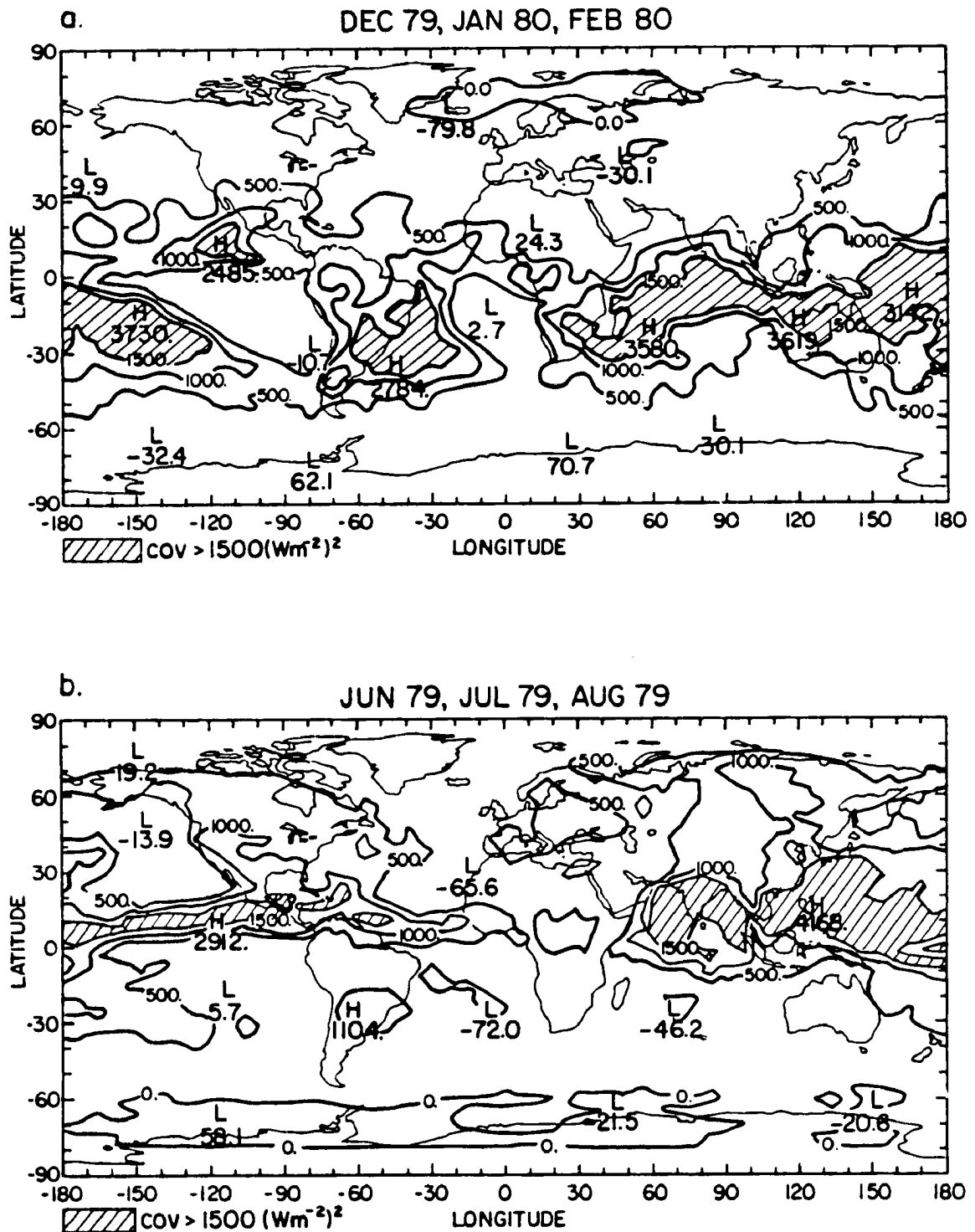


Figure 2.10: Map of the covariance between the outgoing infrared radiation and the absorbed solar radiation for Northern Hemisphere (a) winter, and (b) summer (Wm^{-2})².

2.8 Cloud factor

A large variety of research has already been done on how clouds directly and indirectly affect the net radiation balance of the earth-atmosphere system. However, understanding or modeling of the cloud-radiation-climate feedback mechanisms still constitute, at the present time, one of the most challenging problems in atmospheric research. At short radiative wavelengths, clouds increase the planetary albedo and reduce the amount of absorbed solar energy. A change in the global cloud cover would, therefore, leads to an overall radiative cooling of the atmosphere. At long radiative wavelengths, clouds absorb and reemit infrared radiation, thus reducing the amount of infrared radiation lost to space and enhancing the greenhouse warming of the atmosphere. The magnitude of the infrared effect is proportional to the difference between the cloud top and surface temperatures. An augmentation of the high cloud cover would, therefore, tend to warm the low troposphere. Various methods have been proposed to infer the relative magnitude of the albedo versus the greenhouse effect of clouds. A large range of results have been found when either ERB measurements (Cess, 1976; Ellis, 1978; Campbell and Vonder Haar, 1980; Hartmann and Short, 1980; Ohring and Clapp, 1980), or theoretical model computations (Schneider, 1972; Coakley, 1977; Charlock and Ramanathan, 1985) are used.

2.8.1 Definition

Hartmann and Short (1980) define a sensitivity parameter, the cloud factor, which is the simplest parameter used in the different studies listed above. It only requires measurements of the total outgoing infrared radiation and the planetary albedo, whereas other sensitivity parameters require an additional data set of the global distribution of clouds.

The change in the net radiation due to a change in the cloud cover A_c can be written:

$$\frac{\partial NET}{\partial A_c} = \left(-\frac{\partial IR}{\partial A_c}\right) \left[S_o \left(\frac{\partial \alpha}{\partial IR}\right) + 1\right], \quad (2.4)$$

in which all three partial derivatives result from a variation in A_c only. As pointed out by Hartmann and Short, "... $\left(\frac{\partial \alpha}{\partial IR}\right)$ has the meaning of the change of albedo divided by

the change of outgoing infrared radiation resulting from a change in the cloud cover". In equation 2.4, $(-\frac{\partial IR}{\partial A_c})$ is positive in most cases and

$$C = [S_o(\frac{\partial IR}{\partial \alpha})^{-1} + 1]. \quad (2.5)$$

is the cloud factor. For $C = 1$, the IR effect dominates, and for $C = -N$, the albedo effect is $N + 1$ times as large as the IR effect. The shortwave and longwave effects of clouds on radiation cancel each other for $C = 0$. In the interpretation of the cloud factor, it is assumed that $(\frac{\partial IR}{\partial \alpha})$ mainly results from day-to-day fluctuations in the cloud fraction only. This assumption, as discussed by Hartmann and Short, is excellent at low latitudes above the oceans where large daily variations in the cloud cover do not strongly affect the vertical distribution of the temperature and humidity fields. It becomes less valid above desert continental regions and above the middle latitude storm track regions where cyclogenesis is accompanied by large horizontal advection of temperature and water vapor. Hartmann and Short use narrow-spectral-band converted to broad-band measurements of the outgoing infrared radiation and the planetary albedo taken by the scanner instruments on board the NOAA-4 satellite to obtain the global distribution of the cloud factor. In the next section, we present the first revised maps of the cloud factor computed from the broad-spectral-band ERB measurements from the Nimbus-7 satellite for the winter and summer seasons.

2.8.2 Results

Figure 2.11 shows the geographical distribution of the slope $(\frac{\partial IR}{\partial \alpha})$ obtained from a least-square regression between daily observations of the outgoing infrared radiation and the planetary albedo for the winter and summer seasons. Above regions of deep tropical convection in the summer hemisphere, high frequency of generation, dissipation, and advection of convective clouds throughout both seasons yields relatively large day-to-day fluctuations at both short and long wavelengths, which explains values less than -200 Wm^{-2} . The comparison between Figures 2.10 and Figures 2.11 shows that there is, indeed, a very good correspondence between areas of covariance greater than $1500 (\text{Wm}^{-2})^2$ and of $(\frac{\partial IR}{\partial \alpha})$ less than -200 Wm^{-2} . Above the desert regions, variations in the

outgoing infrared radiation at the top of the atmosphere primarily result from changes in the surface temperature. In the middle latitudes, variations in the cloud cover are also accompanied by large variations in both the temperature and humidity fields, which leads to a greater uncertainty of the actual value of $(\frac{\partial \text{IR}}{\partial \alpha})$. At low latitudes, above clear oceanic regions and stratocumulus areas along the western coasts of the continents, $(\frac{\partial \text{IR}}{\partial \alpha})$ is greater than -100 Wm^{-2} , and may even reach positive values. Analyses of several individual grid-boxes show that, for low cloud regimes, a large range of albedo corresponds to a narrow dispersion of infrared radiation, so that the albedo effect dominates the greenhouse effect. For cloudless areas, characterized by low values of $\sigma(\text{IR})$ and $\sigma(\alpha)$, the dispersion of the longwave and shortwave components is expected to be relatively small, centered around an averaged value of the planetary albedo and the outgoing infrared radiation.

Figure 2.12 shows the geographical distribution of the cloud factor for the winter and summer seasons. There are important geographical variations in the radiative effects of clouds. The cloud factor principally highlights regions of the globe where the albedo effect of clouds dominates their greenhouse effect. It clearly delineates the position and extent of the areas influenced by the presence of widespread stratocumulus clouds along the western coasts of the continents. In summer, these areas are located along the United States and South America, as well as along the western coast of Africa, extending westward into the subtropical oceans. In winter, the stratiform clouds persist along the western coasts of South America and southern Africa but have disappeared from the coasts of the United States and northern Africa. The computation of the cloud factor shows that low-level clouds off the shore of California and northern Africa have a maximum albedo effect during the Northern Hemisphere summer, in contrast with low-level stratiform clouds in the Southern Hemisphere which appear to be more persistent throughout the whole year. Although the global distribution of the cloud factor computed by Hartmann and Short is slightly different than this shown in Figure 2.12, our results lead to an identical conclusion: the albedo effect of clouds dominates and an increase in the global cloud cover would probably lead to an overall cooling of the earth-atmosphere system.

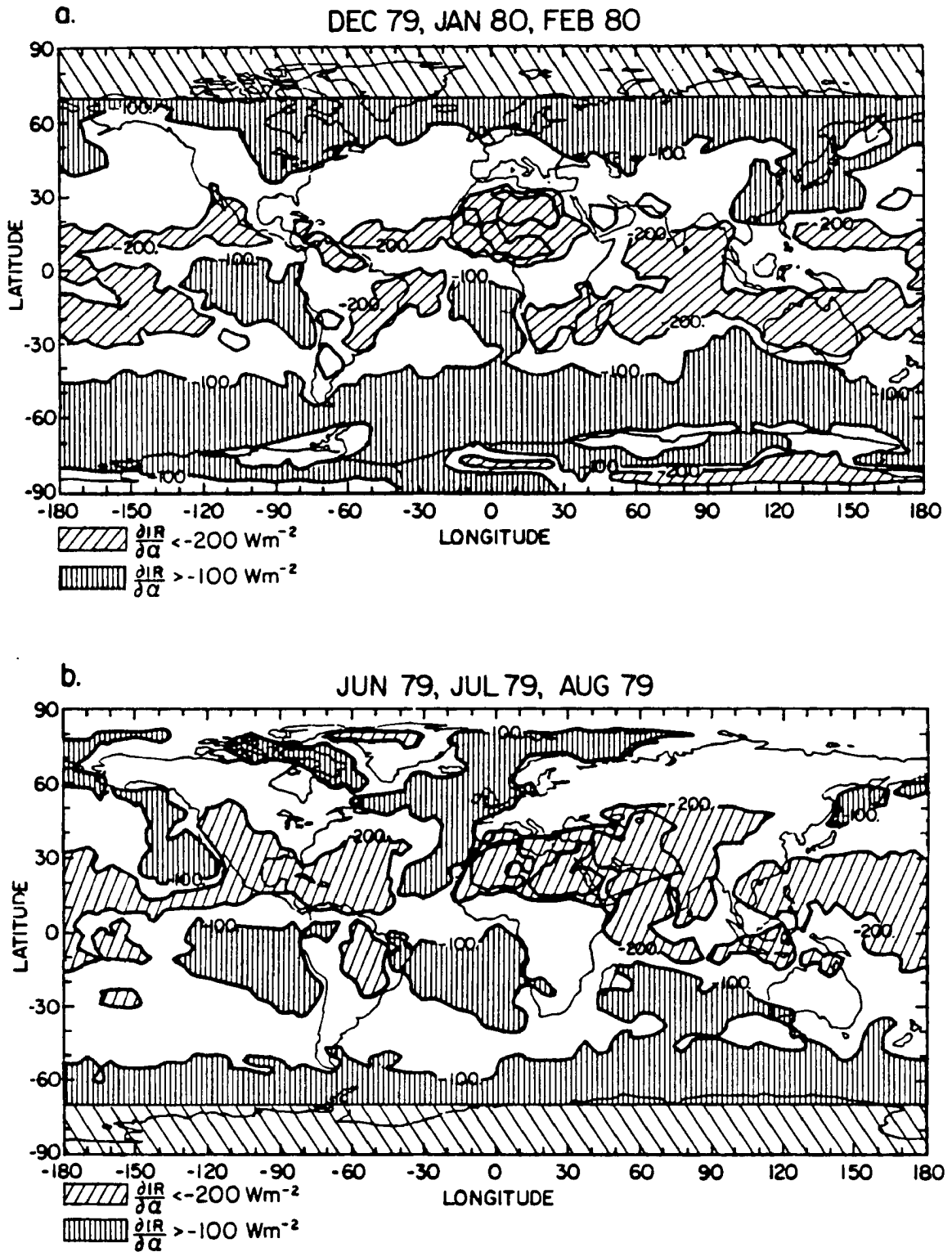


Figure 2.11: Map of the slope $\frac{\partial IR}{\partial \alpha}$ for Northern Hemisphere (a) winter, and (b) summer (Wm^{-2}).

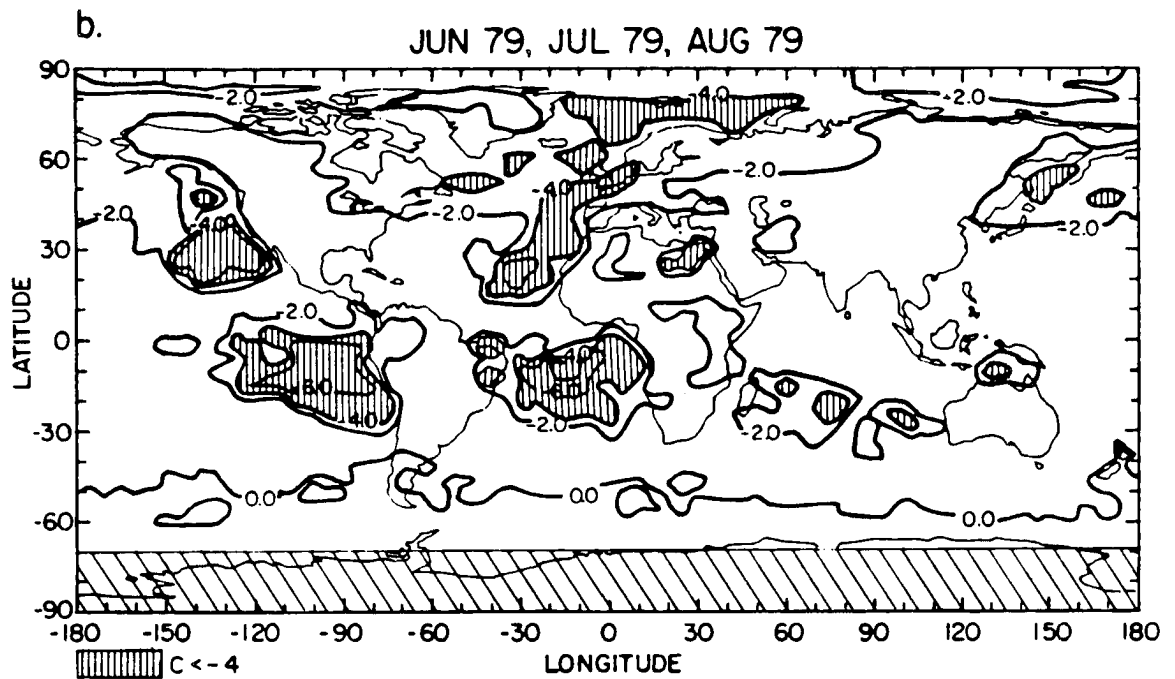
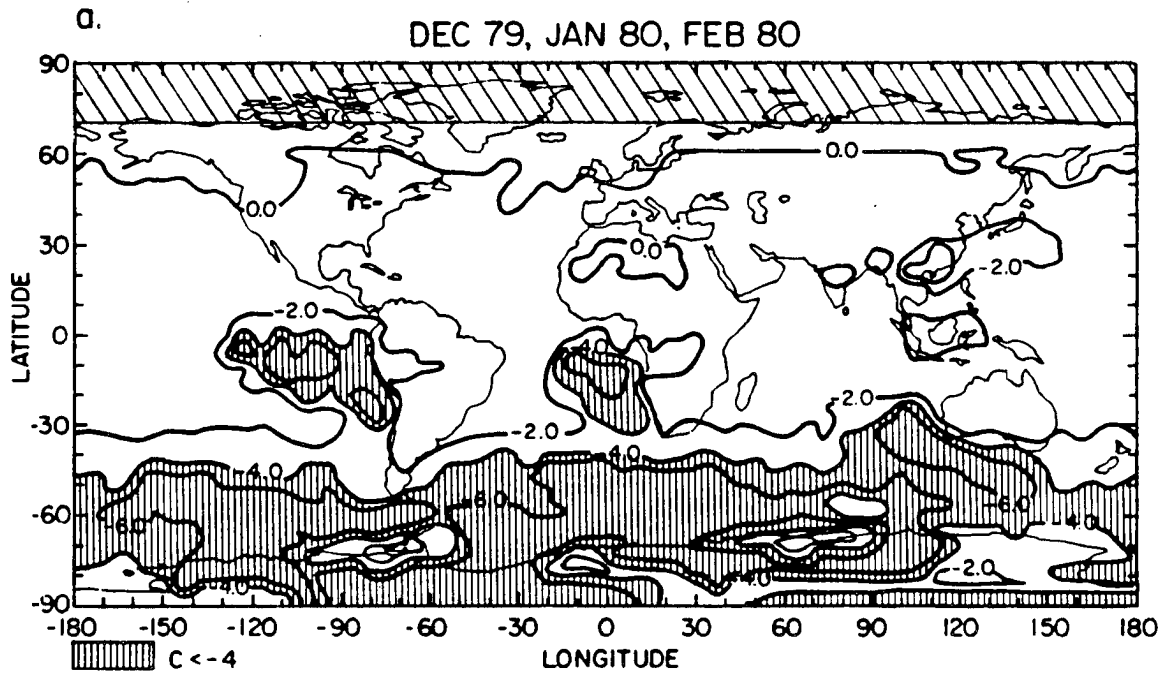


Figure 2.12: Map of the cloud factor $[S_o(\frac{\partial IR}{\partial \alpha})^{-1} + 1]$ for Northern Hemisphere (a) winter, and (b) summer.

2.9 Sensitivity of the temporal variability

2.9.1 Discussion

In the previous sections, the spatial distribution of the temporal variability of the planetary radiation balance was discussed from maps of the standard deviation, computed from the seasonal average, of the daily mean outgoing infrared radiation, the planetary albedo, and the absorbed solar radiation. Both Northern Hemisphere winter and summer seasons were considered and the strong dependence between day-to-day fluctuations in the distribution of the cloud cover and the radiation fields were emphasized. Although we are confident that our computations do provide reliable estimates of the actual variability of the shortwave and longwave components of the top-of-atmosphere radiation balance, we need to take under consideration systematic errors or biases which may result from:

1. The diurnal and seasonal cycles of the outgoing infrared radiation and the planetary albedo.
2. The temporal sampling of the earth's radiation budget which induces systematic errors in the determination of the daily mean radiation fluxes. Its impact on the estimates of $\sigma(\text{IR})$ and $\sigma(\text{ABS})$ is unknown and difficult to quantify from observations taken solely from sun-synchronous, polar orbiting spacecrafts.
3. The spatial averaging of the individual pixels into rectangular grid-boxes of 4.5° side. Analyses of $\sigma(\text{IR})$ particularly showed that the spatial resolution was too coarse to clearly delineate between areas dominated by daily fluctuations in the stratiform cloud field and areas which are mostly cloud-free over the whole season. Increased spatial resolution would certainly yield a better distinction between the two atmospheric conditions.
4. The 3-days on, 1-day off duty of the scanner radiometers on board Nimbus-7. On a seasonal basis, the length of the time series of observations at short and long wavelengths is reduced by about one third, which may actually lead to a decrease in the standard deviation computed from the seasonal average.

The primary goal of this section is to demonstrate that our results discussed earlier on the temporal variability of the radiation balance are not exclusively dependent upon the characteristics of the Nimbus-7 satellite mission, and do provide accurate information of the actual variability of the earth's radiation balance. In the following sections, we compare the geographical distribution and magnitude of $\sigma(\text{IR})$ and $\sigma(\text{ABS})$ against these computed from daily mean observations taken by the scanner radiometers of the multi-satellite Earth Radiation Budget Experiment (ERBE). In addition, we also discuss the global distribution and magnitude of $\sigma(\text{IR})$ computed from Nimbus-7 IR time series against these obtained from measurements taken by the scanners on board the successive NOAA satellites between the time period June 1979-May 1980 to infer:

1. The importance of the diurnal sampling on the calculation of $\sigma(\text{IR})$ and $\sigma(\text{ABS})$. In ERBE, the multiple diurnal samplings from two sun-synchronous satellites and a low-orbit satellite yields a more accurate determination of the daily mean outgoing infrared radiation than that obtained from two observations per day for each location at a fixed local time as from the Nimbus-7 mission.
2. The impact of different orbital characteristics. The TIROS-N and NOAA-6 satellites were launched into sun-synchronous near-polar orbits with respective equatorial crossing times (0300-1500)LT and (0730-1930)LT instead of (1200-2400)LT for the satellite Nimbus-7. NOAA-9 and NOAA-10 which are the two ERBE sun-synchronous satellites respectively have a 1430 LT and 1930 LT ascending node crossing time.
3. The effect of missing days in the Nimbus-7 IR time series. Whereas Nimbus-7 data, observations taken by the NOAA scanners over the same time period between June 1979 and May 1980 are available daily and continuously over the whole globe.
4. The importance of an increased spatial resolution. Daily observations taken by the NOAA and ERBE satellites were averaged into grid-boxes of 2.5° side instead of 4.5° .

2.9.2 Impact of the seasonal cycle

The latitude-time distribution of the monthly mean outgoing infrared radiation shows that it undergoes the largest seasonal cycle in the middle and high latitudes, because of the seasonal variation of the earth's surface and atmospheric temperature fields. To ensure that this effect would not induce any bias in the magnitude of $\sigma(\text{IR})$, the seasonal trend was removed by applying a least-square regression and subtracting the fitted value to each daily observations of the outgoing infrared radiation. This operation transforms the original time series into a stationary time series so that:

$$\frac{1}{N} \sum_{i=1}^N (\text{IR}_i - \tilde{\text{IR}}_i) = 0. \quad (2.6)$$

In equation 2.6, N is the length of the time series, IR_i and $\tilde{\text{IR}}_i$ are respectively the true and fitted value of the radiation field. The standard deviation ($\sigma(\tilde{\text{IR}})$) of the daily field ($\text{IR}_i - \tilde{\text{IR}}_i$) was computed and compared to $\sigma(\text{IR})$ for both winter and summer seasons. There are no significant differences between the magnitude of $\sigma(\tilde{\text{IR}})$ and $\sigma(\text{IR})$. This result was expected because, at low latitudes, the seasonal cycle is small and $\sigma(\text{IR})$ mainly depends upon the fluctuations of the cloud cover, and because, in the middle and high latitudes, $\sigma(\text{IR})$ is small although IR undergoes larger month-to-month variations than at the equator.

2.9.3 Impact of the diurnal sampling

1. Background

Several studies have been investigating the systematic errors induced in estimations of the daily mean infrared and visible observations taken from polar orbiting satellites for each location at a fixed local time (Ramanathan and Dickinson, 1981; Harrison *et al.*, 1983; Saunders *et al.*, 1983a; Saunders *et al.*, 1983b; England *et al.*, 1984; Brooks *et al.*, 1986). These errors may be caused by mainly four different processes: changes in the distribution of cloudiness, variations in the temperature and humidity fields due to advective and convective processes, diurnal temperature variations, especially over land, and changes in the atmospheric optical depth and surface albedo with solar zenith angle.

Saunders *et al.* (1983a) analyze the effect of the temporal sampling from an intercomparison between radiation budget estimates obtained from instruments on board the satellites METEOSAT-1, Nimbus-7, and TIROS-N. They show that errors introduced by inferring daily means from just one or two sun-synchronous polar orbiter observations can reach up to 50 Wm^{-2} for specific areas by comparing METEOSAT daily means with the daily values inferred from the polar orbiters. However, because of the small number of comparisons, the mean differences between the three satellites cannot be considered as statistically significant. Harrison *et al.* (1983) showed that the best sampling capability and lowest errors were obtained with a three-satellite system, i.e., two sun-synchronous satellites with different equatorial crossing times combined with either a 46° or 57° orbit satellite. These results were, among others, later used in defining the multi-satellite ERBE mission. Finally, England *et al.* (1984) study the effects of sampling at fixed intervals in universal time and the errors due to sampling at fixed local time with 12 hourly separations (as for Nimbus-7) from METEOSAT-1 imaging data. They demonstrate the dominating role of cloud variability in temporal sampling errors, especially at short wavelengths. They particularly show that the visible error is typically more than five times greater than at long wavelengths and would be minimized if measurements from a single polar orbiter were taken near 9 am and 9 pm. However, no estimates of the impact of the temporal sampling upon day-to-day fluctuations in the earth's radiation budget have been made from similar comparisons between radiation data taken from geostationary and polar orbiting satellites.

2. Comparison against ERBE data

The implementation of the ERBE program, which started in November 1984, and its scientific objectives are described in detail in Barkstrom and Smith (1986). This experiment consists of three different satellites loaded with identical broad-spectral-band instruments. NOAA-9 and NOAA-10 were both launched into sun-synchronous orbits whereas ERBS (the third ERBE satellite) was positioned into a low inclination precessing orbit, so that a given satellite sub-point can be viewed at multiple local times, as indicated

in Table 2.4. Therefore, and whereas the Nimbus-7 satellite, the combination of data from both satellites does provide a sufficient diurnal coverage which is required to obtain an accurate determination of the earth's radiation budget and to minimize diurnal sampling effects. The ERBE scanner instruments which have almost identical spectral coverage as the Nimbus-7 scanners are completely described in Kopia (1986). The monthly mean and standard deviation, computed from the monthly mean, of the daily-mean outgoing infrared and absorbed solar radiation fields are available, on the so-called S9 Tapes, on rectangular maps of 2.5° latitude-longitude resolution, for July 1985 and January 1986. The monthly means are based on daily calculations of radiant exitances. For the longwave quantities, the daily means are obtained from the extrapolation, interpolation, and diurnal modeling algorithms that operate on the existing longwave estimates (Brooks *et al.*, 1986). The shortwave quantities are based on calculations for specific days and the days are defined to be symmetric about the local solar noon.

Table 2.4

Table 2.4: Characteristics of the ERBE mission and scanner instruments (from Luther *et al.*, 1986, and Kopia, 1986).

SATELLITE	Launch date	Orbit altitude (km)	Orbit inclination
<u>1. ERBE mission:</u>			
ERBS	October 5, 1984	610	57°
NOAA-9	December 12, 1984	872	98°
NOAA-10	March, 1986	833	98°
<u>2. ERBE scanners:</u>			
Channel	Wavelength (μm)		
Shortwave	0.2-5.0		
Longwave	5.0-50.		
Total	0.2-50.		

Figure 2.13 shows the global distribution of $\sigma(\text{IR})$ computed from the ERBE data for January 1986 and from Nimbus-7 data for January 1980. Figure 2.14 shows the global

distribution of $\sigma(\text{IR})$ computed from the ERBE data for July 1985 and from Nimbus-7 data for July 1979. Despite the fact that both data sets do not correspond to the same time period, that the diurnal sampling and the spatial resolution of the observations are completely different, there is an excellent agreement in the magnitude and global distribution of $\sigma(\text{IR})$ between both maps and for both seasons. Regions of high and low values of the standard deviation superimpose very well and the difference in the gradient between areas of high and low variability between both maps can mainly be attributed to the higher spatial resolution of the ERBE data. The excellent agreement between both data sets is also very well seen in the distribution of the zonally-averaged profile of $\sigma(\text{IR})$, as shown in Figure 2.15.

Figures 2.16 and 2.17 present global maps of $\sigma(\text{ABS})$ obtained from both data sets over the same months as Figures 2.13 and 2.14. Figure 2.18 shows the zonally-averaged profile of $\sigma(\text{ABS})$ for January and July. Considering the difference between the two data sets, there is also a very good agreement between the global distribution and magnitude of $\sigma(\text{ABS})$ obtained from ERBE and Nimbus-7 data, but at high latitudes in the summer hemisphere. As at infrared wavelengths, the impact of the diurnal sampling upon the magnitude of the standard deviation of the absorbed solar radiation appears to be small.

3. Conclusion

The comparison of the standard deviation, computed from the monthly mean, of the daily-mean outgoing infrared radiation and daily-mean absorbed solar radiation between the ERBE and Nimbus-7 data sets indicates that the diurnal sampling of the observations has a minor impact upon the computation of day-to-day fluctuations in the radiation balance. Despite the use of a different time period between the two satellite data sets, increased temporal sampling and spatial resolution for the ERBE observations, we found an excellent agreement in the distribution and magnitude of the standard deviation at both infrared and solar wavelengths. In addition, this comparison shows the minor influence of the missing days in the Nimbus-7 time series, at least on a monthly basis.

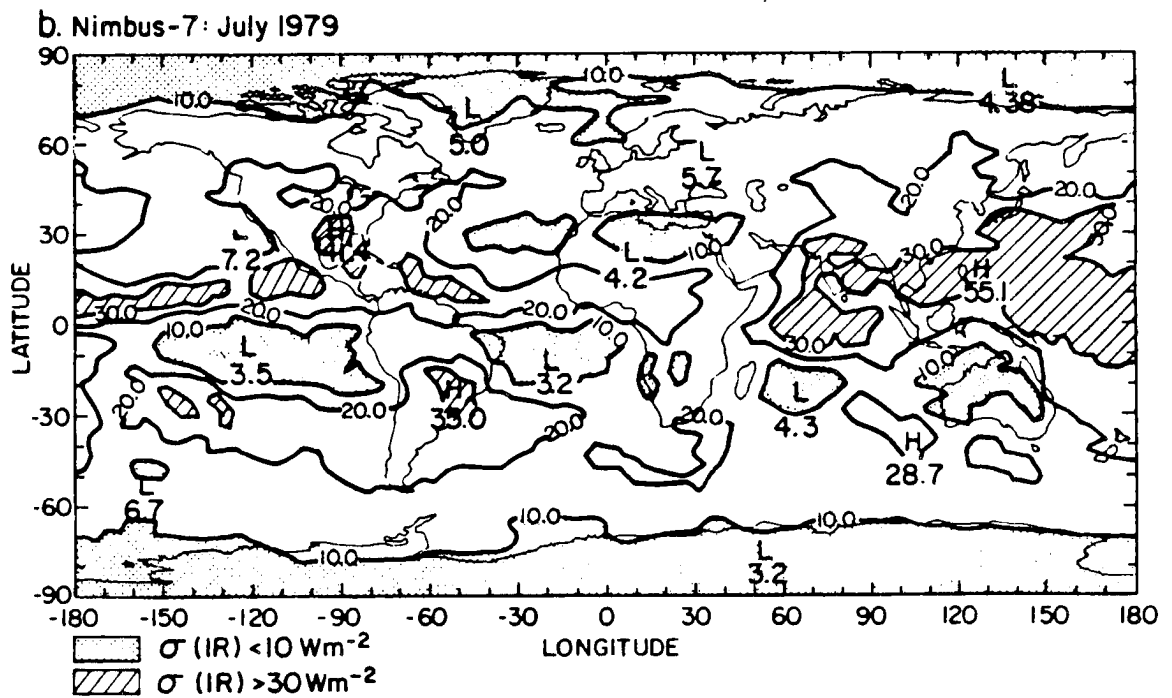
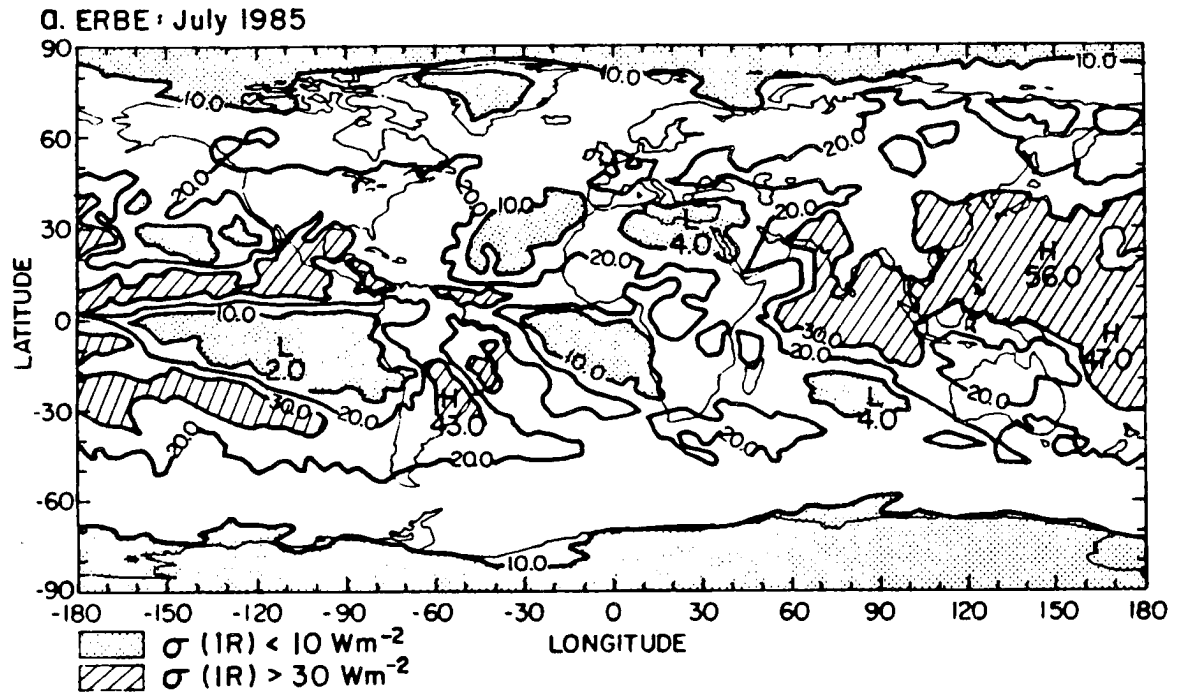


Figure 2.14: Map of the standard deviation of the outgoing infrared radiation (Wm⁻²): (a) ERBE (July 1985), and Nimbus-7 (July 1979).

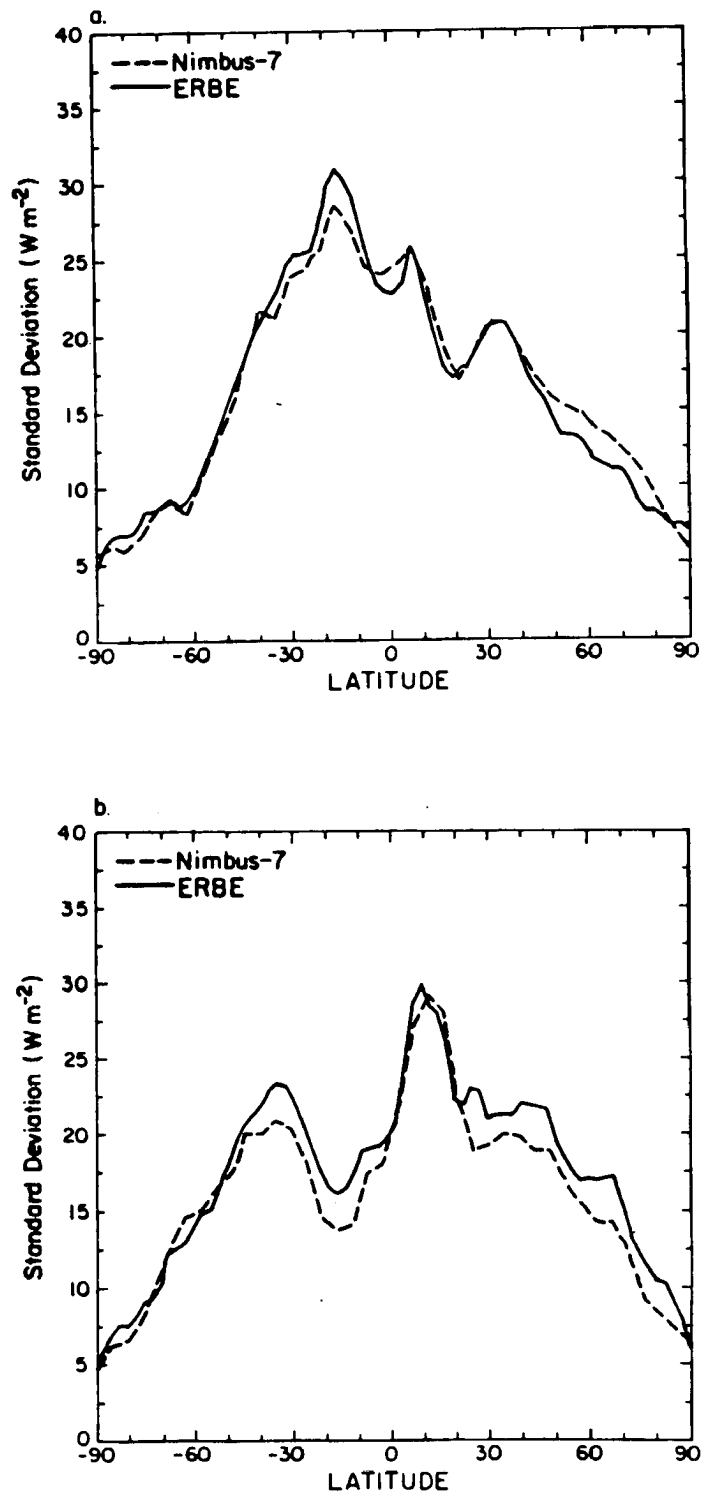


Figure 2.15: Zonally-averaged profile of the standard deviation of the outgoing infrared radiation (W m^{-2}): (a) January, and (b) July.

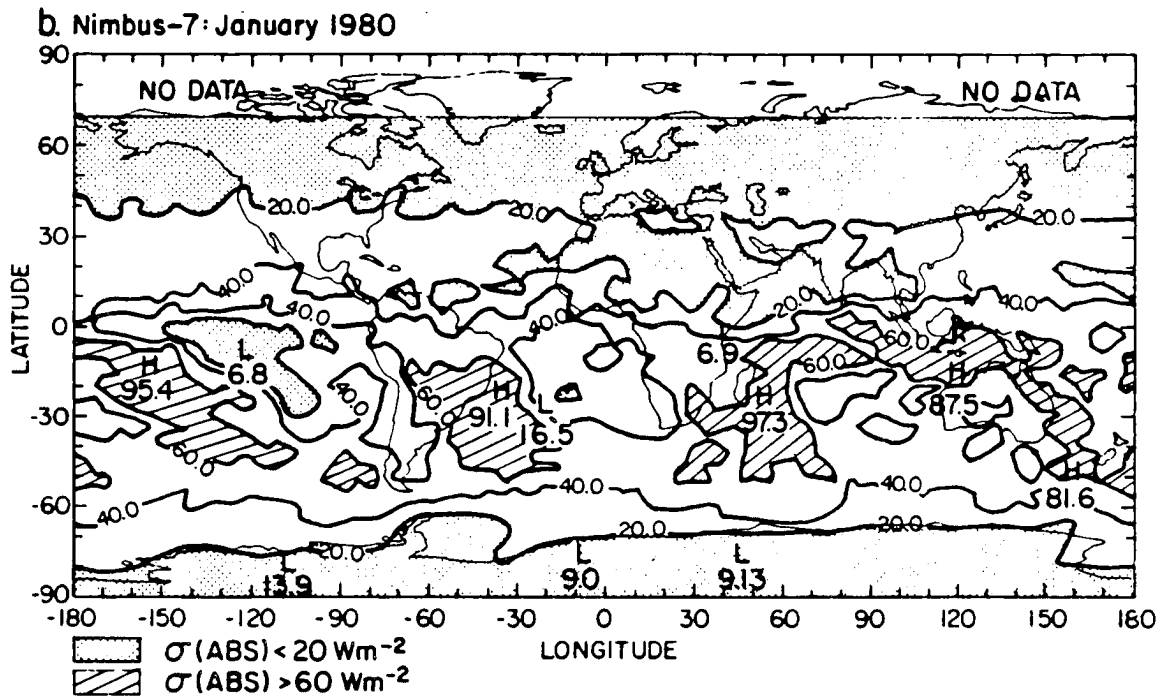
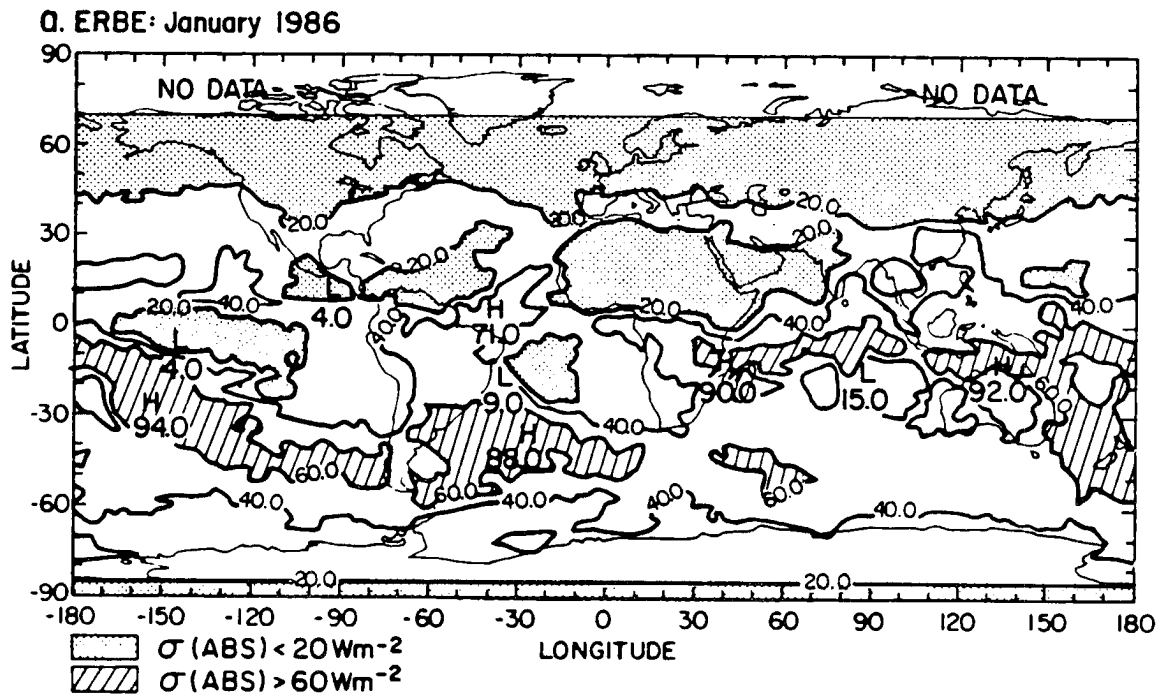


Figure 2.16: Map of the standard deviation of the absorbed solar radiation (Wm^{-2}): (a) ERBE (January 1986), and (b) Nimbus-7 (January 1980).

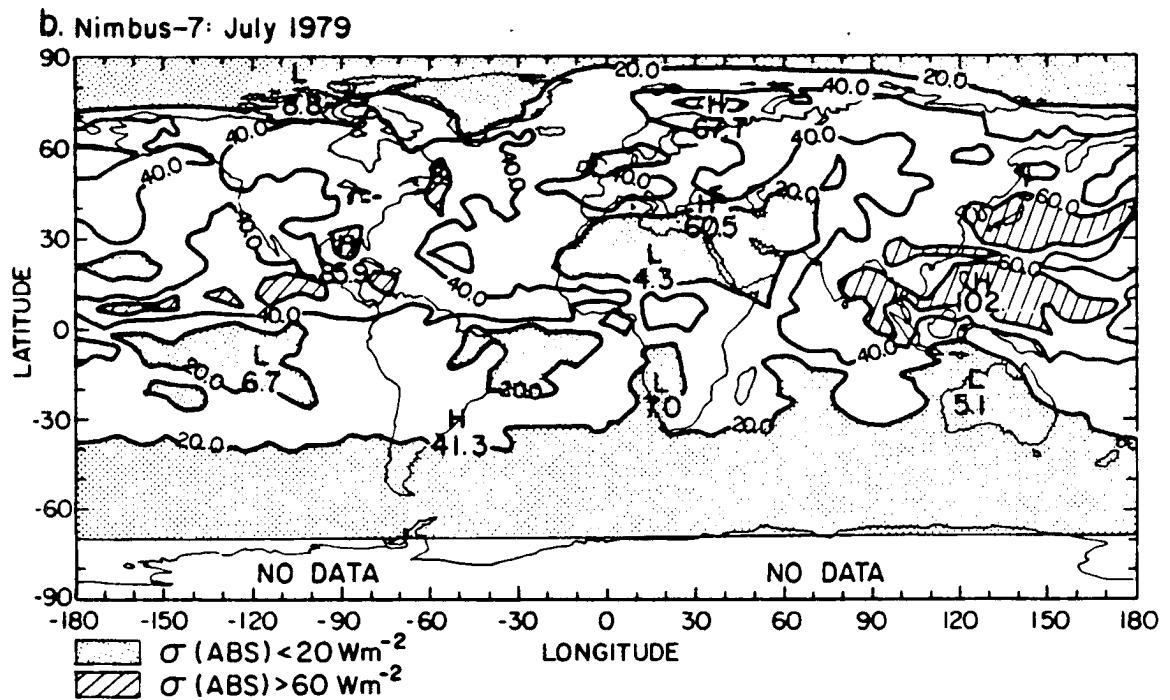
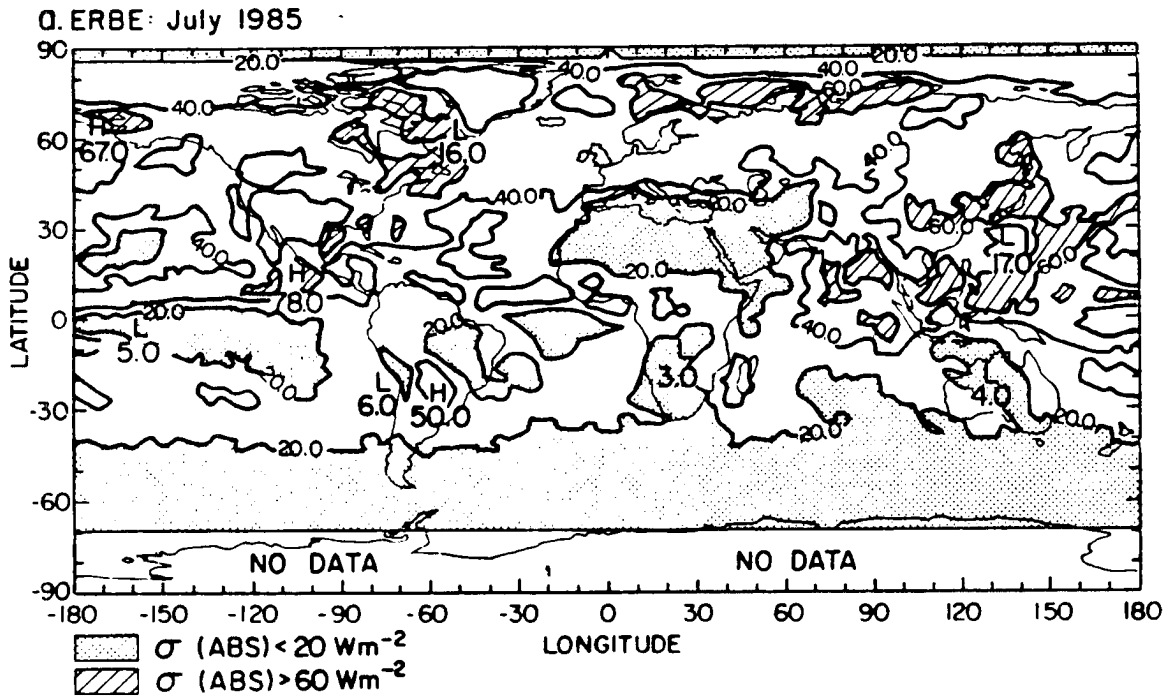


Figure 2.17: Map of the standard deviation of the absorbed solar radiation (Wm^{-2}): (a) ERBE (July 1985), and (b) Nimbus-7 (July 1979).

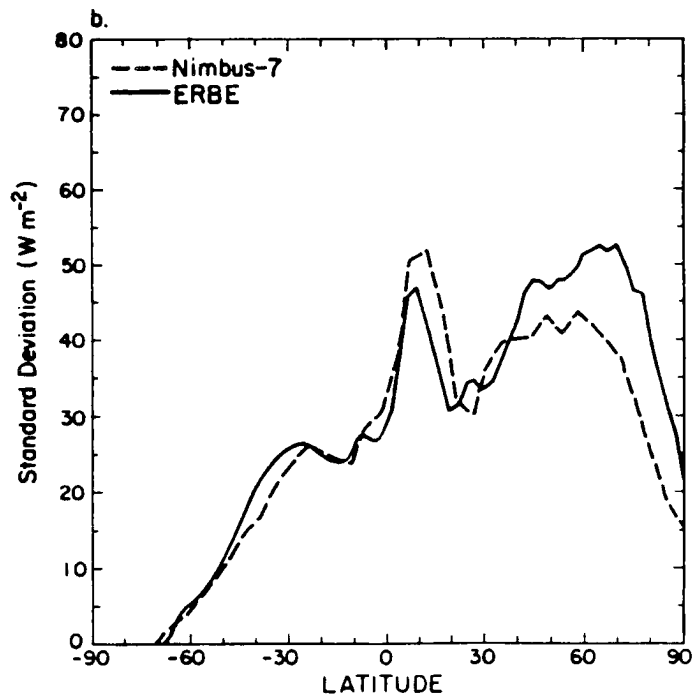
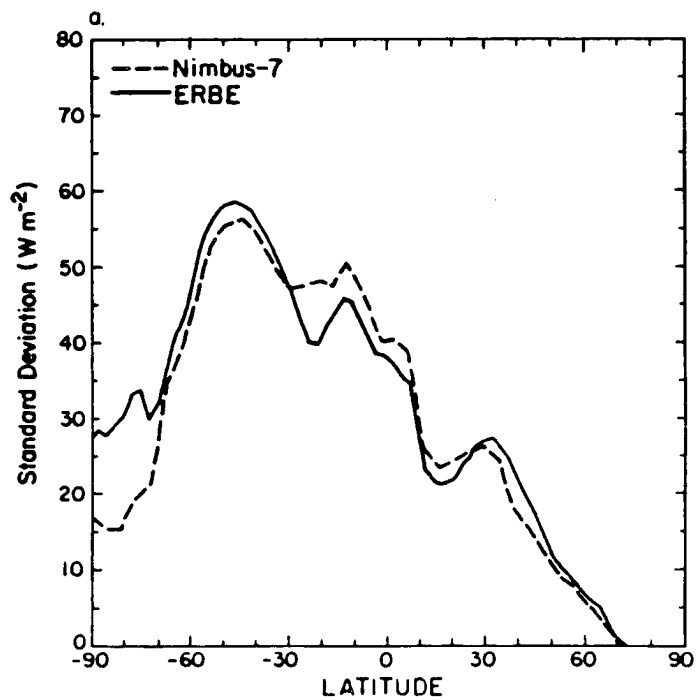


Figure 2.18: Zonally-averaged profile of the standard deviation of the absorbed solar radiation (Wm^{-2}): (a) January, and (b) July.

2.9.4 Comparison against NOAA infrared data

1. NOAA satellite data set

Although primarily designed for imaging and estimates of surface temperatures, scanner radiometers on board the successive NOAA satellites have been providing a continuous record of narrow-spectral-band longwave and shortwave radiances since June 1974. In the NOAA data set, the total outgoing infrared radiation is determined from observations taken in the infrared window [10.5-12.5] μm and the total reflected radiation is determined from observations taken in the visible spectrum [0.5-0.7] μm . Because of the poor agreement between the global distribution of the seasonally-averaged albedo obtained from the narrow- (NOAA) and broad- (Nimbus-7) spectral-band shortwave channels, we decided to limit our comparison to the outgoing infrared radiation field only. Daily observations of the planetary outgoing longwave radiation were obtained from two different series of NOAA operational spacecrafts between June 1979 and February 1980, as indicated in Table 2.5. Gruber and Jacobowitz (1985) discuss how monthly averaged observations from the TIROS-N satellite compare to the NOAA-6 data, to assess the compatibility of both IR time series. In addition, they compare the period of overlap between the TIROS-N data and the broad-spectral-band Nimbus-7 earth radiation data. They found an excellent agreement within about $1\text{-}2\text{ Wm}^{-2}$ in the monthly means on global and hemispheric scales. Comparisons of zonal averages indicate maximum differences as large as 9 Wm^{-2} . Empirical regressions were subsequently used to convert radiances measured in the infrared window into broad-spectral-band values (Ohring *et al.*, 1984). Continuous measurements of the outgoing infrared radiation for the ascending and descending nodes of the satellite orbit are available, daily, on a rectangular grid of 2.5° latitude-longitude resolution. The missing values have also been filled in and flagged as negative values for each daily map. Different orbital characteristics, temporal and spatial samplings between the NOAA and Nimbus-7 satellites, and more important different spectral intervals of the infrared channels lead to measurable differences between the NOAA and Nimbus-7 data sets. However, Smith and Vonder Haar (1988) show that there exists a very good

agreement in the geographical distribution of the seasonally-averaged outgoing infrared radiation for both the winter and summer seasons, and that the differences are within the range of uncertainty which may result from:

1. Different calibration of the narrow angle field-of-view infrared channels.
2. Narrow-spectral-band to broad-spectral-band conversion of the NOAA longwave radiances.
3. Radiance to irradiance conversion using angular dependence models.

Because of the 3-days on, 1-day off cycle of the Nimbus-7 data, it is not possible to calculate the time-lagged autocorrelation coefficients of the outgoing infrared radiation, since such a computation requires the use of continuous time series. The purpose of this section is to show the compatibility between the Nimbus-7 and NOAA data sets, so that we can complete our statistical analysis by computing time-lagged autocorrelation coefficients of the outgoing infrared radiation field from twice daily observations taken by the scanner radiometers on board the NOAA spacecrafts. Discussion of the distribution of the time-lagged autocorrelation coefficients is done in Chapter Four.

Table 2.5

Table 2.5: Characteristics of the Nimbus-7 and NOAA satellites (from Gruber and Jacobowitz, 1985).

SATELLITE	TIROS-N	NOAA-6	Nimbus-7
Infrared window (μm)	10.5-12.5	10.5-12.5	4.5-50.0
Period of record	01-79;01-80	02-80;07-81	11-78;06-80
Equator crossing (LT)	0300-1500	0730-1930	1200-2400
Resolution	4 km	4 km	90 km

2. Impact of the spatial averaging

Figures 2.19 and 2.20 show the global distribution of the standard deviation, normalized by the seasonal average, of the daily mean outgoing infrared radiation ($\sigma_n(\text{IR})$) obtained from the NOAA and Nimbus-7 IR time series for the winter and summer seasons. There is a very good agreement in the global distribution and magnitude of $\sigma_n(\text{IR})$ between the two satellites. As daily mean observations are used, the errors due to different temporal samplings are minimized and the differences observed between the two maps can be explained as mainly resulting from different spatial resolution. In addition, comparison of those two data sets show an excellent agreement in the seasonal average on global and hemispheric scales (Smith and Vonder Haar, 1988). Because of the higher spatial resolution, $\sigma_n(\text{IR})$ computed from the NOAA IR time series shows a more detailed structure than that obtained from Nimbus-7, especially at the boundary between regions of low and high temporal variability. As a whole, regions of $\sigma_n(\text{IR})$ greater than 12 % (respectively less than 4 %) have a greater (lesser) extent when computed from NOAA observations. The averaging of the different pixels into 2.5° instead of 4.5° grid-boxes yields an increased homogeneity within the field-of-view and therefore, a more accurate discrimination between completely overcast, partially cloudy, and completely cloudless boxes. On the other hand, above regions of relatively high outgoing infrared radiation, the averaging of the individual pixels into boxes of 4.5° side produce an averaged value of radiation emitted from completely cloudless pixels, plus the contribution from some neighboring partially cloud pixels. It is also important to note that the 3-days on, 1-day off cycle of the Nimbus-7 time series does not affect the magnitude of $\sigma_n(\text{IR})$.

Figure 2.21 shows the zonally-averaged profile of $\sigma_n(\text{IR})$. For both seasons, there is a fairly good agreement in the latitudinal distribution of $\sigma_n(\text{IR})$ between 30°N and 30°S between both satellites, especially in summer. The greatest difference is observed in the middle and high latitudes at which $\sigma_n(\text{IR})$ obtained from the NOAA data is systematically greater than that computed from Nimbus-7 observations. As for the global maps, this difference may result from different spatial averaging. In the middle latitudes, day-to-day fluctuations in the outgoing infrared radiation arise not only from variations in the cloud

cover, but also from changes in the temperature and humidity fields, due to advective and convective processes. In addition, because of lower atmospheric temperatures and lower-level cloud bases than at equatorial latitudes, the difference in thermal radiation between cloudy and cloudless conditions becomes less pronounced which explains a rather uniform distribution of low variability. This is especially true when $\sigma_n(\text{IR})$ is computed from Nimbus-7 data. The increased spatial resolution of the NOAA data allows to more precisely sensor the variations in outgoing infrared radiation resulting from traveling cyclonic disturbances, which explains higher values of $\sigma_n(\text{IR})$ in the middle latitudes. It is also worthwhile to note the negligible impact of the narrow to broad-band conversion of the NOAA infrared data and the missing days in the Nimbus-7 time series.

3. Impact of the temporal sampling

Global maps of the difference in the outgoing infrared radiation between the ascending and descending nodes of the orbit of a polar-orbiting satellite show large positive differences above the continents and nearshore areas, associated with the diurnal heating of land surfaces and the diurnal modulation of low-level stratiform clouds (Raschke and Bandeen, 1970; Short and Wallace, 1980). There also exists a consistent diurnal variation in longwave emission over regions of intense oceanic convection, associated with diurnal variation of convective (~ 400 mb) and very high (~ 100 mb) clouds as is discussed by Hartmann and Recker (1986) from a 10-year climatology of outgoing infrared radiation measurements taken by the NOAA sun-synchronous satellites for four different equatorial crossing times.

It is difficult to infer the impact of different diurnal samplings on the time variability of the outgoing infrared radiation from direct comparison between Nimbus-7 and NOAA satellite measurements. In addition to different equatorial crossing times, one has to take into account the different spatial resolution and calibration of the scanner instruments, as well as the conversion of the narrow-spectral-band observations into broad-spectral-band values. However, the comparison of between Nimbus-7 and ERBE data in Section 2.9.3 demonstrates that the temporal sampling has a negligible impact on the determination of

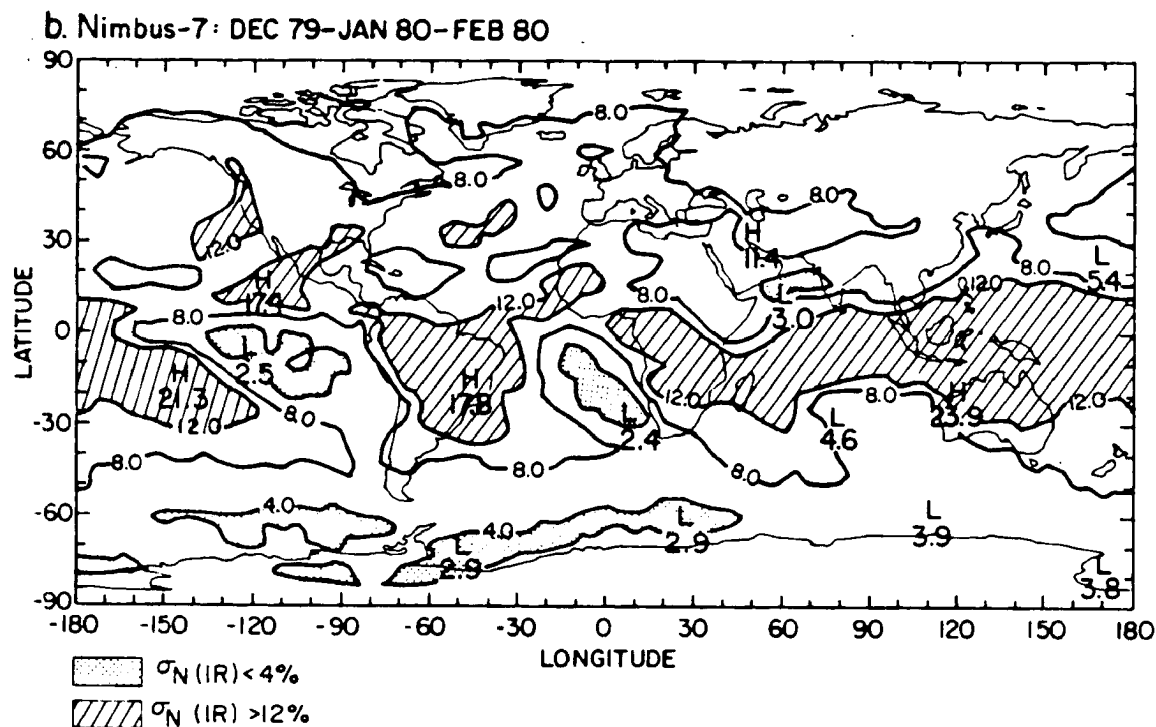
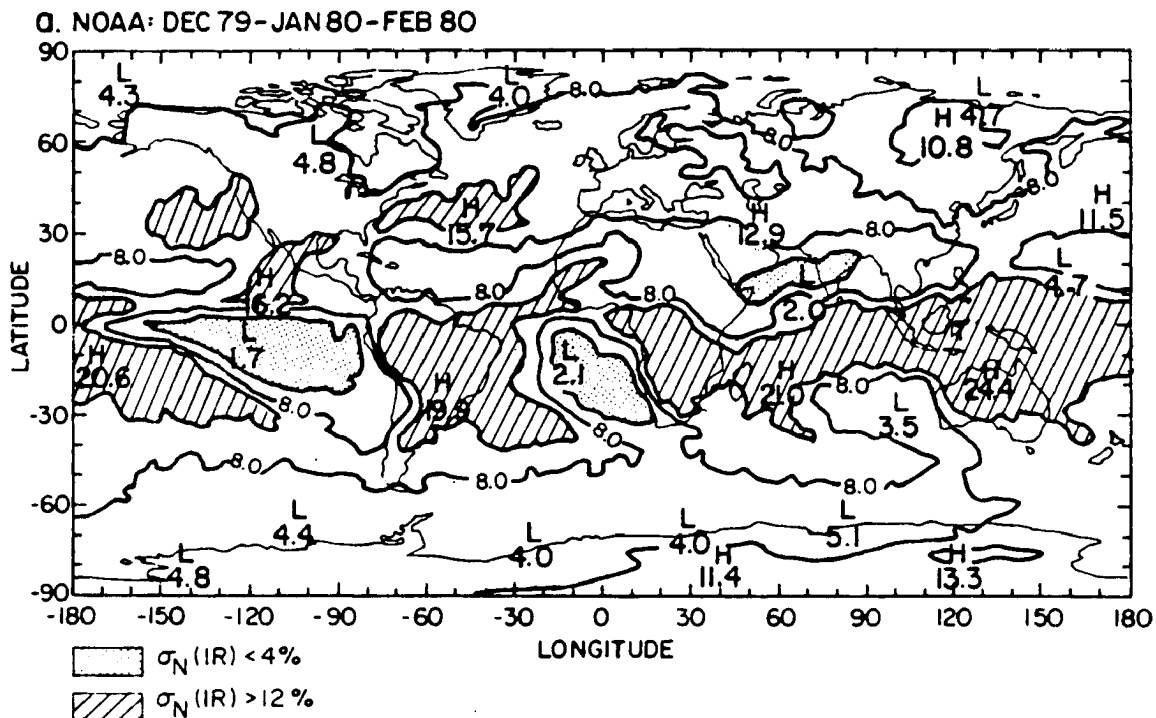


Figure 2.19: Map of the normalized standard deviation of the outgoing infrared radiation for Northern Hemisphere winter (%): (a) NOAA, and (b) Nimbus-7.

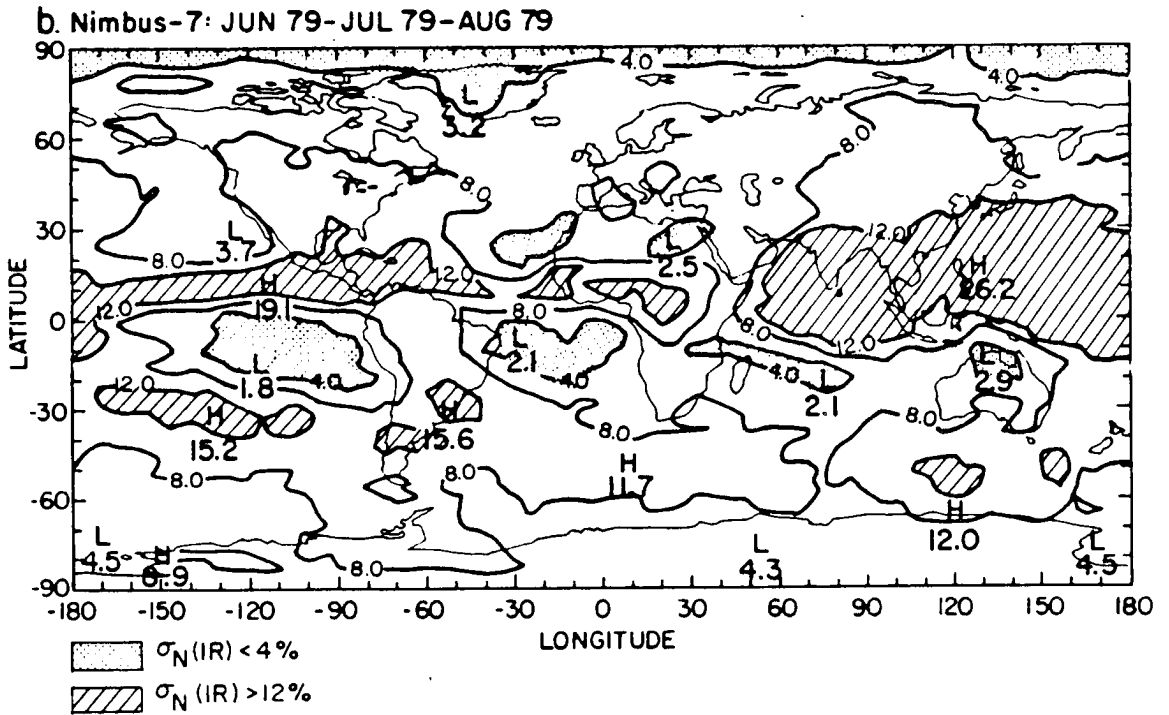
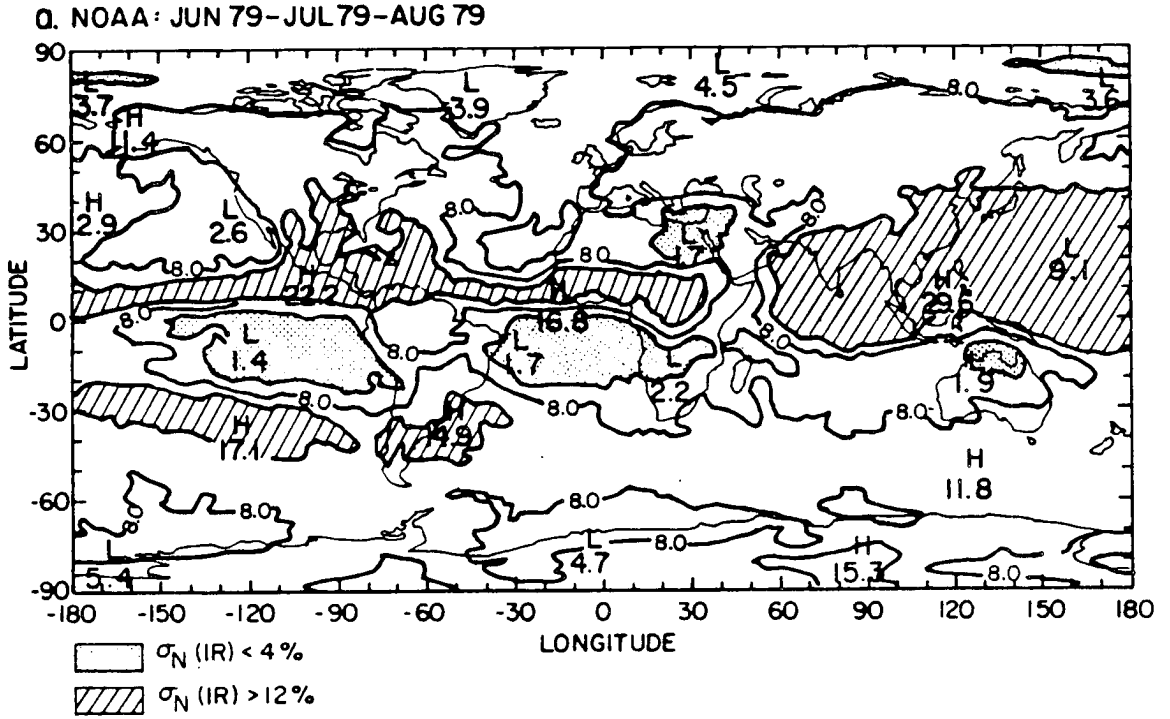


Figure 2.20: Map of the normalized standard deviation of the outgoing infrared radiation for Northern Hemisphere summer (%): (a) NOAA, and (b) Nimbus-7.

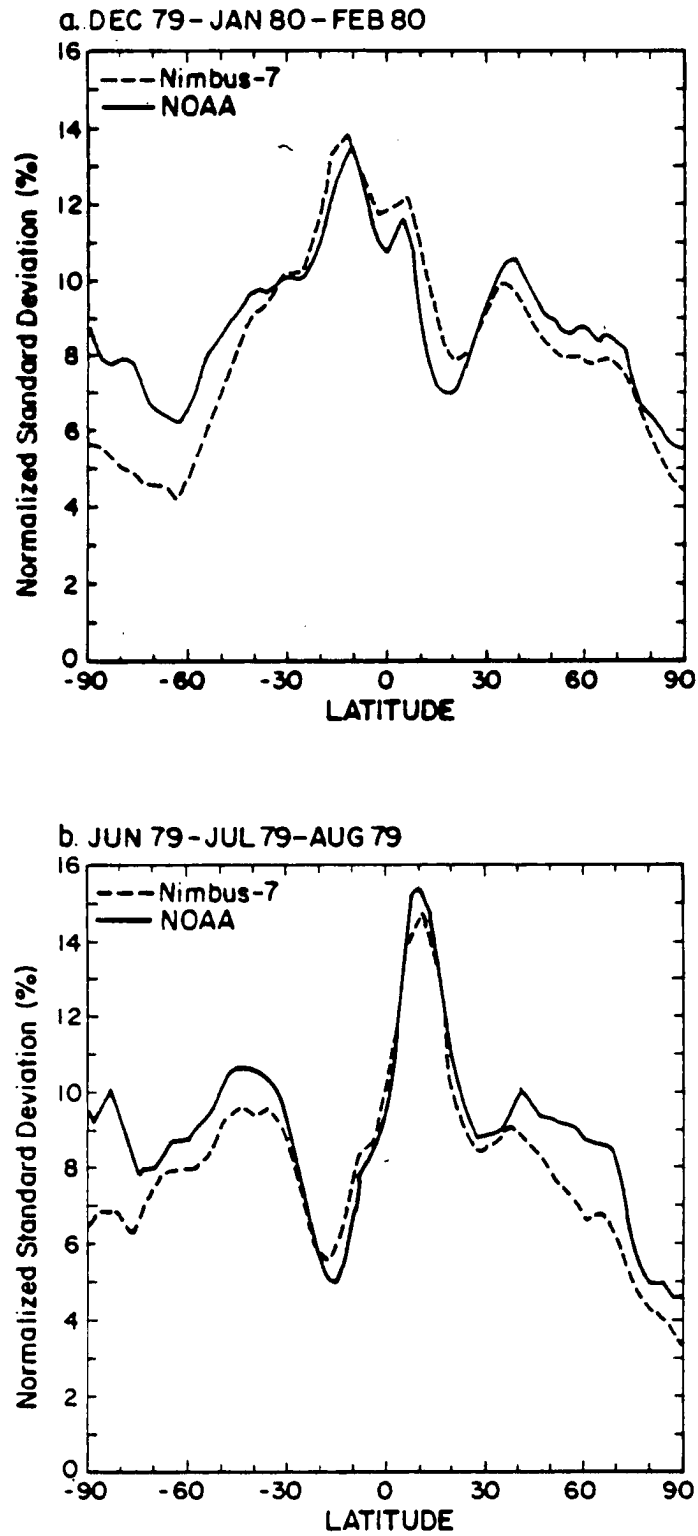


Figure 2.21: Zonally-averaged profile of the normalized standard deviation of the outgoing infrared radiation (%): (a) Northern Hemisphere winter, and (b) summer.

$\sigma(\text{IR})$ and $\sigma(\text{ABS})$. In the previous section, it was shown that the spatial averaging of the individual observations into smaller grid-boxes induced some characteristic differences in the magnitude of the standard deviation of the daily mean value, without, however, significantly altering its global distribution. As day-time and night-time outgoing infrared radiation data, measured at different equatorial crossing times, are available from both satellites, it is interesting to look at the impact of the diurnal sampling on the magnitude of the daily standard deviation.

This impact is investigated by combining every 12-hour observations instead of daily mean values to compute the standard deviation of the outgoing infrared radiation about the seasonal average. As should be expected, this yields an increase in the magnitude of the standard deviation because of the inclusion of the diurnal cycle effect. Figures 2.22 and 2.23 show global maps of the difference (σ_{dif}) between $\sigma(\text{IR})$ computed using twice daily observations and $\sigma(\text{IR})$ computed using daily mean values, from both satellite data sets and for both winter and summer seasons. In order to minimize the importance of a different spatial averaging between the two data sets, and prior to the computation of $\sigma(\text{IR})$, each daily field obtained from the NOAA instruments was, first, averaged into a 4.5° grid-box in order to match the Nimbus-7 format. As it would be observed from maps of the noon minus midnight differences in the seasonally-averaged longwave emission, large positive differences in $\sigma(\text{IR})$ are observed over the continents, because of the diurnal heating of the land surface. The comparison with maps of $\sigma(\text{IR})$ computed from the daily mean outgoing radiation field also indicates that, in the tropics, areas of maximum day-night differences coincide with areas of large standard deviation, above land as well as above the oceans. These differences result not only from surface heating effects, but also from the contribution of the diurnal variation of convective clouds and associated rainfalls. The computation of $\sigma(\text{IR})$ quantifies not only the effect of clouds on the temporal variability of the daily mean outgoing infrared radiation but also the impact of clouds on its diurnal cycle. Figures 2.22 and 2.23 show that there are some significant differences in the global distribution of σ_{dif} between the two satellites. There is a fairly good agreement above the continents, over which σ_{dif} mainly results from the diurnal cycle of the surface temperature.

The largest difference in the distribution of $\sigma(\text{IR})$ between the two satellites is observed above the oceans, over which σ_{dif} computed from NOAA infrared data is systematically larger than that obtained from Nimbus-7 observations. This is especially well seen above the oceanic convective regions, and may be attributed to the difference in the time sampling between the two satellites, as well as some spatial resolution effect. Additional studies may show that the equatorial crossing times of the NOAA satellites may be better suited to pick up the 12-hour differences in the life-cycle of the convective clouds.

2.9.5 Conclusion

The sensitivity of the temporal variability of the planetary radiation balance to temporal and spatial averaging effects was discussed by comparing the standard deviation of the daily mean radiation components computed from Nimbus-7, NOAA, and ERBE data. The very good agreement in the distribution of $\sigma(\text{IR})$ and $\sigma(\text{ABS})$ leads us to conclude that the spatial averaging has a larger impact than the diurnal sampling, which on a global scale, can be considered as negligible. $\sigma(\text{IR})$ and $\sigma(\text{ABS})$ are much more sensitive to the spatial resolution of the satellite measurements, as are the seasonally-averaged fields. In particular, an increased spatial resolution yields a sharper gradient at the boundaries between areas of low and high variability. This comparison also demonstrates that weaknesses in the Nimbus-7 radiation budget data set, especially systematic missing days and relatively low spatial resolution, do not induce systematic biases in the determination of the temporal variability of the shortwave and longwave radiation budget components. As a whole, the Nimbus-7 data set has the overall advantage over the NOAA data set that it was specifically designed for earth's radiation budget studies, and that it directly provides simultaneous broad-spectral-band daily observations of the outgoing infrared radiation and the planetary albedo.

2.10 Summary

In this chapter, the geographical distributions of the seasonal average and standard deviation about the seasonal average, of the daily mean outgoing infrared radiation, the

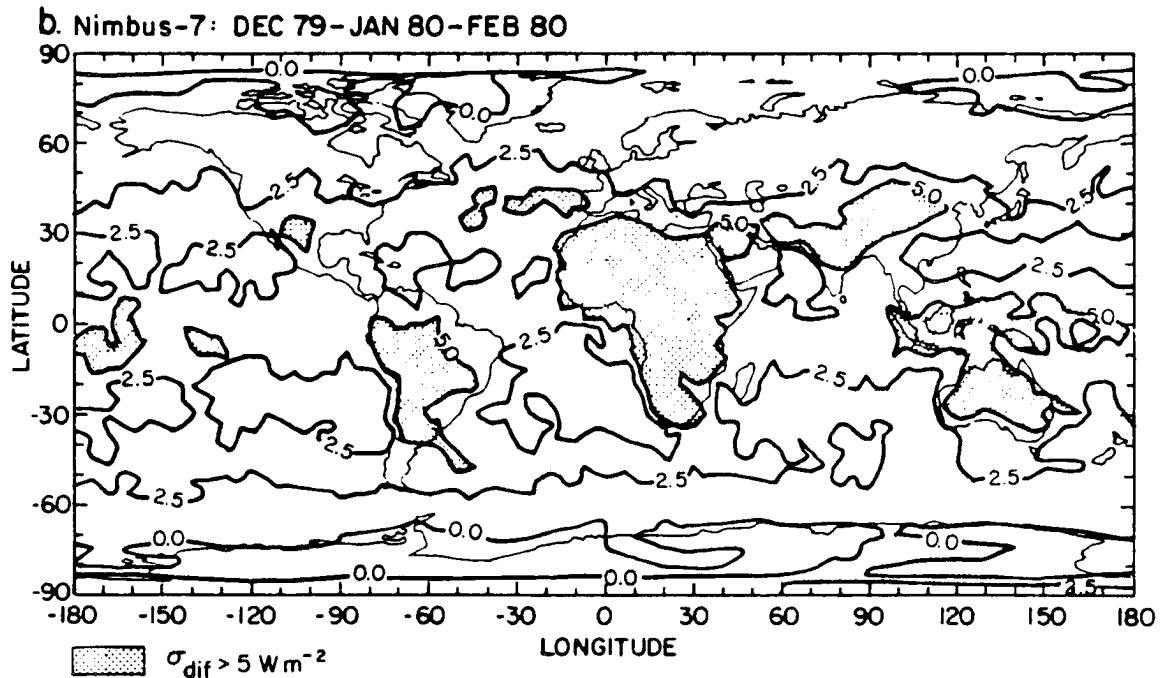
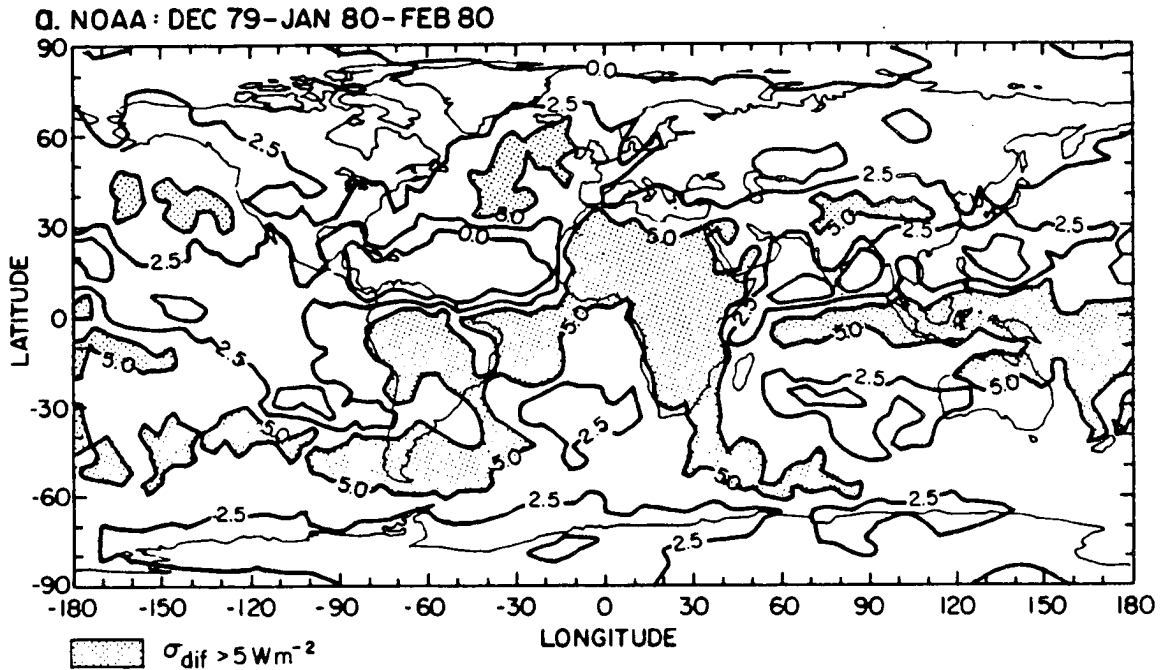


Figure 2.22: Map of the difference between the standard deviation computed from the daily mean and the 12-hour observations of the outgoing infrared radiation for Northern Hemisphere winter (Wm^{-2}): (a) NOAA, and (b) Nimbus-7.

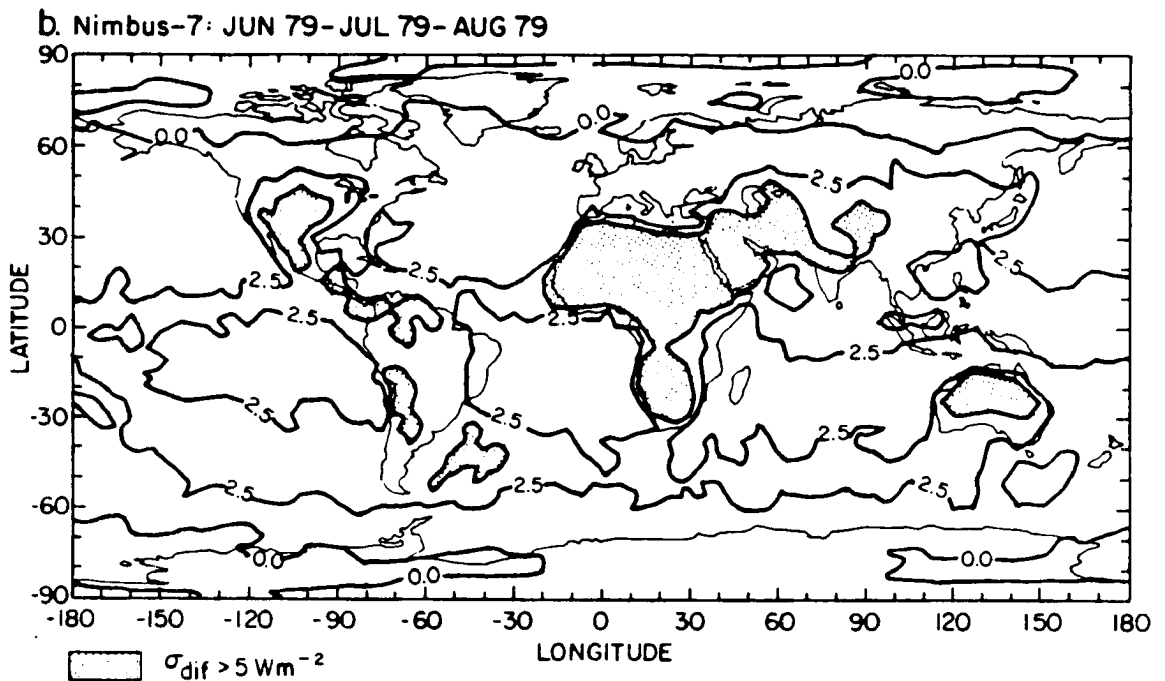
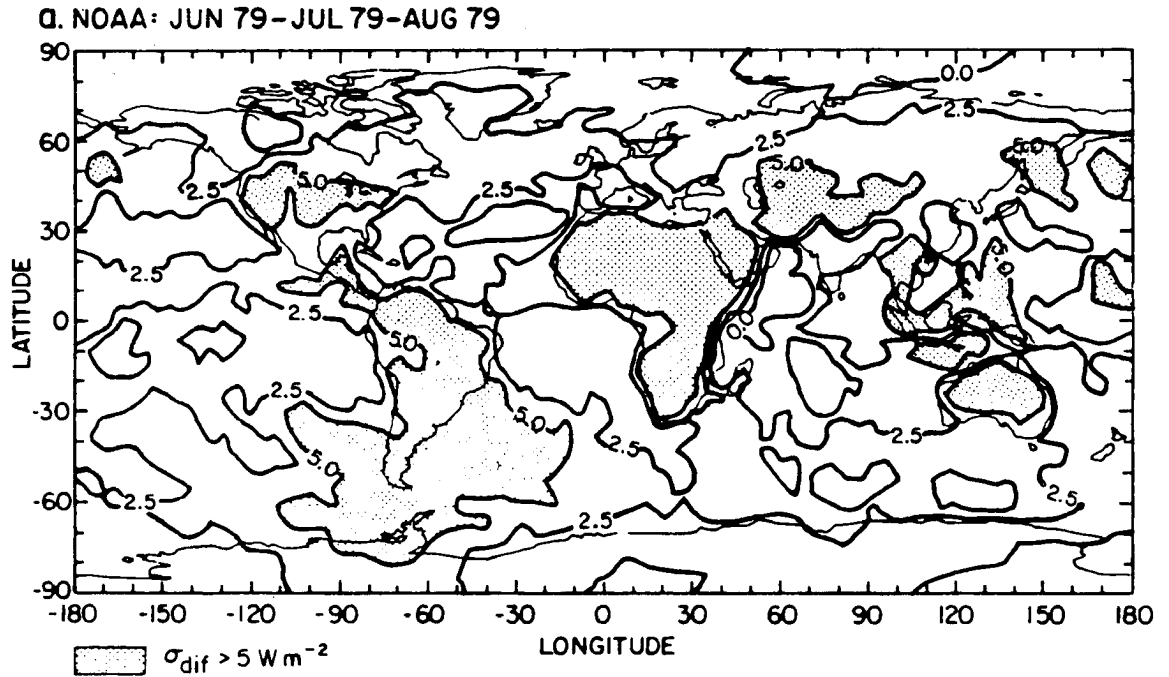


Figure 2.23: Map of the difference between the standard deviation computed from the daily mean and the 12-hour observations of the outgoing infrared radiation for Northern Hemisphere summer (Wm^{-2}): (a) NOAA, and (b) Nimbus-7.

planetary albedo, and the absorbed radiation taken by the NFOV scanners on board Nimbus-7 were discussed for the Northern Hemisphere winter and summer seasons. They were obtained from the only long-term satellite data set of NFOV broad-spectral band observations archived at present and represent, therefore, an extremely valuable contribution to the understanding of cloud-radiation-climate interactions from space, as well as references for the ongoing multi-satellite Earth Radiation Budget Experiment. In particular, limited comparisons between the two data sets, at long and short wavelengths, demonstrate the very good agreement in the determination of day-to-day fluctuations in the radiation balance. Several conclusions can be drawn:

1. The largest climatic signal is observed at low latitudes between 30°N and 30°S, and day-to-day fluctuations of clouds are primarily responsible for the temporal variability of the shortwave and longwave components of the planetary radiation balance.
2. The computation of the standard deviation and the covariance between the outgoing infrared radiation and the absorbed solar radiation helps delineate the location and extent of the regions dominated by intense cumulus activity from regions influenced by the presence by stratiform clouds or cloud-free conditions. In particular, maps of the covariance clearly show the seasonal variation of the location and intensity of the convective and storm track regions.
3. The computation of the cloud factor shows that there are large geographical variations in the radiative effect of clouds. On the whole, the albedo effect of clouds dominates their greenhouse effect, suggesting that a global increase in the cloud cover would lead to an overall cooling of the earth's climate.
4. The spatial averaging of the broad-spectral-band scanner data into a 4.5° grid is too coarse to distinguish between the temporal variability of the relatively cloud-free areas from those dominated by the presence of extended stratocumulus clouds. This limitation in the use of the Nimbus-7 NFOV measurements of the radiation

balance points out the necessity to acquire in the near future, broad-spectral-band scanner data averaged into smaller target areas, to obtain a statistically distinct signal between cloudless and cloudy regions.

5. There exists a very good agreement in the global distribution and magnitude of the standard deviation computed from the Nimbus-7 and NOAA IR time series, over the same time periods, although the two satellite missions and objectives were different. Computations of the time-lagged auto-correlation coefficients from NOAA infrared data will complete, in Chapter Four, our statistical analysis.
6. Finally, comparisons against the NOAA and, especially, the ERBE data sets show that our results do provide accurate estimates of the actual variability of the short-wave and longwave components of the top-of-atmosphere radiation balance. Therefore, we are confident, that they constitute a reliable reference to assess the ability of the NCAR Community Climate Model to reproduce the seasonally-averaged components of the planetary radiation balance and their temporal variability about the seasonal average. This is the primary objective of Chapter Four.

Chapter 3

DESCRIPTION OF THE NCAR COMMUNITY CLIMATE MODEL AND THE SIMULATIONS OF CLIMATE

3.1 Introduction

In this chapter, we introduce the main structural characteristics of the NCAR Community Climate Model (or NCAR CCM), including detailed descriptions of the radiative transfer schemes of short and long wavelengths, and of the cloud prediction scheme. We describe the different long-term simulations of climate which have been archived at the National Center for Atmospheric Research and used in Chapter Four to assess the performance of the GCM to reproduce the mean planetary radiation balance. Finally, we discuss some major problems inherent to CCM1 in comparing model outputs against satellite observations.

3.2 Model description

The latest version of the NCAR CCM, also known as version CCM1, encompasses the latest modifications and improvements brought over the last few years to the original code (or version CCM0), based on the Australian spectral model described in Bourke *et al.* (1977) and Mc Avaney *et al.* (1978). In its most currently used version for long-term simulations of climate, CCM1 is a 12-layer spectral model with a rhomboïdal truncation at wavenumber 15 which, in the physical space, corresponds to a spatial distribution of 4.5° in latitude and 7.5° in longitude. Williamson *et al.* (1987) extensively describes the parameterization of the continuous governing equations required to model the atmospheric flow. The vertical and temporal aspects of the model code are represented using difference approximations while the horizontal aspects are treated by the spectral transform method.

Physical parameterizations and non-linear operations are carried out for all grid-points at a single latitude, the computational sequence being successively repeated for each latitude band. Figure 3.1 summarizes the logic of the model flow for one basic time-step.

The vertical discretization of the atmosphere uses the σ -coordinate system. All prognostic variables and geopotential heights are computed at full- σ levels while the vertical velocity is calculated at half- σ levels, as shown on Figure 3.2. The full- σ values of the grid-levels are listed in Table 3.1 and specified as input variables, whereas the half- σ levels are given as the average of the adjacent full levels. Several input data sets are required at the initialization step of each model run. The single- and multi-level fields contained in the initial atmospheric data set are summarized in Table 3.2. Additional files are acquired to specify initial data used in the radiation parameterization package depending upon the characteristics of the climate simulations.

The bulk of the parameterization of the radiative transfer processes of short and long wavelengths, and of the parameterization of the distribution of clouds are described in Ramanathan *et al.* (1983). The modifications incorporated into the CCM1 version are listed in Williamson *et al.* (1987) and a detailed description of the numerical algorithms can be found in Kiehl *et al.* (1987). Solar and infrared fluxes are calculated at half- σ levels while heating rates are calculated at full- σ levels. Clouds are formed between half- σ levels and centered about full- σ levels. Additional information on the physical parameterization of the radiative transfer processes and of the cloud-radiation interactions are given in the following sections.

3.3 Radiative transfer scheme of short wavelengths

3.3.1 Shortwave spectral interval

The sun can be considered as a blackbody emitting shortwave radiation at an effective temperature of 5800 K. 99% of this energy is radiated within the spectral interval [0.15 - 4.0] μm . Schematically, solar radiation is absorbed by the earth's surface and by the main gaseous constituents of the atmosphere (H_2O , CO_2 , O_3 , O_2), and scattered by aerosols and

A. GRID-POINT SPACE

- Beginning of latitude line: Bring in the grid-data at the current latitude at time-step (n) and (n-1)
 1. Convective adjustment
 2. Computation of clouds
 3. Radiation
 4. Surface energy budget
 5. Vertical diffusion
 6. Computation of the non-linear terms
- End of latitude line

B. SPECTRAL SPACE

- Computation of the spectral coefficients
- Solve the semi-implicit equations
- Compute the horizontal diffusion terms

C. GRID-POINT SPACE

- Beginning of latitude line:
 1. Calculate the grid-data at current latitude at time-step (n+1)
 2. Complete the computation of the horizontal diffusion terms
 3. Write out the grid-data at time-step (n+1)
- End of latitude line

Figure 3.1: Control of the model flow to compute the grid-data at time-step n+1, knowing the grid-data at time-steps n and n-1.

Vertical Index			Variables
1/2	$\sigma = 0$	—————	$\dot{\sigma} = 0$
1	$\Delta\sigma_1, \sigma_1$	- - - - -	$U, V, T, q, \Phi, \eta, \delta, \omega$
1 1/2		—————	$\dot{\sigma}$
2	$\Delta\sigma_2, \sigma_2$	- - - - -	$U, V, T, q, \Phi, \eta, \delta, \omega$
2 1/2		—————	$\dot{\sigma}$
3	$\Delta\sigma_3, \sigma_3$	- - - - -	$U, V, T, q, \Phi, \eta, \delta, \omega$
		• • •	
$k - 1/2$		—————	$\dot{\sigma}$
k	$\Delta\sigma_k, \sigma_k$	- - - - -	$U, V, T, q, \Phi, \eta, \delta, \omega$
$k + 1/2$		—————	$\dot{\sigma}$
		• • •	
$K - 1$	$\Delta\sigma_{K-1}, \sigma_{K-1}$	- - - - -	$U, V, T, q, \Phi, \eta, \delta, \omega$
$K - 1/2$		—————	$\dot{\sigma}$
K	$\Delta\sigma_K, \sigma_K$	- - - - -	$U, V, T, q, \Phi, \eta, \delta, \omega$
$K + 1/2$	$\sigma = 1$	////////////////	$\dot{\sigma} = 0, \Phi_s, p_s, T_s$

Figure 3.2: Vertical discretization of the model atmosphere. K indices refer to full- σ levels, whereas $K \pm \frac{1}{2}$ indices refer to half- σ levels (from Williamson *et al.*, 1987).

cloud droplets. At short wavelengths, the two main absorbers are ozone and water vapor with a weaker contribution from carbon dioxide and oxygen.

1. Ozone

The concentration of O_3 varies with latitude and is maximum around 23 km at the equator. Its absorption bands are located at ultraviolet ($\lambda \leq 0.35 \mu\text{m}$) and visible ($0.5 \mu\text{m} \leq \lambda \leq 0.7 \mu\text{m}$) wavelengths and are responsible for the warming of the stratosphere.

2. Water vapor

H_2O has multiple vibration-rotation bands in the near-infrared ($0.7 \mu\text{m} \leq \lambda \leq 4.0 \mu\text{m}$) and primarily contributes to the warming of the low troposphere.

3. Carbon dioxide and oxygen

CO_2 absorbs solar radiation in the near-infrared around $2.6 \mu\text{m}$ but plays a lesser role than O_3 and H_2O . O_2 has an absorption band around $0.75 \mu\text{m}$ but its contribution to shortwave absorption is also very small.

3.3.2 Clear-sky fluxes

The radiative transfer scheme of short wavelengths is characterized by the following properties:

- Computation of the clear-sky fluxes closely follows the formulation of Lacis and Hansen (1974). The solar spectrum is divided into two spectral intervals, $[0.0-0.9] \mu\text{m}$ and $[0.9-4.0] \mu\text{m}$, to respectively account for ultraviolet and near-infrared absorption.

- The radiative transfer scheme takes into account molecular absorption by H_2O , O_3 , CO_2 and O_2 . O_3 absorption follows the expression of Lacis and Hansen (1974). H_2O absorption is calculated from the parameterization of Kratz and Cess (1985) for the direct beam, and Lacis and Hansen for the reflected beam. Absorption in the near-infrared due to CO_2 is calculated from the expression of Sasamori *et al.* (1972). Finally, O_2 absorption is based on the parameterization of Kiehl and Yamanouchi (1985).

- Rayleigh scattering is taken into account in the ultraviolet-visible spectrum. The direct-beam Rayleigh albedo and the diffuse-beam Rayleigh albedo are respectively written:

$$\alpha_R^{dr} = \frac{0.28}{1 + 6.43 \cos \xi}, \quad (3.1)$$

in which ξ is the solar zenith angle and

$$\alpha_R^{df} = 0.0685. \quad (3.2)$$

• Boundary conditions:

(i) At the top of the model the downward solar flux is written:

$$F_S^\downarrow(Z) = f S_o \cos \xi, \quad (3.3)$$

where S_o is the radiation incident at the top-level of the model, which value is fixed at 1370 W m^{-2} . f is the fractional amount of daylight and depends upon the calendar day. Z is the altitude of the top-level.

(ii) At the surface ($z=0$), the reflected shortwave flux is:

$$F_S^\uparrow(0) = A_S F_S^\downarrow(0), \quad (3.4)$$

where $F_S^\downarrow(0)$ is the downward flux at the surface and A_S the surface albedo. The albedo parameterization is from Briegleb *et al.* (1986) and includes a solar zenith angle dependence of albedo for various surface types.

3.3.3 Cloud-radiation interactions

At short wavelengths, clouds reflect downward radiation and contribute a major to the planetary albedo. Clouds are defined by their horizontal cloud fraction and their cloud albedo. The cloud fraction is internally generated whereas the cloud albedo is given a prescribed value, as explained in section 3.5. Multiple reflections between the different cloud layers, and between cloud layers and the surface are taken into account. Gaseous absorption within the clouds is also included.

3.4 Radiative transfer of long wavelengths

3.4.1 Longwave spectral interval

The earth-atmosphere system can be considered as a blackbody emitting radiation at an effective temperature of 255 K. 99% of this energy is radiated within the spectral interval [4.0 - 100.] μm . Schematically, the two most important processes taking place at long wavelengths are emission and absorption by all solid and liquid materials, and atmospheric gaseous constituents. Scattering processes can be considered negligible in the infrared spectrum.

1. Water vapor

H_2O has a very strong vibration-rotation band centered at 6.3 μm which wings are stretched between 5 and 9 μm . A pure rotational band of variable intensity is located between 18 and 100 μm . Its wings partially overlap towards short wavelengths with the wings of the CO_2 absorption band centered at 15 μm . Because of the abundance of water vapor at low altitudes, these two bands have a very strong influence on the energy balance of the atmosphere.

2. Carbon dioxide

CO_2 has a very strong vibration-rotation band centered at 15 μm . Because of its position close to the maximum of the Planck function at terrestrial temperatures, this band also plays a major role in the radiative balance of the earth-atmosphere system. CO_2 also has two absorption bands centered at 4.3 μm and 5 μm but which are located in a region of small intensity of the Planck function at infrared wavelengths. Two other bands are centered at 9.4 μm and 10.4 μm in the atmospheric window but are non-saturated and have a weaker intensity.

3. Ozone

The most important vibration-rotation band for O_3 is centered at 9.6 μm . This band is also located close to the maximum of emission of the Planck function and strongly influences the terrestrial regime, particularly in the stratosphere. A band of strong intensity is centered around 4.7 μm but corresponds to an area of weak intensity for the Planck function.

4.e-continuum

In addition, absorption by the continuum of water vapor (or e-type absorption) in the atmospheric window between 8 and 13 μm strongly influences the vertical distribution of the radiative cooling rates, especially in the low tropospheric layers.

3.4.2 Clear-sky fluxes

The radiative transfer scheme of long wavelengths is characterized by the following properties:

- Clear-sky fluxes at long wavelengths are computed using the concept of broad-band flux absorptivity to solve the radiative transfer equation. The downward and upward fluxes at a half-pressure level p_k can be respectively written:

$$F_{dr}^{\downarrow}(p_k) = B(0)\epsilon(0, p_k) + \int_0^{p_k} \alpha(p', p_k) \frac{dB}{dp'}(p') dp' , \quad (3.5)$$

and

$$F_{dr}^{\uparrow}(p_k) = \sigma_B T_S^4 - \int_{p_k}^{p_S} \alpha(p', p_k) \frac{dB}{dp'}(p') dp' , \quad (3.6)$$

in which $B(p) = \sigma_B T^4(p)$ is the Stefan-Boltzmann's law. p_S and T_S are the pressure and temperature at the surface. The absorptivity $\alpha(p, p')$ and the emissivity $\epsilon(0, p)$ are respectively:

$$\alpha(p, p') = \frac{1}{\frac{dB}{dT}(p')} \int A_{\tilde{\nu}}(p', p) \frac{dB_{\tilde{\nu}}}{dT}(p') d\tilde{\nu} , \quad (3.7)$$

and

$$\epsilon(0, p) = \frac{1}{B(0)} \int A_{\tilde{\nu}}(0, p) B_{\tilde{\nu}}(0) d\tilde{\nu} , \quad (3.8)$$

in which $A_{\tilde{\nu}}$ is the absorptivity due to a given gas, $B_{\tilde{\nu}}(p')$ is the Planck function, and $\tilde{\nu}$ is the wavenumber in cm^{-1} .

- The radiative transfer scheme takes into account the molecular absorption-emission by H_2O , CO_2 and O_3 . The H_2O absorptivity is computed using the new non-isothermal emissivity scheme of Ramanathan and Downey (1986). The CO_2 absorptance model is from Kiehl *et al.* (1987). Absorption by ozone follows the model of Ramanathan and Dickinson (1979).

- The surface emissivity is non black ($\epsilon < 1$) in the [8-13] μm window region.
- Boundary conditions:

(i) The downward longwave clear-sky flux at the surface is expressed by the relation:

$$F_{dr}^{\downarrow}(p_S) = B(0)\epsilon(0, p_S) + \int_0^{p_S} \alpha(p', p_S) \frac{dB}{dp'}(p') dp', \quad (3.9)$$

while the upward flux at the surface is just:

$$F^{\uparrow}(p_S) = \sigma_B T_S^4. \quad (3.10)$$

(ii) The downward flux at the top-level is $F^{\downarrow}(0) = 0$.

3.4.3 Cloud-radiation interactions

At infrared wavelengths, clouds absorb downward and upward radiation emitted above and below the cloud, and reemit radiation at their own body temperatures. Clouds are specified by their horizontal cloud fraction and their cloud emissivity which are discussed in the next section. Upward and downward infrared fluxes between cloud layers are computed following the method described in Washington and Williamson (1977).

3.5 Cloud cover parameterization

Clouds are predicted after the moist large-scale and convective adjustment schemes of Manabe *et al.* (1965) have been applied. When supersaturation occurs, the temperature and specific humidity fields are simultaneously adjusted to force the atmosphere to be just saturated. The change in the moisture field required to eliminate supersaturation conditions drives the occurrence of clouds in the model and is assumed to go next into precipitation. At a given grid-point, convective or non-convective clouds form whenever the relative humidity exceeds 100 % which is the threshold value for supersaturation to occur. No clouds are allowed in the first layer adjacent to the surface or in the top two layers of the model.

3.5.1 Cloud fraction

- Large scale condensation clouds are formed when the vertical gradient of the equivalent potential temperature, θ_e , is stable ($\frac{\partial \theta_e}{\partial z} \geq 0$). The cloud fraction for stratiform clouds is equal to 95 %.

- Convective clouds are formed in supersaturated layers in which moist convective adjustment takes place ($\frac{\partial \theta_e}{\partial z} < 0$). If N is the number of convectively unstable layers, the cloud fraction A_i in each layer i is:

$$A_i = \frac{0.3}{N}, \quad (3.11)$$

so that the total cloud fraction for convective clouds does not exceeds 30%.

- The total cloud fraction A_T in a vertical column is computed following the random overlap assumption:

$$A_T = 1 - \prod_{i=1}^N (1 - A_i). \quad (3.12)$$

Figure 3.3 from Ramanathan *et al.* (1983) gives a schematic illustration of the vertical distribution of convective and non convective clouds in the model. Extended cirrus shields at the top of the convective clouds and upper tropospheric cloud debris are predicted as large-scale stratiform clouds.

3.5.2 Cloud emissivity

At infrared wavelengths, it can be considered that clouds emit radiation as black bodies, except high-level ice and water clouds which emissivities are usually less than unity. Ramanathan *et al.* (1983) demonstrate that the radiative impact of black cirrus is to enhance the cooling of the polar troposphere whereas a more realistic parameterization of their emissivity leads to significant improvements in model simulations of the atmospheric circulation. Following theoretical calculations and observations of cirrus emissivities (Stephens, 1978; Griffith *et al.*, 1980), the emissivity of large-scale condensation clouds is expressed as a function of the condensed water content in CCM1:

$$\left\{ \begin{array}{ll} \epsilon_c = 1 & \tau LWC > 2.5 \\ \epsilon_c = \frac{1 - \exp(-\tau LWC)}{1 - \exp(-2.5)} & \tau LWC \leq 2.5 \end{array} \right. \quad (3.13)$$

where $\tau = 1000$ and LWC is the accumulated condensed water content expressed in gm cm^{-2} . In the computation of the longwave radiative fluxes, the effective cloud fraction, $A_e = \epsilon_c A_i$ is used, to take into account absorption in the cloud layer.

3.5.3 Cloud albedo

The impact of clouds on the solar albedo is prescribed as a function of the cloud levels. For non-overlapped cloud layers, the direct-beam cloud albedo, α_{dr} , and the diffuse-beam cloud albedo, α_{df} , are defined as:

$$\alpha_{dr} = \frac{\alpha_{cl}}{\alpha_{cl} + \cos\xi}, \quad (3.14)$$

and

$$\alpha_{df} = \frac{\alpha_{cl}}{\alpha_{cl} + 0.5}, \quad (3.15)$$

in which α_{cl} is a parameter which takes the values 0.6, 0.3, and 0.15 for the levels 1-4 (low-level clouds), levels 5 and 6 (middle-level clouds), and 7-13 (high-level clouds), respectively. For overlapped cloud cloud layers, the effective cloud albedo is a more complicated function of α_{dr} and α_{df} to take into account multiple reflections between the various cloud layers, and between clouds and the surface.

3.6 Simulations of climate with CCM1

3.6.1 Long-term simulations archived at NCAR

Four different long-term simulations of climate have been run with CCM1 and archived at the National Center for Atmospheric Research. They are currently used to analyze the contributions of the improvements brought into the original model code to simulate the characteristic features of the atmospheric general circulation. Two 1200-day runs reproduce the mean climate for perpetual January (Case 223) and perpetual July (Case 240) conditions. In these two runs, the global distribution of the incoming solar radiation, the surface albedo, the vertical distribution of ozone, and the sea-surface temperature are held

fixed to January and July climatological values. Two 15-year runs which take into account the seasonal cycle of the input climate parameters are also available without (Case 239) or with (Case 241) an optional parameterization of an interactive surface hydrologic cycle. Both runs were started with the initial atmospheric conditions of January 16, 1975. The model does not include any parameterization of the diurnal cycle. The diurnal variations of the radiation and cloudiness have been recently implemented in the model code and validation tests are being undertaken at the present time. The full radiative transfer calculation is made every 12 hours for daily-averaged insolation conditions while the model time-step is 30 mn for all the other physical processes. The expensive computational cost of the radiative heating rates in long-term climate simulations and the fact that there is no diurnal cycle justify this choice. All four simulations are stored on History Tapes which are volumes of data output by the model every 12 hours, consisting of a sequence of logical records and containing the values of model variables for a series of model days. The History Tapes are archived as files on the NCAR Mass Storage System and can be easily accessed and read using the CCM Modular Processor (Wolski, 1987).

Chervin (1980) shows that a complete description of GCM-simulated climate can be done by means of sampled climate ensembles which are sets of independent and finite time-span realizations. In the following chapters, the ensemble average and ensemble standard deviation of the time averages, standard deviations computed from the time average, and time-lagged autocorrelation coefficients are computed from a set of five independent climate ensembles, following Chervin's technique. While the ensemble average produces a picture of the mean GCM-simulated climate, including its temporal variability, the ensemble standard deviation between the five independent realizations gives an estimate of the model noise. Inside each time sample, the time average, standard deviations about the time average, and time-lagged autocorrelation coefficients of all model-simulated climate parameters are computed from every 12-hour model outputs. As an example, the geographical distribution of the ensemble average and ensemble standard deviation of the seasonally-averaged outgoing infrared radiation is shown in Figure 3.4 for Northern Hemisphere conditions. Figure 3.5 shows the global map of the ensemble average and ensemble

standard deviation of the standard deviation, computed from the seasonal average, of the outgoing infrared radiation. The global distributions of the ensemble standard deviation of the time average and time standard deviation show identical patterns. The magnitude of the ensemble standard deviation of the standard deviation is less than that of the time average by about 4 Wm^{-2} . The largest variability between the five winter seasons is located above the convective activity regions which are characterized by low terrestrial emission and high day-to-day variability, as observed from satellite. Outside those specific areas, the ensemble standard deviations of the time average and time standard deviation respectively drop to values less than 8 Wm^{-2} and 4 Wm^{-2} . Although we did not verify that hypothesis, it is very unlikely that additional climate realizations in the computation of the ensemble average would significantly decrease the ensemble standard deviation.

3.6.2 Stability of the simulated climate

In the use of long-term GCM simulations, one has to be aware of possible climate drift which may result from deficiencies in the parameterization of and bouncing between the physical processes, as well as from the specification of the initial conditions. To insure that the choice of the five independent but consecutive climate realizations among the fifteen total possibilities is not affected by this phenomenon, the ensemble average and ensemble standard deviation of the first five model-years (1975-1980), the last five model-years (1985-1990), and the five model-years chosen for validation of the model-climate (1979-1984), were computed for the temperature field at the σ -levels 0.811 and 0.250, and for the net planetary radiation budget. Table 3.3 shows that the ensemble average of the time average and standard deviation of the globally-averaged temperature and net radiation fields are equal for the three combinations. The computation of the ensemble standard deviation of the time average and standard deviation shows that the model stability increases with the time integration, as indicated by a slight decrease in the ensemble standard deviation. These results demonstrate that the choice of any five consecutive model years will not affect the comparison between the model-simulated and satellite-observed components of the planetary radiation balance.

Finally, objective univariate statistical tests are usually used to assess the ability of general circulation models to simulate climate, based upon the comparison between modeled and observed climate ensembles (Chervin, 1981). The natural variability of modeled climate (Chervin and Schneider, 1976) and the year-to-year variability of real atmospheric observations are measured by the ensemble standard deviation between the individual time-span realizations, and taken into account in the derivation of statistical differences between simulated and observed ensembles. In the following sections, it was not possible to calculate the same set of statistical tests because only one year of NFOV daily data from Nimbus-7 ERB is available for contribution to the model validation. Therefore, in Chapter Four, one has to assume that:

(i) the seasonal average and standard deviation about the seasonal average computed from Nimbus-7 satellite observations provide an accurate representation of the mean radiation budget and its temporal variability. This has been demonstrated from the comparison between outgoing infrared radiation observations taken by the Nimbus-7 and NOAA scanner radiometers over the same time period.

(ii) the difference between model and observations is statistically significant. This will be dependent upon the magnitude of the ensemble standard deviation computed from the five simulated climate ensembles.

3.7 Summary

Among the characteristics of the NCAR Community Climate Model, we see at least three major deficiencies which are likely to produce important discrepancies between the GCM-simulated and observed climate. They are: the relatively low spatial resolution of the model grid, the lack of diurnal variations of the insolation, surface temperature, and cloudiness, and finally, the cloud prediction scheme, especially at short wavelengths.

The spectral truncation at 15 zonal wavenumbers produces a longitudinal resolution of 7.5° while the 40-points Gaussian quadrature scheme gives a latitudinal spacing between grid-points of approximately 4.5° . This spatial resolution is closer to that of satellite observations obtained from WFOV instruments than from relatively NFOV scanner

radiometers. In particular, it is too coarse to accurately simulate the position of the ITCZ over the oceans and the gradient of net radiation between land and oceans. Although Nimbus-7 WFOV observations are also available, they do not cover the whole globe on a daily basis which made us decide to limit our comparison against NFOV data only.

The satellite observations and the model produce instantaneous estimates of the radiation budget components sampled at identical time intervals. The satellite Nimbus-7 flies over a fixed location at approximately the same local time and 12-hour apart, at least for observations away from the poles. The amplitude of the diurnal cycle of outgoing infrared radiation and cloudiness is estimated by the difference between the noon and midnight satellite orbits. Although instantaneous but too far apart to adequately describe the diurnal cycle, every 12-hour radiation observation contains some information of the evolution of the cloudiness over the last 12 hours. This is not the case in the model. We anticipate that the arbitrary full computation of radiation every 12 hours instead of following the diurnal cycle of the insolation will eventually increase the fluctuations of the cloud cover between 12-hour time-steps.

As in most GCMs, the occurrence of clouds in CCM1 mainly depends upon the atmospheric stability, the relative humidity, and their large-scale tendencies. This approximation can be seen, in part, as a compromise between the necessary low spatial resolution of the model-grid to limit the computational cost of long-term simulations, and the inclusion of some sub-grid scale characteristics of the interactions between clouds-radiation effects and the hydrologic cycle. However, the cloud prediction scheme distinguishes only between convective and large-scale clouds, while several schemes in others GCMs include, for instance, a separate parameterization of planetary-boundary layer clouds (Slingo, 1987; Randall *et al.*, 1988). Finally, cirrus clouds from deep convection outflow are, as in most GCMs, predicted as optically thick large-scale supersaturation clouds because of our limited understanding of their development within the convection area and lack of observational support.

The optical properties of clouds are arbitrarily fixed so that the modeled planetary albedo resembles that observed from satellite. The non-inclusion of any cloud optical feedback is a common deficiency in GCMs and we anticipate major discrepancies between the model-simulated and satellite-observed absorbed solar radiation, and in the distribution of the cloud shortwave radiative forcing. Charlock and Ramanathan (1985) discuss the importance of internally generated cloud optics on the albedo field and cloud radiative forcing produced by the NCAR CCM for perpetual January conditions. They particularly show that, at regional scales, the inclusion of the LWC-dependent albedo produces significant changes in the absorbed solar radiation when compared against the non LWC-dependent albedo, as well as a strong dependence upon the dynamical state of the model atmosphere.

In the following chapters, the model-generated planetary radiation balance is compared against satellite observations, and differences between model and observations are explained in view of the deficiencies in CCM1.

Table 3.1

Table 3.1: Vertical σ -coordinate system. σ and σH^* refer to the full- and half-levels.

Level index	σ	Half-level index	σH^*	Level index	σ	Half-level index	σH^*
1	0.991	1	1	7	0.245	7	0.300
2	0.926	2	0.959	8	0.165	8	0.205
3	0.811	3	0.869	9	0.110	9	0.138
4	0.664	4	0.738	10	0.060	10	0.085
5	0.500	5	0.582	11	0.025	11	0.043
6	0.355	6	0.428	12	0.090	12	0.017

Table 3.2

Table 3.2: Initial atmospheric data set.

Variable Name	Description
Multi-level fields	
T	temperature (K)
u	zonal wind component (m s^{-1})
v	meridional wind component (m s^{-1})
q	water vapor specific humidity (KgKg^{-1})
Single-level fields	
ϕ_s	surface geopotential (m^2s^{-2})
ps	surface pressure (Pa)
Ts	surface temperature (K)
Ws	surface wetness (m)
SN	water equivalent snow depth (m)
ORO	surface type flag =0 over ocean =1 over land =2 over sea ice

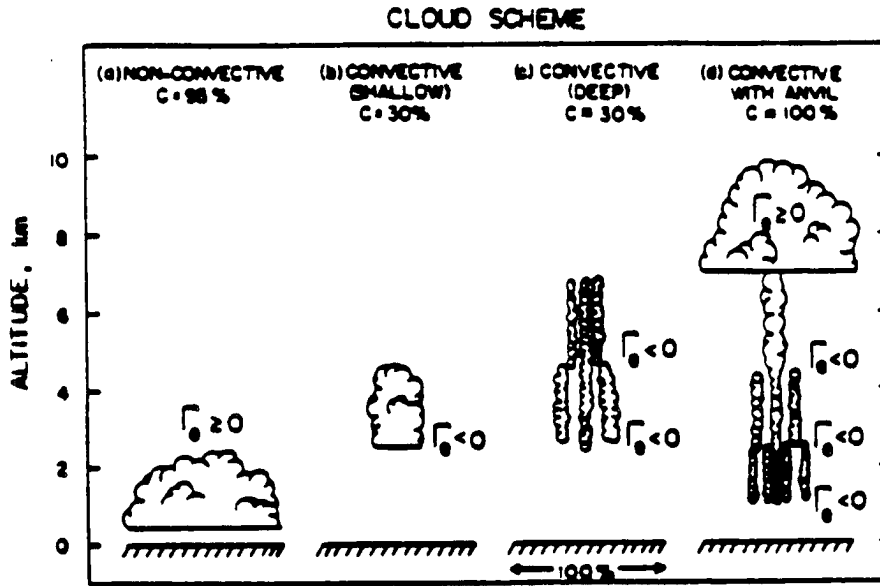


Figure 3.3: Vertical distribution of large-scale condensation and convective clouds. Γ_c is the atmospheric adiabatic lapse rate (from Ramanathan *et al.*, 1983).

Table 3.3

Table 3.3: Global average of the ensemble average and ensemble standard deviation of the time average and time standard deviation (σ) of the temperature (T) and net radiation budget (NET) fields.

<u>A. Ensemble average:</u>						
	T(.811)	σ (T(.811))	T(.25)	σ (T(.25))	NET	σ (NET)
	(K)		(K)		(Wm^{-2})	
1975-1980	276.0	3.1	223.9	3.8	7.9	58.6
1979-1984	276.0	3.1	223.9	3.8	8.0	58.5
1985-1990	276.0	3.1	223.9	3.6	8.1	58.5
<u>B. Ensemble standard deviation:</u>						
1975-1980	0.57	0.29	1.27	0.48	5.2	3.7
1979-1984	0.53	0.27	0.94	0.48	5.3	3.6
1985-1990	0.47	0.27	0.92	0.42	4.9	3.5

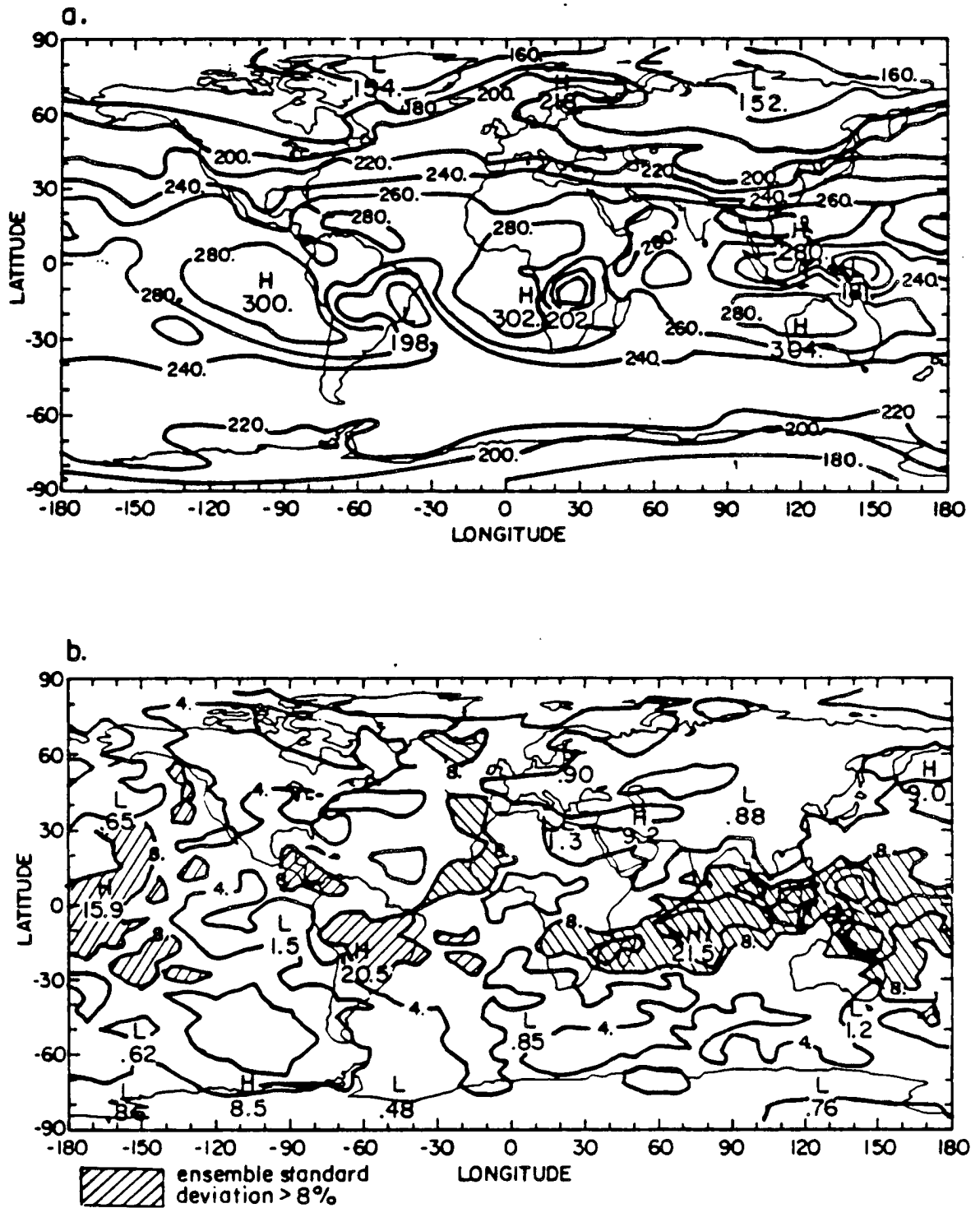


Figure 3.4: Map of (a) ensemble average of time average, and (b) ensemble standard deviation of the time average of the outgoing infrared radiation (Wm^{-2}).

Chapter 4

RADIATION BUDGET STATISTICS FROM CLIMATE SIMULATIONS WITH THE NCAR COMMUNITY CLIMATE MODEL

4.1 Introduction

In Chapter One, we discussed the importance of validating climate simulations made with GCMs against observations, with some emphasis on the role of ERB measurements for objective comparison with model outputs. In particular, polar-orbiting satellites provide global observations of the planetary radiation balance on a regular daily basis which is the necessary conditions that GCMs have to conform to. In this chapter, the model-simulated outgoing infrared radiation, absorbed solar radiation, and planetary albedo are compared against satellite ERB observations to assess the model ability to reproduce the mean planetary radiation budget and its temporal variability. The ensemble averages of the time averages, standard deviations computed from the time average, and time-lagged autocorrelation coefficients of the radiation components generated with CCM1 are computed from the 15-year run including a seasonal cycle (Case 239) for simulated Northern Hemisphere summer and winter seasons (later simply referred as summer and winter). Within each independent time-span realization, every 12-hour model output is used, at short and long wavelengths, to compute the various moment statistics. Table 4.1 gives the list of History Tapes and model days used to produce winter and summer conditions. The model-simulated seasonal average and standard deviation are compared against those computed from Nimbus-7 NFOV data during the time periods June-July-August 1979 and December 1979-January-February 1980. The model-simulated time-lagged autocorrelation coefficients of the outgoing infrared radiation are compared to those computed from the outgoing infrared radiation time series taken by the NOAA scanner radiometers over

the time period between December 1979 and February 1980. In order to match the time interval between model outputs, both ascending and descending node observations from the satellite, instead of daily mean value of the outgoing infrared radiation, are used in the computation of the standard deviation about the seasonal average and the time-lagged autocorrelation coefficients. The impact of the diurnal cycle and other limitations in our comparison between model and observations are discussed in the last section.

Table 4.1

Table 4.1: List of time-span realizations used to build the various climate ensembles.

CASE 239: Seasonal cycle			
Days	History Tapes JUN-JUL-AUG	Days	History tapes DEC-JAN-FEB
	/CSM/CCM1/239/		/CSM/CCM1/239/
1596.0-1687.5	X239107-X239113	1779.0-1868.5	X239119-X239125
1961.0-2052.5	X239131-X239137	2144.0-2233.5	X239143-X239149
2326.0-2417.5	X239156-X239162	2509.0-2598.5	X239168-X239174
2691.0-2782.5	X239180-X239185	2874.0-2963.5	X239192-X239198
3056.0-3147.5	X239204-X239210	3239.0-3328.5	X239216-X239222

4.2 Modeling of the atmospheric circulation

Pitcher *et al.* (1983) use climate simulations for perpetual January and July conditions obtained from an earlier version of the NCAR CCM (CCM0B), to discuss the model performance to simulate the atmospheric general circulation. Comparison of various synoptic fields against real observations highlights some of the model's strengths and weaknesses, and demonstrates that, as a whole, the model can successfully reproduce the large-scale characteristics of the atmospheric motions. Prior to a detailed comparison of the model-generated planetary radiation balance against ERB observations, the distribution of the seasonally-averaged sea-level pressure, atmospheric temperature, precipitation rate, zonal- and meridional-wind components, and the vertical velocity computed with

CCM1 are compared against real circulation data for Northern Hemisphere winter conditions.

Figure 4.1 shows the geographical distribution of the sea-level pressure computed from the model and from January observations compiled by Schutz and Gates (1971). The model captures well the chief characteristics appearing in the observed field. In the winter hemisphere, the Icelandic and Aleutian lows are well positioned and their intensities compare well with the climatological data. However, the strength of the Siberian anticyclone is too high by about 5 mb. In the summer hemisphere, the model simulates very well the position and intensity of the subtropical anticyclones above the oceans but fails to reproduce the sharp latitudinal decrease of the sea-level pressure around 50°S. Pitcher *et al.* (1983) suggest that this may result from the smoothed topography of the model at these latitudes.

In Figure 4.2, the global distribution of the model simulated surface-air temperature is compared against observations taken by Schutz and Gates (1971). The model reproduces the main features contained in the data. In the winter hemisphere, the temperature sharply decreases along the western coasts of the continents, although the isolines are not as tight as seen from observations. At equatorial latitudes, the near-surface temperature above the oceans is about 5 K colder although the seasonal cycle of the sea-surface temperature is included in the model simulation. Figure 4.3 shows the latitude-height distribution of the zonal mean atmospheric temperature. The main deficiency of the climate simulation is that the tropospheric and stratospheric temperatures are systematically colder by about 5 to 10 K.

Figure 4.4 presents the geographical distribution of the winter precipitation rate computed from the model and from observations compiled by Schutz and Gates (1972). In the winter hemisphere, observations show that the precipitation rate is maximum above the North Pacific and North Atlantic storm-track regions in the middle latitudes. In the summer hemisphere, regions of heavy rainfall are also regions of deep tropical activity: along the ITCZ in the Pacific and Atlantic oceans, above the continents (Amazon Basin,

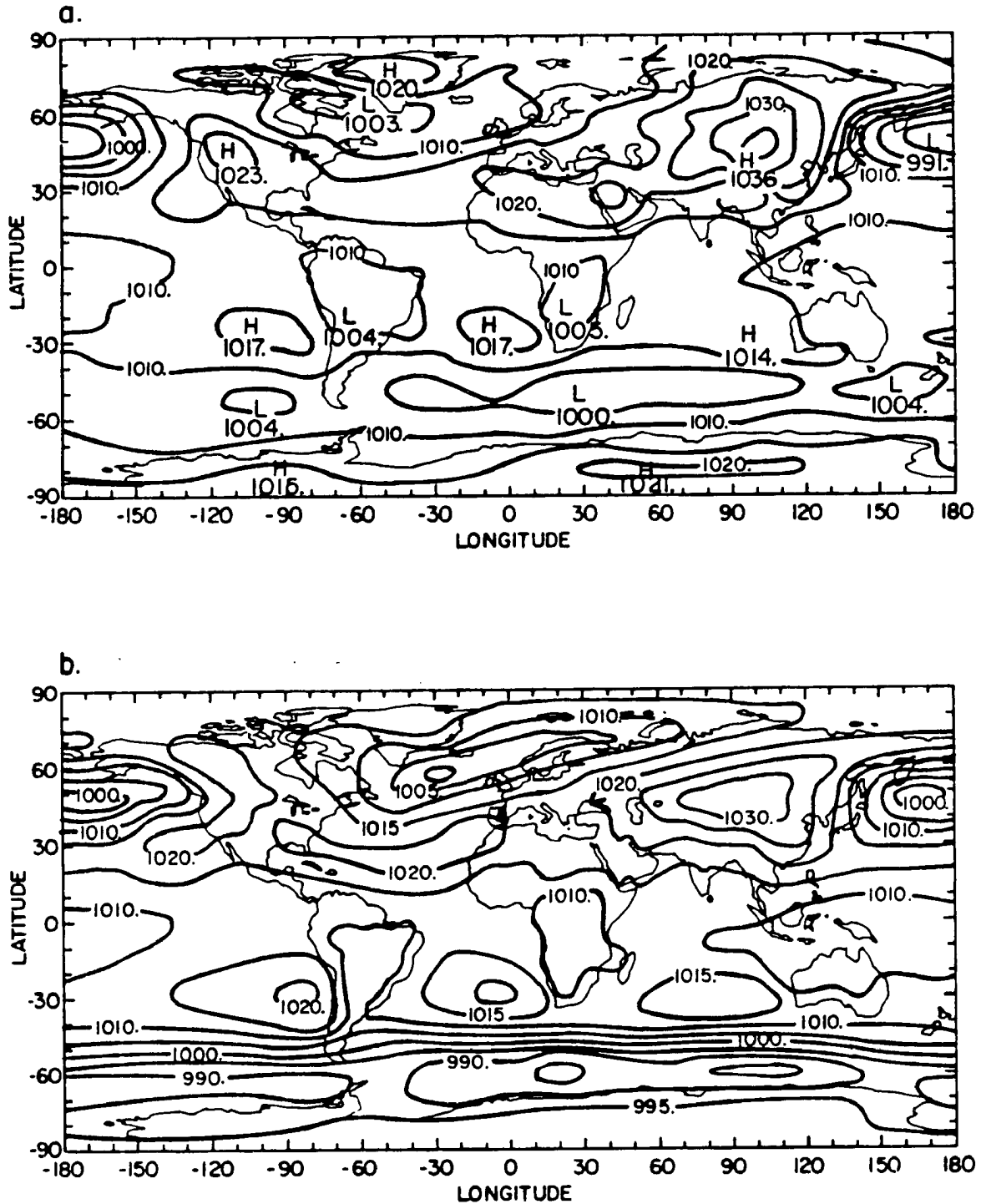


Figure 4.1: Map of the seasonally-averaged sea-level pressure for Northern Hemisphere winter (mb): (a) computed distribution from the model, and (b) observed distribution compiled by Schutz and Gates (1971).

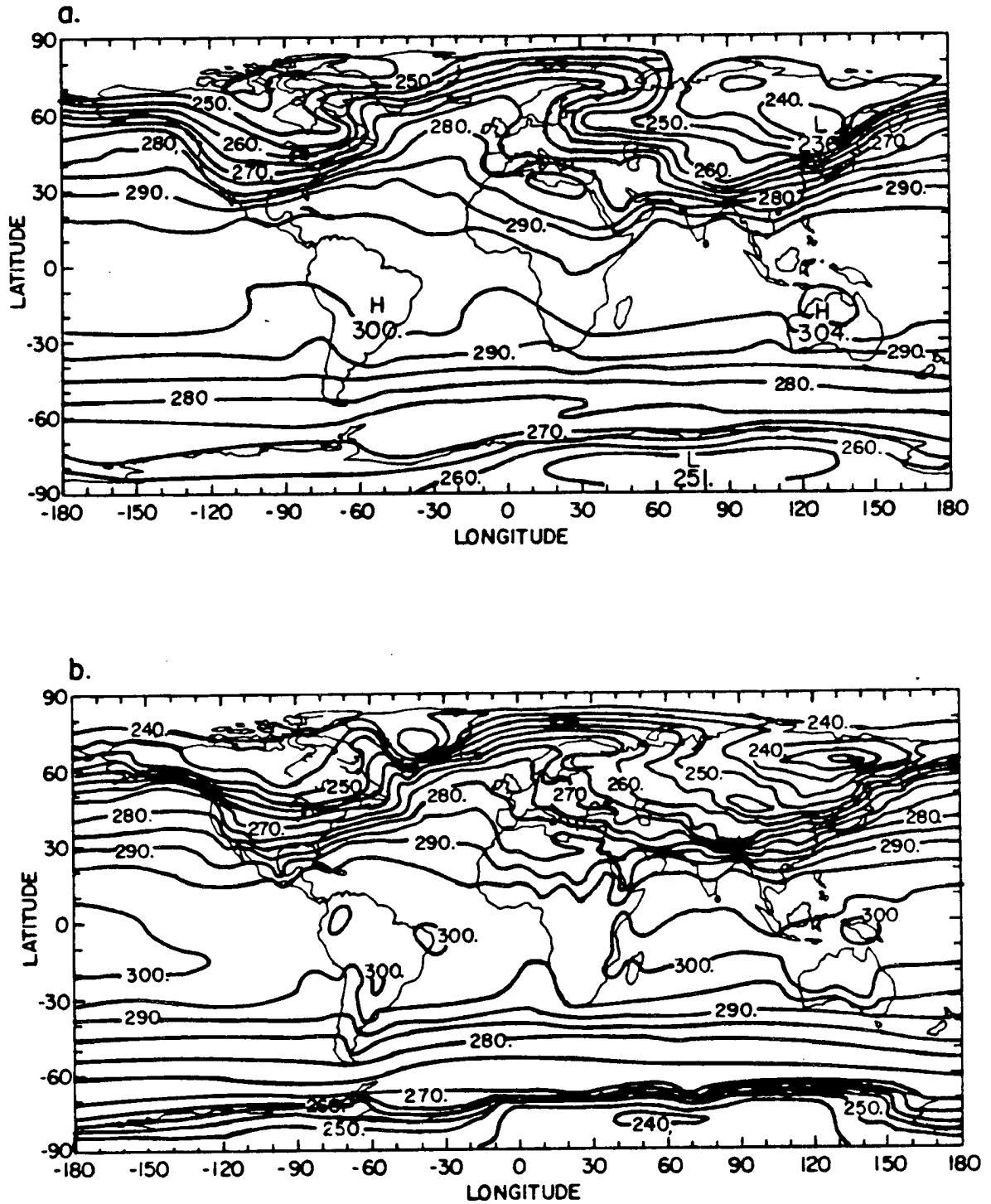


Figure 4.2: Map of the seasonally-averaged surface-air temperature for Northern Hemisphere winter (K): (a) computed distribution from the model, and (b) observed distribution compiled by Schutz and Gates (1971).

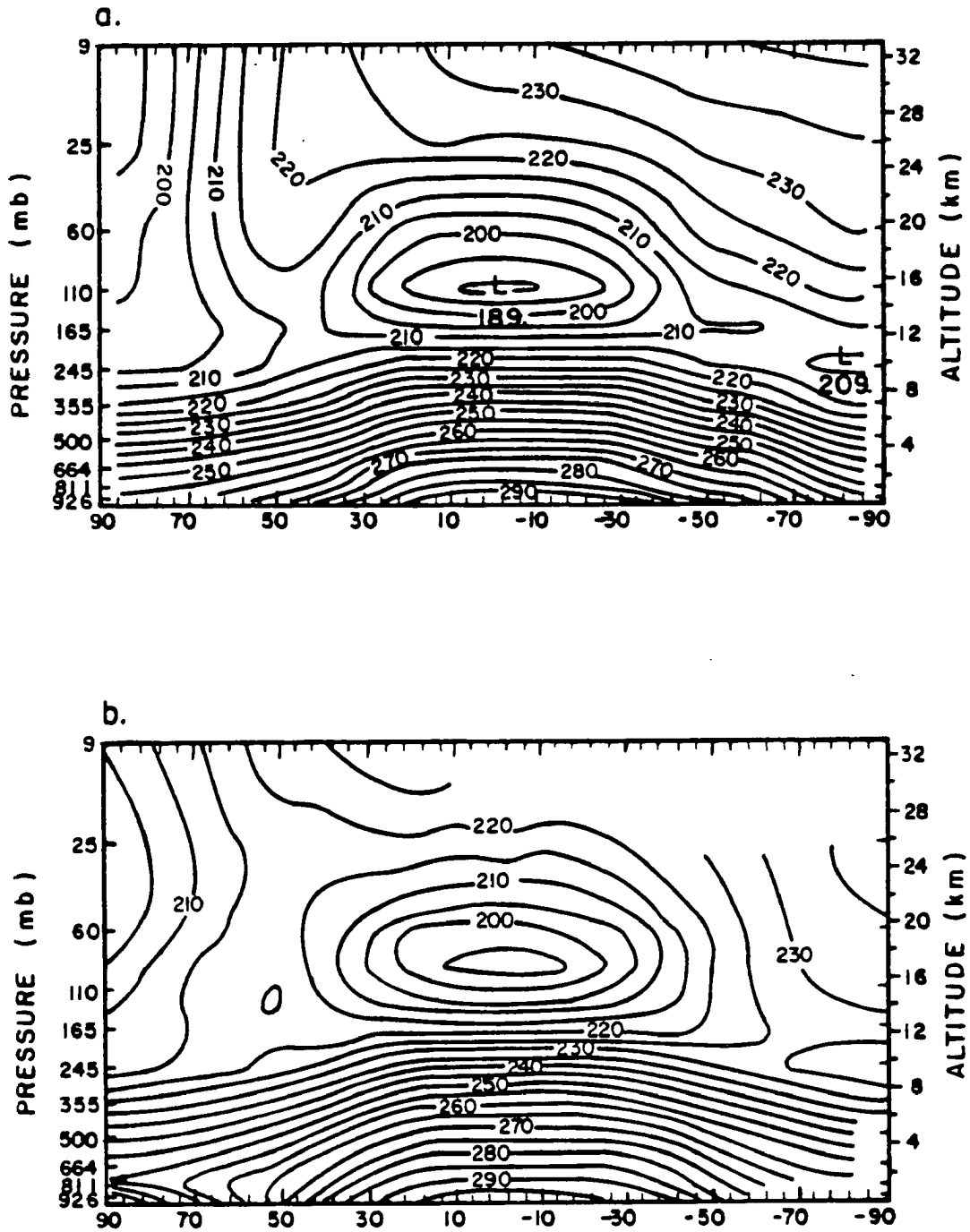


Figure 4.3: Latitude-height distribution of the seasonally-averaged zonal mean temperature for Northern Hemisphere winter (K): (a) computed distribution from the model, and (b) observed distribution compiled by Newell *et al.* (1972).

southern Africa), and over the monsoon region in southeast Asia. The hydrologic cycle is one of the most difficult process to successfully parameterize in GCMs. CCM1 captures most of its characteristic features in both hemispheres, but the magnitude of the precipitation rate is too large by about a factor of two when compared against climatological data. This systematic bias is very well seen in regions of intense convection in the summer hemisphere and has been discussed in Pitcher *et al.* (1983) who stress the need for an improved representation of the moist processes.

Figures 4.5 and 4.6 represent the latitude-height distribution of the zonally-averaged zonal- and meridional-wind components computed from the model, and from winter observations obtained by Newell *et al.* (1972). The model reproduces successfully the characteristic features of the wind components. The middle-latitude tropospheric jets are very well positioned in latitude and height, and have the same intensity as the observed jets. However, the model overestimates the strength of the near-surface easterlies by about 5 m s^{-1} . The meridional-wind component also agrees well with the winter climatological observations. The hemispheric asymmetry in the atmospheric circulation is well apparent, the circulation being the strongest in the winter hemisphere. The upper branch of the Hadley cell circulation also agrees well with observations although its modeled intensity is about 1 m s^{-1} weaker than that observed. Finally, Figure 4.7 shows the latitude-height distribution of the zonal mean vertical velocity, $\omega = \frac{dp}{dt}$. The comparison against observations compiled by Newell *et al.* (1972) shows that the model reproduces accurately the position and strength of the ascending and descending branches of the Hadley cell circulation in winter.

The comparison between various seasonally-averaged synoptic fields simulated with CCM1 and obtained from climatological data for Northern Hemisphere winter conditions shows the model's ability to reproduce the characteristic features of the atmospheric circulation. The main deficiencies in the climate simulation, which had been previously pointed out by Pitcher *et al.* (1983), are that the atmospheric temperatures are too cold and the intensity of the precipitation rate too strong when compared against winter observations.

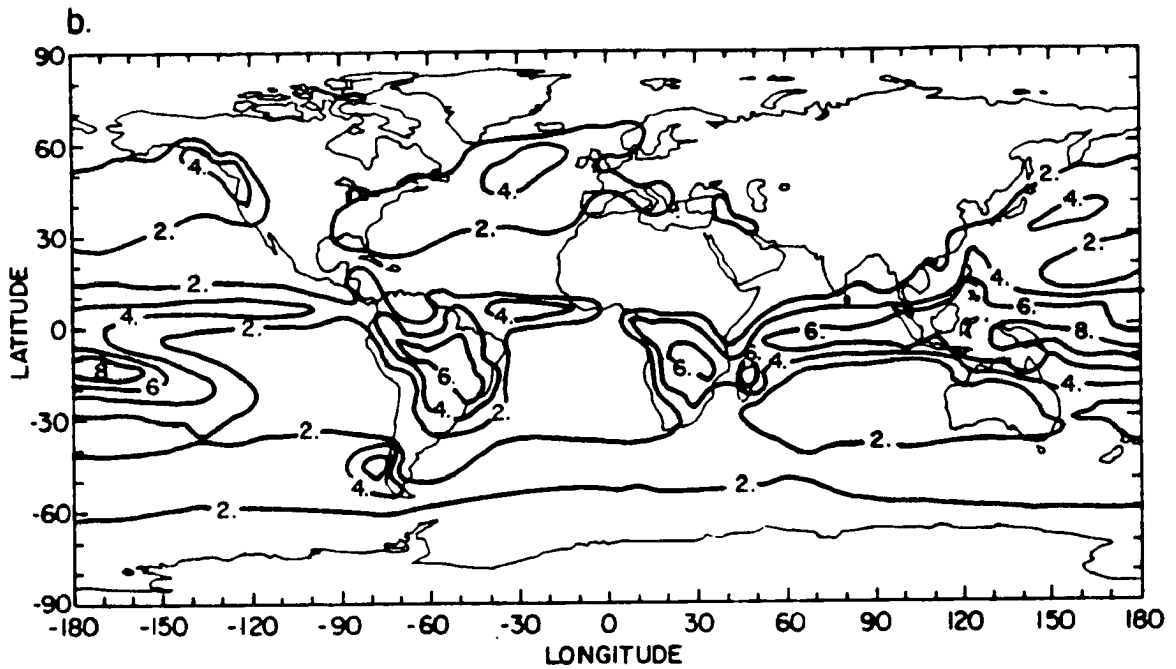
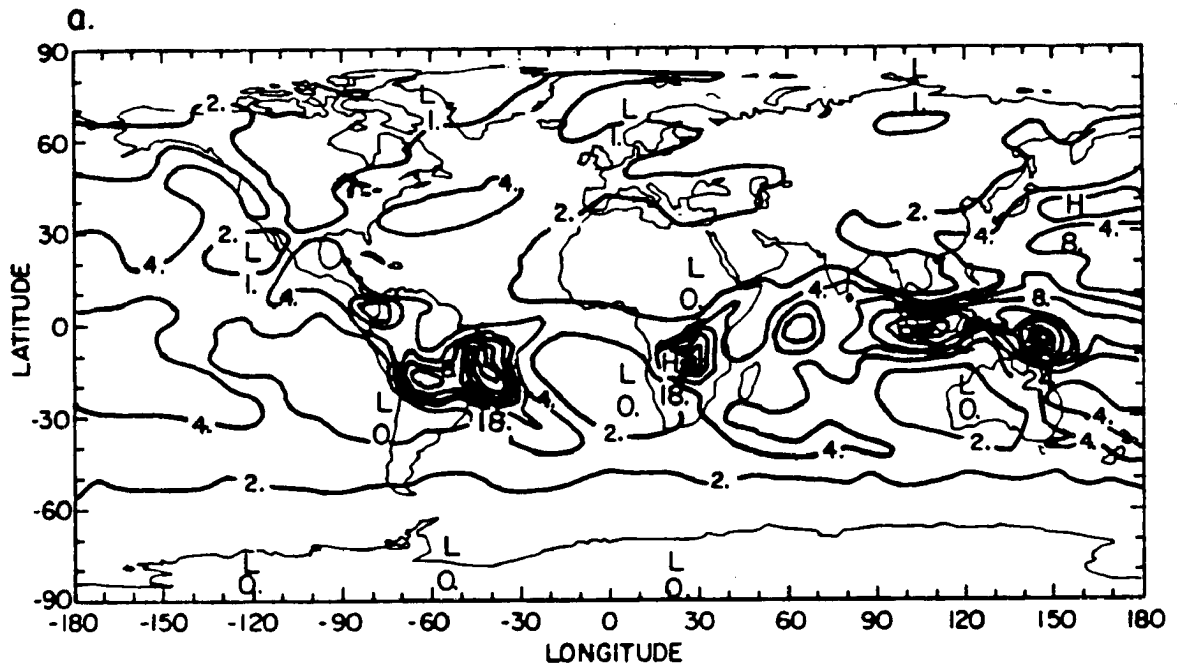


Figure 4.4: Map of the seasonally-averaged precipitation rate for Northern Hemisphere winter (mm day^{-1}): (a) computed distribution from the model, and (b) observed distribution compiled by Schutz and Gates (1972a).

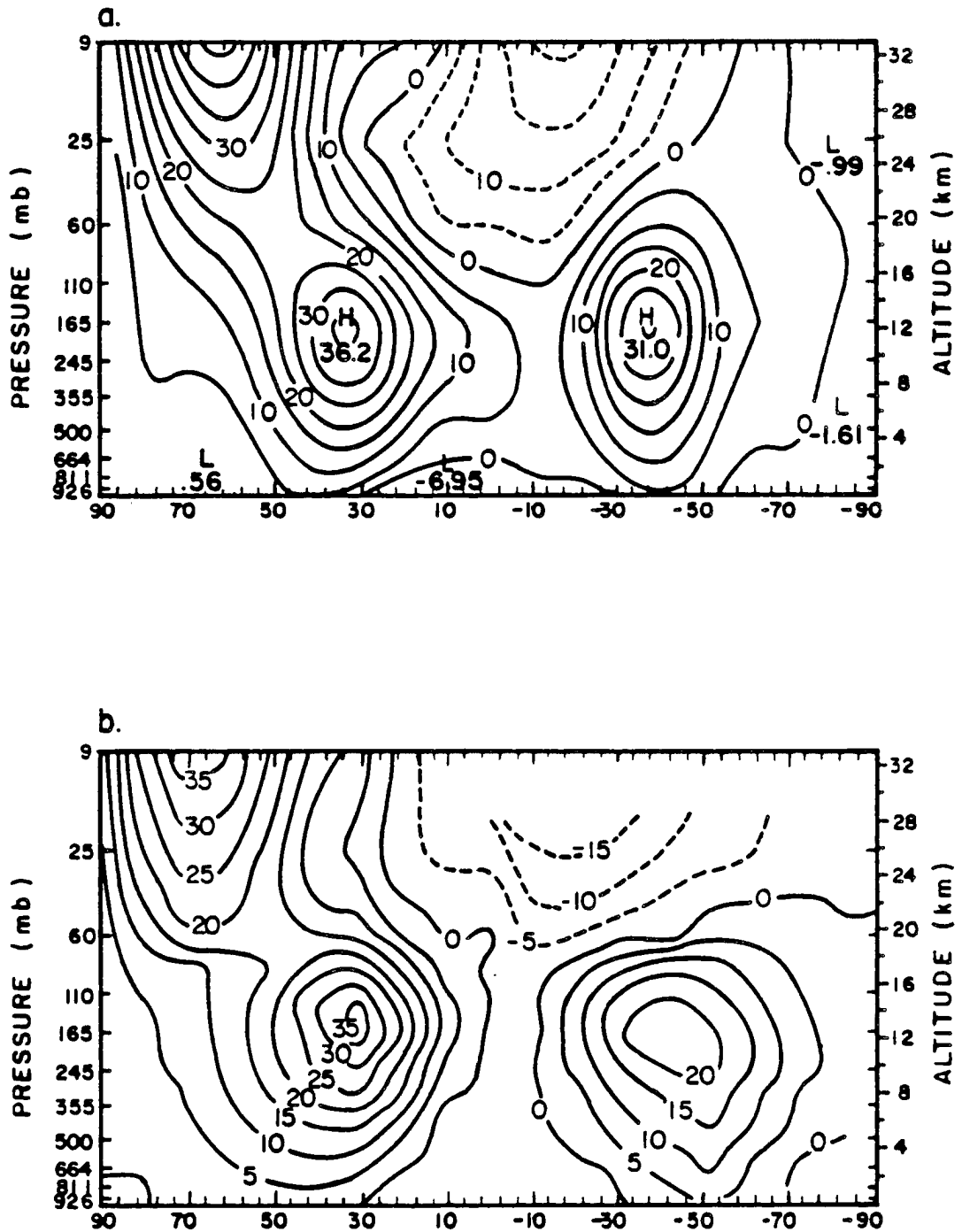


Figure 4.5: Latitude-height distribution of the seasonal average of the zonal mean zonal-wind component for Northern Hemisphere winter (m s^{-1}): (a) computed distribution from the model, and (b) observed distribution compiled by Newell *et al.* (1972).

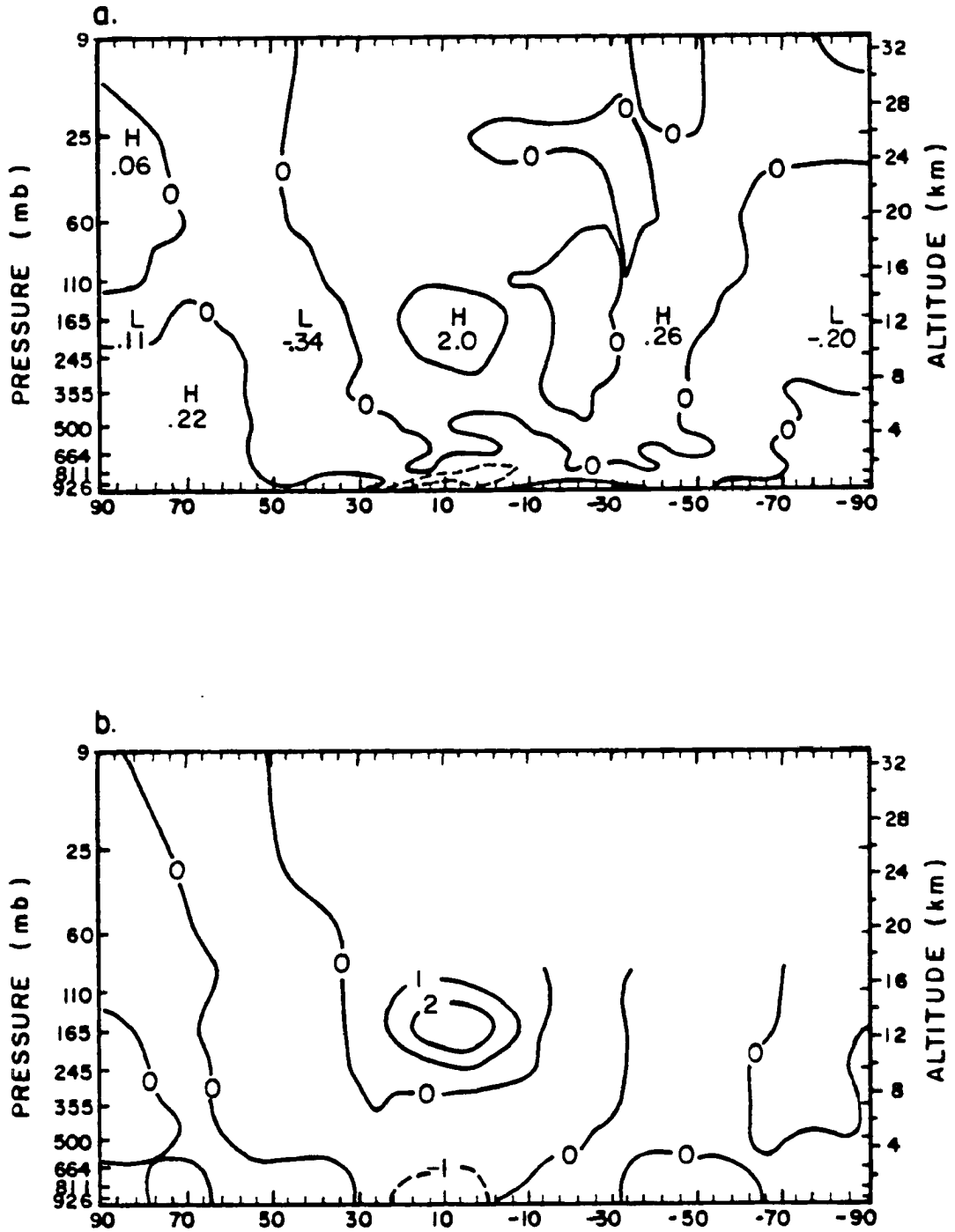


Figure 4.6: Latitude-height distribution of the seasonal average of the zonal mean meridional-wind component for Northern Hemisphere winter (m s^{-1}): (a) computed distribution from the model, and (b) observed distribution compiled by Newell *et al.* (1972).

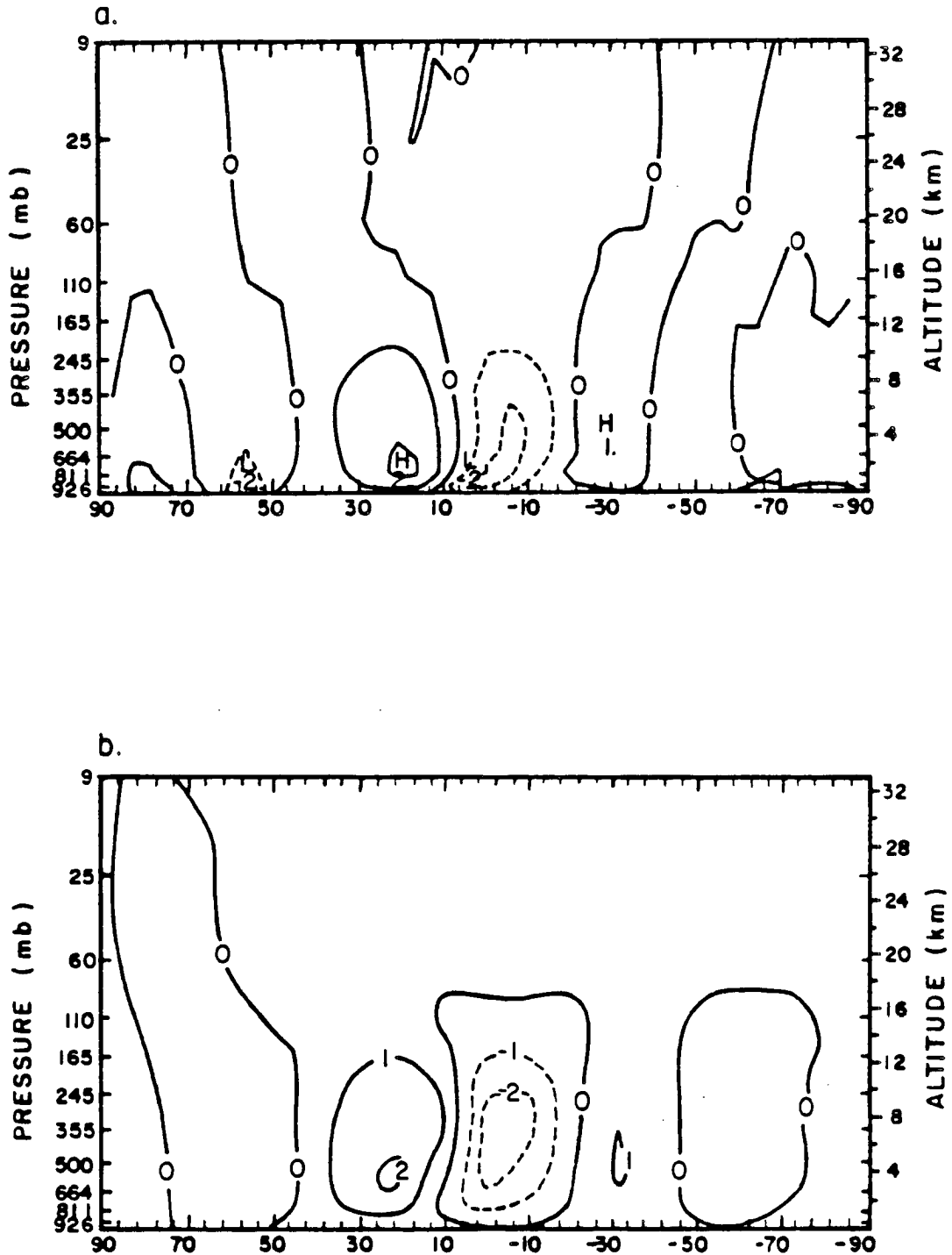


Figure 4.7: Latitude-height distribution of the seasonal average of the zonal mean vertical velocity for Northern Hemisphere winter (10^{-4}mbs^{-1}): (a) computed distribution from the model, and (b) observed distribution compiled by Newell *et al.* (1972).

4.3 Outgoing infrared radiation

4.3.1 Seasonal average

The global distribution of the seasonally-averaged outgoing infrared radiation (IR) computed from the model and measured by the scanner radiometers on board Nimbus-7 is shown in Figures 4.8 and 4.9 for the winter and summer seasons. As a whole, the model-simulated IR reproduces fairly well the positions of high and low emission of outgoing infrared radiation for both seasons. However, its gradient at the boundaries between regions of high and low infrared emission is not as sharp as that observed from satellite NFOV IR data. The areas of high infrared emission above the relatively cloud-free subtropical oceans are overestimated whereas those of low infrared emission above the oceanic convective regions are underestimated when compared against satellite observations. Figure 4.8 shows that the model underestimates the intensity of the monsoon region across the Indian ocean, as well as the extent of the belt of high outgoing infrared radiation between the eastern coast of Africa and India. The position of the ITCZ across the Pacific and Atlantic oceans is not as clearly apparent as from NFOV satellite data, as observed in Figure 4.9. On the other hand, the location and intensity of the regions of deep tropical convection in the summer hemisphere, and the seasonal shift of the monsoon region are very well reproduced with CCM1.

The zonally-averaged distribution of the seasonally-averaged outgoing infrared radiation is plotted in Figure 4.10 for both seasons. The zonal averages computed from the model are systematically larger than those computed from satellite NFOV IR data. The best agreement is found in the middle latitudes, especially in the winter hemisphere. The largest difference between model and observations is observed between 20°N and 20°S, and reaches as much as 25 Wm^{-2} in winter and 33 Wm^{-2} in summer around the equator. Most of this difference can be attributed to the low spatial resolution of the model-grid in contrast to the relatively narrow angle field-of-view of the scanners. The effect of low spatial resolution is to smooth out the horizontal distribution and to degrade the regional characteristics of the outgoing infrared radiation field. The outgoing infrared radiation

becomes less sensitive to the field-of-view at higher latitudes because its intensity decreases and its distribution becomes more zonal towards the poles. The spatial resolution of CCM1, for a rhomboïdal truncation at wavenumber 15, is closer to that obtained from a WFOV instrument, and one comes up with a better agreement when WFOV observations are used. Some of the differences between the simulated and observed outgoing infrared radiation fields in the tropics can be attributed to a lack of water vapor absorption (especially e-type absorption), an underestimate of the total cloud cover above the deep tropical convective activity regions, or by the treatment of the interactions between clouds and longwave radiation.

4.3.2 Standard deviation about the seasonal average

The geographical distribution of the standard deviation of the outgoing infrared radiation ($\sigma(\text{IR})$) and its relationship with the global distribution of the seasonally-averaged field have been discussed from satellite observations in Section 2.4. It is shown that most of the variability of the outgoing infrared radiation can be mostly attributed to day-to-day fluctuations in the cloud cover at equatorial latitudes, with an increasing impact of fluctuations in the temperature and humidity fields in the middle latitudes. At low latitudes, areas of high (respectively low) values of $\sigma(\text{IR})$ coincide exactly with areas of low (respectively high) IR values. This correspondence is also very well seen between IR and $\sigma(\text{IR})$ computed with CCM1, as shown in Figures 4.11 and 4.12. However, as already discussed for the model-simulated seasonal average, the gradient of $\sigma(\text{IR})$ at the boundaries between areas of low and high standard deviation is not as sharp as from observations, especially in the tropics. Again, this difference results from the spatial resolution difference between model and observations.

The geographical distribution of $\sigma(\text{IR})$ matches that obtained from satellite observations but the magnitude of $\sigma(\text{IR})$ is systematically larger by approximately a factor of two. This is very well seen above regions of low seasonal average and high standard deviation. For instance, above the winter monsoon region, $\sigma(\text{IR})$ computed from satellite data is equal to 57 Wm^{-2} compared to a value greater than 85 Wm^{-2} from the model. Above

the summer monsoon region, $\sigma(\text{IR})$ is respectively equal to 50 Wm^{-2} and 85 Wm^{-2} . This discrepancy between model and observations is clearly observed in the zonally-averaged profile of $\sigma(\text{IR})$ shown in Figure 4.13. Both distributions show the same latitudinal distribution with a maximum at low latitudes and decreasing amplitude poleward, but the magnitude of $\sigma(\text{IR})$ computed from the model is systematically greater than that computed from satellite observations by a factor of two.

4.4 Planetary albedo

It is a much more difficult task to simulate the global distribution of the planetary albedo accurately than it is to simulate the global distribution of longwave emission. The troposphere is practically transparent to solar radiation, except in its lowest layers due to absorption by large concentration of water vapor. Therefore, the vertical distribution of the solar upward and downward fluxes is strongly dependent upon the reflectivity of the earth's surface and the cloud albedo. In the model, the ground, vegetation, ocean and sea-ice albedo is computed as a function of the snow cover, the zenith angle, and the wavelength. An external albedo data set provides visible and infrared albedos for strong and weak zenith angle dependence, and the fraction of grid-box with strong zenith angle dependence. Crude parameterization of the shortwave optical properties of clouds and the surface albedo, especially at the snow/ice boundary, can be held responsible for most of the discrepancies between model and observations.

4.4.1 Seasonal average

The global distribution of the seasonally-averaged planetary albedo (α) computed from the model and derived from scanner measurements is shown in Figures 4.14 and 4.15 for the winter and summer seasons. The discrepancies between the simulated and observed fields are important to note. In both seasons, the increase of the albedo at high latitudes is poorly simulated by the model. The simulated albedo jumps to values greater than 48 % around 60° of latitude whereas the observed albedo increases gradually towards the poles. This directly results from the parameterization of the surface albedo at the snow/ice boundary. The model does not predict planetary boundary-layer clouds

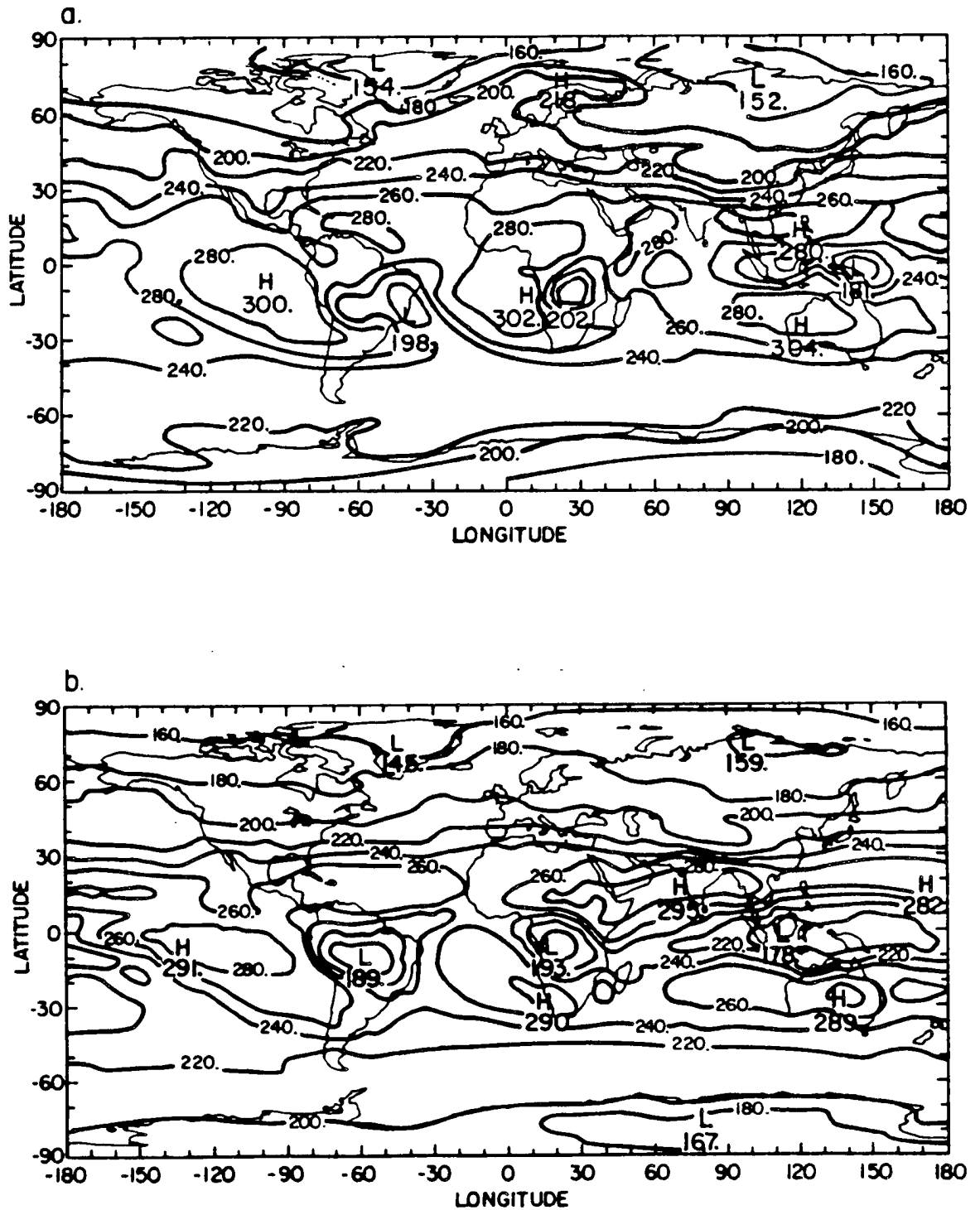


Figure 4.8: Map of the seasonal average of the outgoing infrared radiation for Northern Hemisphere winter (Wm^{-2}): (a) computed distribution from the model, and (b) observed distribution from Nimbus-7.

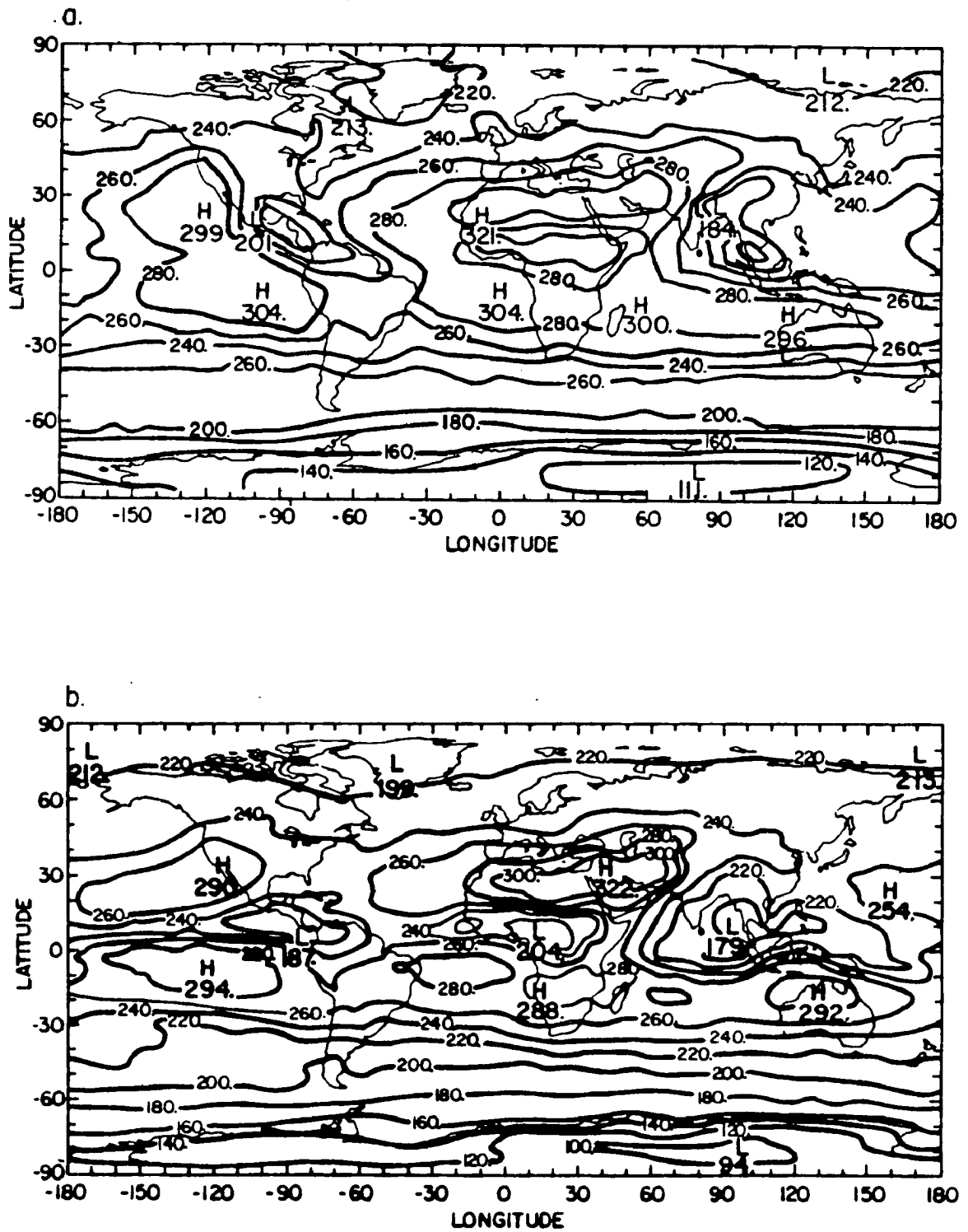


Figure 4.9: Map of the seasonal average of the outgoing infrared radiation for Northern Hemisphere summer (Wm^{-2}): (a) computed distribution from the model, and (b) observed distribution from Nimbus-7.

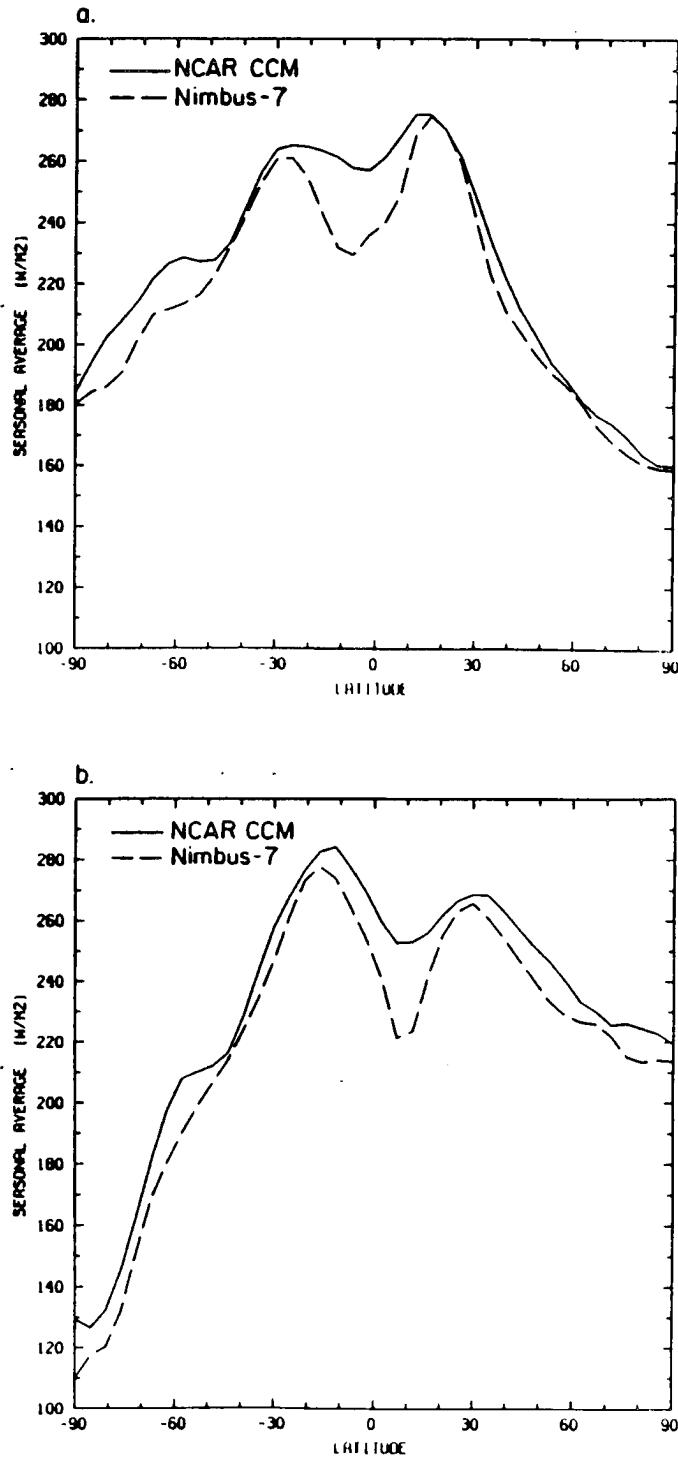


Figure 4.10: Zonally-averaged distribution of the seasonally-averaged outgoing infrared radiation (Wm^{-2}): (a) Northern Hemisphere winter, and (b) summer.

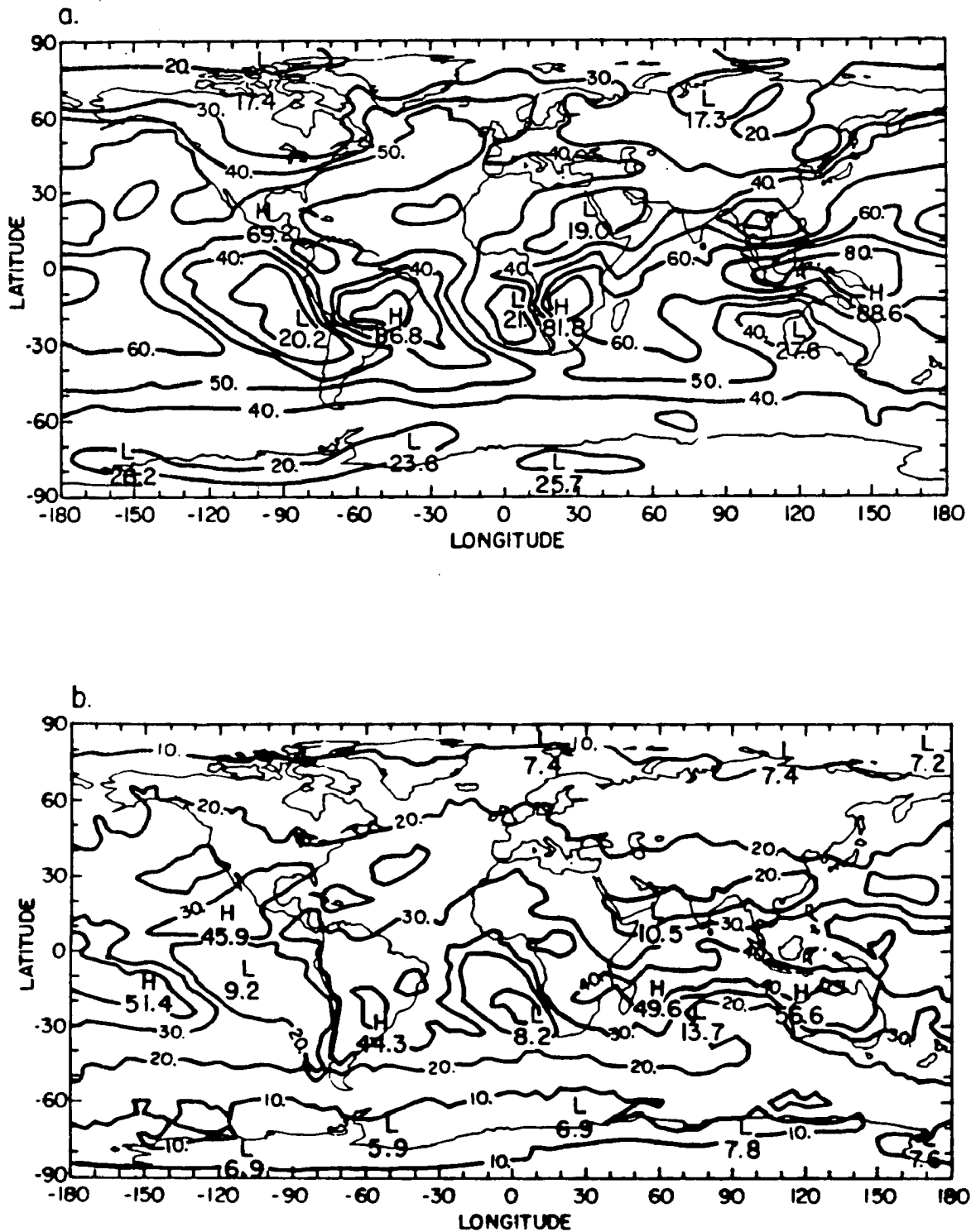


Figure 4.11: Map of the standard deviation of the outgoing infrared radiation for Northern Hemisphere winter (Wm^{-2}): (a) computed distribution from the model, and (b) observed distribution from Nimbus-7.

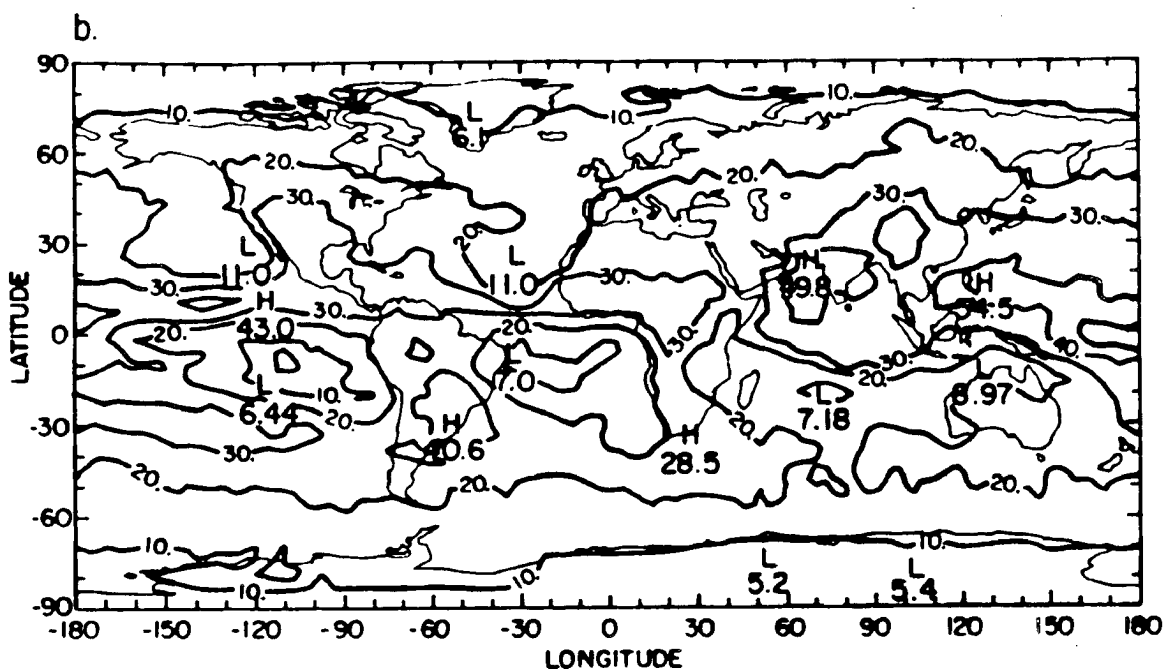
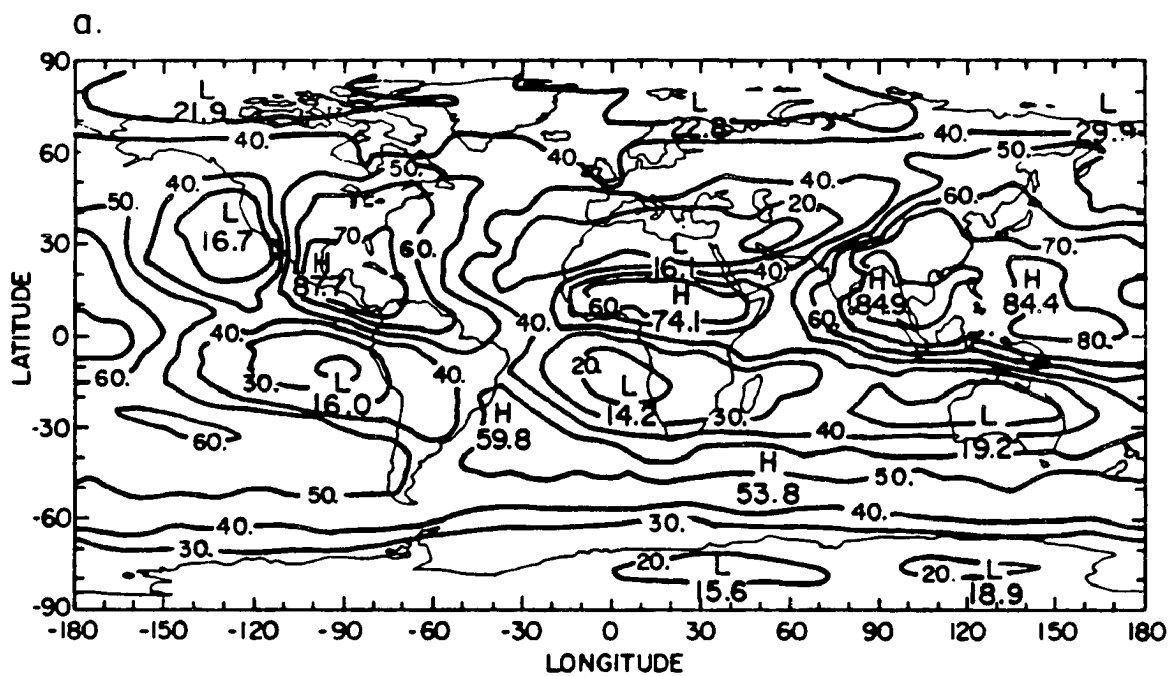


Figure 4.12: Map of the standard deviation of the outgoing infrared radiation for Northern Hemisphere summer (Wm^{-2}): (a) computed distribution from the model, and (b) observed distribution from Nimbus-7.

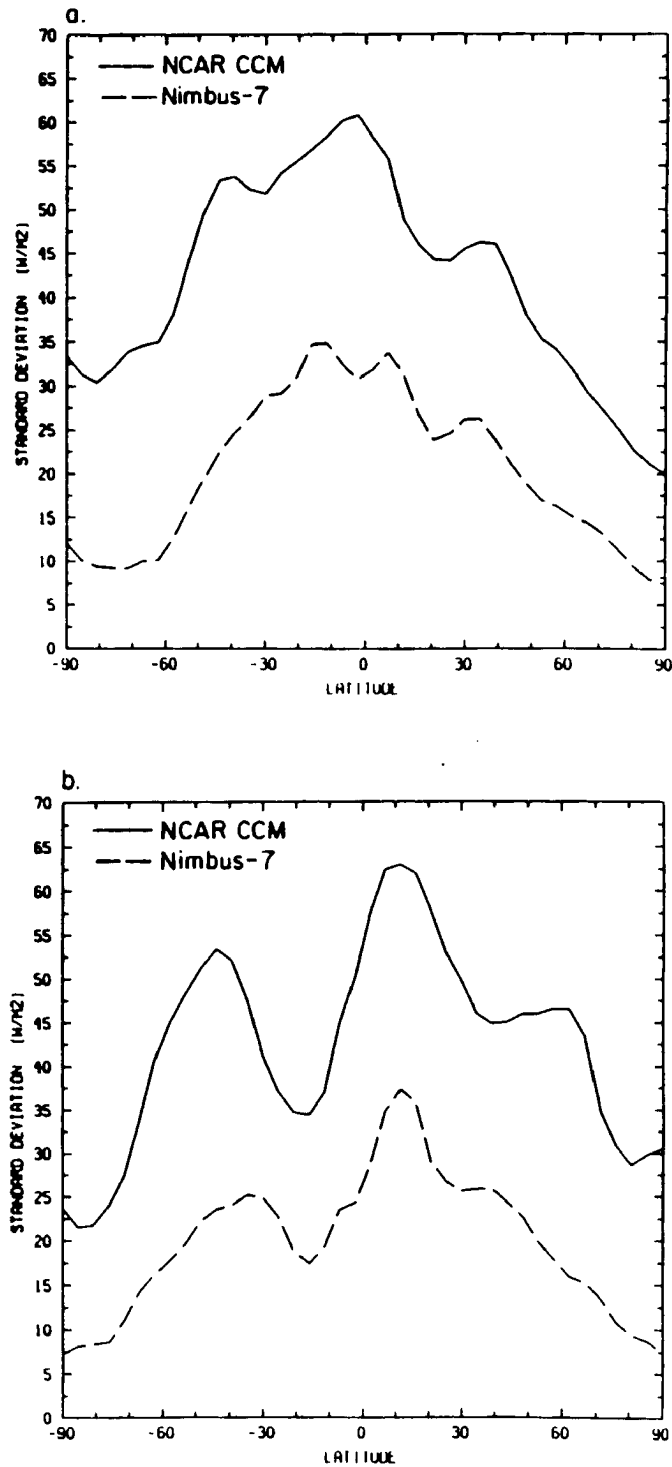


Figure 4.13: Zonally-averaged distribution of the standard deviation of the outgoing infrared radiation (Wm^{-2}): (a) Northern Hemisphere winter, and (b) summer.

along the western coasts of the continents. The first consequence is that areas of low α above the subtropical oceans are mislocated and positioned too close to the coasts. Along these areas, Nimbus-7 measures α values greater than 24 %. The second consequence is that α is generally too high above the actual location of the cloud-free oceanic regions. Finally, the prescribed cloud optical thickness yields α values about 10 % lower than those obtained from satellite above the tropical convective activity regions over land and oceans. The deficient parameterization of the planetary albedo is very well seen in the zonally-averaged profile of α shown in Figure 4.16. The comparison between model and satellite observations shows that α is underestimated at all latitudes in CCM1, especially in the summer hemisphere. In particular, the model completely fails to simulate its maximum in the tropics and its increased magnitude above the middle latitude storm track regions. As a result, the zonal distribution of the planetary albedo is constant with latitude, except in the polar regions.

4.4.2 Standard deviation about the seasonal average

The global distribution of the standard deviation of the planetary albedo ($\sigma(\alpha)$) computed from the model and from satellite observations is shown in Figures 4.14 and 4.14. In the model, there is a good correlation between the distributions of α and $\sigma(\alpha)$. As from observations, areas of high (respectively low) values of $\sigma(\alpha)$ superimpose well with areas of high (respectively low) α values. However, and as for the seasonal average, the geographical distribution of $\sigma(\alpha)$ is poorly simulated when compared against observations. The zonally-averaged profile of $\sigma(\alpha)$ is shown in Figure 4.19 for both seasons and clearly shows the difference in its magnitude between model and observations. As at long wavelengths, there is a factor of two difference in $\sigma(\alpha)$ computed from the model-simulated and satellite-observed planetary albedo.

4.5 Absorbed solar radiation

The deficient parameterization of the shortwave radiative transfer processes above cloudy areas is better analyzed by looking at the absorbed solar radiation than the planetary albedo. Figures 4.20 and 4.21 show the global distribution of the seasonally-averaged

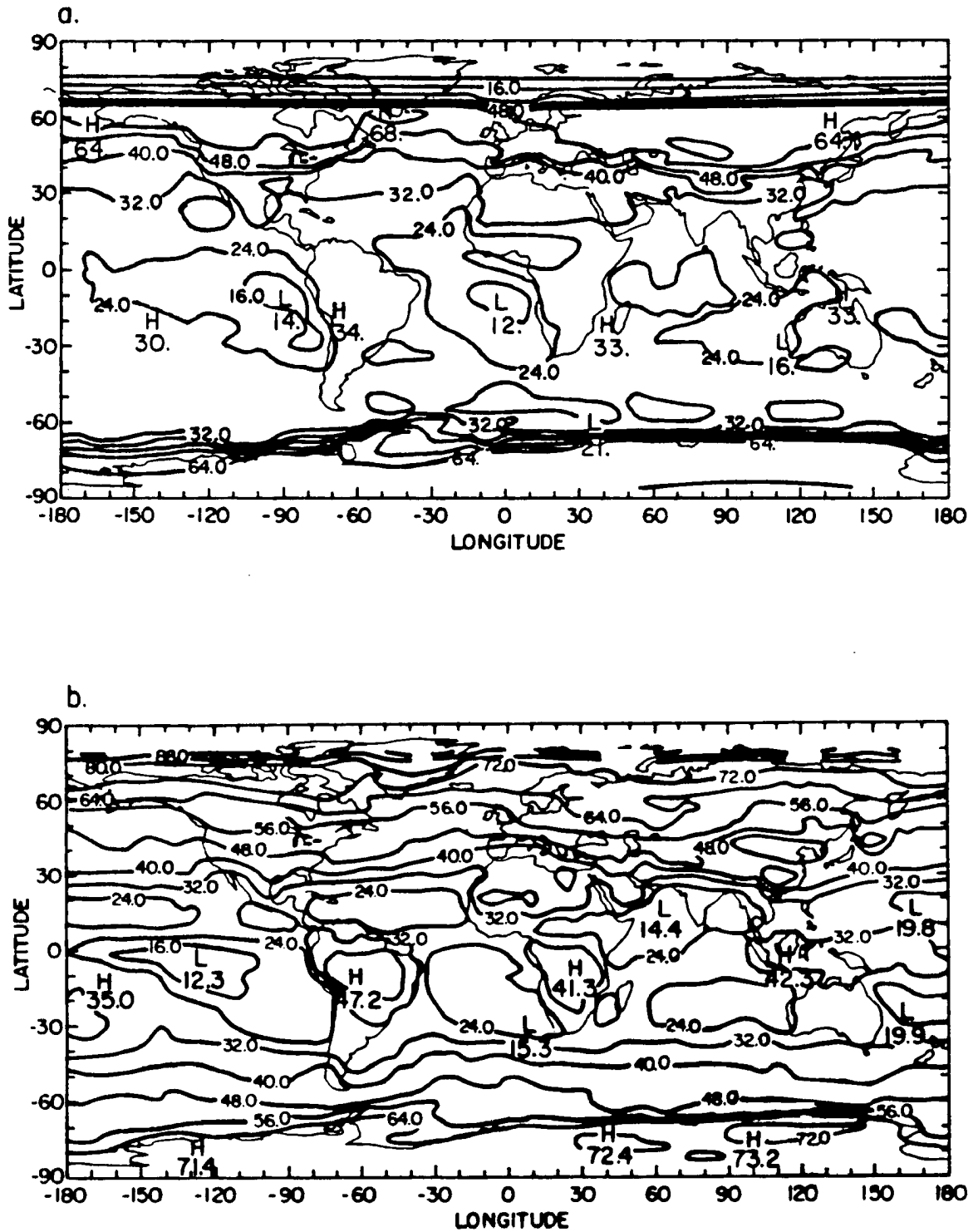


Figure 4.14: Map of the seasonal average of the planetary albedo for Northern Hemisphere winter (%): (a) computed distribution from the model, and (b) observed distribution from Nimbus-7.

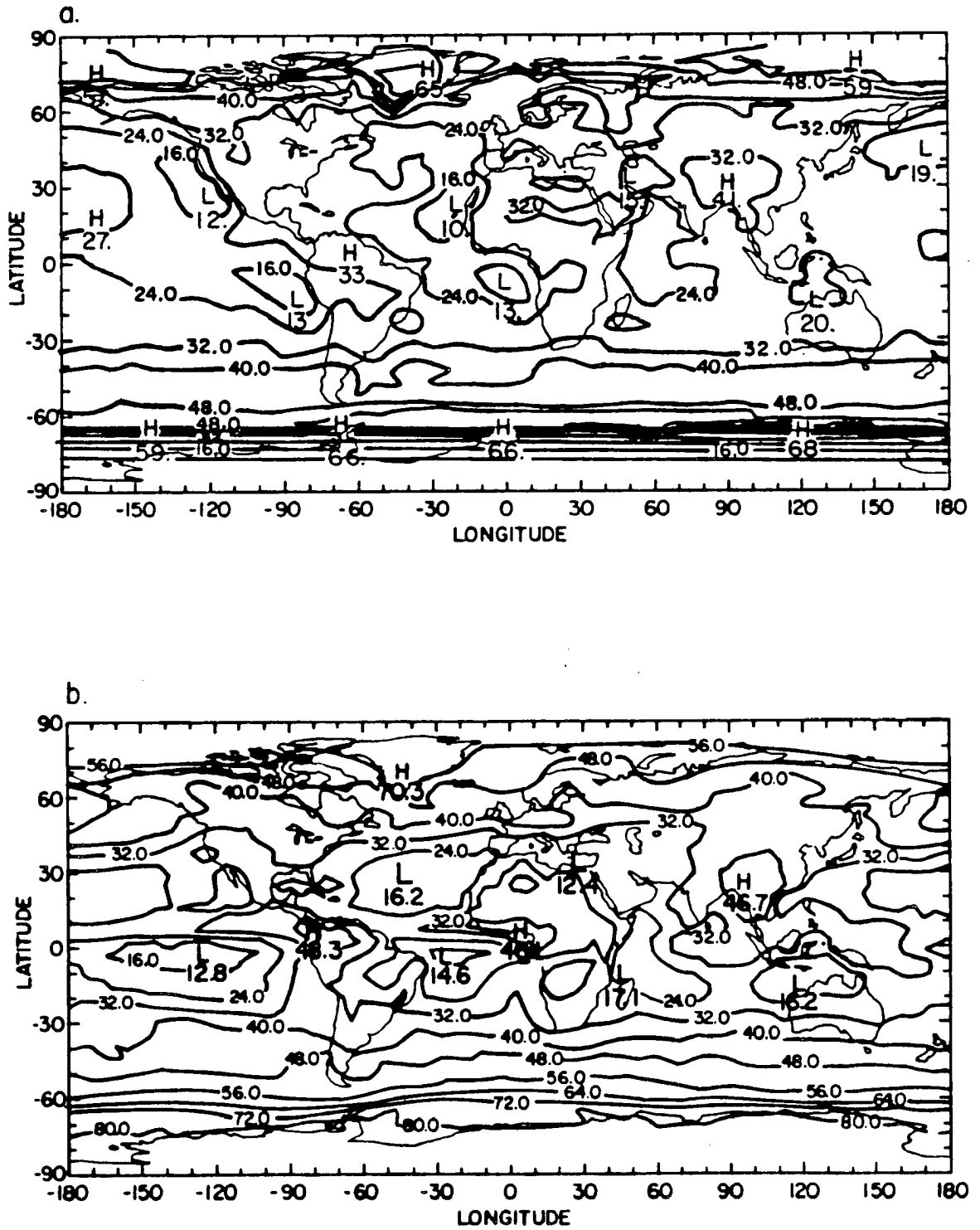


Figure 4.15: Map of the seasonal average of the planetary albedo for Northern Hemisphere summer (%): (a) computed distribution from the model, and (b) observed distribution from Nimbus-7.

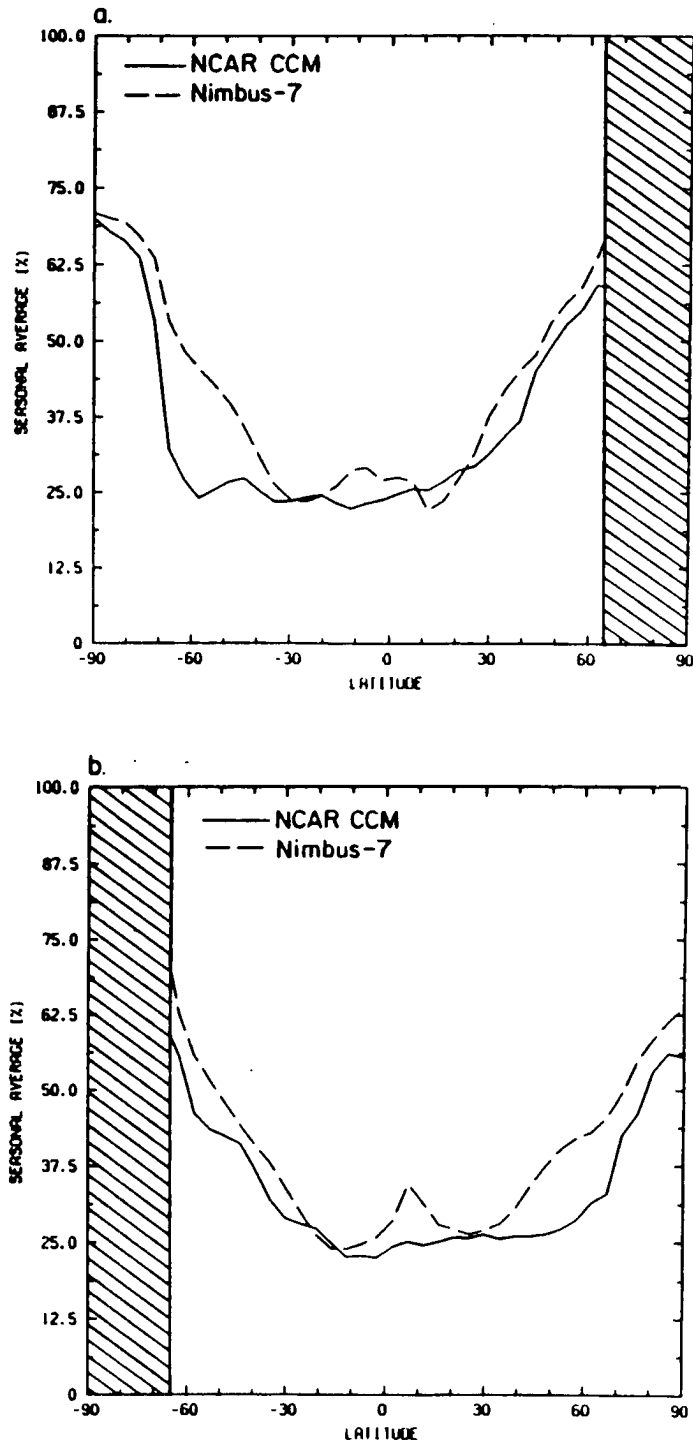


Figure 4.16: Zonally-averaged distribution of the seasonal average of the planetary albedo (%): (a) Northern Hemisphere winter, and (b) summer.

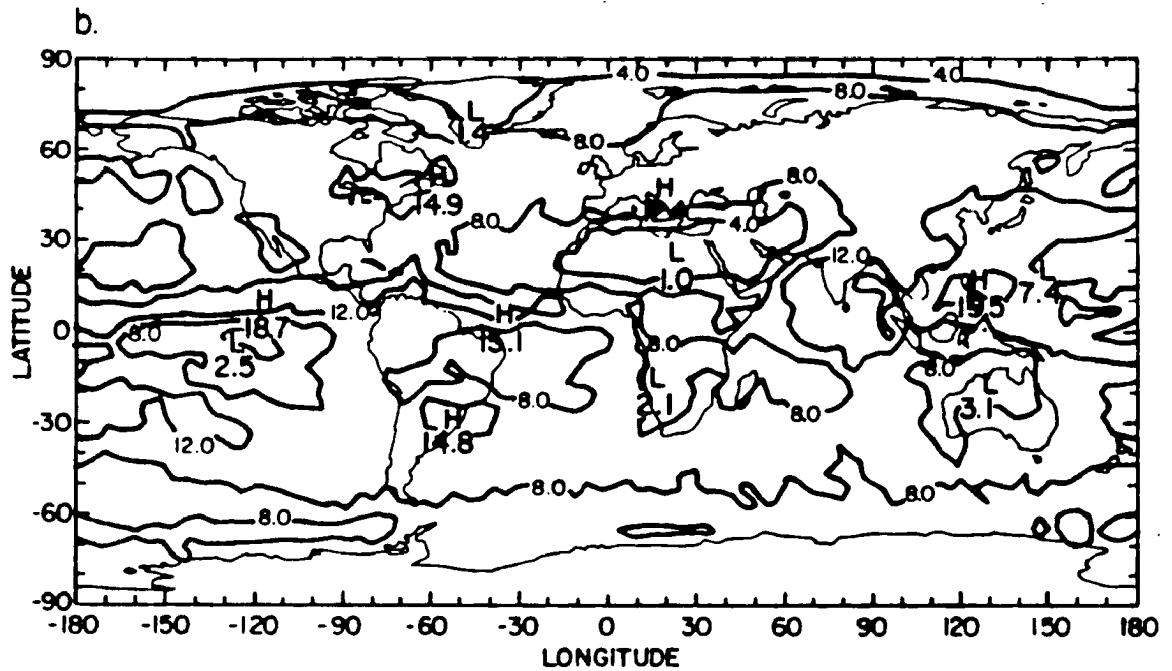
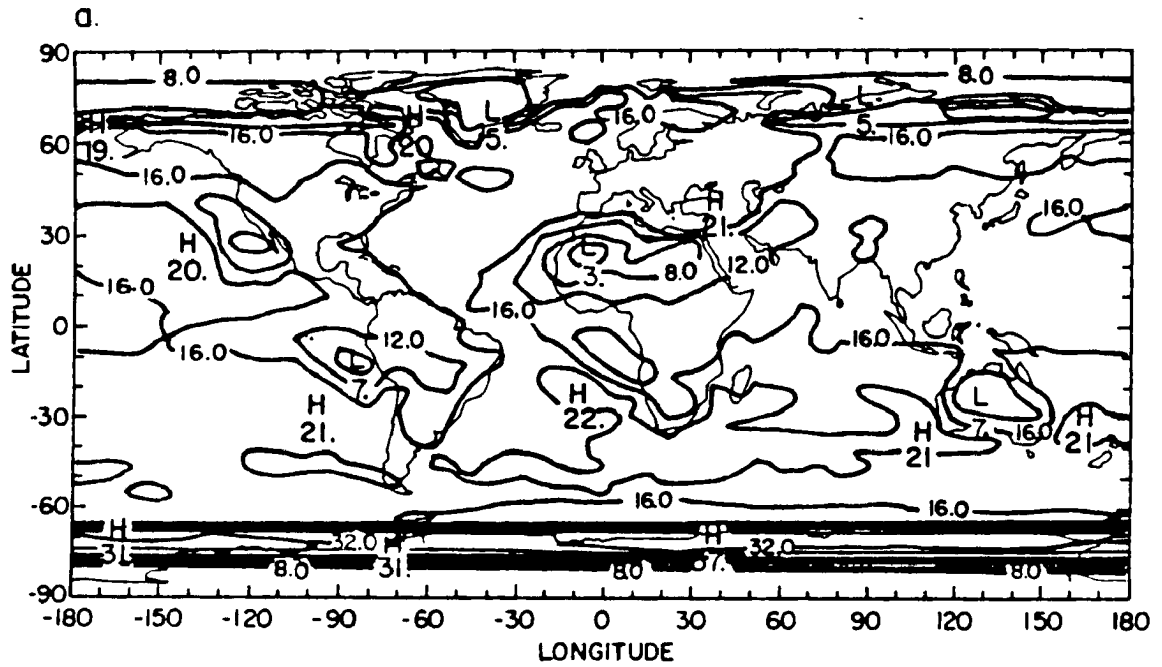


Figure 4.18: Map of the standard deviation of the planetary albedo for Northern Hemisphere summer (%): (a) computed distribution from the model, and (b) observed distribution from Nimbus-7.

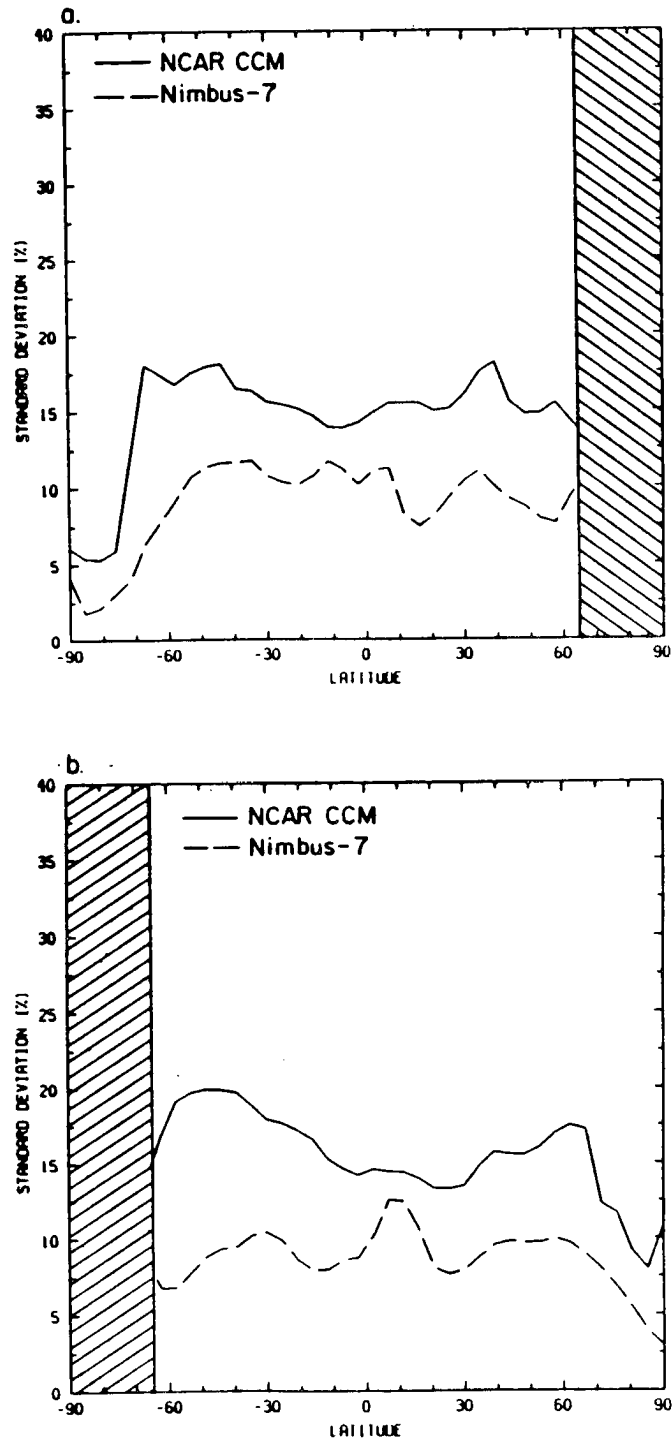


Figure 4.19: Zonally-averaged distribution of the standard deviation of the planetary albedo (%): (a) Northern Hemisphere winter, and (b) summer.

absorbed solar radiation obtained from the model and satellite observations for both seasons. The agreement is very good in the winter hemisphere because of the shadowing impact of the poleward decrease of the incident solar radiation at the top of the atmosphere. In the summer hemisphere and for both seasons, the distribution of absorbed solar radiation in the model is spatially uniform, except above the cloud-free regions which are mislocated along the western coasts of the continents. Whereas observed from satellite, there is a weak gradient of absorbed solar radiation between land and oceans, or between cloudy and cloud-free regions. The underestimation of the cloud albedo is very well seen in the zonally-averaged distribution of the absorbed solar radiation shown in Figure 4.22. On a zonal average, the difference between model and observations is as large as 80 Wm^{-2} in the middle latitudes. Analyses of the global distribution of the model-generated short-wave radiation field emphasize the need of an improved parameterization of the optical properties of clouds. In addition to these significant differences in the seasonally-averaged distribution, the variability of the absorbed solar radiation, as for the outgoing infrared radiation, is also overestimated by about a factor of two. The global and zonally-averaged distributions of the standard deviation of the absorbed solar radiation are shown in Figures 4.23 to 4.25 and complete those of the planetary albedo discussed in the previous section.

4.6 Temporal correlation of the outgoing infrared radiation

4.6.1 Background

The comparison of the standard deviation of the outgoing infrared radiation, the absorbed solar radiation, and the planetary albedo between climate simulations with CCM1 and Nimbus-7 observations shows that the temporal variability of the model-generated radiation fields is about two times larger than that computed from satellite data. This indicates that the model atmosphere evolves faster than the actual atmosphere. The computation of the autocorrelation functions provides additional information on the speed at which the simulated atmosphere loses its memory and some insights into the origins of the discrepancy between model and observations. Clouds have a strong signature on

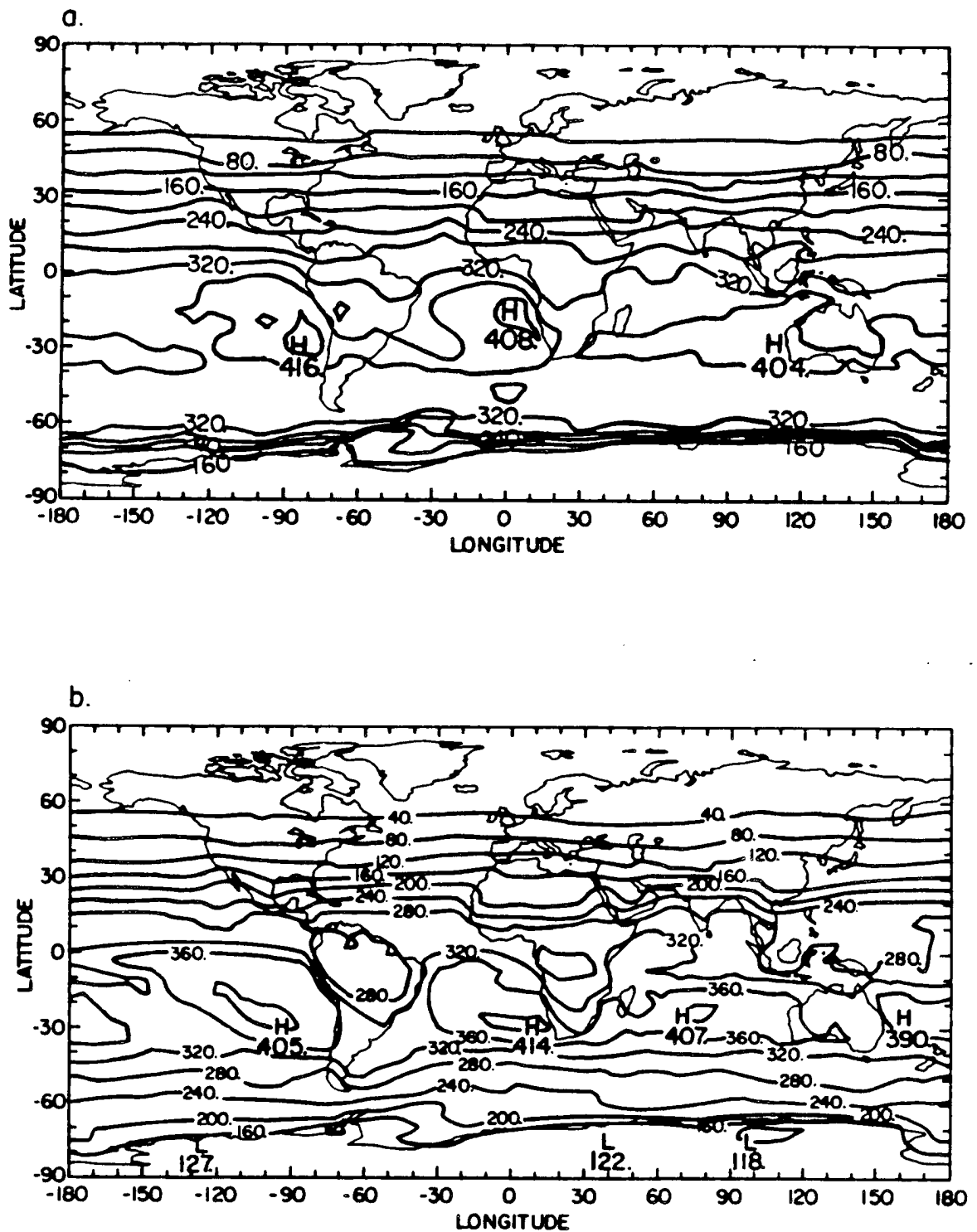


Figure 4.20: Map of the seasonal average of the absorbed solar radiation for Northern Hemisphere winter (Wm^{-2}): (a) computed distribution from the model, and (b) observed distribution from Nimbus-7.

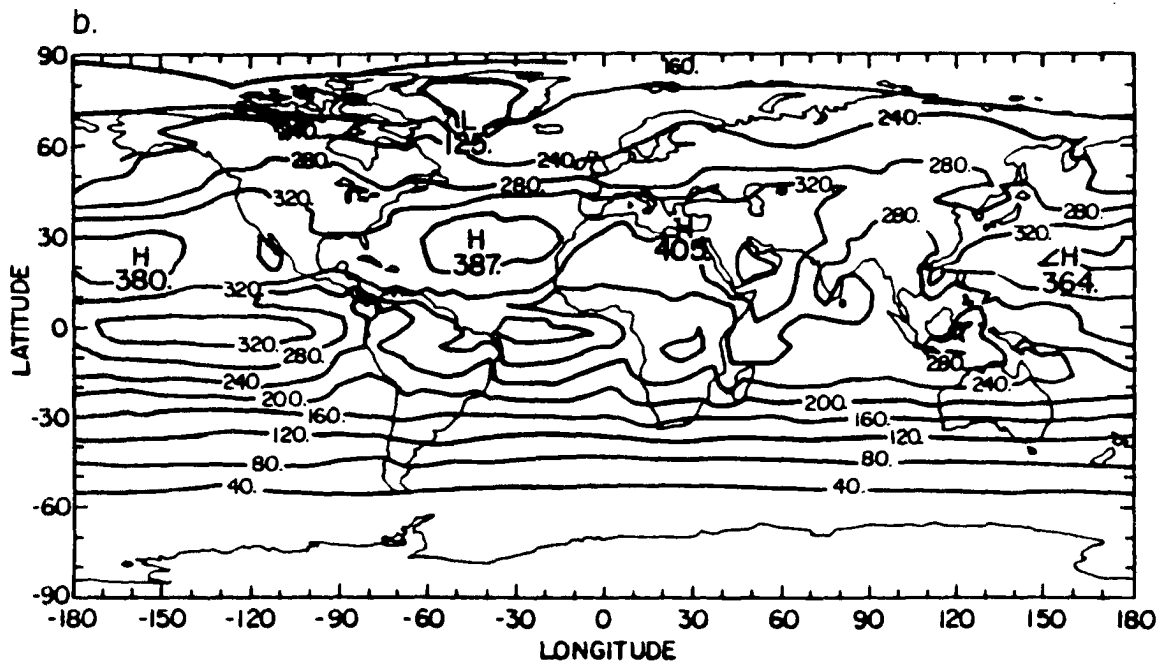
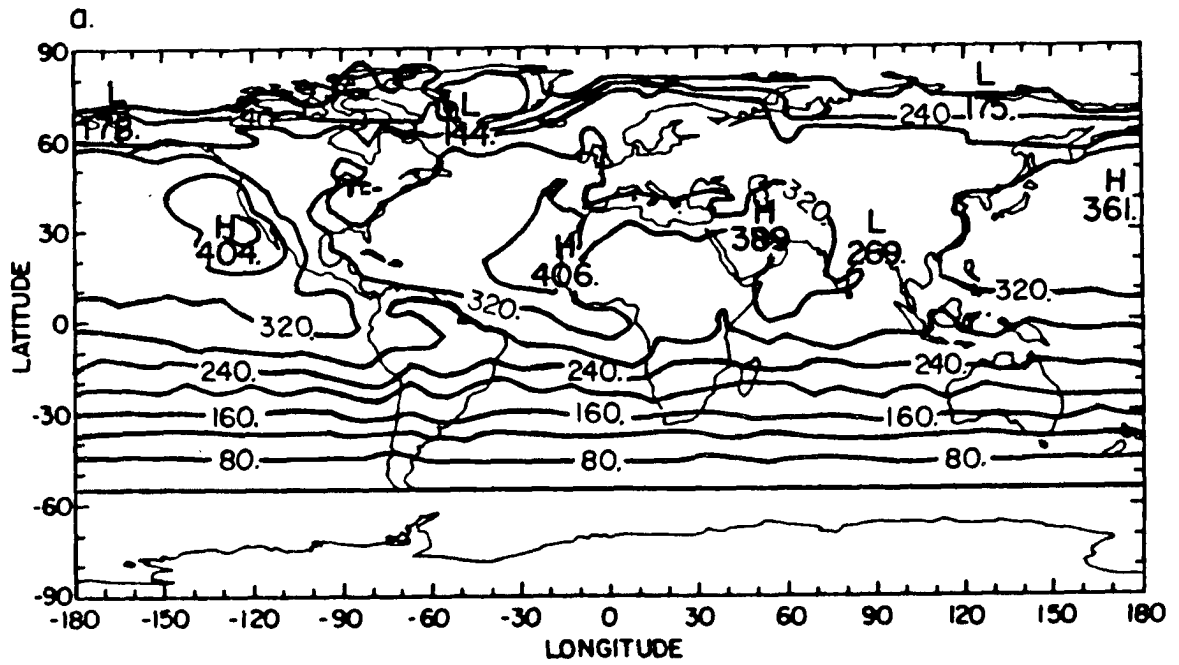


Figure 4.21: Map of the seasonal average of the absorbed solar radiation for Northern Hemisphere summer (Wm^{-2}): (a) computed distribution from the model, and (b) observed distribution from Nimbus-7

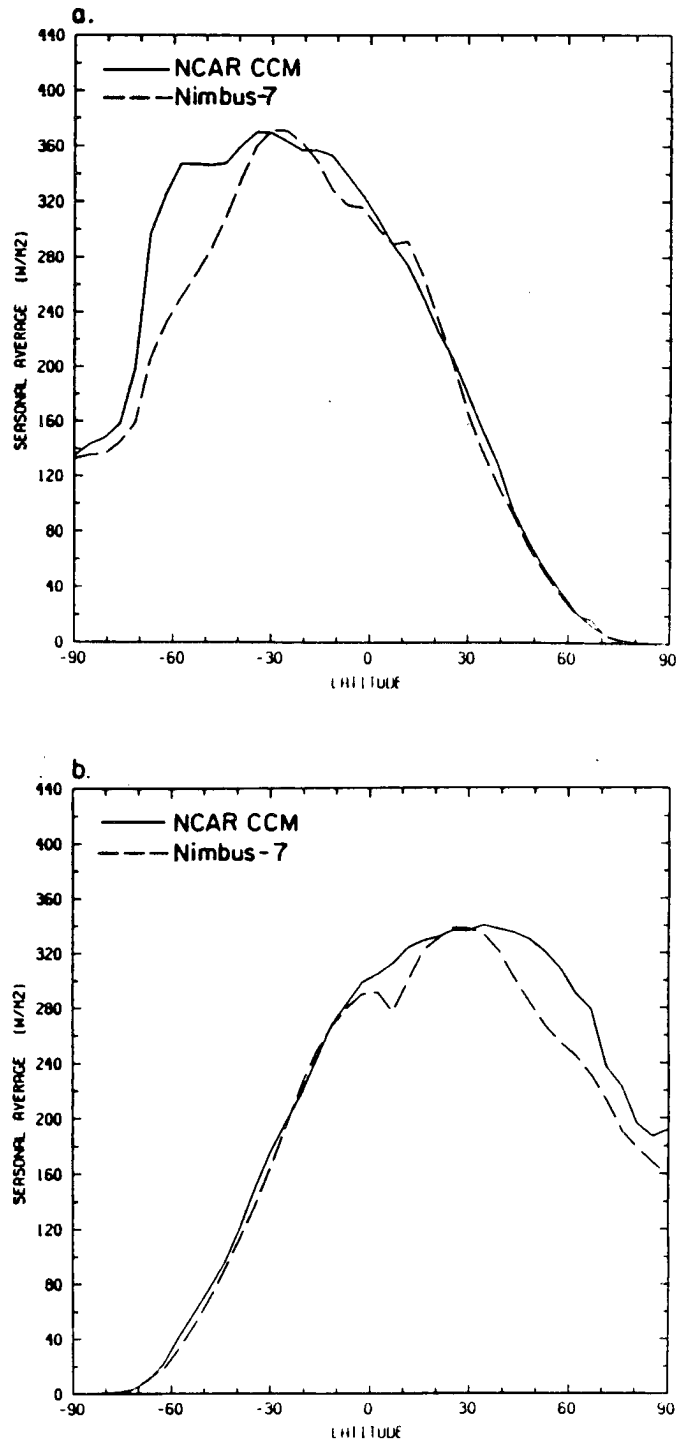


Figure 4.22: Zonally-averaged distribution of the seasonal average of the absorbed solar radiation (Wm^{-2}): (a) Northern Hemisphere winter, and (b) summer.

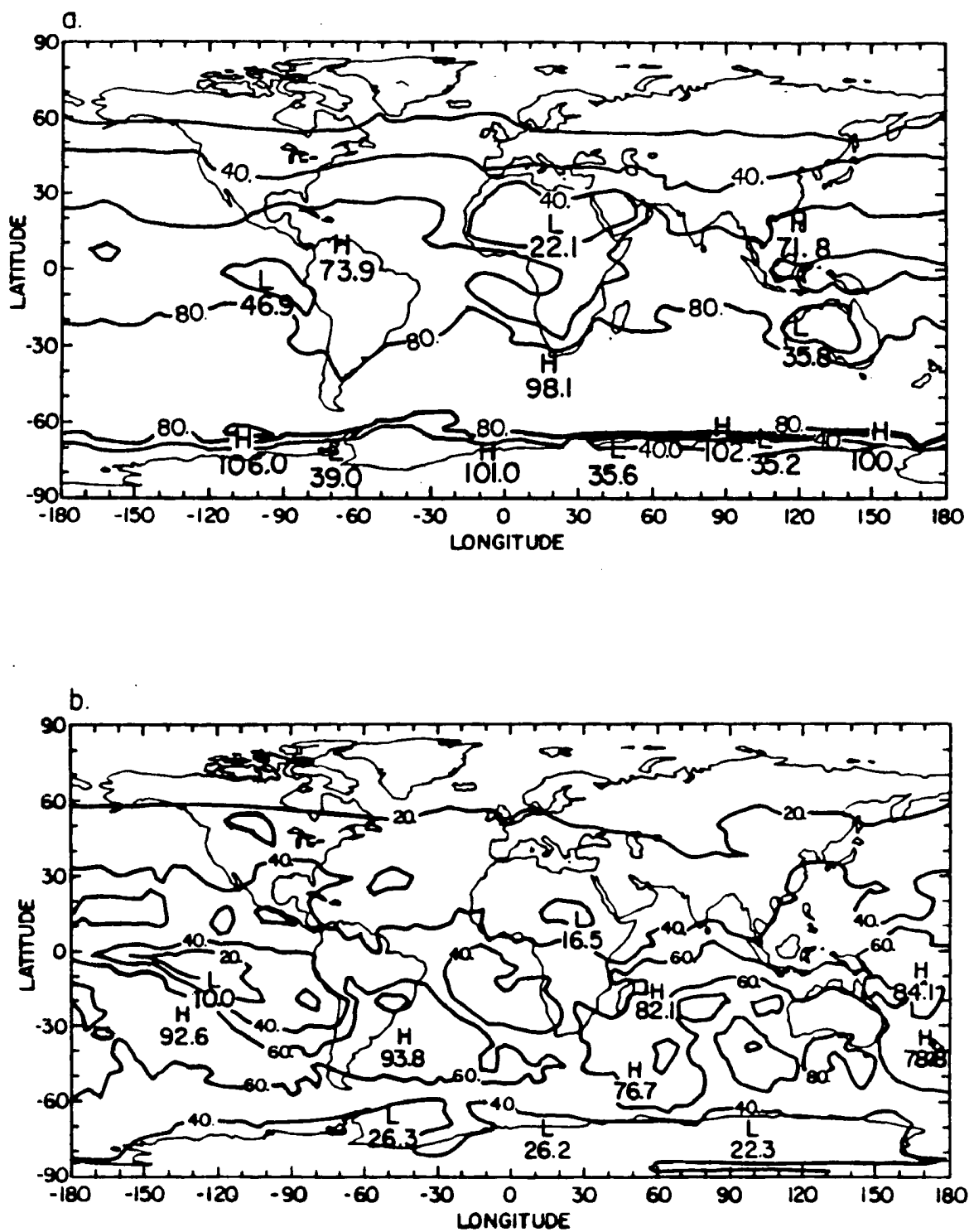


Figure 4.23: Map of the standard deviation of the absorbed solar radiation for Northern Hemisphere winter (Wm^{-2}): (a) computed distribution from the model, and (b) observed distribution from Nimbus-7.

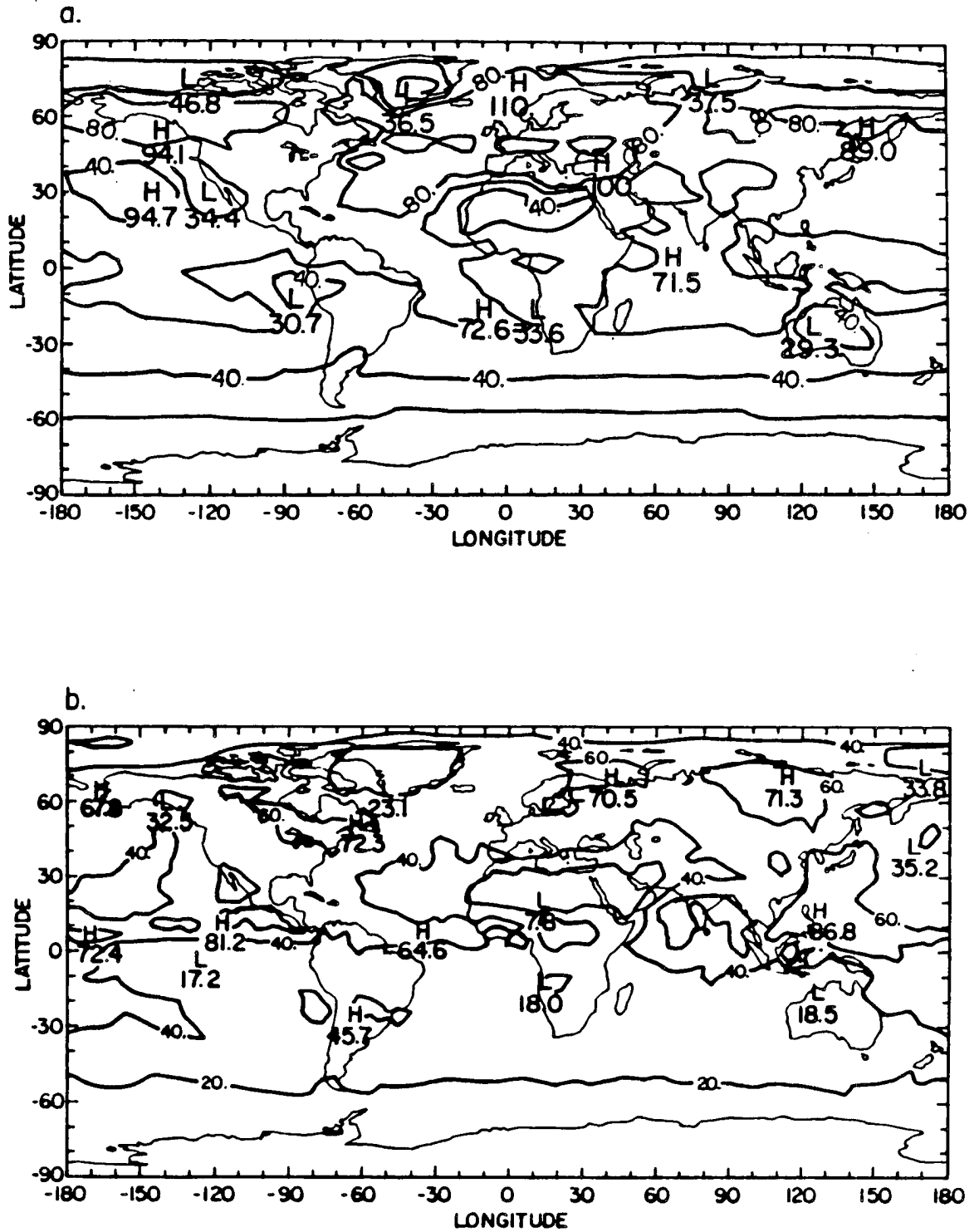


Figure 4.24: Map of the standard deviation of the absorbed solar radiation for Northern Hemisphere summer (Wm^{-2}): (a) computed distribution from the model, and (b) observed distribution from Nimbus-7

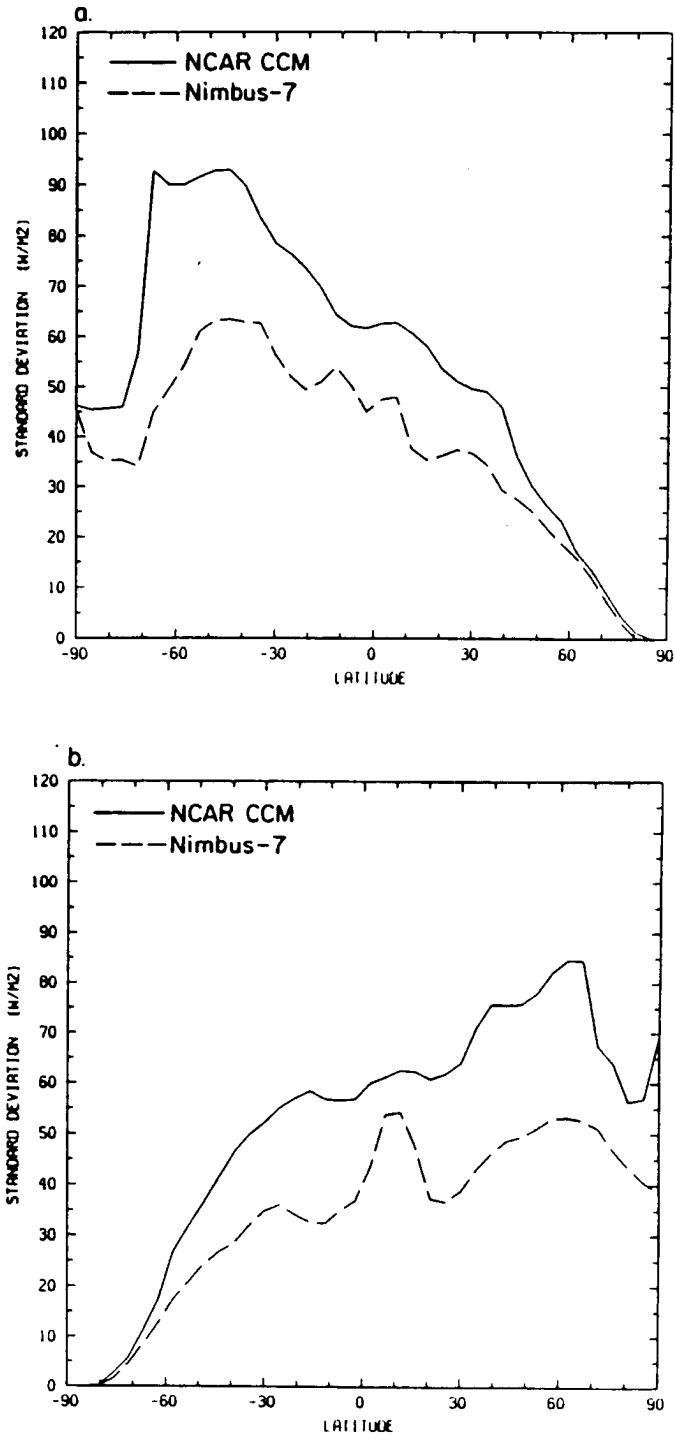


Figure 4.25: Zonally-averaged distribution of the standard deviation of the absorbed solar radiation (Wm^{-2}): (a) Northern Hemisphere winter, and (b) summer.

the global distribution of the outgoing infrared radiation and day-to-day fluctuations in the total cloud cover explains most of the variance in the radiation field. Cahalan *et al.* (1982) compute the time-lagged autocorrelation coefficients of the outgoing infrared radiation from observations taken by the scanner radiometers on board the NOAA operational spacecrafts. They particularly show that fluctuations in the radiation field arise from the passage of cloud systems through a grid-box as well as the creation and destruction of clouds inside the box. Therefore, there is a direct relationship between the temporal correlation of the outgoing infrared radiation and the change in cloudiness through advection, evaporation, and precipitation processes.

The autocorrelation coefficient of the outgoing infrared radiation at lag L is expressed by the relation:

$$r(L) = \frac{\sum_{i=1}^{N-L} (IR_i - \overline{IR})(IR_{i+L} - \overline{IR})}{\sum_{i=1}^N (IR_i - \overline{IR})^2}, \quad (4.1)$$

in which N is the length of the time series, IR_i the daily outgoing infrared radiation, and:

$$\overline{IR} = \frac{1}{N-L} \sum_{i=1}^{N-L} IR_i. \quad (4.2)$$

In this section, we compute the time-lagged autocorrelation coefficients of the model-generated and satellite-observed outgoing infrared radiation, and explain the difference in the correlation functions in term of the evolution of the cloud field.

4.6.2 Satellite-derived correlation

The NFOV data taken by the Nimbus-7 scanner radiometers were recorded on a 3-day on, 1-day off cycle. Therefore, it is not possible to calculate the time-lagged autocorrelation coefficients of the outgoing infrared radiation from this data set, since such a computation requires the use of continuous time series. Instead twice daily continuous observations taken by the NOAA scanners over the winter period December 1979-January-February 1980 are used for this purpose. The characteristics of the NOAA mission and the compatibility between the NOAA and Nimbus-7 data sets were discussed in Chapter Two. It was particularly emphasized upon the minor impact of the diurnal sampling on the calculation of the successive moment statistics.

Figures 4.26, 4.27, and 4.28 show the global distribution of $r(L)$ for every 12-hour lag up to $L = 3$ days. At a 1-day lag, $r(L)$ is greater than 30 % over most of the globe, except in the middle latitudes where it is mostly negative. The time correlation decreases rapidly with increasing time lags but the speed at which it occurs varies considerably from one latitude band to the next. At a 3-day lag, areas of $r(L)$ greater than 30 % are limited to the subtropical desert regions and to regions influenced by cold continental air masses in the winter hemisphere. $r(L)$ is mostly negative outside those specific areas. One of the most interesting features in the global distribution of $r(L)$ is the difference between convective activity regions in the tropics and the middle latitude storm track regions, the latter showing a faster decorrelation for increasing time lags. This results from the increased persistence of the convection within individual grid-boxes at low latitudes, by opposition with the passage of fast moving frontal systems through boxes in the middle latitudes. The second interesting feature in the global distribution of the correlation is the sign difference in $r(L)$ every 12-hour lag because of the diurnal cycle of the outgoing infrared radiation. This is especially well seen above the desert areas because of the day-night difference in the surface radiative heating. Finally, Figure 4.29 shows the zonally-averaged profile of $r(L)$ for L up to 5 days. For simplicity, the zonal averages are plotted separately for in phase and out of phase correlation. As already seen on the global maps, $r(L)$ decreases rapidly with increasing L and the fastest decrease occurs between 30°N and 30°S . The maximum of $r(L)$ in the subtropics and its minimum in the tropics are more pronounced for the in phase zonal distribution. Finally, the decorrelation of the outgoing infrared radiation reaches an asymptotic state for lags greater than 5 days.

In this section, as for the computation of the seasonal average and standard deviation from Nimbus-7 infrared data, only one winter of NOAA observations is used to compute $r(L)$. The use of a multi-year data set would not modify significantly $r(L)$ at small time lags, but would smooth out the slope of $r(L)$ for increasing values of L . The main features of the global distribution of the correlation are in good agreement with that discussed in Cahalan *et al.* (1982) and obtained from multi-year observations.

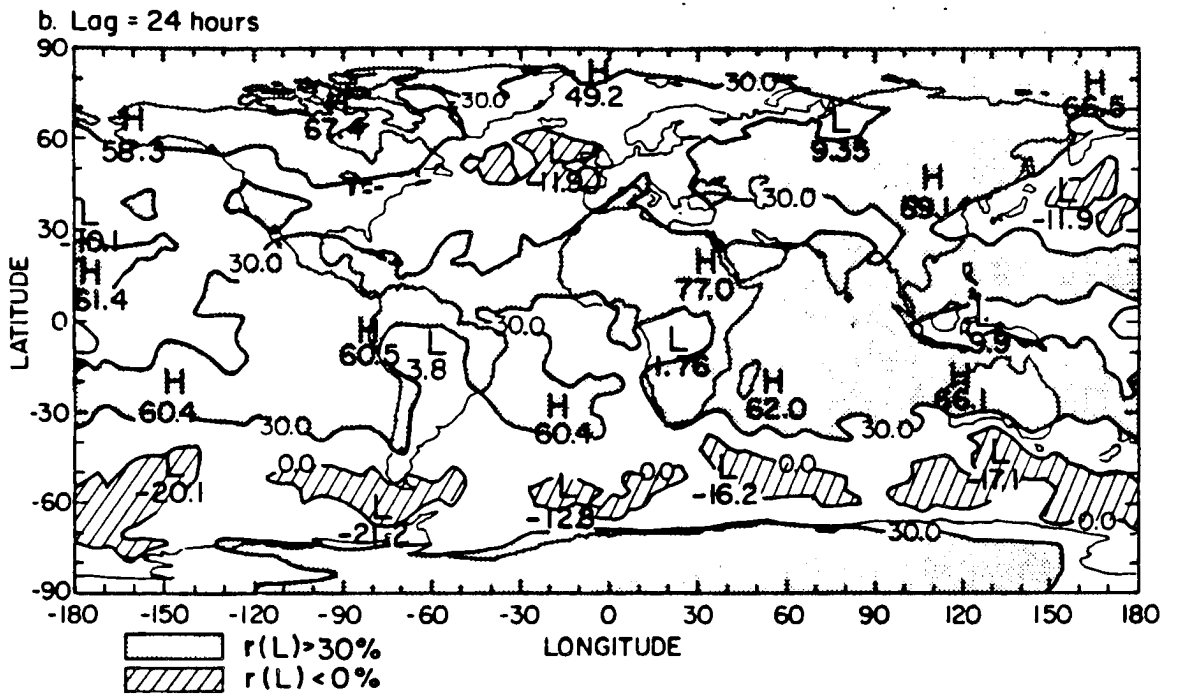
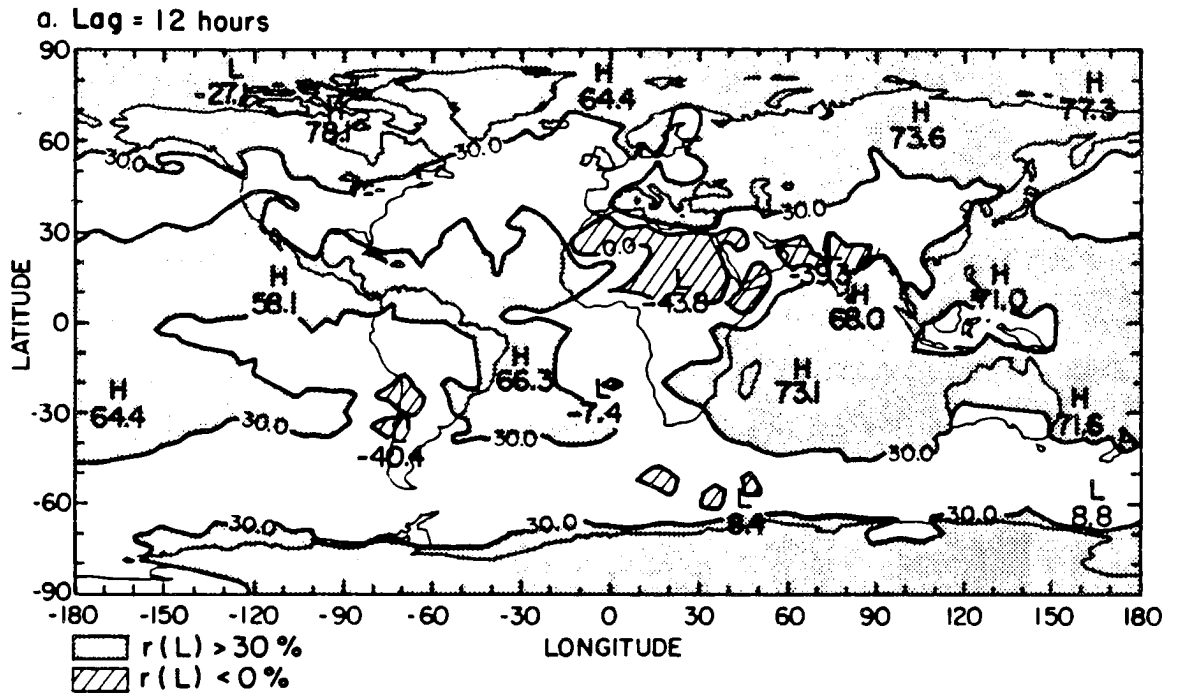


Figure 4.26: Map of the autocorrelation coefficient of the outgoing infrared radiation, computed from NOAA IR data, for Northern Hemisphere winter (%): (a) 12-hour lag, and (b) 24-hour lag.

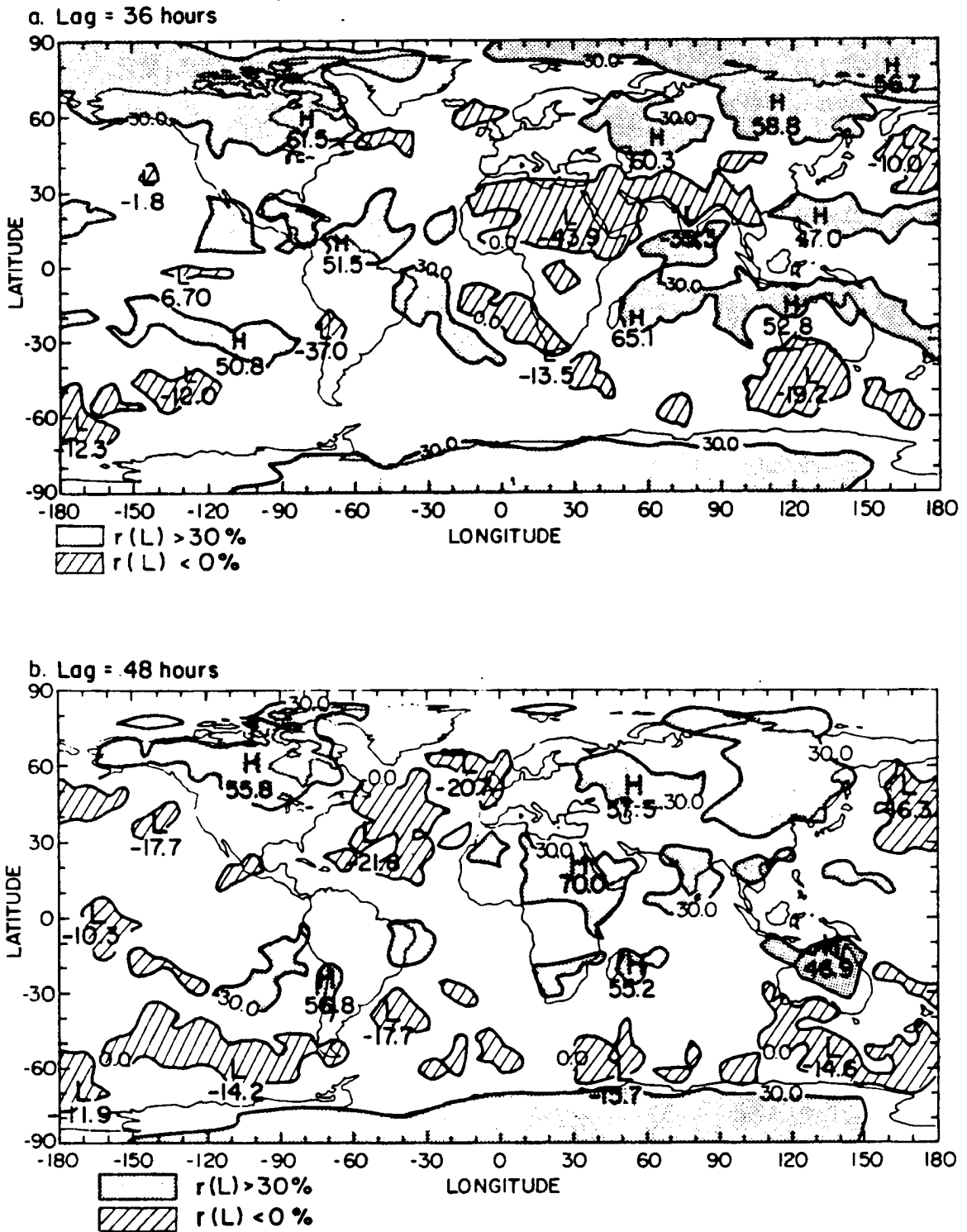


Figure 4.27: Map of the autocorrelation coefficient of the outgoing infrared radiation, computed from NOAA IR data, for Northern Hemisphere winter (%): (a) 36-hour lag, and (b) 48-hour lag.

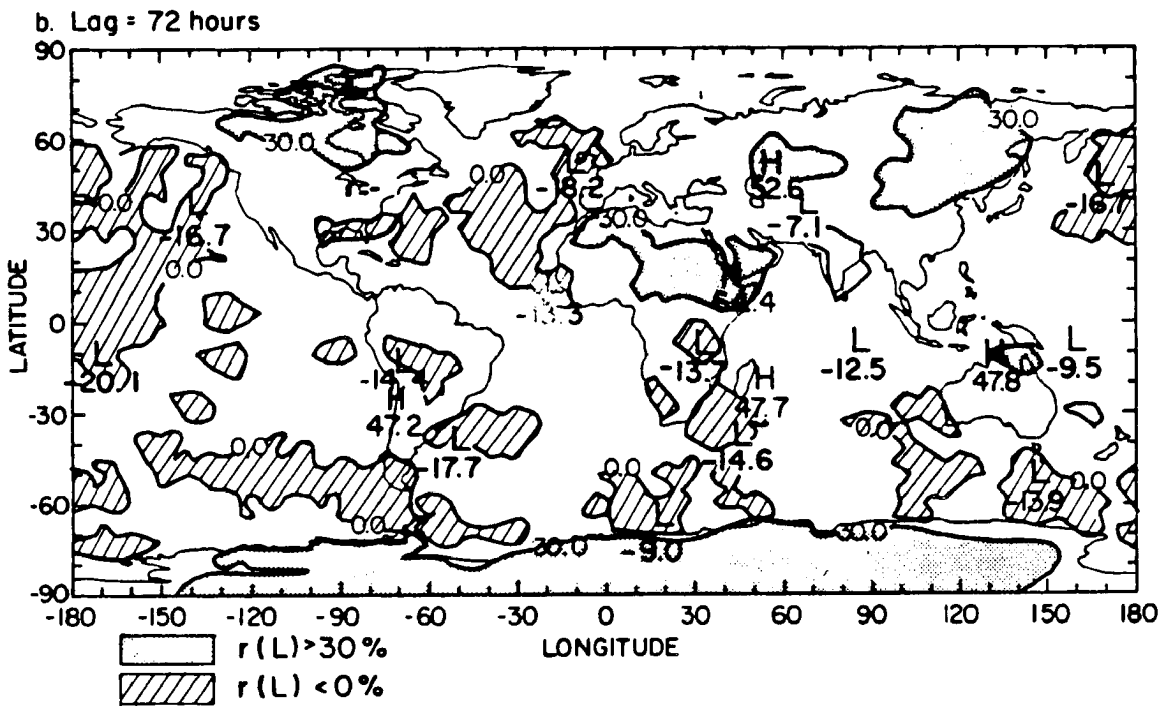
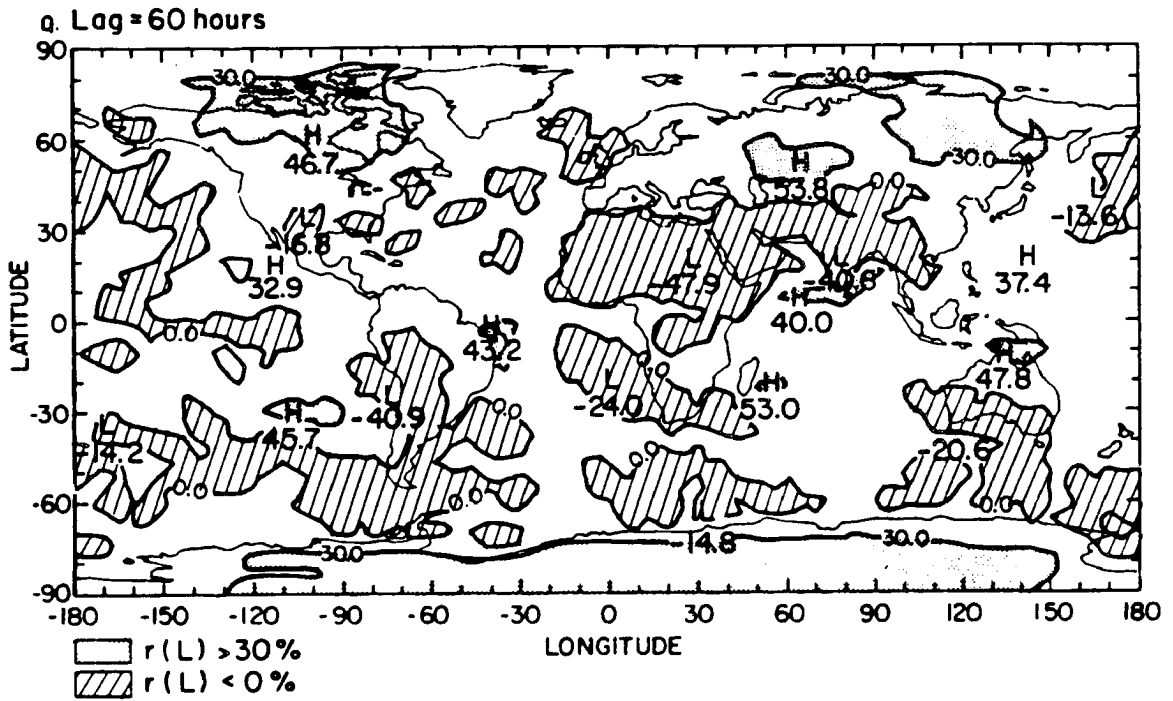


Figure 4.28: Map of the autocorrelation coefficient of the outgoing infrared radiation, computed from NOAA IR data for Northern Hemisphere winter (%): (a) 60-hour lag, and (b) 72-hour lag.

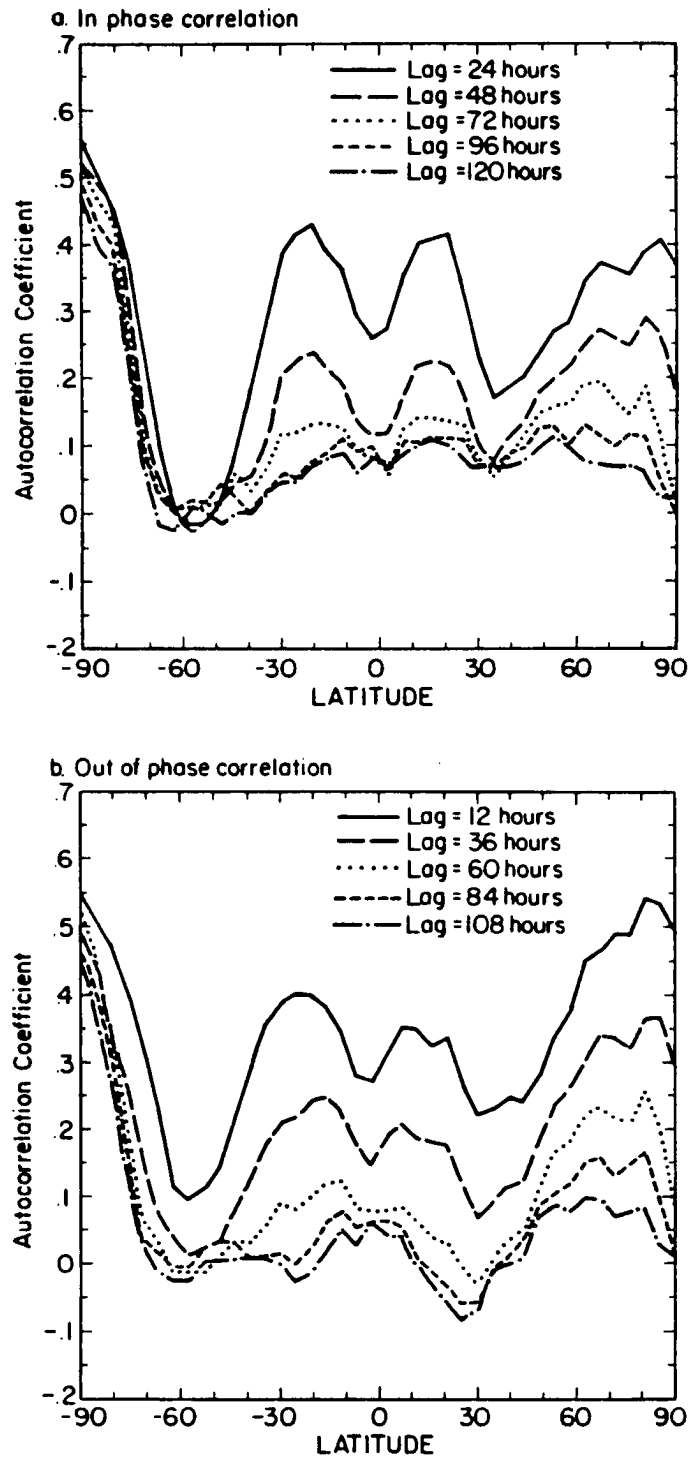


Figure 4.29: Zonally-averaged distribution of the time-lagged autocorrelation coefficients of the outgoing infrared radiation (%): (a) in phase correlation, and (b) out of phase correlation.

4.6.3 Model-derived correlation

The time-lagged autocorrelation coefficients of the model-generated outgoing infrared radiation are computed for successive 12-hour lags for Northern Hemisphere winter conditions and compared against those obtained from satellite IR time series. The comparison between model and observations is made for in phase correlation only, over every 24-hour lag, to eliminate the impact of the diurnal cycle of the radiation field. The global distribution of the ensemble average and ensemble standard deviation of $r(L)$ at lags 1, 2, and 3 days are shown in Figures 4.30, 4.31, and 4.32. As from observations, the correlation at a 1-day lag is positive in the tropics and the polar regions, and mostly negative in the middle latitudes, especially above the storm track regions over the Pacific and Atlantic oceans. There are several important differences in the distribution of the correlation between model and observations. On the one hand, the model underestimates $r(L)$ over the continents in the winter hemisphere which may result from the decreased persistence and intensity of the cold and dry air masses when compared against observations. On the other hand, the model overestimates $r(L)$ above the deep tropical convective activity regions which may result from an increase persistence of the convective clouds. The comparison against climatological data pointed out the factor of two difference in the precipitation rate above the heavy rainfall regions in the tropics. The comparison of the distribution of $r(L)$ between model and observations shows that the model-generated correlation decreases more dramatically than that computed from observations over the whole globe. This is also very well seen in the zonally-averaged profile of $r(L)$ shown in Figure 4.33. The zonal averages of $r(L)$ computed from the model are systematically less at all lags and the difference between model and observations is as large in the tropics and the middle latitudes, especially in the winter hemisphere. Finally, the increased decorrelation in the model is consistent with the factor of two difference in the temporal variability between the model-generated and satellite-derived outgoing infrared radiation.

The comparison of the autocorrelation coefficient of the outgoing infrared radiation computed from the model and satellite IR time series is made difficult because of the

increased noise in the simulated correlation with increasing time lags. As shown in Figure 4.30, 4.31, and 4.32, the ensemble standard deviation of the time-lagged autocorrelation coefficients of the outgoing infrared radiation looks randomly distributed in space and there are large variations across the five independent climate realizations. The zonally-averaged profiles of the ensemble average and ensemble standard deviation of $r(L)$ are shown in Figure 4.34. As previously observed in the global distribution, the ensemble average of $r(L)$ rapidly decreases with increasing time-lags whereas the ensemble standard deviation is relatively constant about an averaged value of 7.5 % for all lags. This indicates that the departure of $r(L)$ for each individual realization from the mean distribution increases with increasing time-lags. Chervin finds identical relationships between the ensemble average and ensemble standard deviation of the time-lagged autocorrelation coefficients of the temperature field computed for perpetual January conditions with CCM1. His study and our results show that a single finite time-span climate realization is not sufficient to adequately describe the temporal behavior of the GCM-simulated climate but that, in addition, the exact number of realizations required to obtain a satisfactory description of climate is not obvious. Because of the increased error attached to the actual value of $r(L)$ for increasing L at individual grid-point, and because of the computational cost to obtain $r(L)$ from five independent climate ensembles, we decided to focus our comparison on a global scale and for correlation less than 3 days.

4.7 Discussion

In view of the magnitude of the difference in the temporal variability between the model-generated and satellite-observed radiation fields, it is legitimate to ask the question if major problems in comparing outputs from physically-based but highly parameterized climate models against space-borne observations do not systematically include systematic biases which may affect the validity our results. We see at least two major problems: (1) The longwave and shortwave radiative fluxes are computed at individual and regularly spaced grid-points in the model, whereas the satellite observations produce estimates of the radiation fields for grid-boxes of approximately equal surface area; (2) There is not any

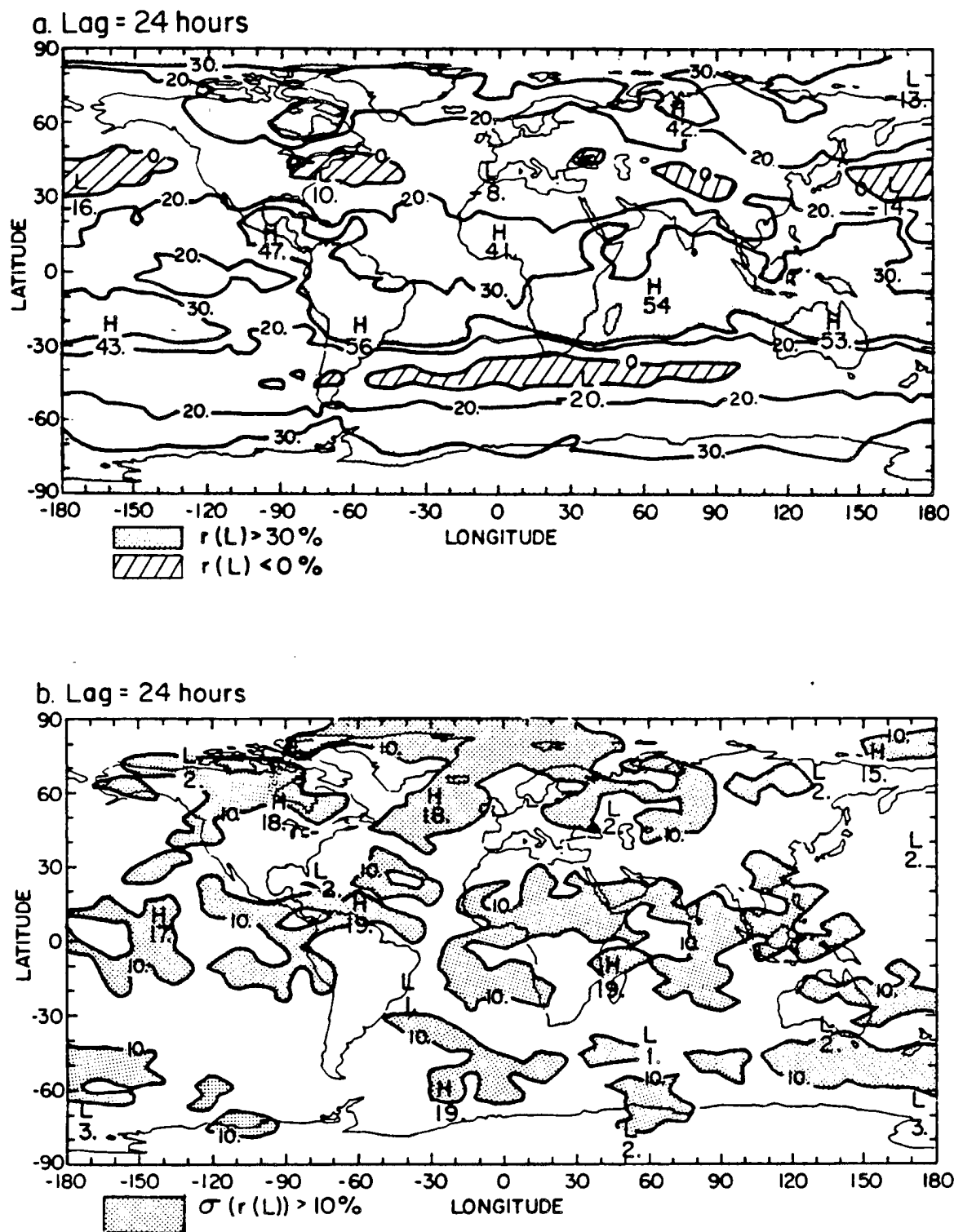


Figure 4.30: Map of the 24-hour lag autocorrelation coefficient of the model-generated outgoing infrared radiation for Northern Hemisphere winter (%): (a) ensemble average, and (b) ensemble standard deviation.

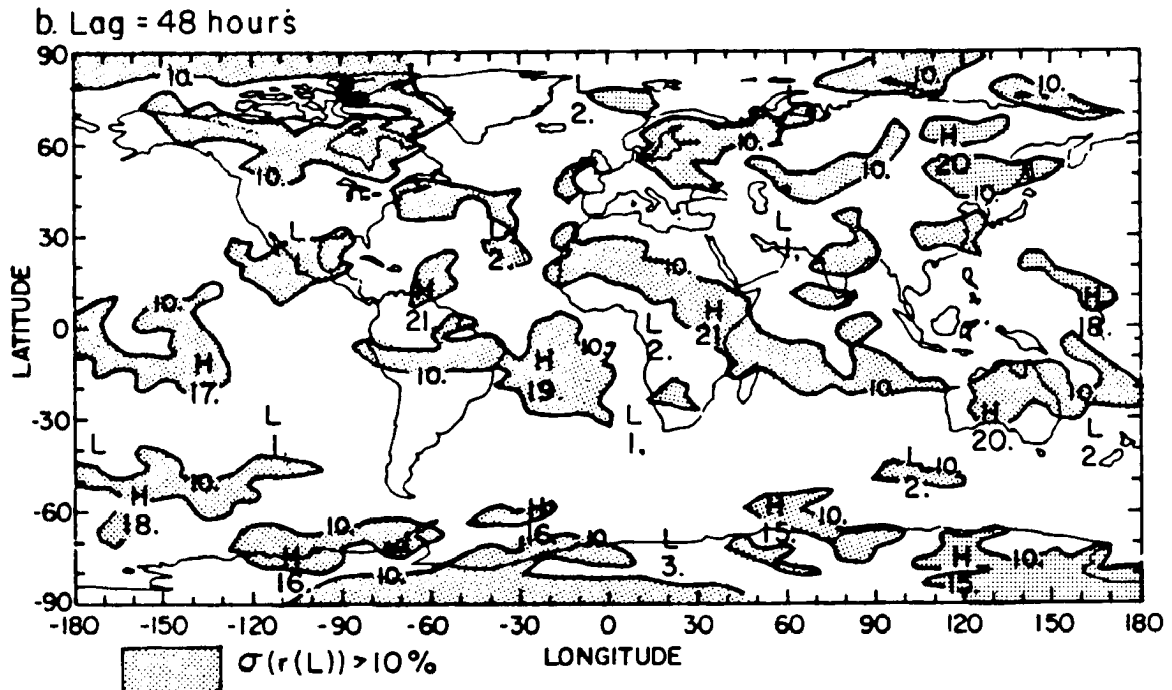
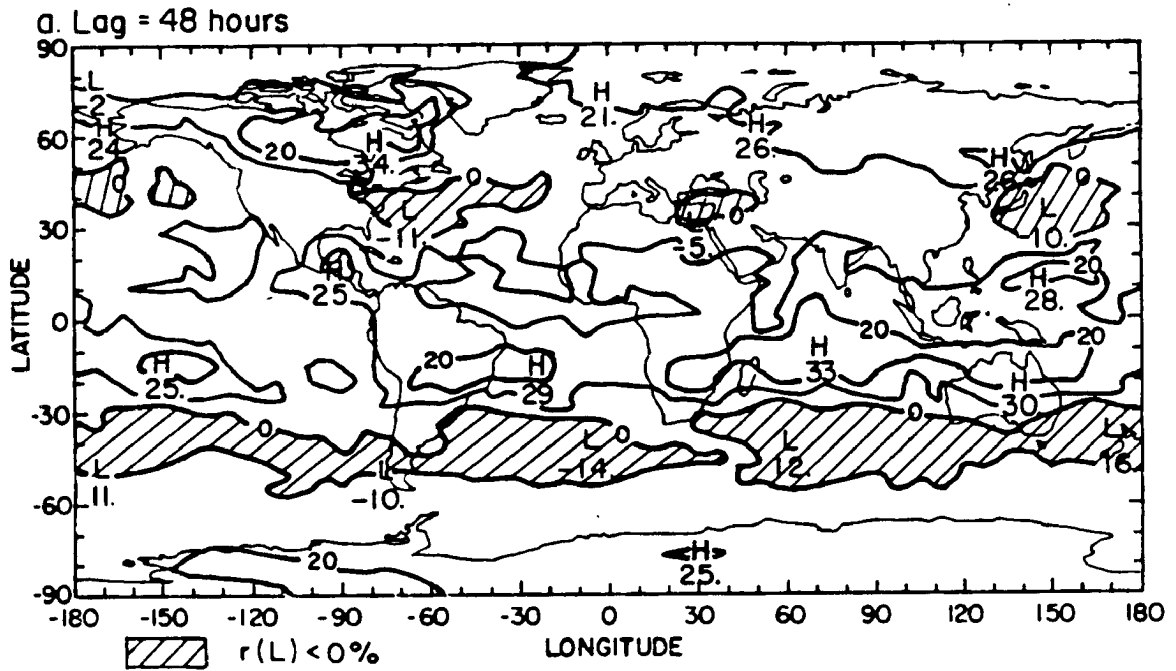


Figure 4.31: Map of the 48-hour lag autocorrelation coefficient of the model-generated outgoing infrared radiation for Northern Hemisphere winter (%): (a) ensemble average, and (b) ensemble standard deviation.

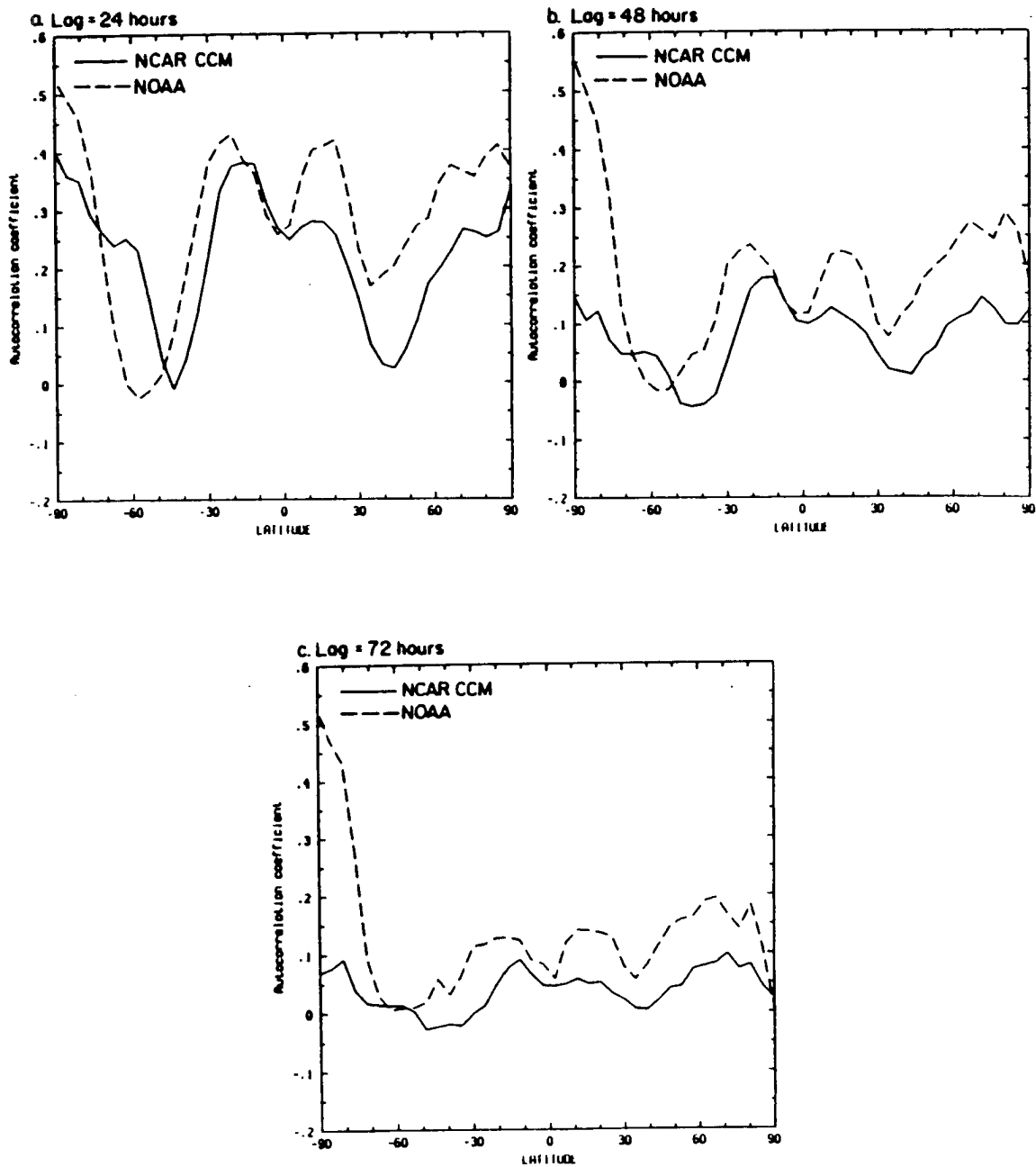


Figure 4.33: Zonally-averaged distribution of the time-lagged autocorrelation coefficient of the outgoing infrared radiation at a 24-hour lag, 48-hour lag, and 72-hour lag (%), for Northern Hemisphere winter.

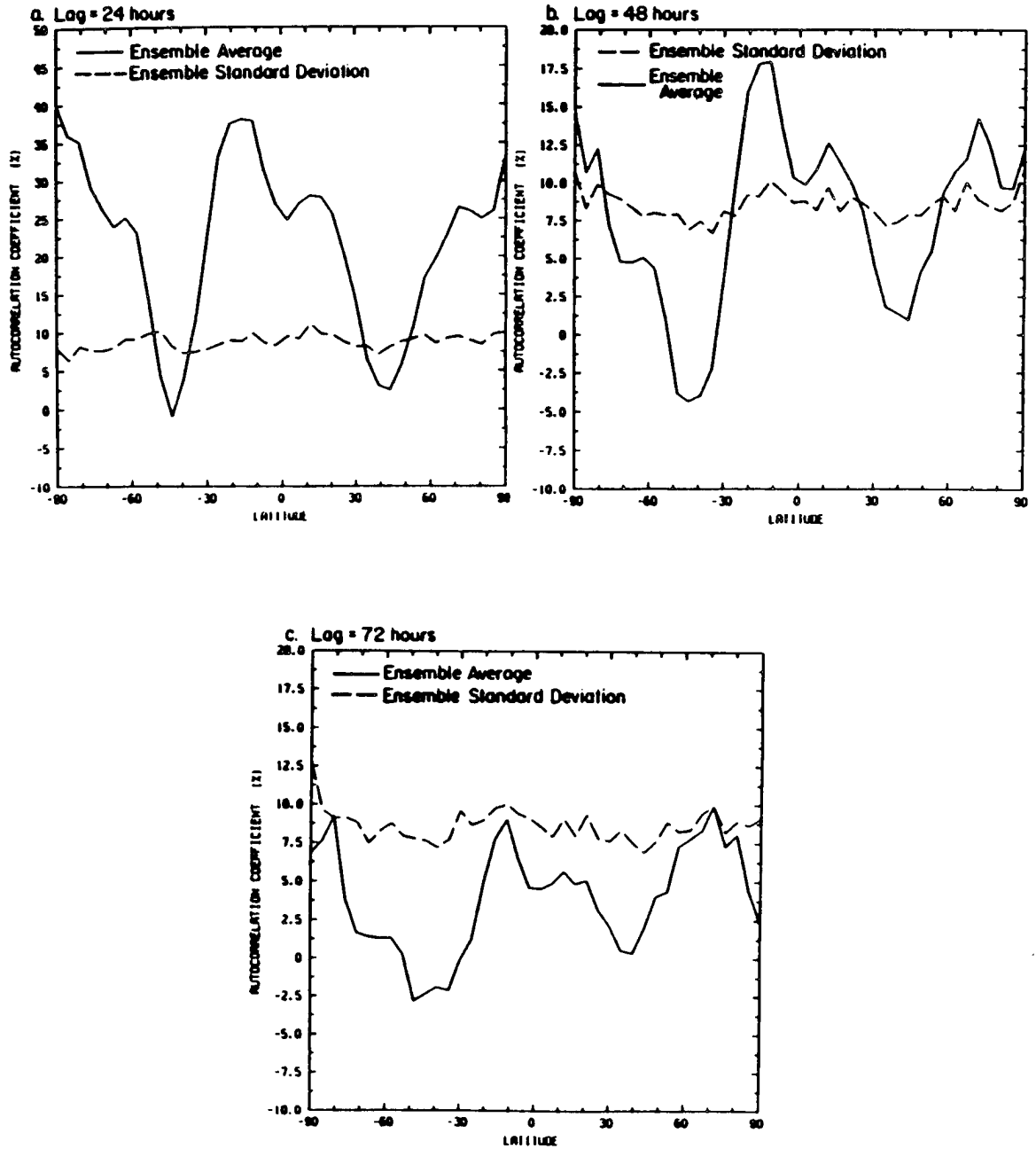


Figure 4.34: Zonally-averaged distribution of the time-lagged autocorrelation coefficient of the model-generated outgoing infrared radiation (%): (solid line) ensemble average, and (dashed line) ensemble standard deviation.

diurnal cycle in the model whereas the standard deviation, computed from the seasonal average, of the outgoing infrared radiation is computed by combining both day-time and night-time satellite measurements instead of daily mean values.

In Chapter Two, we discussed the importance of the spatial resolution on the computation of the standard deviation from satellite measurements. The increased field-of-view of the scanner instruments and the averaging of the individual pixels into smaller boxes in the NOAA Experiment yield a sharper gradient at the boundary between clear-sky and cloudy regions. It also increases (respectively decreases) the standard deviation above areas of high (respectively low) variability. This results from a higher homogeneity inside the grid-box and a more accurate identification of the target scene type (land, water, snow/ice, cloud). All grid-boxes are not, however, completely homogeneous and the difference in the radiation field between satellite orbits depends not only upon the destruction and creation of clouds within a box, but also upon the passage of cloud systems through the grid-box. On the other hand, the radiation fluxes and cloud fraction are computed at single grid-points in CCM1 which are, or completely cloudy or completely cloud-free. In addition, the clouds do not have any realistic life-cycles and the advection of cloudiness is excluded in the model. In view of the magnitude of the difference in the temporal variability of the radiation fields, it is obvious that this problem plays a minor role in explaining the discrepancy between model and observations.

In order to keep the same sampling interval than in the GCM, we decided to combine day-time and night-time satellite observations instead of daily mean values to compute the standard deviation of the outgoing infrared radiation. This choice also compensates for the missing days in the Nimbus-7 data set. Figure 4.35 shows the impact of the noon-midnight difference in the global distribution of $\sigma(\text{IR})$ computed from the Nimbus-7 IR data, for the winter and summer seasons. As expected, the largest difference between $\sigma(\text{IR})$ computed from every 12-hour observations and daily mean value of the outgoing infrared radiation, is positive over the whole globe which indicates that increased time samplings actually increases the standard deviation. It is the largest over the desert regions and convective

activity regions over the oceans and reaches values as large as 20.7 Wm^{-2} in some areas. Although we cannot verify this hypothesis at the present time in CCM1, there is no reason to believe that the inclusion of a diurnal cycle would not produce the same effect on the computation of $\sigma(\text{IR})$, as long as we keep the same sampling interval between model and observations.

The impact of the diurnal cycle on the temporal variability of the GCM-simulated radiation fields can be estimated from climate simulations produced by the CSU general circulation model, formerly named the UCLA/GLA GCM (Randall, private communication, 1988). A description of the current CSU GCM, in particular the cloud prediction scheme, is given in Harshvardhan *et al.* (1988) and Randall *et al.* (1988). In contrast to the NCAR CCM, a full computation of the longwave and shortwave radiative heating rates is made every hour to adequately describe the diurnal cycle of the incident solar radiation, the surface temperature, and the cloudiness. The nine-level, four by five degree version of the model was used to run June-July and December-January simulations.

Figure 4.36 shows the zonally-averaged distribution of the standard deviation of the model-simulated outgoing infrared radiation, computed from the 0 and 12 LT instantaneous values (solid line) and from the daily mean (dotted line). In order to simulate the satellite time sampling, the daily mean is a weighted average of the noon and midnight values. The inclusion of the diurnal cycle in the model increases the zonal averages of the standard deviation when every 12-hour samples are used instead of daily mean values. As from satellite observations, the diurnal cycle effect is the greatest at low latitudes in the summer hemisphere because of the increased surface heating and diurnal cycle of the convective clouds. As for the NCAR CCM, the CSU GCM overestimates the temporal variability of the outgoing infrared radiation at low latitudes by about a factor of two. In contrast with CCM1, a closer agreement between model and observations is observed in the middle and polar latitudes, especially for the Northern Hemisphere winter season. This comparison shows that the inclusion of the diurnal cycle in CCM1 would actually increase the variability of the radiation fields, as in the CSU GCM and satellite observations. We are, therefore, confident that, although it certainly induces a greater uncertainty in

the computation of the daily average, the lack of diurnal variations in CCM1 does bias our computation of the standard deviation of the simulated radiation budget.

4.8 Summary

The globally-averaged planetary radiation budget measured by the scanner radiometers on board Nimbus-7 and generated with CCM1 is summarized in Table 4.2 for the Northern Hemisphere winter and summer seasons. The ability of the NCAR Community Climate Model to reproduce the mean planetary radiation budget components and their temporal variability can be summarized as follows:

1. The NCAR CCM reproduces successfully the geographical distribution of the seasonally-averaged outgoing infrared radiation for Northern Hemisphere winter and summer conditions when compared against those obtained from Nimbus-7 NFOV data. The distribution of the model-simulated seasonally-averaged planetary albedo and absorbed solar radiation does not match as well because of the crude representation of the surface albedo and the prescribed optical properties of clouds.
2. The global distribution of the standard deviation about the seasonal average of the model-simulated outgoing infrared radiation is similar to that obtained from satellite IR data. However, the magnitude of $\sigma(\text{IR})$ is systematically greater by about a factor of two than that computed from observations over the entire globe. The difference of temporal variability between model and satellite observations is also observed at short wavelengths.
3. The time-lagged autocorrelation coefficients of the outgoing infrared were computed from the model time-series and for every 12-hour observations taken by the NOAA scanner instruments. The correlation in the radiation field decreases faster than in the real atmosphere which is consistent with the higher variability of the model-generated radiation fields. Because of the low spatial resolution of the model-grid, we decided to avoid any regional comparison as well as any computation of combined time-space correlation.

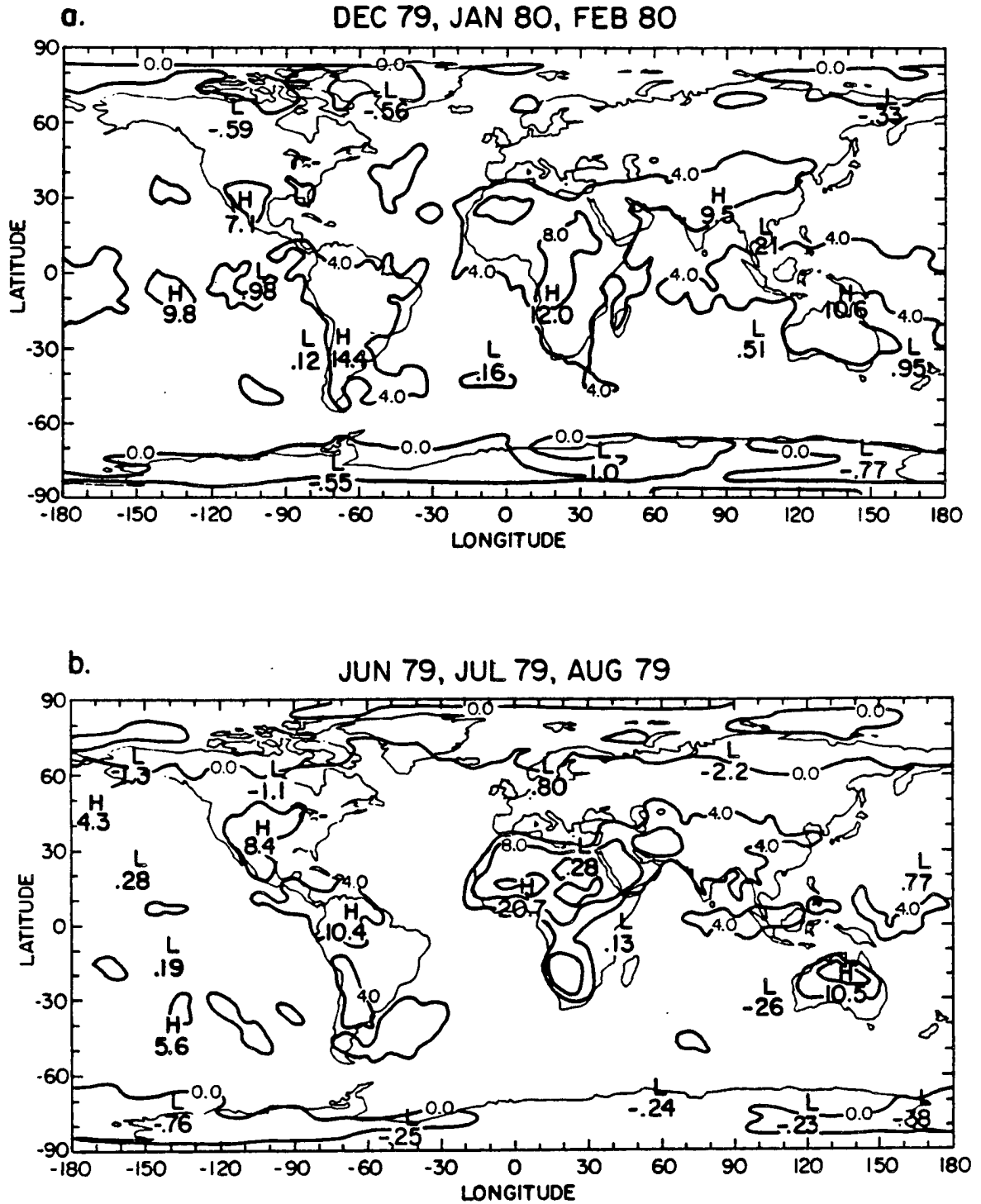


Figure 4.35: Map of the difference between the standard deviation of the outgoing infrared radiation computed from every 12-hour observations and daily mean values (Wm^{-2}): (a) Northern Hemisphere winter, and (b) summer.

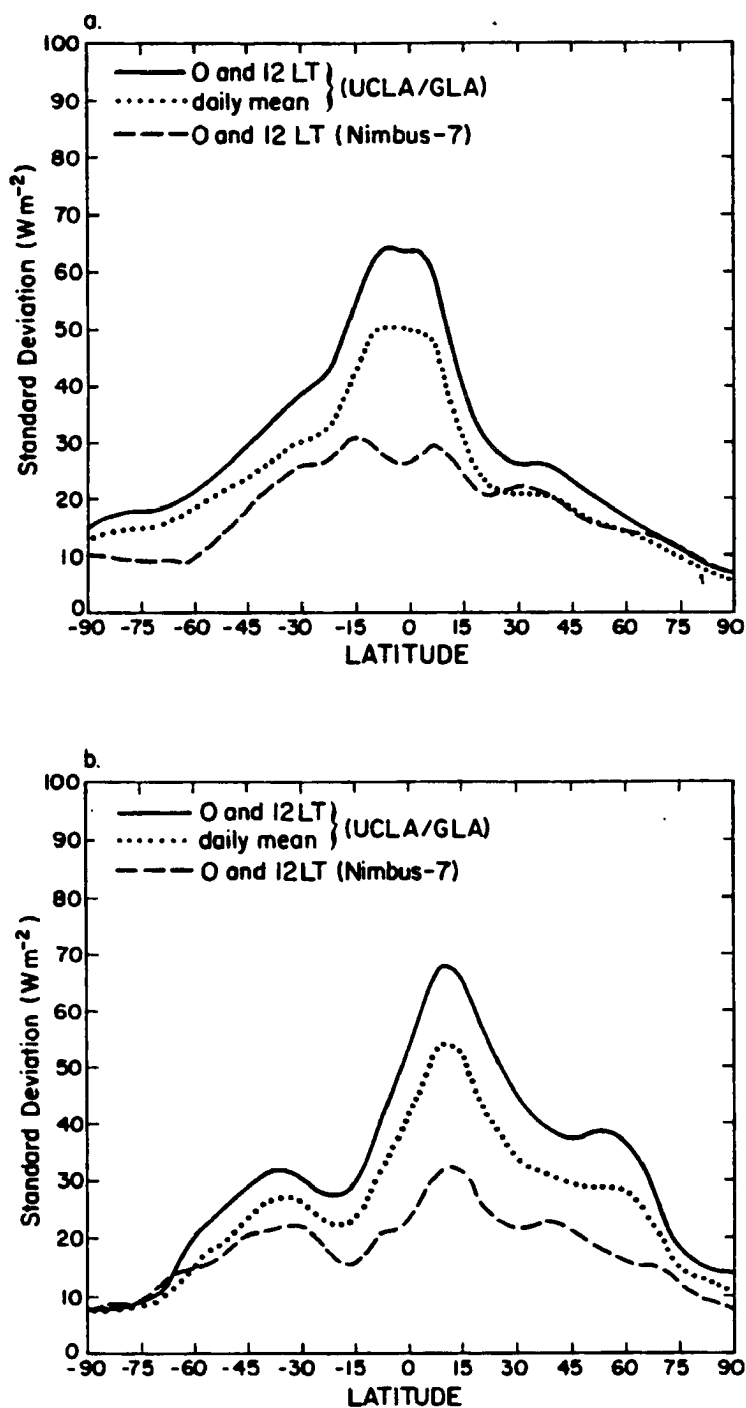


Figure 4.36: Zonally-averaged distribution of the standard deviation of the outgoing infrared radiation produced with the CSU GCM (Wm^{-2}): (a) Northern Hemisphere winter, and (b) summer (Randall, private communication, 1988)

The comparison between the model-generated radiation fields and measured by the NFOV scanner radiometers on board the satellite Nimbus-7 has helped identify a major deficiency in the simulation of climate with the NCAR Community Climate Model. The GCM reproduces successfully the mean steady state of the earth-atmosphere climate system but fails to simulate its temporal variability. In view of the impact of clouds on the planetary radiation balance, including its day-to-day fluctuations, it is suspected that the model simulation of the interactions between the clouds and the radiative, thermodynamic, and dynamic processes, may explain the faster decorrelation in CCM1. In the following chapters, we identify the origins of the discrepancy between model and satellite observations, and propose modifications which have to be included into the model code to reduce the blinking of the atmosphere.

Table 4.2

Table 4.2: Globally-averaged values of the seasonal average and standard deviation of the Nimbus-7 and model-generated radiation fields. All the fields are given in Wm^{-2} , except the planetary albedo which is in %.

	Dec-Jan-Feb		Jun-Jul-Aug	
	Nimbus-7	CCM1	Nimbus-7	CCM1
<u>Seasonal average</u>				
Outgoing infrared radiation	230.4	240.0	236.3	246.8
Absorbed solar radiation	235.1	248.1	224.0	236.0
Planetary albedo	33.6	31.0	32.8	29.9
<u>Standard deviation</u>				
Outgoing infrared radiation	24.3	46.9	23.1	46.3
Absorbed solar radiation	42.0	59.4	37.0	55.8
Planetary albedo	9.7	15.6	9.1	16.2

Chapter 5

INFLUENCE OF THE MODEL-GENERATED CLOUDINESS ON THE TEMPORAL VARIABILITY OF THE RADIATION BUDGET COMPONENTS

5.1 Introduction

In Chapter Four, the most striking result is the difference in the temporal variability between the model-generated and satellite-observed radiation fields. In contrast to the relatively good agreement in the distribution of the seasonal average, the standard deviation computed from the seasonal average, of the outgoing infrared radiation, the planetary albedo or the absorbed solar radiation, is about two times larger when computed with CCM1. Because of the impact of cloudiness on radiation at short and long wavelengths, and because clouds evolve faster in time and space than the temperature and humidity fields, it is legitimate to suspect that the treatment of the interactions between clouds, radiation, and the other physical processes in the model, may actually be responsible for the blinking of the simulated atmosphere. The primary objective of this chapter is to show that the high frequency of occurrence of clouds in the model can be accounted by the difference in the temporal variability of the radiation fields.

In the first section, the total cloud cover predicted with CCM1 is compared against the total cloud cover derived from radiance measurements taken by the Temperature Humidity Infrared Radiometer (THIR) and Total Ozone Mapping Spectrometer (TOMS), both instruments aboard the Nimbus-7 satellite. Although this comparison is subjective to the cloud algorithm used to estimate the total cloud amount from space-borne observations, the use of this new data set is very attractive because it covers the same time period and corresponds to the same time sampling as the Nimbus-7 ERB Experiment.

The comparison, in Section Two, between the time variability of the cloud longwave radiative forcing and the total outgoing infrared radiation, and of the cloud shortwave radiative forcing and the total absorbed solar radiation, strongly suggests that the deficient representation of the cloud life-cycles explains increased fluctuations in the model-simulated planetary radiation budget. In the last section, the impact of reduced interactions between clouds and the other physical processes in the model, especially hydrologic processes, is described. In view of the deficiencies in the parameterization of the coupling between clouds, and the radiative, dynamic, and hydrologic processes, two experiments to study the sensitivity of the cloud and radiation fields, including their temporal variability, to a different cloud prediction scheme and to a change in the large-scale precipitation efficiency are proposed. They aim to: 1) To define strategies which should be taken to reduce the discrepancy between the model outputs and the satellite observations; and 2) To estimate the importance of correctly reproducing the life-cycle of clouds on the general circulation of the model-simulated atmosphere.

5.2 Model-generated versus satellite-derived total cloudiness

5.2.1 Background

A new global multi-level cloud climatology has been derived from the combination of infrared radiances from THIR (Hwang, 1982), UV reflectivities from TOMS (Heath, 1978), and surface temperature and snow/ice cover archived by the Air Force from their three-dimensional Nephanalysis Program (Fye, 1978).

a. THIR data

The two channel scanning radiometer measures earth thermal radiation from two spectral bands during day and night. A 10.5 to 12.5 μm (11.5 μm) window channel provides an image of the cloud cover and temperature of the cloud-top, land, and ocean surfaces. A 6.5 μm to 7.0 μm channel provides information on the moisture and possibly the cirrus cloud content of the middle and upper troposphere. The ground resolution at the sub-satellite point is 6.7 km and 20 km for the 11.5 and the 6.7 μm channels, respectively.

b.TOMS data

The TOMS instrument is a single monochromator which measures UV backscattered radiation at six different wavelengths from 0.313 to 0.380 μm sequentially in three-degree steps along the scan. The 0.360 and 0.380 μm wavelengths, which are not absorbed by ozone, are included in the cloud algorithm to provide an estimate of the UV reflectivity of a surface below or within the atmosphere. Measurements of the incoming solar irradiance at these wavelengths are also made to compute the directional albedos from the backscattered radiances.

c.Air Force Analysis

The Terrain Height Analysis, Snow/Ice Analysis, and Surface Temperature Analysis data fields used in the Air Force 3-D Cloud Nephanalysis are included to report the terrain height, the snow/no snow conditions, and surface temperature estimates in the Nimbus-7 cloud analysis. They are used to compute the cloud/no cloud threshold of the radiative temperature of the target area.

d.Cloud algorithm

The cloud algorithm is of the bispectral threshold type and completely described in Stowe *et al.* (1988). For day-time observations (or the ascending node of the satellite), the method uses two independent estimates of total cloud amount: 1) the infrared (IR) algorithm, a threshold technique based on the 11.5 μm radiance measurements of THIR and the Air Force surface temperature; and 2) the ultraviolet (UV) algorithm, a linear interpolation method based on the 0.37 μm surface reflectivity measured by TOMS. Each THIR 11.5 μm radiance observation contained in a Subtarget area (STA), each about $(165\text{km})^2$, is classified as being either clear, low, middle, or high altitude cloud depending on its magnitude relative to precomputed radiance thresholds. The computation of the radiative temperature appropriate for the cloud/no cloud threshold takes into account adjustments for atmospheric attenuation and partially filled field-of-views, and random uncertainties resulting from horizontal variations in the surface temperature within the STA. Provided that the STA is sunlit, the cloud amount is estimated independently from

a linear relationship between UV reflectivity, averaged for all snow-free TOMS data, and cloud amount. These independent IR and UV cloud estimates are then combined by a bispectral algorithm into one value of cloud amount. The bispectral method results in total cloud amounts close to the infrared estimate when the IR algorithm indicates a large amount of middle- and high-level clouds, but close to the UV estimate when IR low-level cloud and clear amount are large. For night-time observations (or the descending node of the satellite), only the IR algorithm is used.

This multi-year archival, also referred to as the Cloud-Matrix (CMATRIX) data set, includes the parameters of cloud amount in three height categories (low, middle, high), estimates of cirrus clouds, warm clouds, deep convective clouds, and the radiance of associated cloud-tops and the underlying surface. As for the ERB Experiment, the STA products have been further processed into ERB target area averages (500km)². Both daily and monthly averages are available on the CMATRIX tapes. The comparison of the satellite-derived total cloudiness against geosynchronous satellite (GOES) images shows that the Nimbus-7 cloud climatology does provide the necessary requirements for various studies of climate modeling and for studies related to the earth radiation budget (Stowe, 1988). The Nimbus-7 cloud climatology, which covers a six-year period from April 1979 to March 1985, does not have the same accuracy as that derived from ISCCP (Schiffer and Rossow, 1983) because it includes radiance measurements from one sun-synchronous satellite instead of from the combination of four geostationary satellites and one polar orbiter, and because of the lesser degree of sophistication in the cloud algorithm. However, it is the only multi-month data set available at present for use in conjunction with ERB measurements. In the following sections, twice daily estimates of the global total cloud cover over the time period between December 1979 and February 1980 are used for validation of the model-generated cloudiness and its temporal variability, for Northern Hemisphere winter conditions.

5.2.2 Seasonal average and standard deviation

The global distribution of the seasonal average and standard deviation of the model-generated and satellite-derived total cloud cover is shown in Figures 5.1 and 5.2. The

zonally-averaged profiles of both quantities are shown in Figure 5.3. Because of the increased uncertainty in the depiction of clouds from satellite radiance measurements at high latitudes, we limit our comparison to between 60°N and 60°S. Satellite-derived cloud estimates show that overcast atmospheric conditions prevail above the convectively active regions over the continents in the southern hemisphere, the South Pacific Convergence Zone, the winter monsoon area, and the middle latitude storm track regions over the oceans. Minimum cloud cover is depicted over the major desert regions and the cold land surfaces in the winter hemisphere. As for the radiation fields, there is a sharp gradient at the boundary between areas of low and high cloudiness. In contrast to the Nimbus-7 cloudiness between completely overcast and cloud-free regions, the cloud cover predicted with CCM1 is more uniformly distributed in space. This results from the fact that a model grid-point is either completely clear or completely cloudy while a satellite target area may be partially filled with clouds, and also from the model planetary boundary layer which is mostly overcast while satellite-derived low-level cloud amounts are underestimated when high-level clouds are present. The amount of cloudiness above the tropical convective activity regions and the middle latitude storm track regions is underestimated in the model when compared against observations, which may be partially attributed to the prediction of the intensity of the convection. As already discussed in Chapter Four, the underestimation of cloud amount yields a reduced minimum in the outgoing infrared radiation above the local position of the ITCZ.

The most important information from this comparison is the striking difference in the temporal variability of the total cloud cover between model and observations. The magnitude of the standard deviation is directly related to the frequency of occurrence of clouds which results from the formation and dissipation of clouds within a target area, or from the passage of cloud systems through the area. For the satellite-derived cloud field, the persistence of clouds over the deep tropical convective activity regions and the middle latitude storm track regions yields values of the standard deviation less than 20 %. These areas are characterized by seasonally-averaged cloudiness close to 100 %. Outside those regions and except for the desert regions, the standard deviation increases with increasing

cloudiness because of the lower frequency of occurrence of clouds within the target area. There is absolutely no resemblance in the distribution of the standard deviation between the model-derived and satellite-observed total cloud cover. In the model, the standard deviation is close to 45 % over the whole globe, except above limited areas such as the Sahara desert and the winter monsoon region for which its lower magnitude is still, however, two times greater than that computed from observations.

The difference in the distribution of the total cloud cover between model and observations is very well seen in Figure 5.3. There is almost no latitudinal gradient in the model-derived cloudiness and the amount of clouds is lower at all latitudes. In addition, the factor of two difference in the magnitude of the zonally-averaged cloudiness explains that of the standard deviation of the model-generated radiation fields.

5.2.3 Temporal correlation

As for the outgoing infrared radiation, the computation of the autocorrelation coefficients of the total cloud cover at successive time lags provides an estimate at the speed of which the cloud field breaks up. Because of the strong signature of clouds at infrared wavelengths, we expect a strong correspondence in the distribution of the temporal correlation between the cloud and radiation fields, especially from observations. As one example on how to simultaneously use radiation budget data and radiance-derived total cloud cover to study cloud-radiation-climate interactions from space-borne observations only, Figure 5.4 shows the zonally-averaged profile of the 1-day, 2-day, and 3-day lag autocorrelation coefficients of the outgoing infrared radiation and total cloud cover computed from the NOAA ERB and Nimbus-7 Cloud Experiments. Both the radiation and cloud fields show an identical latitudinal distribution, with a higher correlation in the total cloudiness in the summer hemisphere, and a lower correlation in the total cloudiness above the middle latitude winter storm track regions. Changes in the THIR and TOMS radiances and narrow-band converted to broad-spectral-band measurements of the outgoing infrared radiation similarly result from changes in cloudiness, and in the temperature and humidity fields. Therefore, some of the difference in the correlation between the cloud and radiation

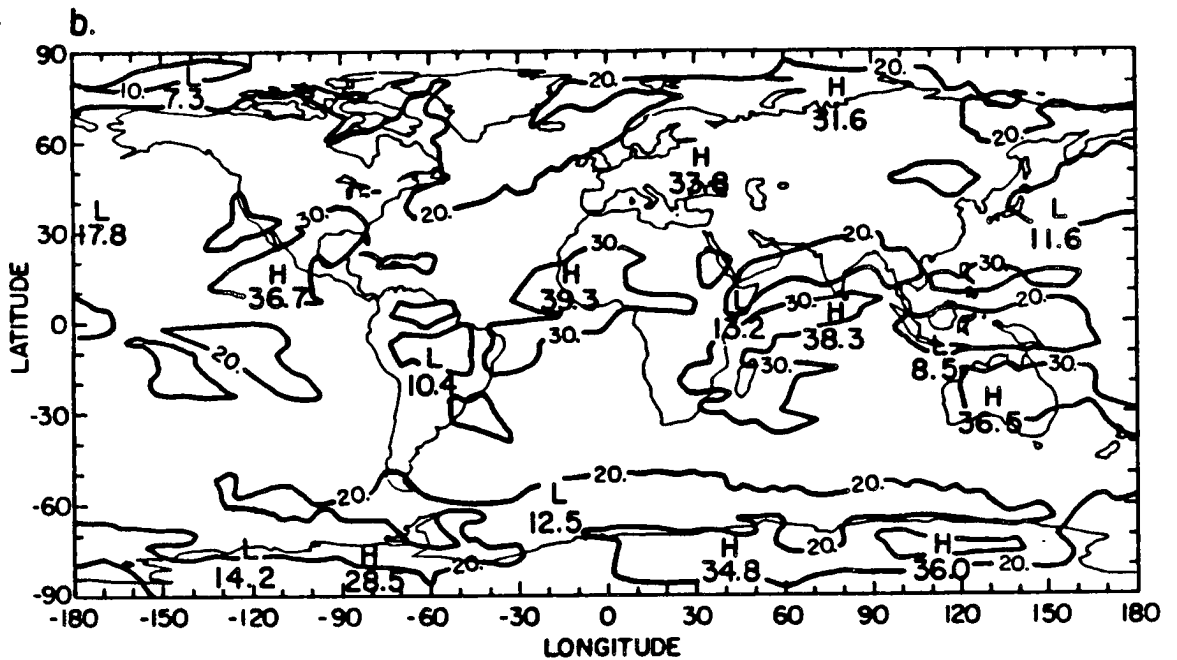
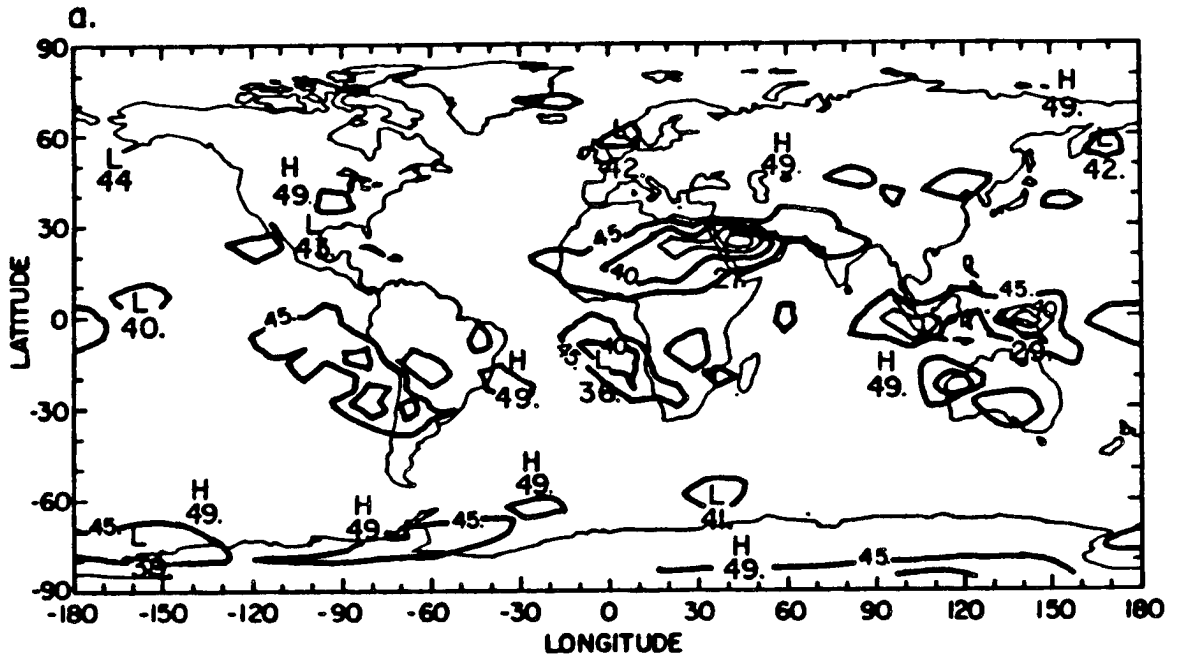


Figure 5.2: Map of the standard deviation of the total cloudiness for Northern Hemisphere winter (%): (a) computed distribution from the model, and (b) satellite-derived distribution from Nimbus-7 (CMATRIX).

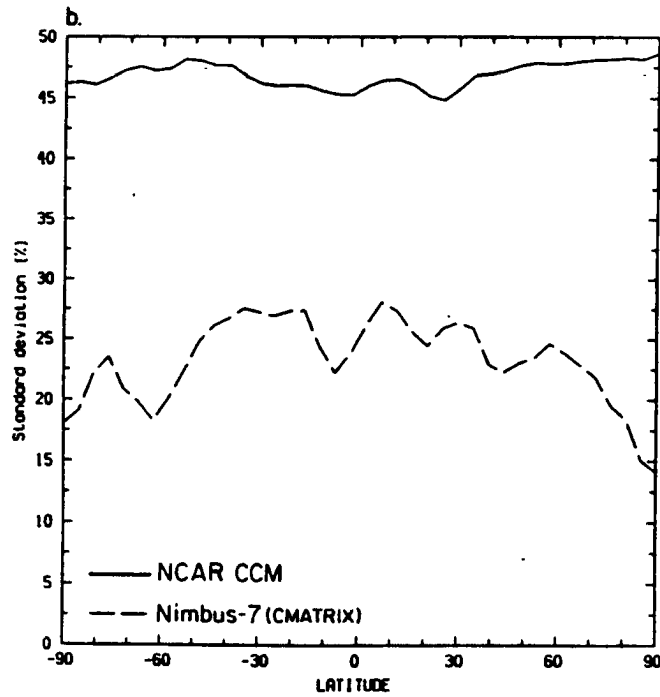
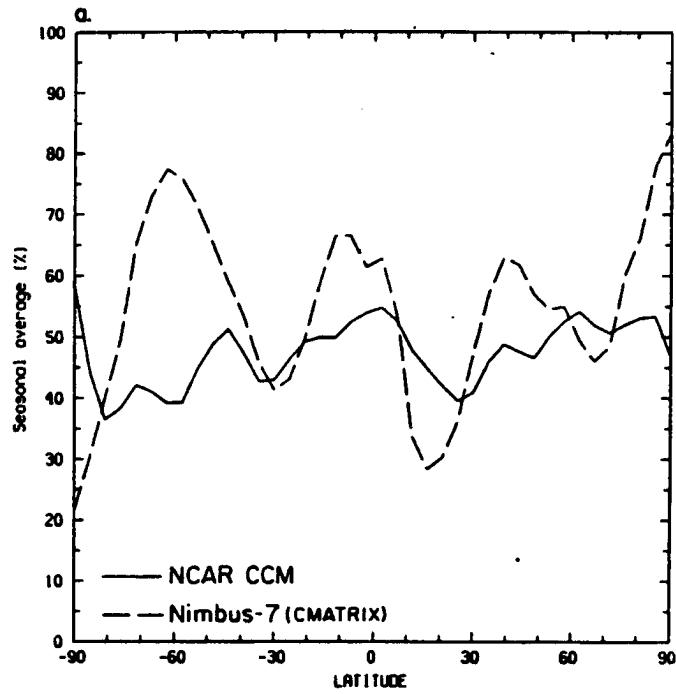


Figure 5.3: Zonally-averaged distribution of the total cloudiness for Northern Hemisphere winter (%): (a) seasonal average, and (b) standard deviation.

fields can be attributed to the cloud/no cloud threshold and to a different spatial resolution between the two data sets. It would be interesting to study the cross-correlation between the cloud amount for various cloud types and the total outgoing infrared radiation. This is one of the primary objective of the ongoing ERB and ISCCP Experiments.

Figures 5.5, 5.6, and 5.7 show the global distribution of the 1-day, 2-day, and 3-day lag autocorrelation coefficients of the model-generated and satellite-derived total cloudiness. Figure 5.8 shows the zonally-averaged distribution of $r(L)$ for all three lags. As for the outgoing infrared radiation at a 1-day lag, the correlation in the total cloud cover is maximum and positive between 30°N and 30°S , and at the polar latitudes, negative in the middle latitudes. On the one hand, the change in cloudiness above the cyclogenetic areas mainly results from advection of large-scale clouds associated with frontal disturbances through a satellite grid-box. On the other hand, the change in cloudiness above the convective activity regions mainly results from the creation and destruction of clouds inside the grid-box. As seen from the top of the atmosphere, and because of the time sampling of the satellite, it appears as if the grid-box containing convective clouds were completely overcast most of the time. This explains the difference in the correlation between the convective and large-scale type clouds. In addition, and as for the radiation field, we observe important regional differences in the decrease of the correlation in the total cloud cover with increasing time lags.

There are striking differences in the distribution of the correlation between model and observations. As computed from the satellite-derived cloud cover, $r(L)$ varies between convective activity and middle latitude storm track regions. However, there is a dramatic drop in the magnitude of the correlation of the model-predicted clouds with increasing time-lags. This is very well seen in the zonally-averaged distribution of $r(L)$ and comes into logic agreement with that of the standard deviation. At a 2-day lag, $r(L)$ is close to zero or negative over the whole globe while it stays greater than 30 % above cloudy regions when computed from satellite-derived cloudiness. This indicates that the model cannot reproduce realistically the life-cycle of clouds.

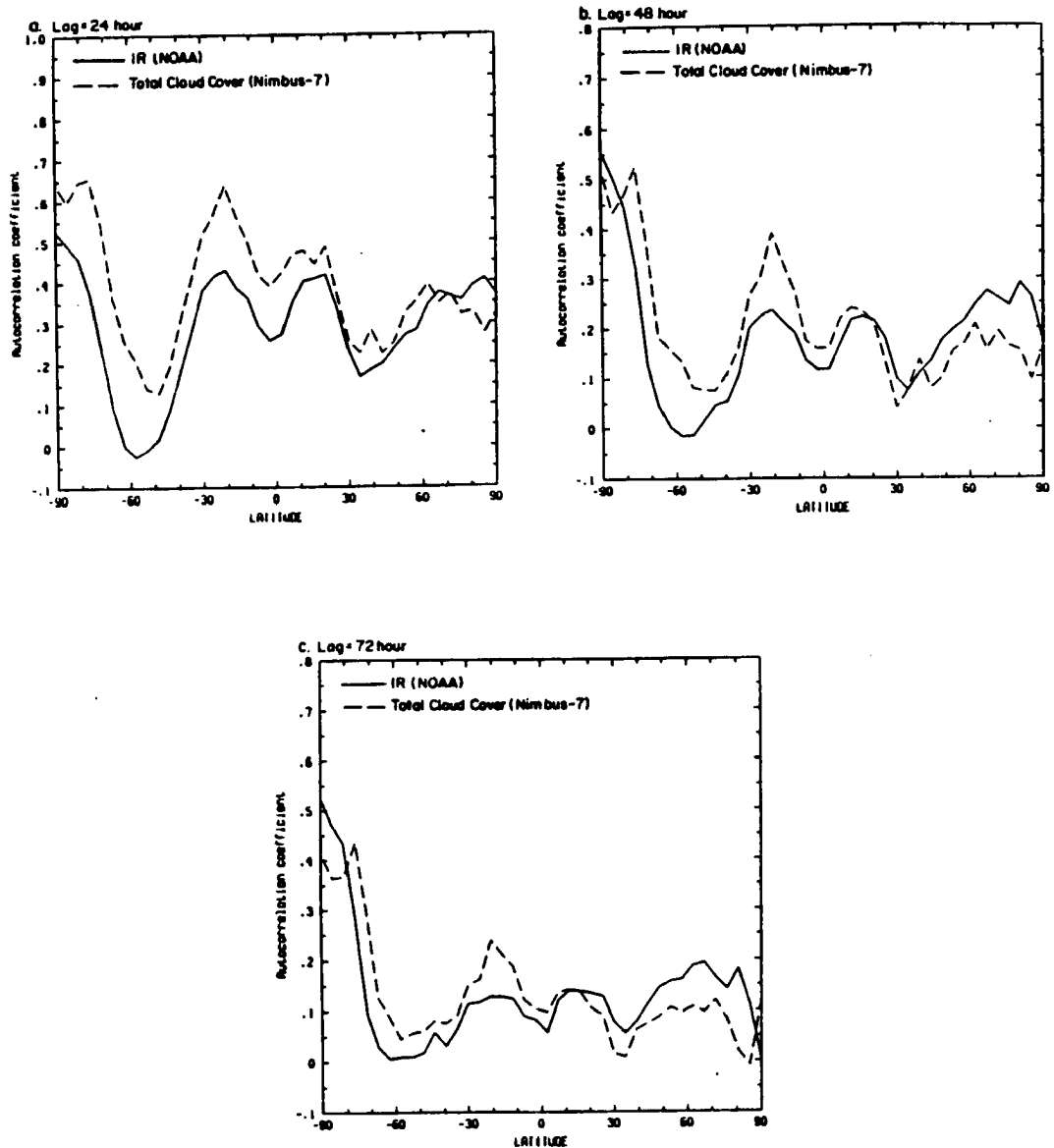


Figure 5.4: Zonally-averaged distribution of the time-lagged autocorrelation coefficients of the total cloud cover (CMATRIX) and outgoing infrared radiation (NOAA ERB) for Northern Hemisphere winter conditions (%): (a) 24-hour lag, (b) 48-hour lag, and (c) 72-hour lag.

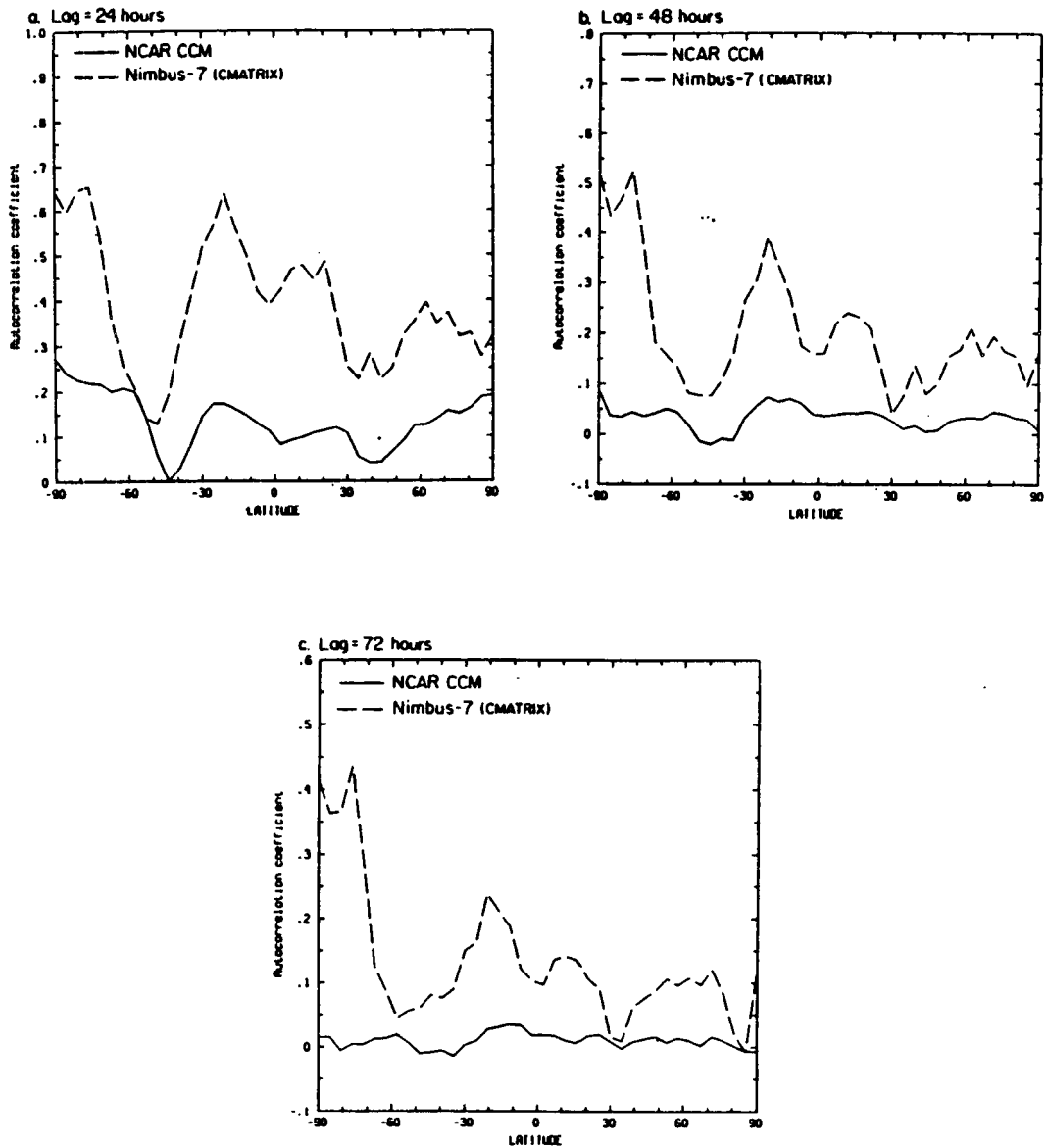


Figure 5.8: Zonally-averaged distribution of the time-lagged autocorrelation coefficient of the total cloudiness for Northern Hemisphere winter (%): (a) 24-hour lag, (b) 48-hour lag, and (c) 72-hour lag.

5.2.4 Conclusion

The total cloud cover predicted with CCM1 was compared against that derived from radiance measurements taken by the THIR and TOMS instruments on board Nimbus-7, for the Northern Hemisphere winter season. This section completes our comparison, made earlier in Chapter Four, between the model-generated and satellite-observed radiation fields. The validity and limitations of our comparison, resulting from inherent difficulties in comparing the model outputs against satellite-derived clouds, are identical as those in discussing the radiation fields. There exists a major difficulty in the climate model-generated cloud field. The model-simulated cloud field has an unnatural flicker which yields a factor of two difference in the temporal variability of the total cloud cover between model and observations, and unrealistic life-cycles of clouds. These results are supported by independent comparisons, made in the previous chapter, of the model-generated radiation fields with radiation budget measurements taken by the Nimbus-7 and NOAA satellites.

5.3 Cloud radiative forcing

The sensitivity of the longwave and shortwave components of the planetary radiation balance to a change in cloudiness has been extensively studied in the past, as summarized by Ohring and Gruber (1983). Among the numerous parameters developed to compute the sensitivity of the radiation fields to a change in the cloud cover, the concept of cloud radiative forcing (Ramanathan, 1987) offers the advantage that cloud-radiation interactions can be quantitatively estimated without support of any additional data set of the distribution of clouds.

5.3.1 Definition

The mathematical expression of the net radiative forcing of clouds is obtained from the planetary radiation balance equation:

$$NET = S_o(1 - \alpha) - IR. \quad (5.1)$$

In Equation 5.1, NET is the net radiation, $S_o(1 - \alpha)$ the absorbed solar radiation, and IR the total outgoing infrared radiation. The contribution of the overcast and cloud-free portions of the sky to the total planetary albedo, α , can be written:

$$\alpha = (1 - A_c)\alpha_d + A_c\alpha_c, \quad (5.2)$$

in which α_d and α_c are respectively the clear-sky and overcast albedos, and A_c the cloud fraction. Similarly, the total (clear plus overcast) outgoing infrared radiation can be separated between the radiation emitted from the overcast and cloud-free regions:

$$IR = (1 - A_c)IR_d + A_cIR_c, \quad (5.3)$$

in which IR_d and IR_c are respectively the clear-sky and cloudy outgoing infrared radiation. After manipulations, Equations 5.2 and 5.3 can be rewritten:

$$\alpha = \alpha_d - CS_T, \quad (5.4)$$

and

$$IR = IR_d - CL_T. \quad (5.5)$$

CS_T and CL_T are respectively the cloud shortwave and cloud longwave radiative forcings which are obtained from the relations:

$$CS_T = \alpha_d - \alpha, \quad (5.6)$$

and

$$CL_T = IR_d - IR. \quad (5.7)$$

By substituting Equations 5.6 and 5.7 into Equation 5.1, we obtain:

$$NET = [S_o(1 - \alpha_d) - IR_d] + [S_oCS_T + CL_T], \quad (5.8)$$

or

$$NET = NET_d + [S_oCS_T + CL_T]. \quad (5.9)$$

In Equation 5.9, the first right-hand side member is the net radiation for completely cloud-free conditions while the second right-hand side member is the total impact of clouds on the net radiation. On the one hand, α is usually greater than α_{cl} , except above snow/ice covered surfaces, so that CS_T is generally negative. The presence of clouds decreases the amount of absorbed solar radiation and the albedo of clouds yields an overall cooling of the earth's climate. On the other hand, at long wavelengths, clouds act as a lid by reducing the thermal emission of the atmosphere and the earth's surface, but their contribution to the greenhouse warming considerably varies with the cloud-top temperature or cloud-top height, as well as the cloud emissivity and cloud amount. However, CL_T is positive in most cases, and the longwave effect of clouds generally enhances the tropospheric warming. Both CS_T^{\dagger} and CL_T show important variations at regional scales.

In Equations 5.6 and 5.7, the total and clear-sky fluxes are measured by an on-board satellite scanner or wide field-of-view instruments. CS_T and CL_T are comprised of the direct radiative effect of clouds, plus the contribution of embedded feedback mechanisms between the moisture field, temperature lapse rate, and cloudiness, especially at infrared wavelengths. The most important difficulty in estimating the radiative forcing of clouds from satellite-borne measurements comes from the determination of the clear-sky fluxes. α_{cl} and IR_{cl} can be obtained from scanner data by selecting pixels corresponding to the largest outgoing infrared radiation and lowest planetary albedo values. Ramanathan (1987) discusses the limitations of using this threshold method and the uncertainty of the clear-sky flux estimates due to spatial inhomogeneities within the pixel or completely overcast conditions. Ellis (1978) conducted one of the first studies in which clear-sky albedo and outgoing infrared radiation were derived from WFOV satellite observations. The data set, described in Ellis and Vonder Haar (1976), combines radiation budget measurements taken by the Nimbus-3 satellite for four semi-monthly periods along with a 29-month composite of measurements from six polar orbiting satellites between July 1964 and May 1971. Clear-sky fluxes are obtained by selecting grid-areas corresponding to combined estimates of minimum albedo and maximum outgoing infrared radiation values from 7-day

time series. The annually- and globally-averaged cloud effect in net flux is found to be equal to -20 Wm^{-2} and shows important seasonal, hemispheric, and land-ocean contrasts.

Similarly, Equations 5.6 and 5.7 can be used to derive the cloud radiative forcing in GCM climate simulations for which α_{cl} and IR_{cl} are computed for identical surface and atmospheric conditions as α and IR , but without clouds. In the next sections, the cloud radiative forcing of long and short wavelengths generated with CCM1, including its temporal variability, is analyzed for Northern Hemisphere winter conditions.

5.3.2 Longwave forcing

Figure 5.9 shows the global distribution of the seasonal average (CL_T) and standard deviation ($\sigma(CL_T)$) of the total cloud longwave radiative forcing. CL_T is positive everywhere because clouds obstruct radiation below the cloud base while emitting radiation at a colder cloud-top temperature than the underlying atmosphere or the surface. Below the cloud base, clouds enhance the warming of the atmosphere and the earth's surface by increasing downward longwave radiation back to the surface. The greenhouse effect of clouds is somewhat proportional to the temperature difference between the cloud-top and surface temperatures. Tropical convective clouds and associated extended cirrus anvils are, therefore, more efficient to warm the earth-atmosphere system and the earth's surface than middle latitude frontal clouds. As a result, CL_T is greater in the tropical than in the middle latitudes. The standard deviation of the cloud longwave radiative forcing shows identical global patterns and magnitude as that of the total outgoing infrared radiation. In particular, areas of high (respectively low) values of $\sigma(CL_T)$ superimpose very well with areas of high (respectively low) values of CL_T .

The radiative impacts of clouds in the atmosphere and at the earth's surface can be independently studied. The cloud radiative forcing of the surface is obtained as in Equation 5.7 by computing the difference between the clear-sky and cloudy net longwave surface fluxes. The cloud radiative forcing of the atmosphere is computed as a residual by taking the difference between the cloud forcing at the top of the atmosphere and at the earth's surface. Figure 5.10 shows the global distribution of the seasonal average (CL_S) and

standard deviation ($\sigma(\text{CL}_S)$) of the cloud radiative forcing of the surface. Figure 5.11 shows the global distribution of the seasonal average (CL_A) and standard deviation ($\sigma(\text{CL}_A)$) of the cloud radiative forcing of the atmosphere. The comparison between Figures 5.10 and 5.11 shows that the partition between the longwave cloud forcing of the surface and the atmosphere varies with the cloud height. CL_S is positive over the whole globe because clouds increase downward longwave radiation below the cloud base, therefore warming the earth's surface. CL_S is greater at high than at low latitudes because middle latitude frontal clouds have a greater potential for surface warming than tropical convective clouds due to their warmer cloud base temperatures. In addition, the lower troposphere is not as opaque as in the tropics which yields an enhanced contrast between cloudy and clear-sky conditions. CL_A is negative everywhere, except above the tropical convective activity regions. On the one hand, tropical convective clouds and associated cirrus anvils are more efficient at reducing the loss of outgoing infrared radiation because of their cold cloud top temperatures, than they are at increasing downward radiation because of the small difference between the cloud base and clear-sky emission in the upper troposphere. On the other hand, extratropical clouds are more efficient at increasing downward radiation because of their warm cloud base temperatures, than they are at reducing atmospheric and ground thermal emission because of the small difference between the cloud top and surface temperatures. As for CL_T , there is a direct correspondence between areas of high (respectively low) values of CL_S or CL_A and areas of high (respectively low) values of $\sigma(\text{CL}_S)$ or $\sigma(\text{CL}_A)$. Our results are identical as those presented by Slingo and Slingo (1988), in which the effects of the forcing of tropical and extratropical clouds on the atmospheric general circulation are discussed from a 510-day run of the NCAR CCM for perpetual January conditions.

Figure 5.12 shows the zonally-averaged distribution of the seasonal average and standard deviation of the cloud longwave radiative forcing at the top of the atmosphere, of the surface, and the atmosphere. The standard deviation of the clear-sky outgoing infrared radiation (IR_{cl}) is added to the bottom figure. The latitudinal profiles of CL_S and CL_A

clearly show the partition of the radiative effect of tropical and extratropical clouds between the atmosphere and the surface. $\sigma(\text{CL}_T)$ has a similar distribution as $\sigma(\text{IR})$, with a maximum above the seasonal position of the ITCZ and decreasing amplitude towards the poles. The difference between the two profiles corresponds to the standard deviation of the clear-sky outgoing infrared radiation arising from fluctuations in the temperature and moisture fields. In contrast to the standard deviation of the radiation components corresponding to cloudy conditions, the zonal averages of $\sigma(\text{IR}_{cl})$ never exceed 15 Wm^{-2} . From this comparison, it is obvious that clouds drive the temporal variability of the total outgoing infrared radiation.

5.3.3 Shortwave forcing

The comparison between the model-generated absorbed solar radiation and the satellite-observed radiation field, in Chapter Four, outlined serious difficulties in the parameterization of the shortwave radiative transfer in CCM1. Therefore, we would expect to see major discrepancies in the simulated cloud shortwave radiative forcing if we were to compare it against that derived from satellite measurements. In the following paragraphs, we focus our analysis on the impact of clouds on the temporal variability of the cloud radiative forcing in the model only.

Figure 5.13 shows the global distribution of the seasonal average (CS_T) and standard deviation ($\sigma(\text{CS}_T)$) of the total cloud shortwave radiative forcing. As at long wavelengths, the impact of clouds in the atmosphere and at the surface can be independently analyzed. Figure 5.14 shows the global distribution of the seasonal average (CS_S) and standard deviation ($\sigma(\text{CS}_S)$) of the cloud radiative forcing of the surface. Figure 5.15 shows the global distribution of the seasonal average (CS_A) and standard deviation ($\sigma(\text{CS}_A)$) of the cloud radiative forcing of the atmosphere. Clouds reduce the amount of solar radiation absorbed in the atmosphere and at the earth's surface, so that CS_T is negative over the whole globe. The cloud forcing is maximum over the middle latitudes in the Southern Hemisphere where both the incident solar radiation and the cloudiness are large. In the absence of clouds, the troposphere is practically transparent to solar radiation, so

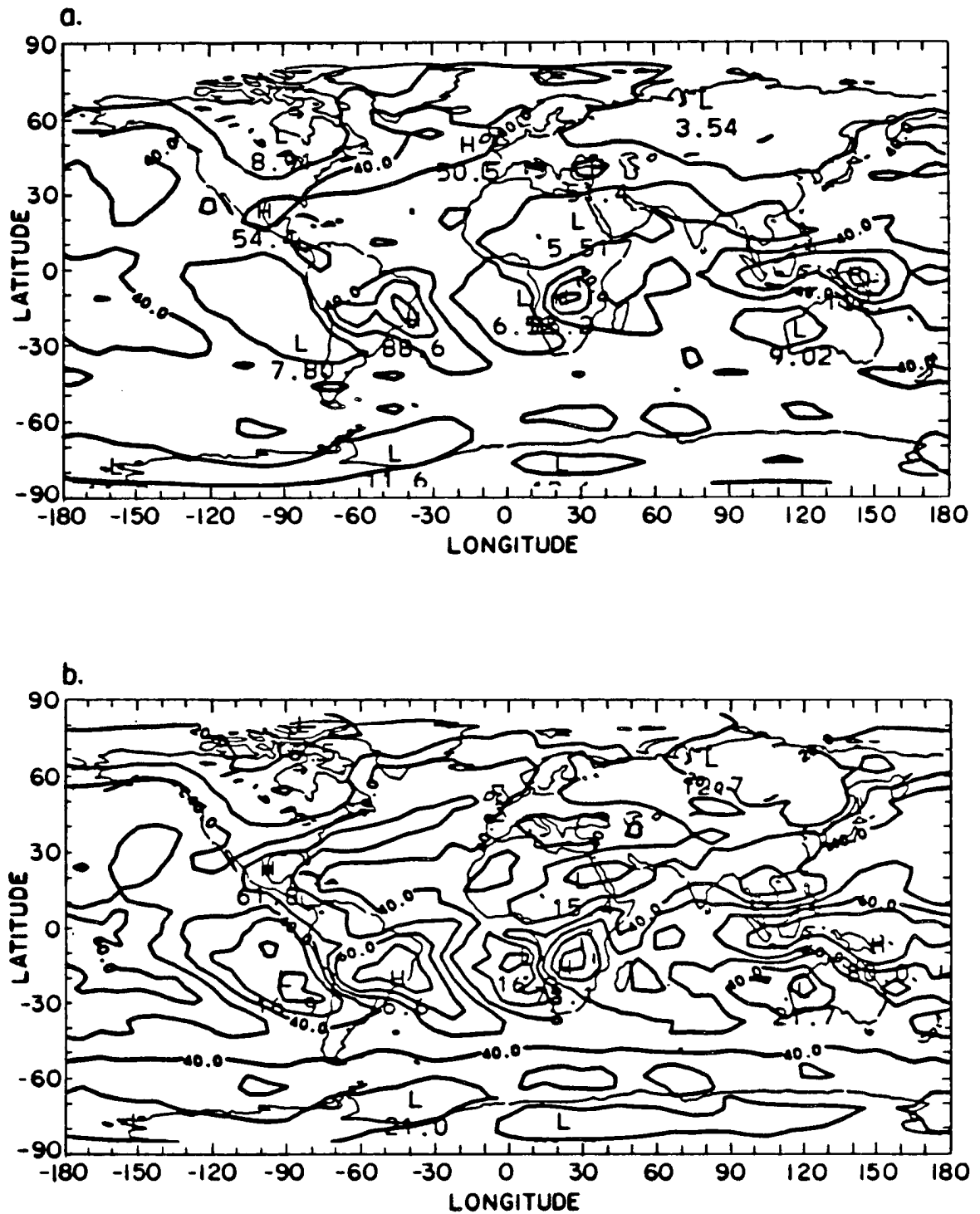


Figure 5.9: Map of the total cloud longwave radiative forcing for Northern Hemisphere winter (Wm^{-2}): (a) distribution of the seasonal average, and (b) distribution of the standard deviation.

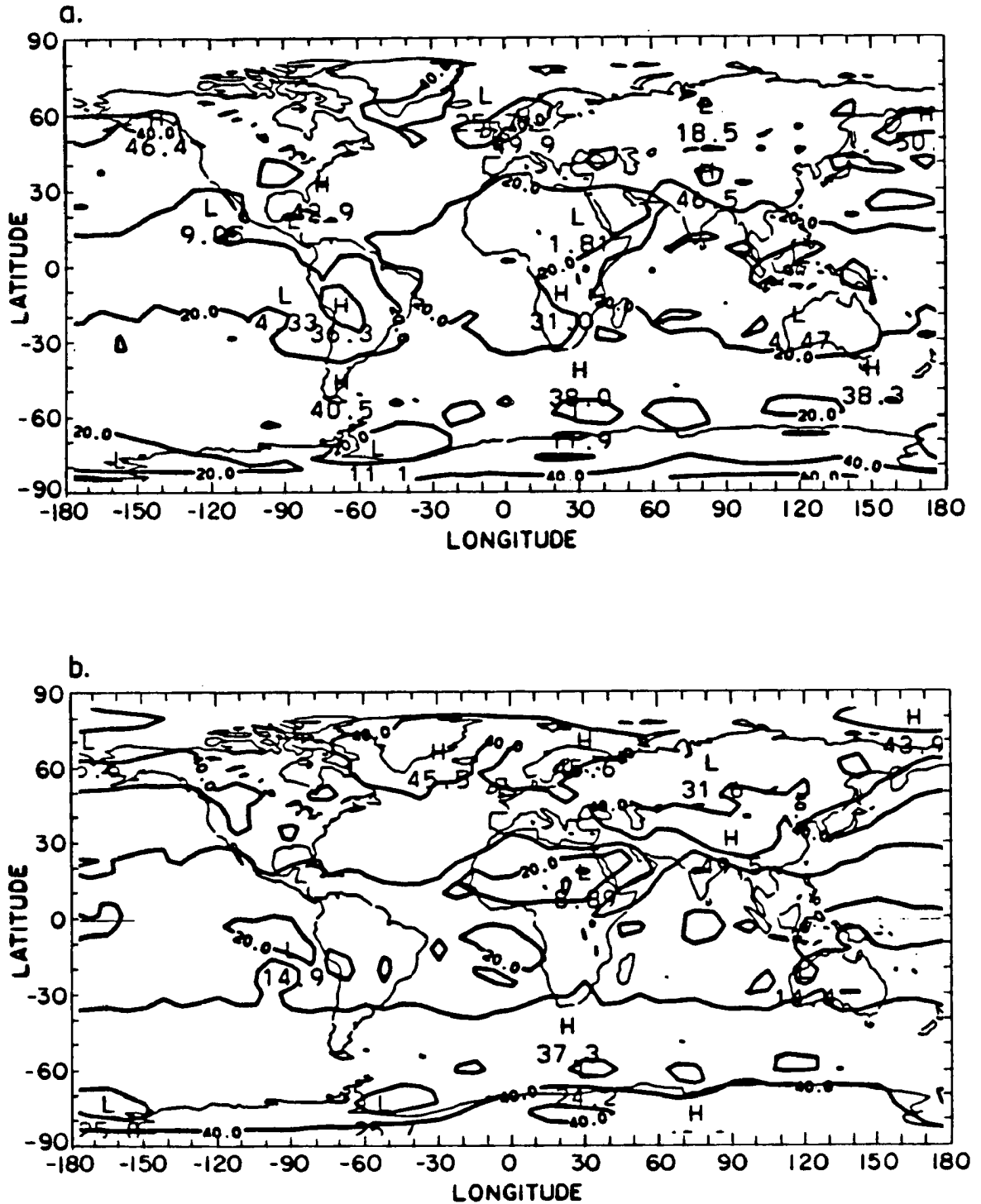


Figure 5.10: Map of the cloud longwave radiative forcing of the surface for Northern Hemisphere winter (Wm^{-2}): (a) distribution of the seasonal average, and (b) distribution of the standard deviation.

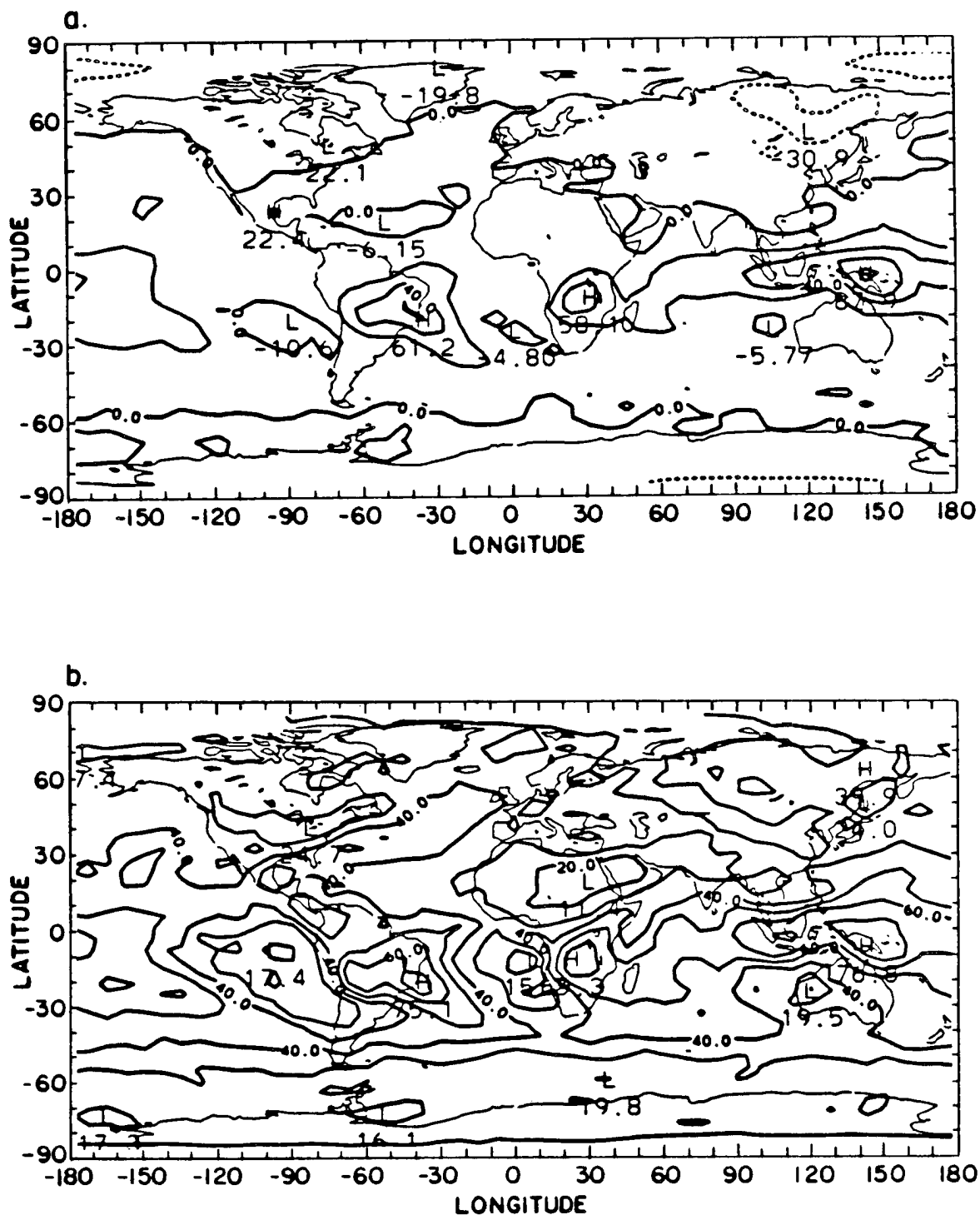


Figure 5.11: Map of the cloud longwave radiative forcing of the atmosphere for Northern Hemisphere winter (Wm^{-2}): (a) distribution of the seasonal average, and (b) distribution of the standard deviation.

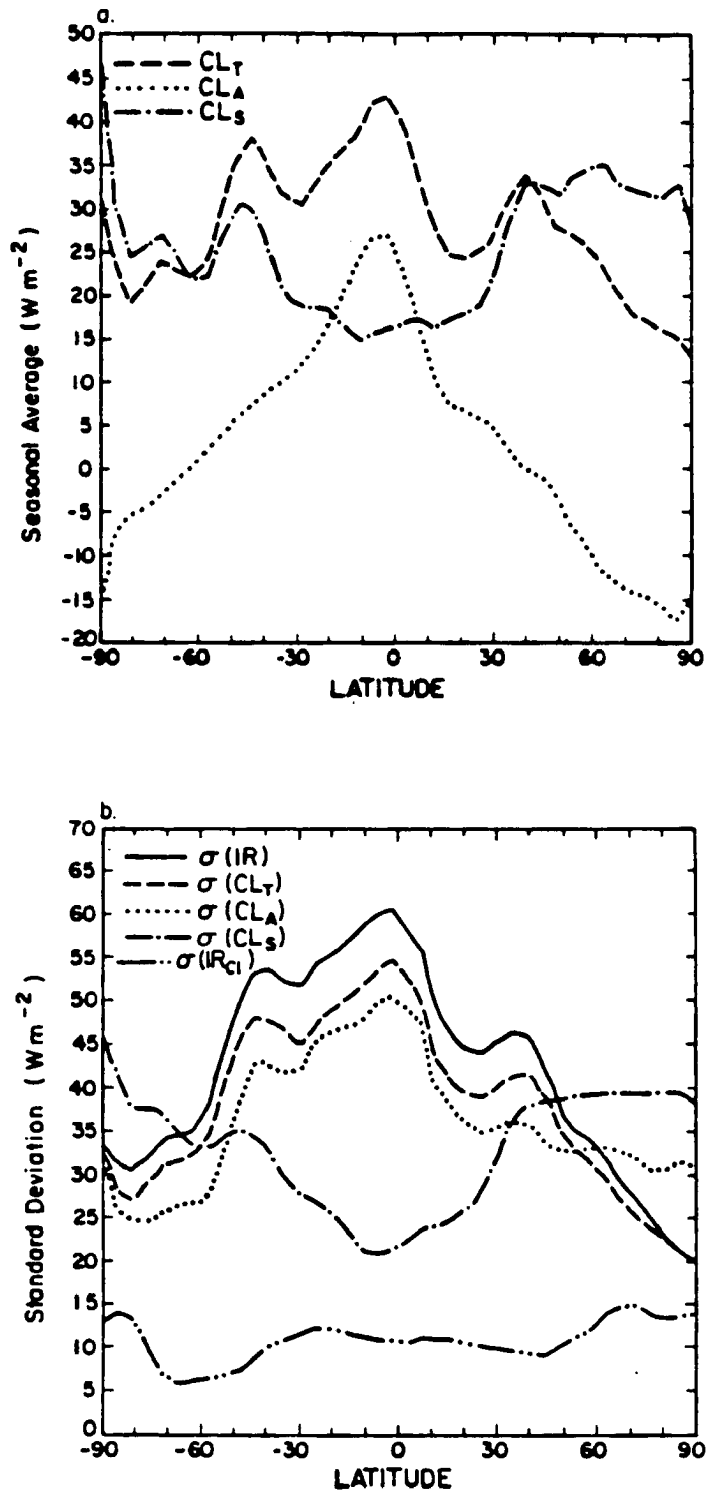


Figure 5.12: Zonally-averaged distribution of the cloud longwave radiative forcing for Northern Hemisphere winter (Wm^{-2}): (a) distribution of the seasonal average, and (b) distribution of the standard deviation.

that the shortwave effect of clouds primarily affects the earth's surface rather than the atmosphere. This is very well seen between the seasonally-averaged distributions of CS_S and CS_A . Finally, the global distributions of $\sigma(CS_T)$ and $\sigma(CS_S)$ resemble very closely that of $\sigma(ABS)$, which, as at long wavelengths, corroborates the primary impact of clouds on the temporal variability of the radiation budget.

Figure 5.16 shows the zonally-averaged distribution of the seasonal average and standard deviation of the cloud shortwave radiative forcing at the top of the atmosphere, of the surface, and the atmosphere. The standard deviation of the clear-sky absorbed solar radiation (ABS_{cl}) is added to the bottom figure and primarily results from the seasonal cycle of the insolation, especially over the middle and high latitudes. In contrast to the forcing at the top of the atmosphere and at the surface, the zonally-averaged cloud radiative forcing of the atmosphere, including its temporal variability, has a small latitudinal dependence and does not exceed -10 Wm^{-2} . On the other hand, the zonal averages of $\sigma(CS_T)$ and $\sigma(CS_S)$ have an equal magnitude and explain most of the variability in the total absorbed solar radiation.

5.3.4 Conclusion

Extended validations of the global and zonally-averaged distributions of the simulated cloud longwave and shortwave radiative forcings will be possible, in the immediate future, from combined estimates of the total and clear-sky radiation fluxes from the ERBE experiment. Table 5.1 provides global averages of the various quantities discussed in the above sections. The net radiative effect of the total cloud cover is equal to -20.4 Wm^{-2} , corresponding to an overall cooling of the earth-atmosphere system by the albedo effect. Analyses of the standard deviation of the clear-sky and cloudy radiation components prove that the variability of the planetary radiation balance is almost exclusively driven by fluctuations in the total cloudiness. They further support our earlier hypothesis that unrealistic cloud-life cycles generated in CCM1 are, indeed, responsible for the blinking of the model atmosphere.

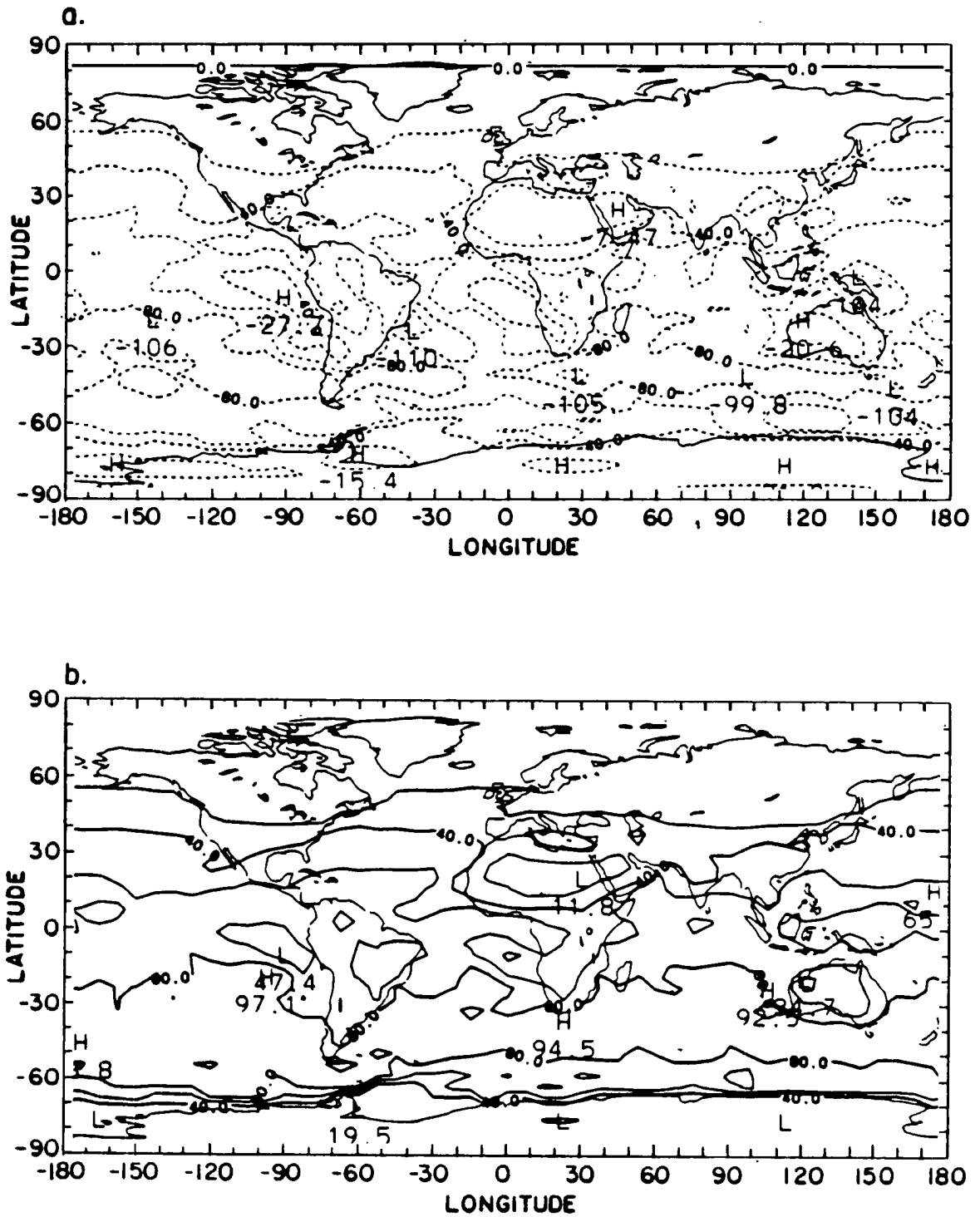


Figure 5.13: Map of the total cloud shortwave radiative forcing for Northern Hemisphere winter (Wm^{-2}): (a) distribution of the seasonal average, and (b) distribution of the standard deviation.

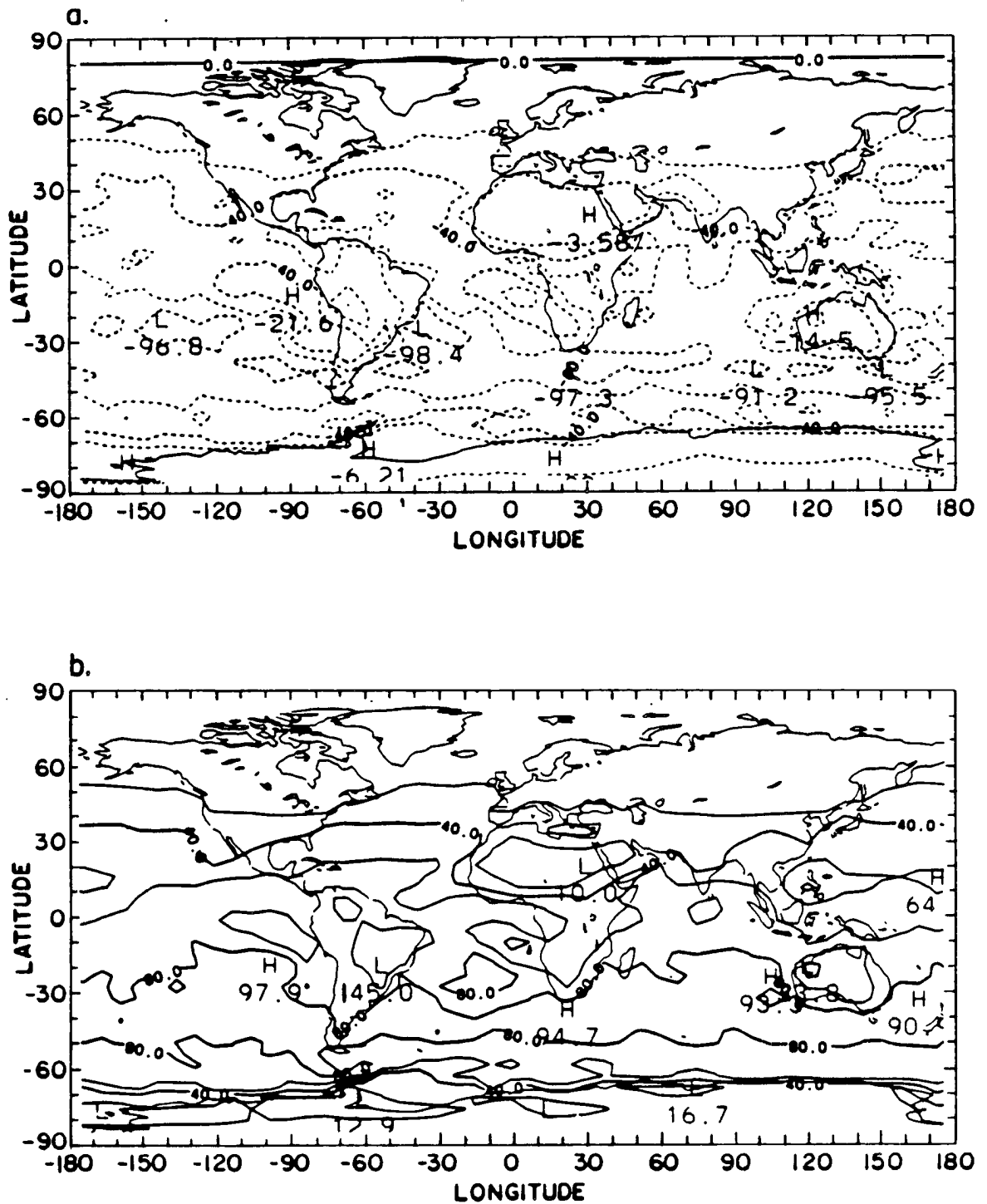


Figure 5.14: Map of the cloud shortwave radiative forcing of the surface for Northern Hemisphere winter (Wm^{-2}): (a) distribution of the seasonal average, and (b) distribution of the standard deviation.

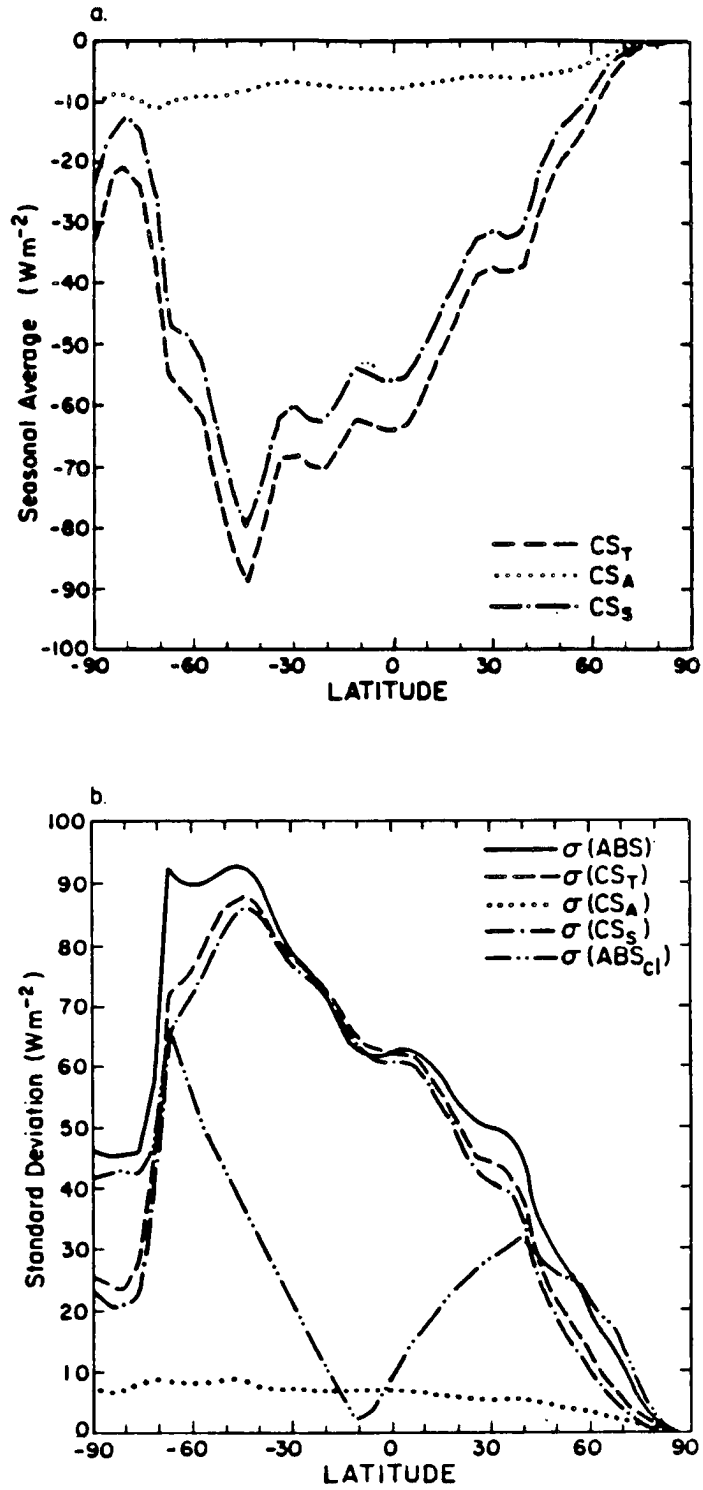


Figure 5.16: Zonally-averaged distribution of the cloud shortwave radiative forcing for Northern Hemisphere winter (Wm^{-2}): (a) distribution of the seasonal average, and (b) distribution of the standard deviation.

5.4 Cloud-Atmosphere interactions

5.4.1 Origins of the interactions

Arakawa (1975) clearly summarizes the multiple interactions between clouds and the various physical processes in the atmospheric general circulation. They are:

1. The coupling of dynamical and hydrological processes through the heat of condensation and vaporization (evaporation), and the redistribution of heat and momentum.
2. The coupling of radiative and dynamical-hydrological processes through the reflection, absorption, and emission of radiation.
3. The coupling of hydrological processes in the atmosphere and at the surface through precipitation.
4. The coupling between the atmosphere and ground through modification of the radiative and turbulent transfer at the surface.

A complete simulation of these different couplings in physically-based climate models requires an explicit calculation of the cloud liquid water content which, at the present time, is ignored in most general circulation models. Its inclusion as a prognostic variable to the parameterization of the interactions listed above would yield major improvements in general circulation modeling for it allows:

1. That the radiative properties of clouds at short and long wavelengths can be explicitly related to this parameter. The albedo of clouds can, then, be expressed as a function of the cloud optical depth τ instead of being prescribed as a function of the cloud height:

$$\tau = \frac{3}{2} \cdot \frac{LWC}{\rho r_e}, \quad (5.10)$$

in which LWC is the cloud liquid water content, ρ the water density, and r_e the effective radius of the cloud droplets. At infrared wavelengths, the cloud emissivity can, then, follow the relation derived by Stephens (1978) or Griffith (1980):

Table 5.1

Table 5.1: Globally-averaged cloud radiative forcing at the top of the atmosphere (TOA), of the surface (SFC), and of the atmosphere (ATM), computed from the model-generated radiation fields for Northern Hemisphere winter.

A. Longwave radiative forcing (Wm^{-2}):	Seasonal average	Standard deviation
TOA cloudy outgoing infrared	240.0	46.9
TOA clear-sky outgoing infrared	270.5	10.5
Total cloud forcing	30.5	42.1
SFC cloudy net outgoing infrared	71.1	36.5
SFC clear-sky net outgoing infrared	94.2	14.4
Cloud forcing of the surface	23.1	30.3
ATM cloudy outgoing infrared	168.9	42.7
ATM clear-sky outgoing infrared	176.3	13.6
Cloud forcing of the atmosphere	7.4	38.9
B. Shortwave radiative forcing (Wm^{-2}):	Seasonal average	Standard deviation
TOA cloudy absorbed solar	248.1	59.5
TOA clear-sky absorbed solar	299.0	23.2
Total cloud forcing	-50.9	54.3
SFC cloudy absorbed solar	191.3	57.3
SFC clear-sky absorbed solar	235.2	19.7
Cloud forcing of the surface	-43.9	52.4
ATM cloudy absorbed solar	56.8	7.8
ATM clear-sky absorbed solar	63.8	6.0
Cloud forcing of the atmosphere	-7.0	6.0

$$\epsilon_c = 1 - \exp(-k LWC), \quad (5.11)$$

in which k is the wavelength integrated coefficient. Finally, the cloud fraction can be expressed by the ratio:

$$A_c = \frac{RH - RH_c}{RH_s - RH_c}, \quad (5.12)$$

in which RH_s and RH_c are the supersaturation relative humidity and prescribed value at which condensation is allowed to start. In this case, clouds may form before supersaturation conditions occur. The change in the relative humidity (RH) depends upon the cooling rates due to evaporation of cloud droplets and raindrops, and moisture flux convergence.

2. The partition between precipitating (rain and large ice crystals) and non-precipitating (cloud droplets and small ice crystals) components which, in turn, provides the potential to improve model precipitating amounts.
3. To induce physically-based life-cycles for convective and non-convective clouds. The liquid water content can be retained in the atmosphere and mixed through horizontal motions or turned into precipitation. This process simulates the advection, or the creation and destruction of clouds at a model grid-point. This has major implications as far as the modelization of the life-times of extended cirrus anvils above convective activity regions and advection of cloud debris are concerned.

A model for non-convective condensation processes including prediction of the cloud water content for possible use in large-scale dynamical model is discussed in Sundqvist (1978). The model equations include not only release of latent heat and precipitation but also of cloud mass. Details of the condensation processes (formation of cloud droplets, growth to rain drops, and evaporation from drops) are also parameterized. Results show the model's ability to simulate reasonable evolution times and water content of clouds, as well as to give reasonable precipitation amounts. However, the disadvantage of using similar schemes in three-dimensional climate modeling are their computational expensive cost and the difficulty to verify the adequacy of the results due to limited availability of liquid water content data.

5.4.2 Interactions in the NCAR CCM

In contrast to the real atmosphere, the NCAR CCM presents severe limitations in the simulation of the interactions between clouds, and the radiative, dynamic, and hydrologic processes taking place in the atmosphere and at the earth's surface.

There is no explicit prediction of the liquid water content and it is implicitly assumed that the sub-grid scale condensation is part of larger-scale condensation regimes associated with synoptic-scale weather events. Clouds form whenever the relative humidity exceeds 100 % and the cloud fraction is fixed to an arbitrary value depending upon the cloud type. The cloud albedo is prescribed as a function of the cloud height and albedo feedback mechanisms between clouds and radiation are neglected. As a result, the only direct interaction of clouds is the modification of the vertical distribution of the radiative heating and cooling rates, while the coupling between clouds and the dynamic-hydrologic processes remain limited to radiatively-induced changes in the temperature field.

The adiabatic adjustment scheme for dry and moist convective adjustments, and for large-scale condensation, follows the parameterization of Manabe *et al.* (1965). The scheme particularly implies that all the water condensed in the atmosphere falls instantaneously as precipitation to the to the ground. The temperature and specific humidity fields are simultaneously corrected, and the atmosphere is forced to be just saturated by removing the excess moisture. As no horizontal advection of liquid water is permitted, the redistribution of the equivalent water mass back into the atmosphere, takes place through release of latent heat at the surface.

In view of the reduced interactions between clouds and the thermodynamic processes, resulting from the non-inclusion of the liquid water as a prognostic variable and from the treatment of condensation as a complete rainout process, it is clear that cloud life-cycles cannot be realistically simulated in the model. Such model deficiency becomes obvious in looking at time series of the total cloud cover for individual model grid-points and overlapping satellite grid-areas. Figures 5.17 and 5.18 show two examples of such time

series selected, in the Pacific Ocean above the ITCZ and the winter storm track region. Every 12-hour model-predicted and satellite-derived estimate of the total cloud cover is plotted. There are absolutely no resemblance between model and observations. To respect the moist adiabatic adjustment scheme, model clouds precipitate and are recomputed every time-steps. As the occurrence of clouds depends upon an arbitrary supersaturation threshold of the relative humidity, a slight increase in the moisture field may radically change the atmosphere from clear-sky to completely overcast conditions. As a result, and considering that the cloud fraction at individual σ -level can only take four different values (0., 30., 95., or 100. %), the total cloud amount may abruptly change from 0. to 100. % over a 12-hour time lapse. Time series of the total cloud fraction at single σ -level actually show identical 12-hour jump between 0. and 100. %. Analyses of the time series of the cloud cover explain the fast decorrelation of the model-generated cloud fields. Therefore, it is clearly justified to say that the blinking of the atmosphere simulated with CCM1 has to be attributed to the high frequency of on and off occurrence of clouds which results from non-realistic parameterization of their life-cycles.

5.5 Sensitivity experiments with the NCAR CCM

Independent analyses of the total cloud cover predicted with CCM1 against estimates derived from satellite radiance measurements, and of the temporal variability of the cloud radiative forcings at infrared and solar wavelengths, strongly support our hypothesis that clouds are responsible for the factor of two difference in the standard deviation of the model-generated radiation fields. In view of the limitations in the cloud prediction scheme and in the treatment of the interactions between clouds and the radiative, dynamic, and hydrologic processes, we suspect that an arbitrary cloud/no cloud threshold based upon the relative humidity only, or a complete rainout process, produce the unnatural flicker of the model-generated cloudiness. We propose to investigate these two hypotheses in two different simulations of climate made with CCM1 for perpetual January conditions.

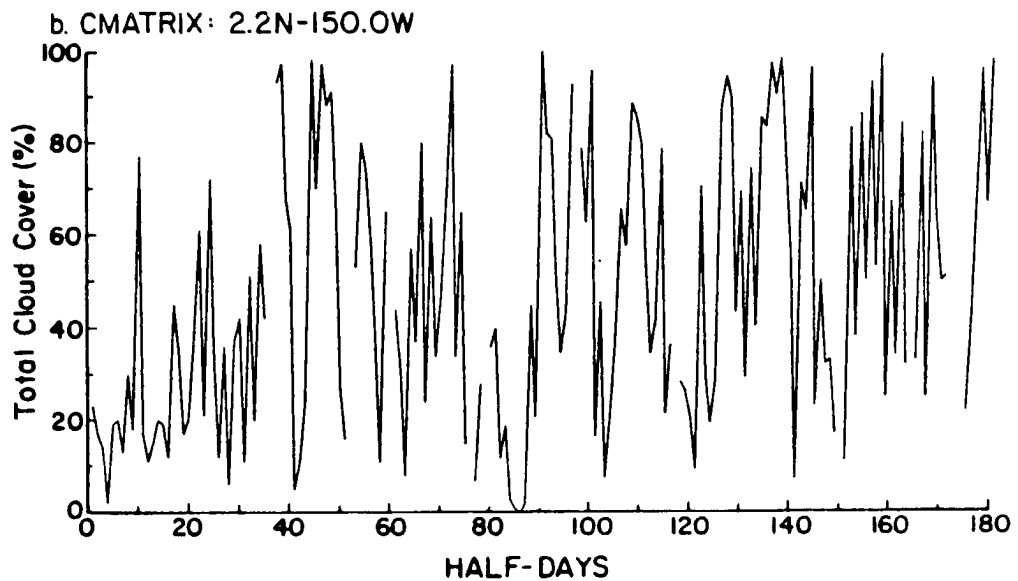
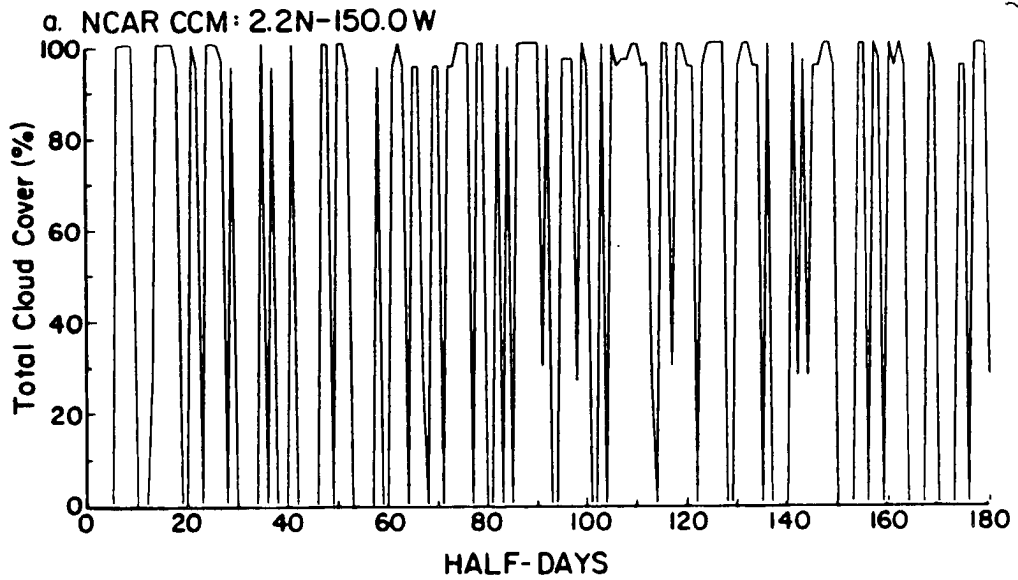


Figure 5.17: Time series of the total cloud cover at a single grid-point located at 2.2°N-150.0°W, for Northern Hemisphere winter (%): (a) predicted with the NCAR CCM and, (b) derived from satellite radiances (CMATRIX).

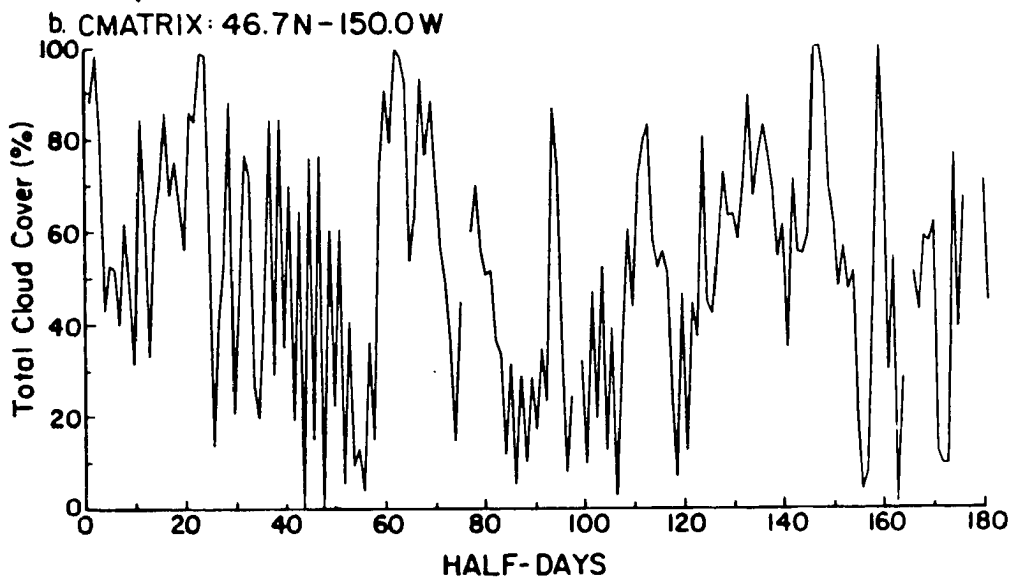
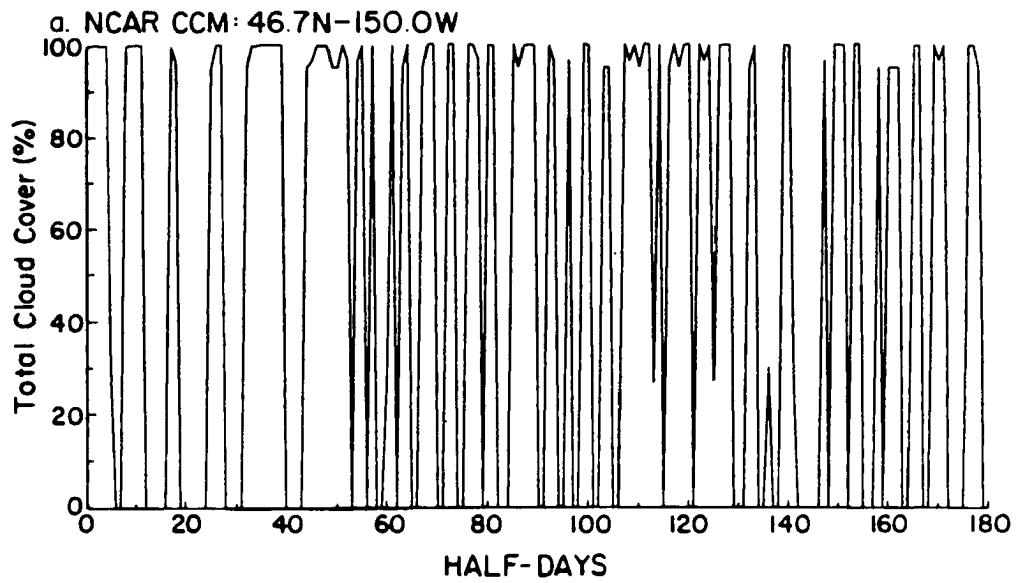


Figure 5.18: Time series of the total cloud cover at a single grid-point located at 46.7°N - 150.0°W , for Northern Hemisphere winter (%): (a) predicted with the NCAR CCM, and (b) derived from satellite radiances (CMATRIX).

5.5.1 Impact of the cloud/no cloud threshold assumption

In the cloud prediction scheme, clouds are assigned single prescribed values (95 % cloudiness for large-scale clouds and 30 % cloudiness for convective clouds) once supersaturated conditions are reached. The supersaturation relative humidity is fixed to 100 %. This particularly implies that condensation occurs in and clouds fill the complete grid-square. In the real atmosphere and few limited-areas cloud models, condensation starts and clouds actually form before the relative humidity has reached a 100 %, allowing for sub-grid scale cloud cover. It is evident that the prescription of arbitrary cloud fractions describing two kinds of clouds only, will fail to realistically reproduce the distribution of the cloud cover, and especially its temporal variability.

We want to test the sensitivity of the NCAR CCM to an alternate cloud prediction scheme which would allow for a wider range of cloud amounts with the aim to: 1) To show that the use of a different scheme in CCM1, in which the formation of clouds primarily depends upon some large-scale synoptic fields and their tendencies, will not reduce the blinking of the model-generated radiation fields on a global scale; and 2) To infer that the treatment of the sub-grid scale interactions between clouds and the hydrologic cycle is more important to improve than the prediction of the actual total cloud cover. The response of the planetary radiation budget to the distribution of the cloudiness, with an emphasis on its temporal variability, is analyzed from a 510-day simulation in which the CONTROL cloud prediction scheme has been replaced by an adapted version of that routinely used in the general circulation forecast model of the European Centre for Medium Range Weather Forecast (ECMWF). The chief differences between the ECMWF and CONTROL climate Experiments are extensively discussed in Chapter Six.

5.5.2 Impact of the rainout process assumption

The nature of the possible interactions between clouds and the hydrologic cycle is constrained by the moist convective and large-scale condensation adjustment schemes. It is particularly unrealistic to assume that all the condensed water has to be automatically removed from the atmosphere and that clouds precipitate every 12-hour time-step. The

actual solution of an improved partition between advection, evaporation, and precipitation is the inclusion of the liquid water as a prognostic variable in GCM simulated climate. In the near future, increased measurements from space-borne microwave instruments should help understand the global distribution of liquid water content in relation with the cloud field and provide improved relationships between liquid water and cloud amount. However, and as a first attempt to reduce the blinking of the model-generated cloudiness, it would be interesting to analyze the model sensitivity when the atmosphere is forced to hold more moisture than actually allowed by the adjustment schemes. What would be the response of the model-simulated general circulation if only a fraction of the condensed water produced by the large-scale condensation scheme fell to the ground while the remaining fraction was reevaporated and added back into the moisture field? What is the importance of producing more realistic cloud life-cycles and improved temporal variability in the radiation fields in GCM simulations, for climate sensitivity experiments and studies of climate changes? In Chapter Seven, the sensitivity of CCM1 to a reduced large-scale precipitation rate is analyzed with an emphasis on the induced modifications in the general circulation of the model atmosphere.

5.6 Summary

In this Chapter, we formally demonstrated that unrealistic simulations of cloud life-cycles in CCM1 did explain the on and off blinking of the model-generated components of the planetary radiation budget. Separate analyses of the temporal variability of the total cloud cover and the cloud radiative forcings corroborated this assumption. They further suggested that the cloud prediction scheme, and the treatment of the interactions between clouds and the physical processes, could be held responsible for the various discrepancies between model and observations. Finally, we selected two experiments with primary objectives to help define the directions which should be taken towards an improved model performance, and decide the importance of correctly reproducing the temporal variability of the atmosphere in GCM-based climate research.

Chapter 6

INFLUENCE OF THE ECMWF CLOUD PREDICTION SCHEME ON THE MODEL-GENERATED RADIATION FIELDS

6.1 Introduction

In Chapter Five, analyses of the radiative forcing of clouds at long and short wavelengths showed that its temporal variability was as large as that of the total outgoing infrared and absorbed solar radiation. It was concluded that the cloud prediction scheme and/or the treatment of the interactions between clouds, radiation, and the other physical processes in the model were responsible for the factor of two difference between the variability of the model-generated and satellite-observed radiation balance components. In the model, clouds form if the relative humidity exceeds a 100 % supersaturation threshold and are assigned arbitrary values depending on their cloud type. The moist adiabatic adjustment treats condensation as a rainout process and clouds are recomputed at each model time-step. As a result, the frequency of occurrence of clouds depends upon instantaneous fluctuations of the specific humidity around the supersaturation level. This particularly implies that, between two time-steps, atmospheric conditions in a model grid-square can change from cloud-free to completely overcast. We know that this assumption is physically not correct, for in the real atmosphere, condensation starts and clouds form before the relative humidity reaches 100 %.

The primary objective of this chapter is to analyze the influence of a cloud prediction scheme, different than that originally used in CCM1, on the variability of the model-generated radiation fields while the treatment of the interactions between clouds, radiation, and the hydrologic processes remain unchanged. In particular, we want to show that any

scheme, based on the prediction of cloud amounts in term of some large-scale parameters only, cannot correctly reproduce the life-cycle of clouds which depends upon sub-grid scale motions. We indirectly verify this hypothesis by analyzing changes in the variability of the radiation balance components induced by changes in the distribution of the cloud cover. Although clouds are also predicted as functions of the large-scale synoptic fields, the alternate cloud scheme distinguishes between four different cloud types and the cloud amount varies with the relative humidity.

The parameterization of clouds described in Chapter Three (and later referred as CONTROL scheme) is replaced by an adapted version of the cloud prediction scheme operationally implemented in the forecast model of the European Centre for Medium Range Weather Forecast (later referred as ECMWF scheme). The basic frame of this alternate cloud scheme is identical to that routinely used in the ECMWF general circulation model and follows the configuration originally proposed by Slingo (1980). The response of the NCAR CCM to the cloud prediction equations, as well as to different convection schemes, is discussed in Slingo and Slingo (1988). The sensitivity of the time-variability of the radiation balance components to the distribution of cloudiness is analyzed from a 510-day simulation for perpetual January conditions. Ensemble averages of the monthly average and standard deviation of the climate variables are obtained from a set of five independent time-span realizations, following the method described in Appendix B. Table 6.1 gives a list of the days and corresponding *History Tapes* used to simulate mean January conditions in the CONTROL and ECMWF climate experiments.

6.2 Description of the ECMWF cloud prediction scheme

The cloud prediction equations are derived from GATE data (Slingo, 1980) and further revised by Slingo (1987). The complete development of the fractional cloud cover scheme and a limited validation of the global distribution of the cloudiness using retrieved observations from Nimbus-7 can be found in that article. The original cloud scheme was adjusted to the CCM code and allows four different cloud types which have been given the

names convective (cumulus, cumulonimbus), high (cirrus), middle (altostratus, altocumulus) and low (stratus, stratocumulus) clouds. Figure 6.1 gives a schematic illustration of the vertical cloud distribution and the division into high-, middle-, low-level clouds.

6.2.1 Convective clouds

The convective cloud cover (A_C) is computed from the time-averaged precipitation rate (P) obtained from the model's convection scheme:

$$A_C = a + b \ln P \quad (6.1)$$

in which a and b are empirical constants. The convective cloud base and cloud top are obtained from the convection scheme. A_C cannot exceed 80% based on results from GATE data (Slingo, 1980). In the case of deep convection, only 25% of the predicted cloud amount is allowed to occupy the full depth of the convective column, the remaining 75% being treated as low-level shallow convection.

6.2.2 High-level clouds

The scheme distinguishes between two different types of high-level clouds (A_H).

- Cirrus associated with outflow from deep convection:

$$A_H = 2.0(A_C - 0.3), \quad (6.2)$$

if the convection extends above 400 mb and the convective cloud fraction is greater than 40%.

- Cirrus associated with extratropical and frontal disturbances. A_H is a function of the large-scale relative humidity (RH):

$$A_H = \left[\text{Max}\left(0.0, \frac{RH - 0.9}{0.2}\right) \right]^2 \quad (6.3)$$

in which 90% is chosen as the threshold relative humidity for supersaturation to start.

6.2.3 Middle-level clouds

Middle-level clouds (A_M) mainly form in association with tropical disturbances and extratropical frontal systems:

$$A_M = \left[\text{Max} \left(0.0, \frac{RH_e - 0.8}{0.2} \right) \right]^2, \quad (6.4)$$

in which

$$RH_e = RH(1.0 - A_C). \quad (6.5)$$

In equation 6.5, RH_e is the relative humidity of the layer after adjustment for the presence of convective clouds.

6.2.4 Low-level clouds

Low-level clouds (A_L) are classed into two categories; those associated with tropical disturbances and extratropical fronts, and those associated with the planetary boundary-layer.

- First class: They are parameterized using the relative humidity and vertical velocity (ω) fields.

$$A'_L = \left[\text{Max} \left(0.0, \frac{RH_e - 0.9}{0.2} \right) \right]^2, \quad (6.6)$$

and

$$\begin{aligned} A_L &= 0.0 && \text{if } \omega \geq 0.0 \\ A_L &= A'_L(-10\omega) && \text{if } \omega \geq -0.1 \\ A_L &= A'_L && \text{otherwise.} \end{aligned} \quad (6.7)$$

- Second class: They are associated with low-level inversions in temperature and humidity. They are parameterized using the potential temperature lapse rate ($\frac{\Delta\theta}{\Delta p}$) in the most stable layer below 750 mb. An additional dependence on the relative humidity at the base of the inversion (RH_{base}) has been introduced to prevent clouds forming under dry inversions as over deserts and in the winter pole.

$$A'_L = -16.67 \frac{\Delta\theta}{\Delta p} - 1.167 \quad (6.8)$$

and

$$\begin{aligned} A_L &= 0.0 && \text{if } RH_{base} < 0.6 \\ A_L &= A'_L \left(1.0 - \frac{0.8 - RH_{base}}{0.2}\right) && \text{for } 0.6 \leq RH_{base} \leq 0.8 \\ A_L &= A'_L && \text{otherwise.} \end{aligned} \quad (6.9)$$

6.2.5 Discussion

This cloud prediction scheme has been implemented operationally in the ECMWF medium range forecast model in May 1985 and, although derived from observations only, has been providing a reasonable prediction of cloudiness and some benefits for the forecast as a whole (Slingo, 1987). It is, by far, more complicated than that routinely used in the NCAR CCM. In contrast to the cloud prediction scheme in the CONTROL simulation, the ECMWF scheme includes an empirical relationship between convective clouds and associated cloud anvils, and the rainfall rate. Instead of being an instantaneous value based upon the supersaturation threshold at a specific time-step, the convective cloud amount is determined from the precipitation rate averaged over the 12 hours prior to a call to the cloud and radiation routines. The fraction of cirrus clouds associated with outflow from deep convection depends linearly upon the convective cloud amount. Above heavy tropical rainfall regions, for which these two cloud types are simultaneously observed, we can expect an increased cloudiness with slower fluctuations in time than in the CONTROL run. For clouds predicted upon a supersaturation threshold, the cloud fraction is computed as a quadratic function of the relative humidity instead of being assigned one specific value. Finally, the last major difference with the CONTROL scheme is the inclusion of the vertical velocity and potential temperature lapse rate in the determination of the low-level clouds. Analyses of the cloud radiative forcings will show that both parameterizations produce different distributions of the time-averaged radiation fields without, however, modifying substantially their temporal variability.

6.3 Distribution of the ECMWF cloud types

In addition of being available at all σ -levels, the ECMWF cloudiness was also stored on the *History Tapes* by cloud types. Analyses of the monthly average and standard deviation, computed from the monthly average, of the convective, high-, middle-, and low-level clouds help explain the differences in the planetary radiation balance between the ECMWF and CONTROL simulations. The global distributions of the four cloud types and the total cloud cover are shown in Figures 6.2 to 6.6. Because of their major impact upon the temporal variability of the cloud longwave and shortwave radiative forcings, we focus our discussion on the distribution of the convective and high-level clouds and their contribution to the fluctuations of the total cloud cover. Figures 6.2 and 6.3 show that convective activity regions in the tropics and the middle latitudes are capped with a high-level cloud shield. This is the result of the linear relationship between the amount of convective and cirrus clouds associated with outflow from deep convection when the convection extends above 400 mb. Although those areas are, with the polar latitudes, the most overcast, they are also characterized by a lesser variability of the total cloud cover than areas which are actually less cloudy. This infers that, whereas in the CONTROL simulation, fluctuations in the total cloud cover do not systematically increase with increasing clouds, but also vary with the cloud type.

A possible explanation is the parameterization of the convective clouds, and consequently, the high-level clouds associated with them, as functions of the time-averaged precipitation rate instead of as prescribed amounts upon instantaneous values of the relative humidity and potential temperature lapse. For areas of high humidity content, the probability to have a precipitation rate accumulated over 12 hours greater than zero, is greater than the probability of the relative humidity to exceed 100% and the potential temperature lapse rate to be unstable at any time-step. The combination of convective clouds forming more often and varying with the averaged precipitation rate diminishes the difference in the cloud fraction computed at a single grid-point between two time-steps. This introduces an increased coupling between clouds and the hydrologic processes than

that produced in the CONTROL simulation. This argument is further supported by considering the map of the monthly average and standard deviation of the high-level clouds. Outside strong convectively active regions, cirrus clouds are associated with extratropical and frontal disturbances. Their formation depends, as in the CONTROL simulation, on a saturation threshold and their fractional area is computed as a quadratic function of the relative humidity. Although the amount of frontal cirrus is less than that of cirrus associated with deep convection, Figure 6.3 shows that their variability also exceeds 40% and has to be attributed from prescribing their probability of occurrence upon an instantaneous value of the relative humidity. The middle- and low-level cloud amounts are prescribed as that of the extratropical and frontal cirrus. Their impact on the total cloud cover is to increase its variability with increasing cloudiness, as shown in Figures 6.4 and 6.5. In the following sections, analyses of the total cloud cover, the longwave and shortwave radiative forcings of clouds, and the earth radiation budget components demonstrate that differences between the ECMWF and CONTROL simulations can be explained in term of the convective and high-level cloud parameterization.

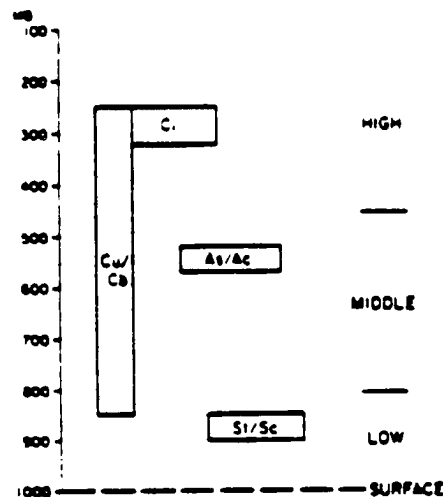


Figure 6.1: Schematic representation of the vertical distribution of clouds in the model and the division into high-, middle-, and low-level clouds (from Slingo, 1987).

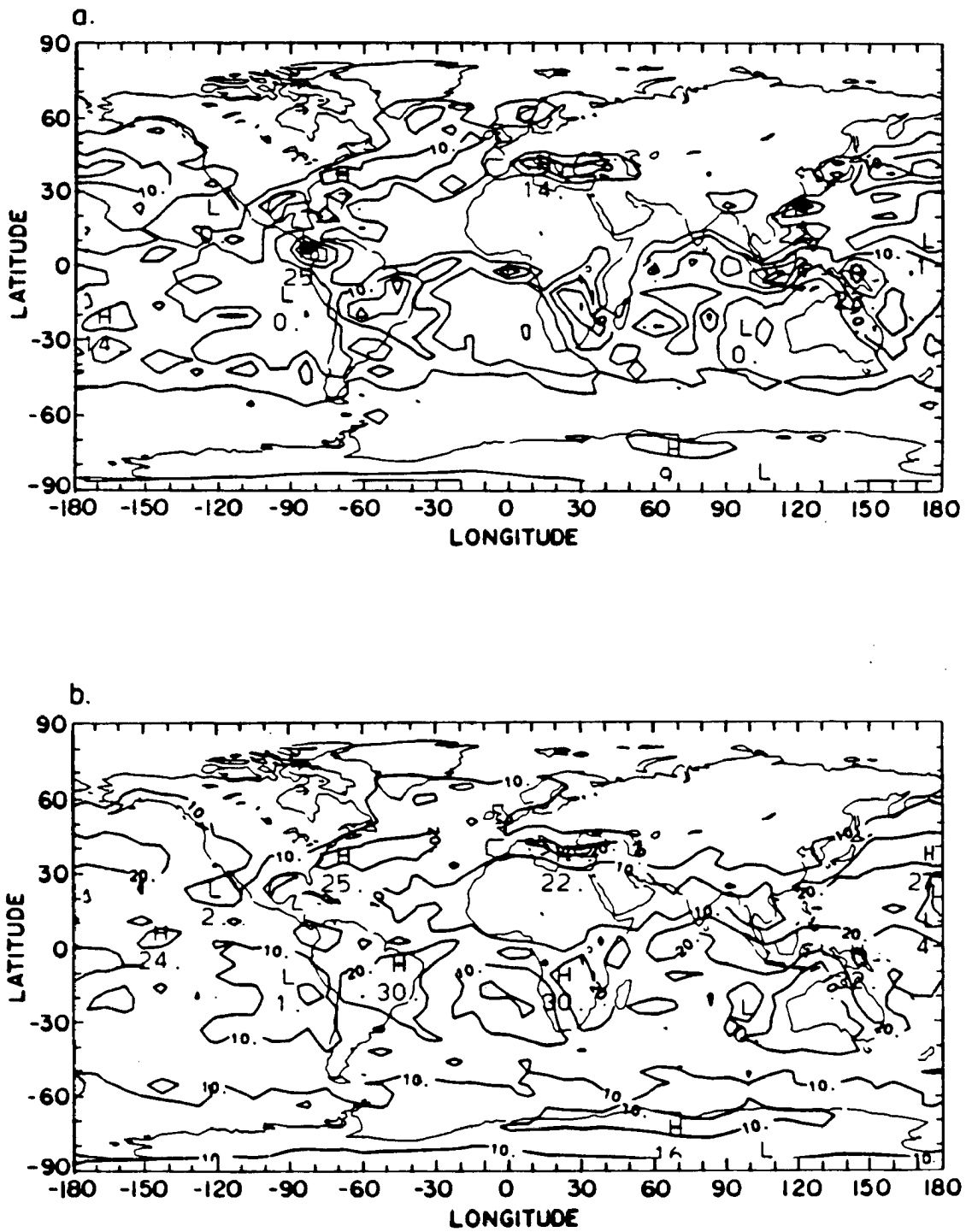


Figure 6.2: Map of the ECMWF convective cloud cover (%): (a) monthly average, and (b) standard deviation.

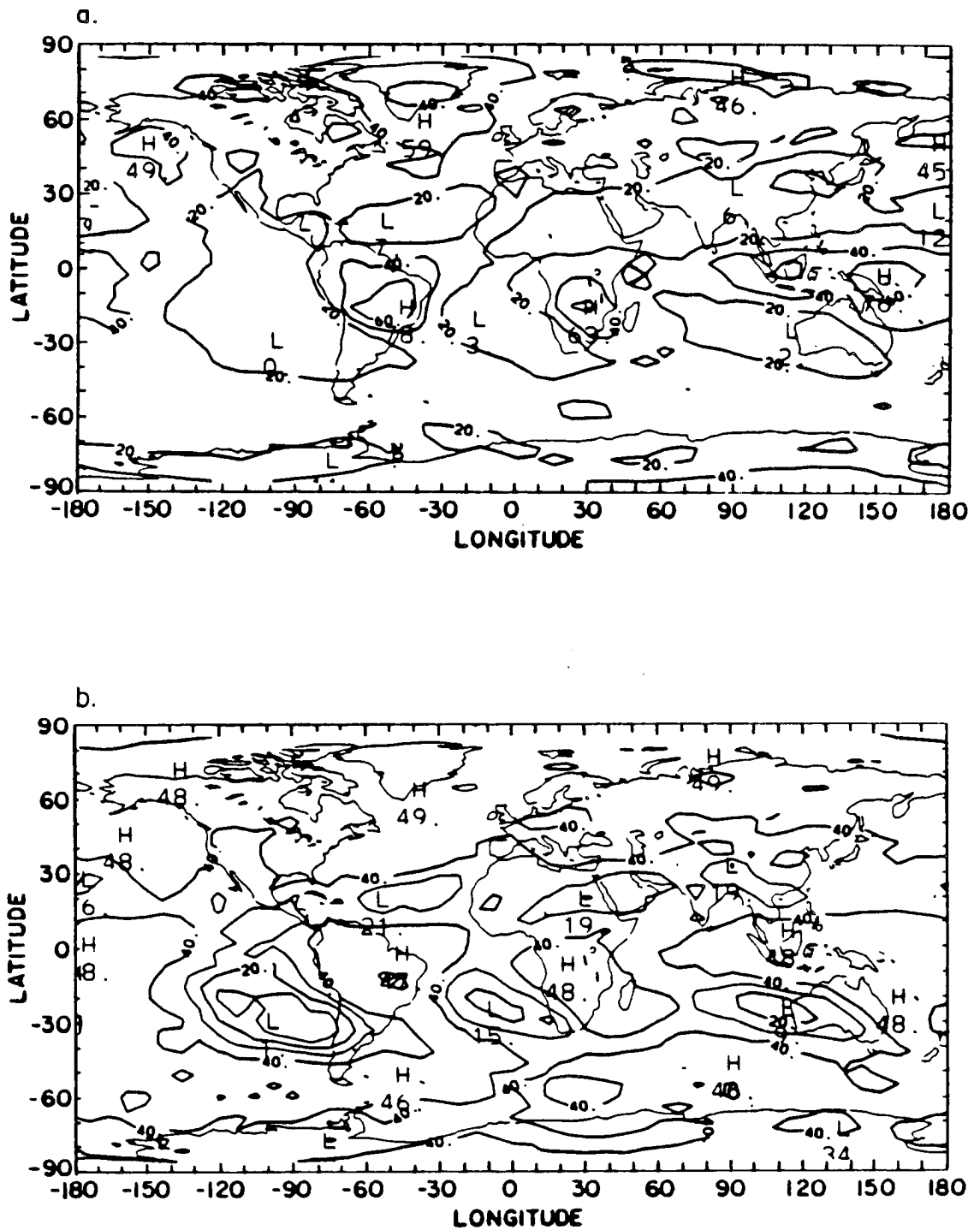


Figure 6.3: Map of the ECMWF high-level cloud cover (%): (a) monthly average, and (b) standard deviation.

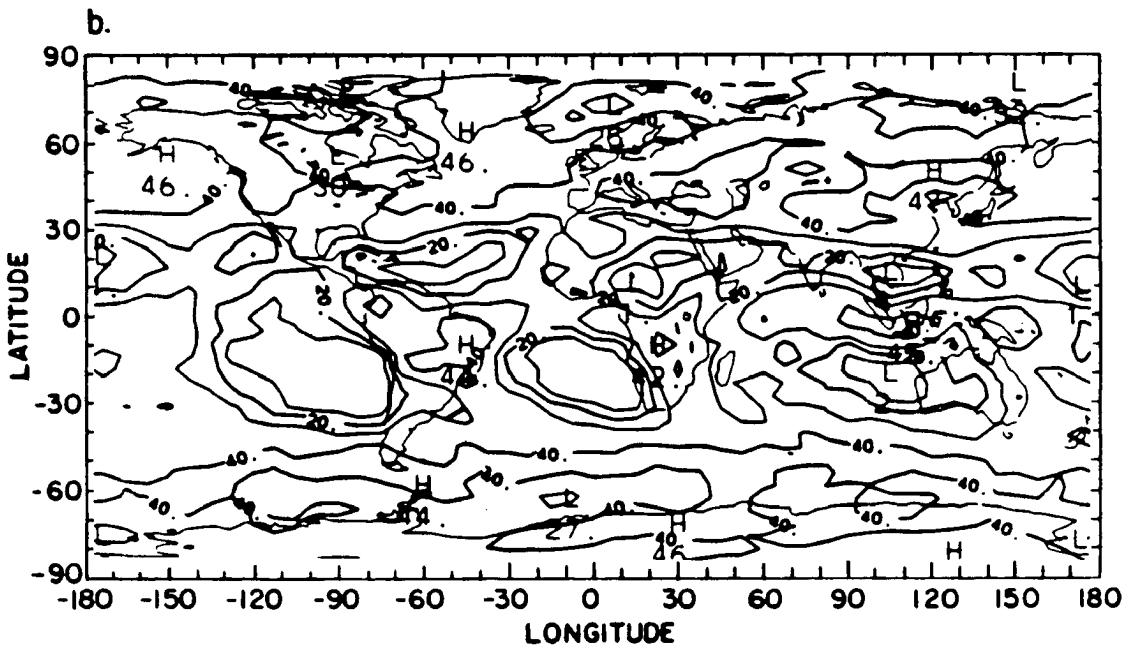
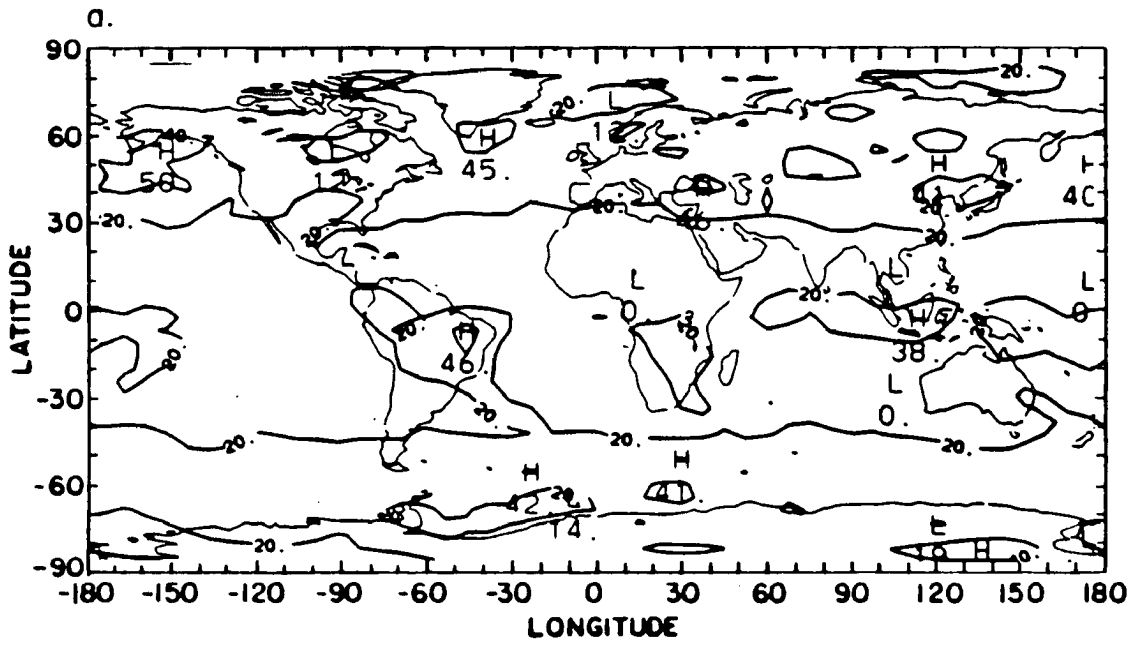


Figure 6.4: Map of the ECMWF middle-level cloud cover (%): (a) monthly average, and (b) standard deviation.

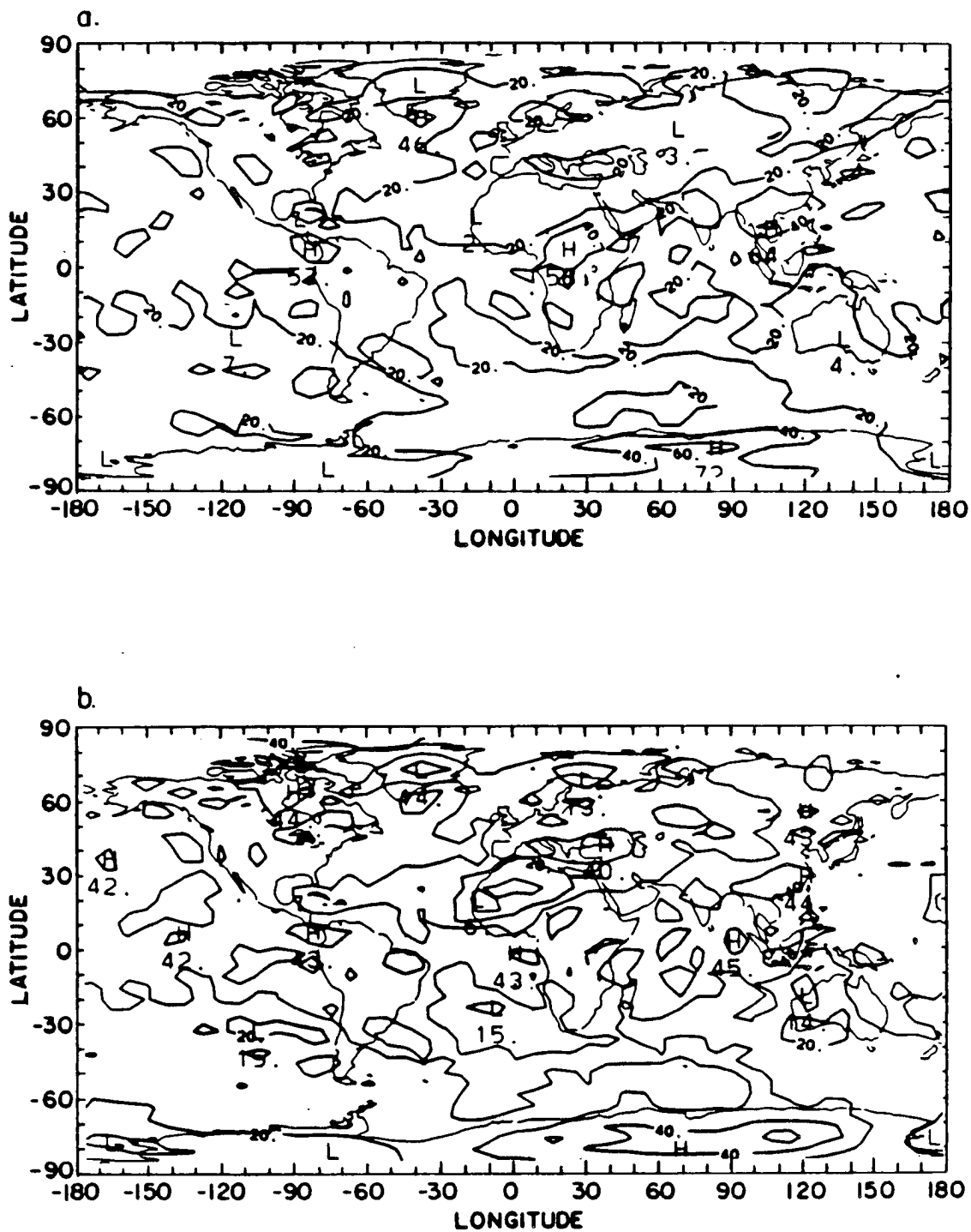


Figure 6.5: Map of the ECMWF low-level cloud cover (%): (a) monthly average, and (b) standard deviation.

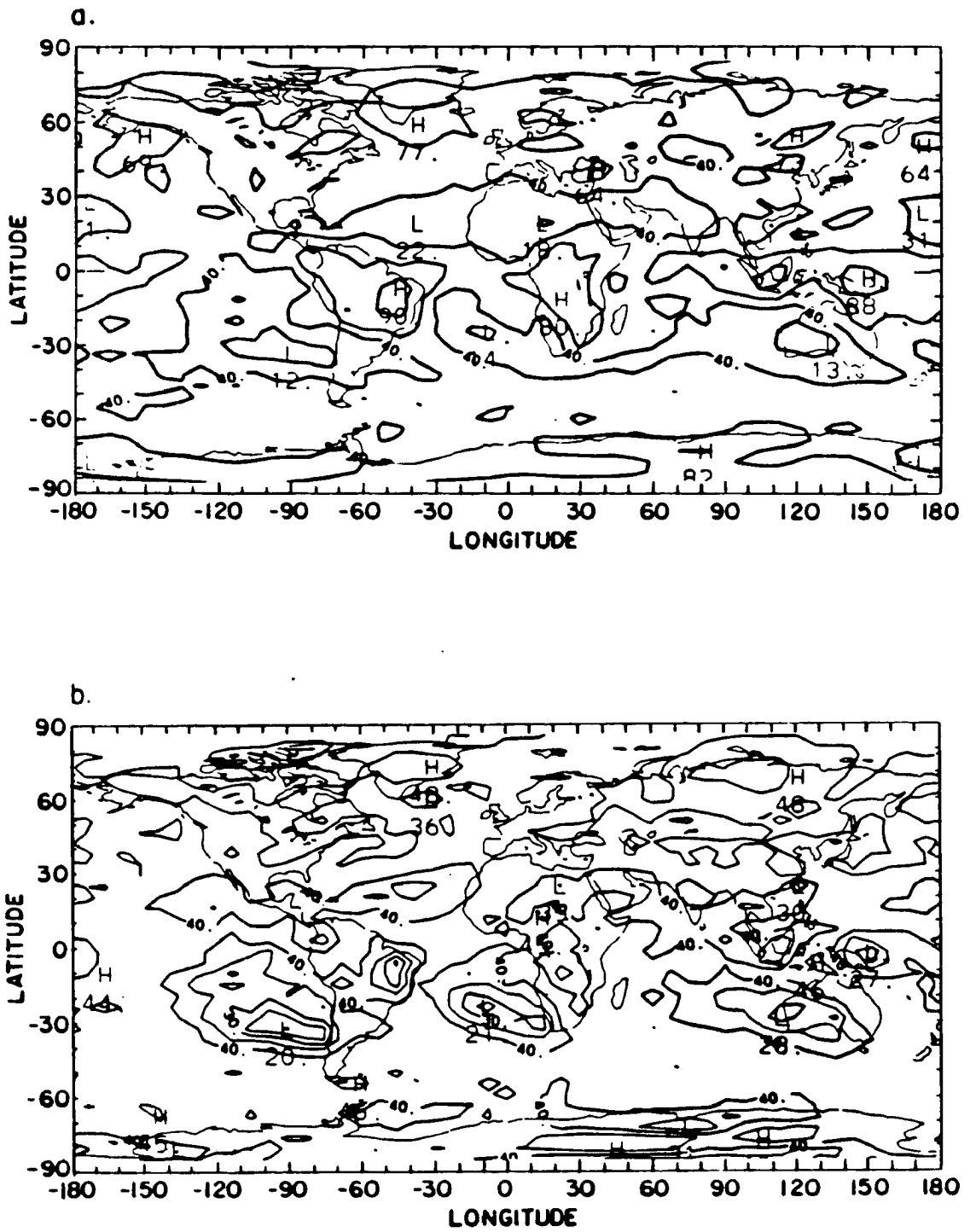


Figure 6.6: Map of the ECMWF total cloud cover (%): (a) monthly average, and (b) standard deviation.

6.4 ECMWF versus CONTROL distribution of the cloud cover

The ECMWF prediction scheme yields specific differences in the temporal and spatial distributions of the cloud cover.

6.4.1 Difference in the time series

Figure 6.7 shows two 90-day time series of the total cloud cover obtained from the CONTROL and ECMWF simulations for single grid-points located at 150°W in the tropics (2.2°N) and the middle latitudes (46.7°N). In the CONTROL run, clouds are assigned fixed values depending on their cloud type. For non-convective clouds, the fractional cloud is assumed to be 95% whereas, for convective clouds, the maximum cloud cover cannot exceed 30%. In the CONTROL simulation, both time series clearly indicate the systematic 12-hour jump of the total cloud cover between clear-sky and overcast conditions. On the other hand, the ECMWF cloud fraction can take a wider range of intermediate values between 0 and 100%, because parameterized as linear (convective clouds and cirrus from convective outflow) or quadratic (low- and middle-level clouds, extratropical and frontal cirrus) functions of the large-scale synoptic fields. Both time series show that the ECMWF total cloud fraction also jumps from 0 to 100%, but that as a whole, does not undergo as large 12-hour oscillations as in the CONTROL case. For both grid-points, the time-averaged total cloud cover computed with the ECMWF prediction scheme is higher than that obtained in the CONTROL simulation and also has a lesser time variability. Figure 6.8 shows the corresponding time series for the outgoing infrared radiation. For both simulations, the outgoing infrared radiation undergoes large 12-hour fluctuations over 90 days. For the selected grid-points, the higher total cloud cover in the ECMWF simulation leads to a decrease in the outgoing infrared radiation equal to 30.1 W m^{-2} at 2.2°N and 10.8 W m^{-2} at 46.7°N. However, although the variability of the total cloudiness in the ECMWF simulation is less than that of the CONTROL run, $\sigma(\text{IR})$ is greater by 4.5 W m^{-2} at 2.2°N which may result from larger 12-hour fluctuations in the temperature and humidity fields. Figure 6.9 shows the corresponding times series for the planetary albedo. As at long wavelengths, the planetary albedo undergoes large 12-hour fluctuations

over a 90-day time period. The increased total cloud cover in the ECMWF run yields an increase in the planetary albedo equal to 0.9 % at 2.2°N and 1.9 % at 46.7°N. The decreased variability of the total cloud cover leads to a decrease in the standard deviation of the planetary albedo for both grid-points. As the troposphere is practically transparent to solar radiation, and the optical properties of clouds and the surface albedo are identically prescribed in both simulations, changes in the standard deviation of the planetary albedo can be directly attributed to the impact of the ECMWF prediction scheme.

6.4.2 Difference in the global distribution

Figure 6.10 presents the geographical distribution of the monthly average and standard deviation, computed from the monthly average, of the total cloud cover obtained from the CONTROL simulation. The total cloud cover exceeds 60 % above the major tropical convective activity regions and the middle-latitude storm track regions over the oceans in the winter hemisphere. Areas of minimum cloud cover are found above the major desert regions over the continents and close to the western coasts of the continents in the summer hemisphere. As already discussed from the comparison between the model-simulated and satellite-observed radiation fields, the cloud prediction scheme routinely implemented in the NCAR CCM fails to simulate the extended and persistent stratiform clouds commonly observed on the eastern sides of the Pacific and Atlantic oceans. As a result, the position of the subtropical anticyclones is too close to the western coasts of the continents in the summer hemisphere. The map of the standard deviation of the total cloud cover shows that its variability exceeds 40 % over most of the globe, except above areas of minimum cloud cover and limited areas which stay mostly overcast over a long time period, as the deep tropical convective activity regions.

Figure 6.11 presents the global distribution of the difference in the monthly average and standard deviation of the total cloud cover between the ECMWF and CONTROL experiments. The ECMWF scheme predicts more clouds over the continents, the polar regions, and the ITCZ over the oceans. It predicts less clouds above the subtropical oceanic regions. In addition, because of the additional parameterization of the low-level clouds associated with the planetary boundary layer using the potential temperature lapse

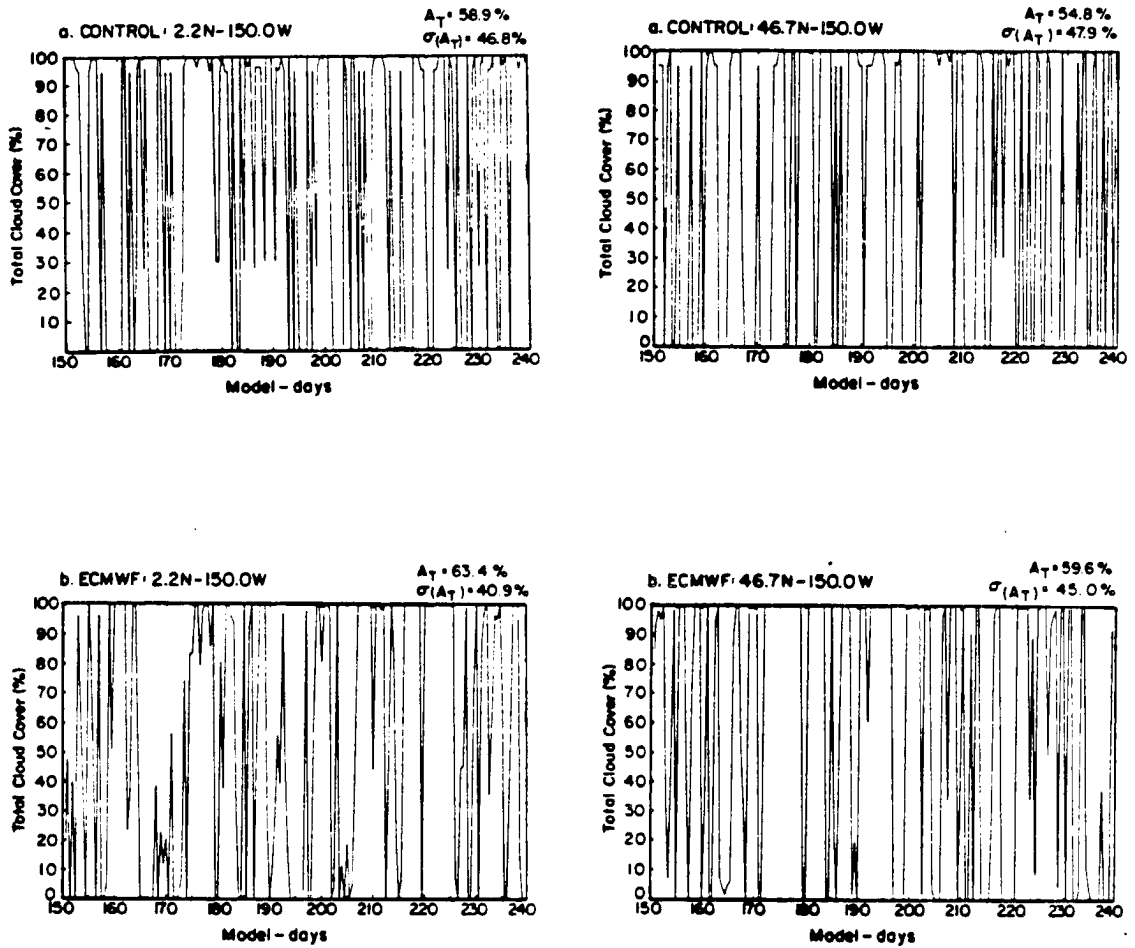


Figure 6.7: 90-day time series of the total cloudiness at a single grid-point located at 2.2°N-150°W and 46.7°N-150°W obtained with (a) the CONTROL, and (b) the ECMWF cloud prediction schemes, for January conditions (%).

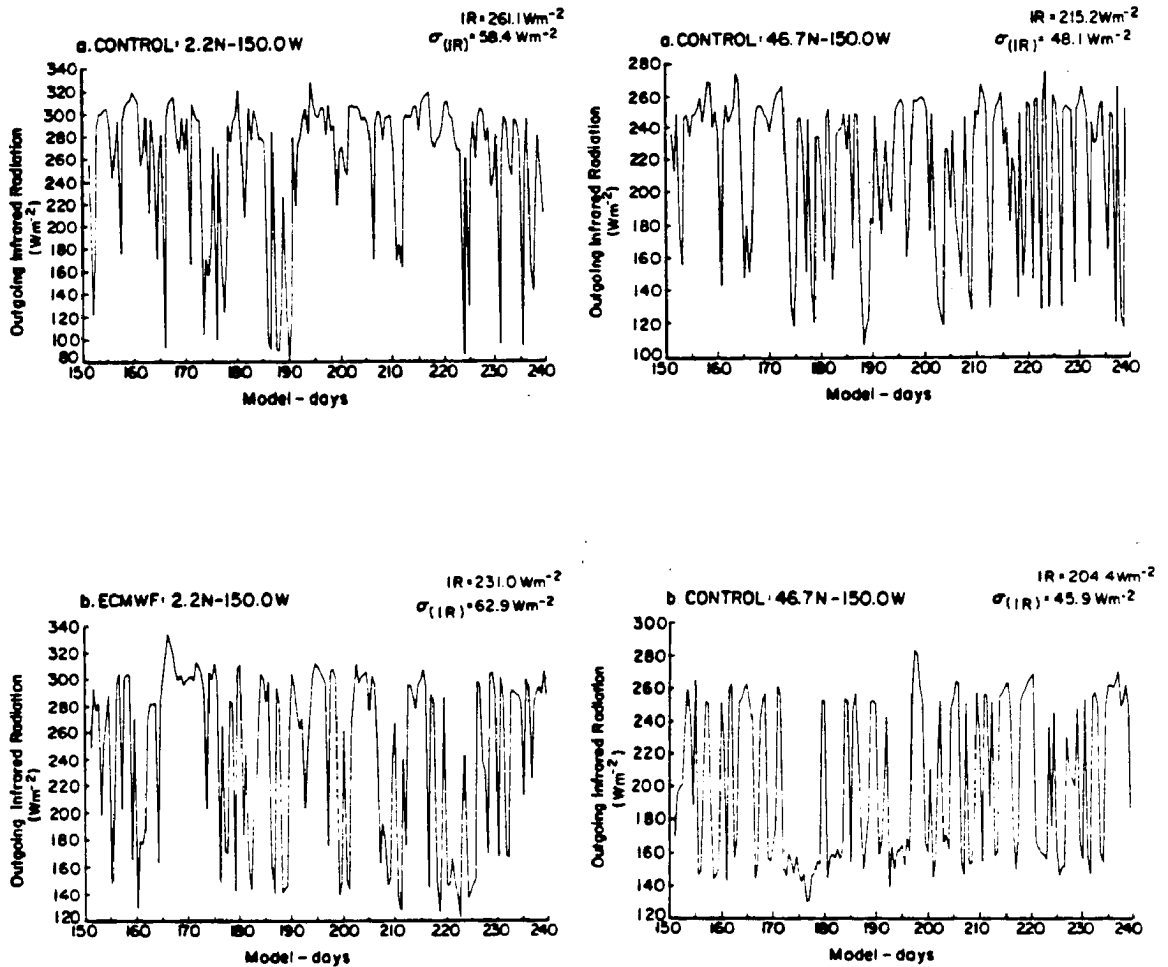


Figure 6.8: 90-day time series of the outgoing infrared radiation at a single grid-point located at 2.2°N-150°W and 46.7°N-150°W obtained with (a) the CONTROL, and (b) the ECMWF cloud prediction schemes, for January conditions (W m⁻²).

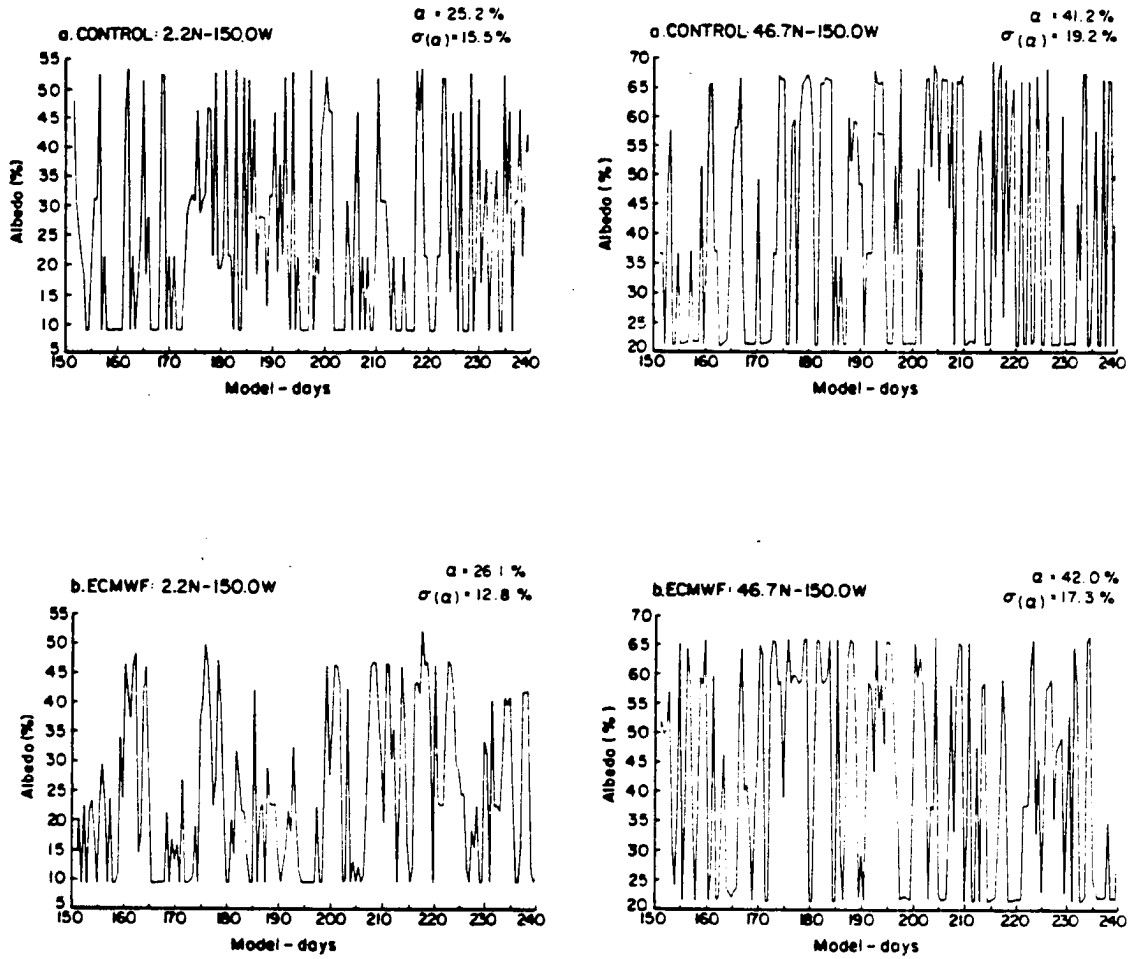


Figure 6.9: 90-day time series of the planetary albedo at a single grid-point located at 2.2°N-150°W and 46.7°N-150°W obtained with (a) the CONTROL, and (b) the ECMWF cloud prediction schemes, for January conditions (%).

rate below 750 mb, the ECMWF produces a more accurate representation of the location of the stratiform clouds along the western sides of the continents. There is a global decrease in the standard deviation of the total cloud cover, especially between 30°N and 30°S, except above the Sahara desert where the ECMWF scheme predicts more clouds than the CONTROL simulation. Map of the standard deviation of the total cloud cover obtained from the ECMWF simulation shows that areas of low variability correspond not only to clear-sky regions, but also to most of the areas dominated by deep tropical convective activity. This feature is not observed at all or strongly diminished for convective activity regions in the CONTROL simulation. The comparison between the ECMWF and CONTROL cloud cover can only be made at individual σ -levels because convective and large-scale condensation clouds are not separately stored in the CONTROL run. Analyses of the difference in the monthly-averaged cloud cover in the successive layers show that the increase in the total cloud cover above the convective activity regions results, in the ECMWF simulation, from an increase in the cloud cover below 355 mb capped by a decrease in cloudiness at higher levels. The decreased cloudiness above 355 mb may result from that the convection does not penetrate the troposphere as high as in the CONTROL simulation or from the linear relationship between the convective and cirrus cloud amounts. In both cases, the decreased cloud cover in the upper troposphere contributes to the decreased variability of the total cloud cover while the increased cloudiness at lower levels has the inverse effect. To explain simultaneously the increase in the total cloud cover and its decreased variability, the only possible solution is to advocate the stabilizing influence of the convective and associated cirrus clouds in the ECMWF simulation. In the middle latitudes, the increased cloud cover is accompanied by a small but positive difference in its variability and results from an augmentation of the cloud fraction at all σ -levels. This result is consistent with the fact that the occurrence of extratropical middle- and high-level clouds depends on a supersaturation threshold in both prediction schemes.

6.4.3 Difference in the vertical distribution

The ECMWF and CONTROL cloud schemes also predict different vertical distribution of clouds. Figure 6.12 shows the latitude-height distribution of the monthly average

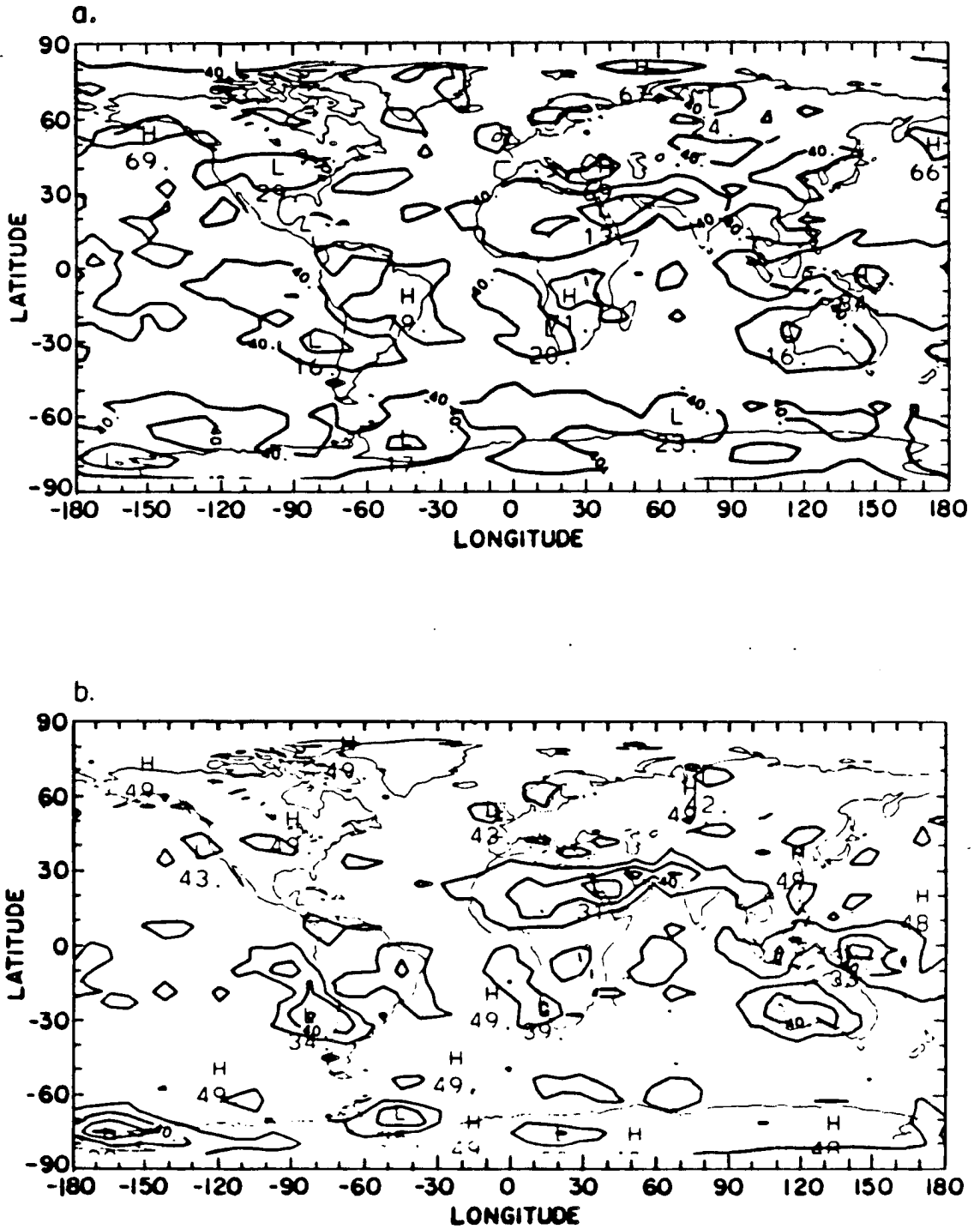


Figure 6.10: Map of the total cloud cover computed from the CONTROL simulation, for January conditions (%): (a) distribution of the monthly average, and (b) distribution of the standard deviation.

and standard deviation of the cloudiness obtained from the CONTROL simulation. The lowest atmospheric layers (below $\sigma = .664$) are completely filled with clouds at almost every latitude whereas the cloud cover is minimum in the middle troposphere ($\sigma = .500$). The height of the cloud envelope follows the decrease of the tropopause level between the equator and the poles. In the middle latitudes, high-level clouds have a cloud-top height around 8 km whereas the maximum convective cloud amount is located above 12 km along the ITCZ. This indicates that the tropopause and the tropospheric layer beneath it serve as a lid to the upward motion which is responsible for the formation of clouds in the upper model troposphere. The latitude-height distribution of the standard deviation is identical to that of the monthly average with high (respectively low) variability associated with large (respectively small) cloud amounts. In addition, there is no dependence between the magnitude of the standard deviation and the height of the cloud layer. Figure 6.13 shows the latitude-height distribution of the difference in the monthly average and standard deviation of the cloudiness between the ECMWF and CONTROL simulations. On a zonal average, the ECMWF scheme predicts less low-level clouds below $\sigma = .664$, more mid-tropospheric clouds, and less high-level clouds above $\sigma = .355$. The difference in the high-level cloud amount arises from that the CONTROL scheme assigns 95 % of cloudiness whenever stable condensation occurs above the convective cloud-top whereas cirrus anvils depend linearly upon the convective cloudiness in the ECMWF simulation. In addition, some modifications were introduced in the moist convective adjustment scheme in the ECMWF simulation which may affect the highest level of convection. There is a direct correspondence between the difference in the time average and standard deviation of the cloudiness between the two simulations. The decrease in the time-averaged cloudiness is accompanied by a decrease in its time variability, and inversely, an increase in the time-averaged cloudiness in the middle troposphere yields an increase in its variability. Finally, Figures 6.14 and 6.15 give examples of the vertical distribution of the cloud cover for several individual grid-points located in the tropics and the middle latitudes. As already seen on a zonal average in Figure 6.12 for the CONTROL experiment, the selected grid-points show a minimum cloudiness in the middle troposphere which is actually more

pronounced in the low than the middle latitudes. In addition, above regions dominated by convective activity, this minimum is located at lower altitude for the grid-points above land because of surface heating effect. On the other hand, the vertical distribution of clouds obtained from the ECMWF simulation is not characterized by this systematic minimum in the middle troposphere and has a more constant profile with height (but for the grid-point at 47.6°N, 90°W).

Figures 6.7 to 6.15 show that the ECMWF cloud prediction scheme produces different distribution of the cloud cover in time and space when compared against that obtained from the CONTROL experiment. As the cloudiness interacts with the physics of the model through radiatively-induced changes in the temperature field, it is very likely that the ECMWF scheme may yield different distributions of the time-averaged temperature and relative humidity fields, and of their temporal variability. This effect may, in turn, be important upon the monthly average and temporal variability of the radiation budget components, especially at long wavelengths.

6.5 ECMWF versus CONTROL temperature field

The latitude-height distribution of the temperature field obtained with the NCAR CCM for Northern Hemisphere winter conditions is compared against observations in Chapter Four. Figure 6.16 shows the latitude-height distributions of monthly-averaged temperature field and its standard deviation obtained from the CONTROL run for perpetual January conditions. In the troposphere, the largest variability in the temperature field takes place in the middle-latitudes below $\sigma = .664$ in the winter hemisphere. Map of the time variance for the 4.5 km temperature field shows that maxima are found over the mid-Pacific and mid-Atlantic oceans which are the preferred regions in the model for cyclonic activity (Chervin, 1980). The difference in the time average and standard deviation of the temperature field between the ECMWF and CONTROL simulations is shown in Figure 6.17. The difference in the vertical distribution of cloudiness between the two simulations has the largest impact on the temperature field in the upper troposphere. The decrease of the high-level clouds at low latitudes in the ECMWF simulation

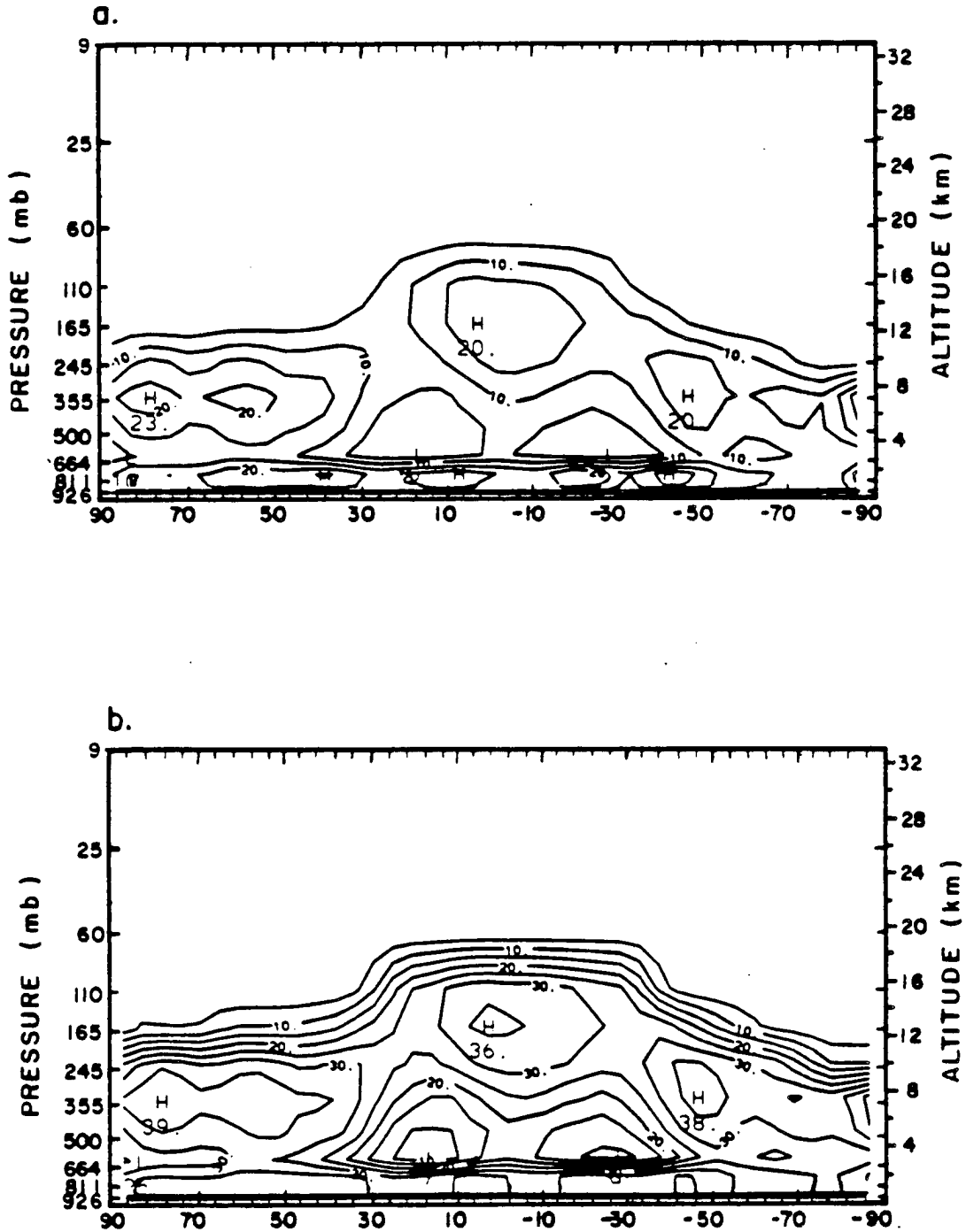


Figure 6.12: Latitude-height distribution of the cloud cover obtained from the CONTROL simulation (%): (a) monthly-average, and (b) standard deviation.

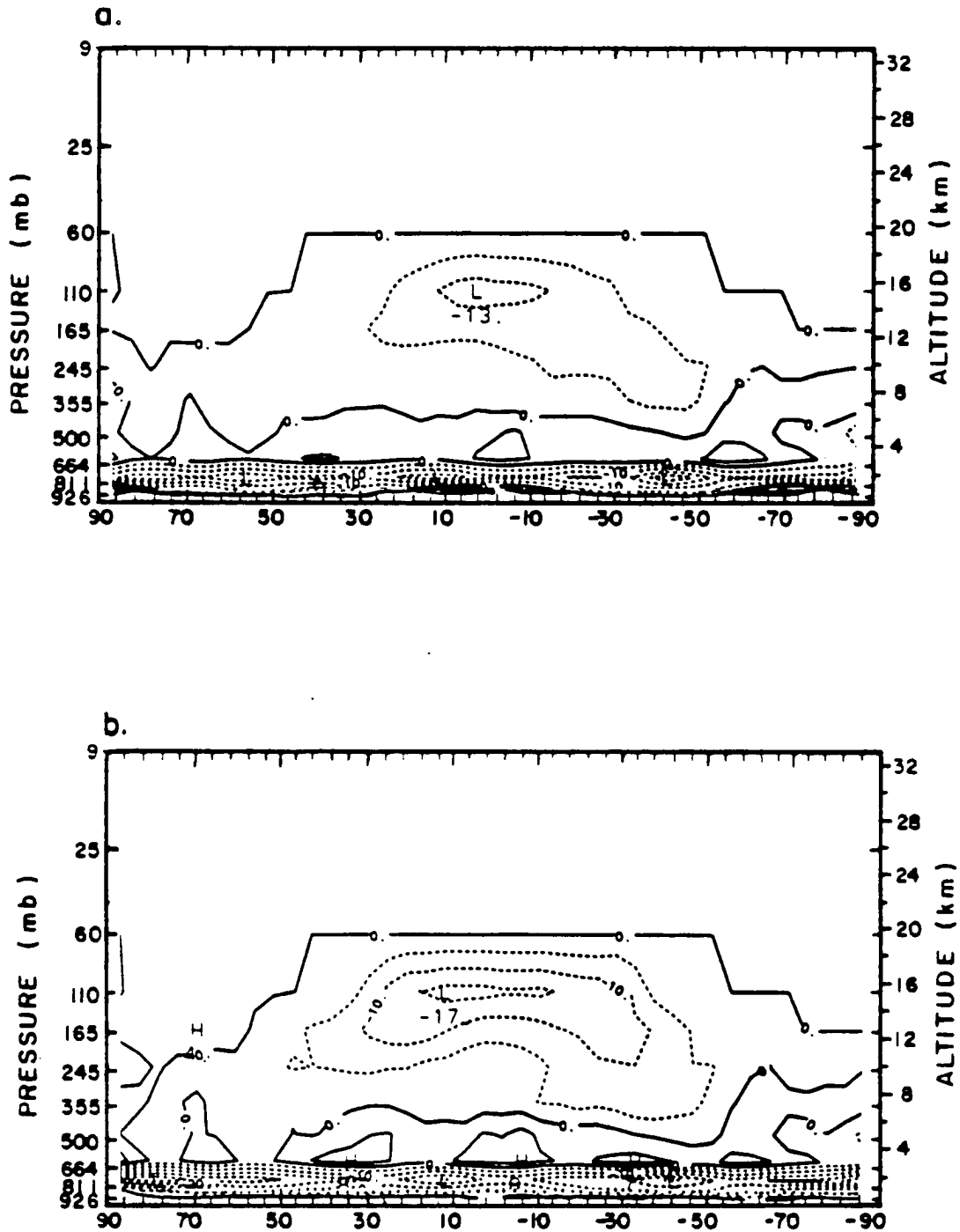


Figure 6.13: Latitude-height distribution of the difference in the cloud cover between the ECMWF and CONTROL simulations (%): (a) monthly average, and (b) standard deviation.

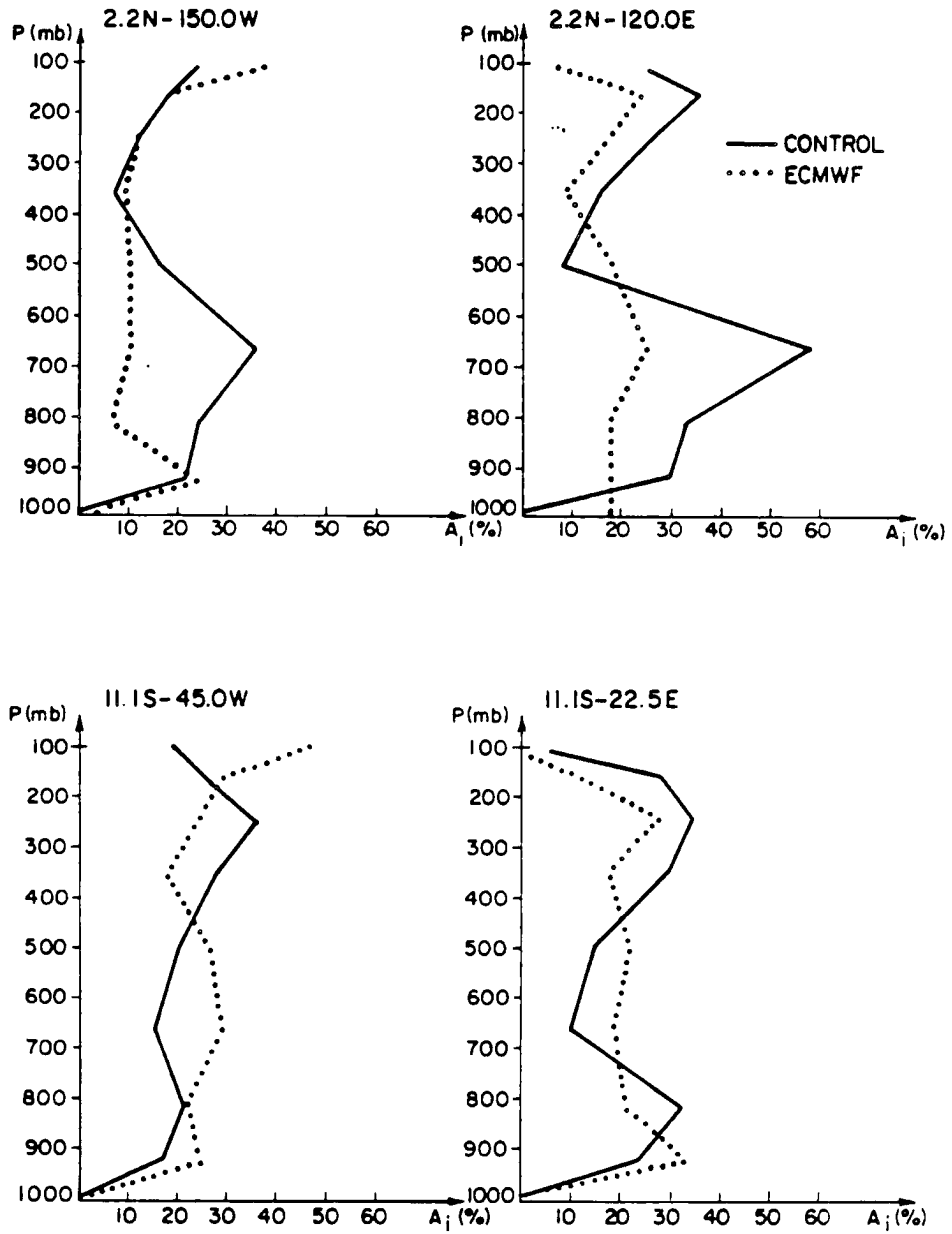


Figure 6.14: Vertical distribution of the cloudiness for single grid-points located at low latitudes (%).

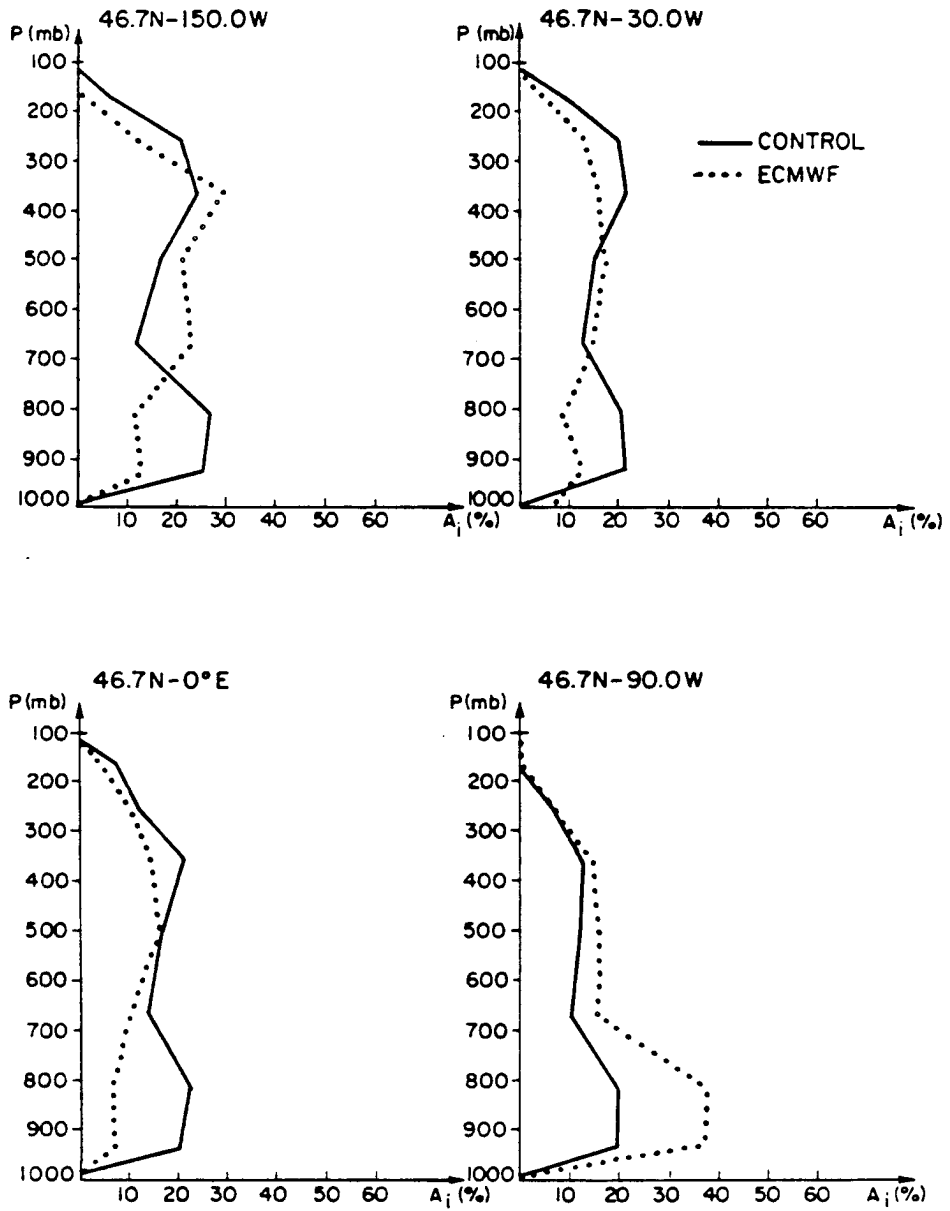


Figure 6.15: Vertical distribution of the cloudiness for single grid-points located in the middle latitudes (%).

produces, through changes in the distribution of the longwave radiative heating rates, a strong warming around $\sigma = .110$. The impact of the decreased cloudiness in the ECMWF simulation below $\sigma = .664$ is less than that in the upper troposphere because of warmer cloud-top temperatures. Finally, the change in the standard deviation of the temperature does not exceed .5 K in the troposphere and can be considered negligible.

In the real atmosphere, clouds interact with the dynamical and hydrological processes through the heat of condensation and evaporation, and the redistribution of heat and momentum (Arakawa, 1975). In the NCAR CCM, and for both simulations, the interactions between clouds and the physical processes are limited to radiatively-induced changes in the temperature only, so that the impact of clouds upon the variability of the temperature and humidity fields is small. As a result, study of the correlation in time and space of both synoptic fields provides information on the speed at which the atmosphere would lose its memory for mostly clear-sky conditions. Therefore, it is important to compare the global distribution of the time-lagged autocorrelation coefficients at increasing time-lags to infer that, if the atmospheres simulated in the ECMWF and CONTROL simulations have an identical history, the differences, if any, in the temporal variability of the planetary radiation balance, can mostly be attributed to the direct radiative effects of clouds. This is particularly important at long wavelengths because of the sensitivity of the longwave radiative heating rates to changes in the temperature and humidity fields.

Figures 6.18, 6.19, and 6.20 show maps of the time-lagged autocorrelation coefficients of the temperature at lags 1, 2, and 3 days at $\sigma = .811$ computed for both climate simulations. Variations in the temperature field, through horizontal advection associated with fast moving frontal systems in the middle latitudes and latent heat release in the deep tropical convective regions yield an important decrease in the correlation at a 1-day lag. On the other hand, the temperature evolves two times more slowly in the cloud-free subtropics and the cold polar regions where more stable atmospheric conditions prevail. The map at the 1-day lag shows that there are some differences between the ECMWF and CONTROL experiments in the global distribution of the correlation coefficient, especially in the middle latitudes in the Northern Hemisphere. The correlation in the temperature

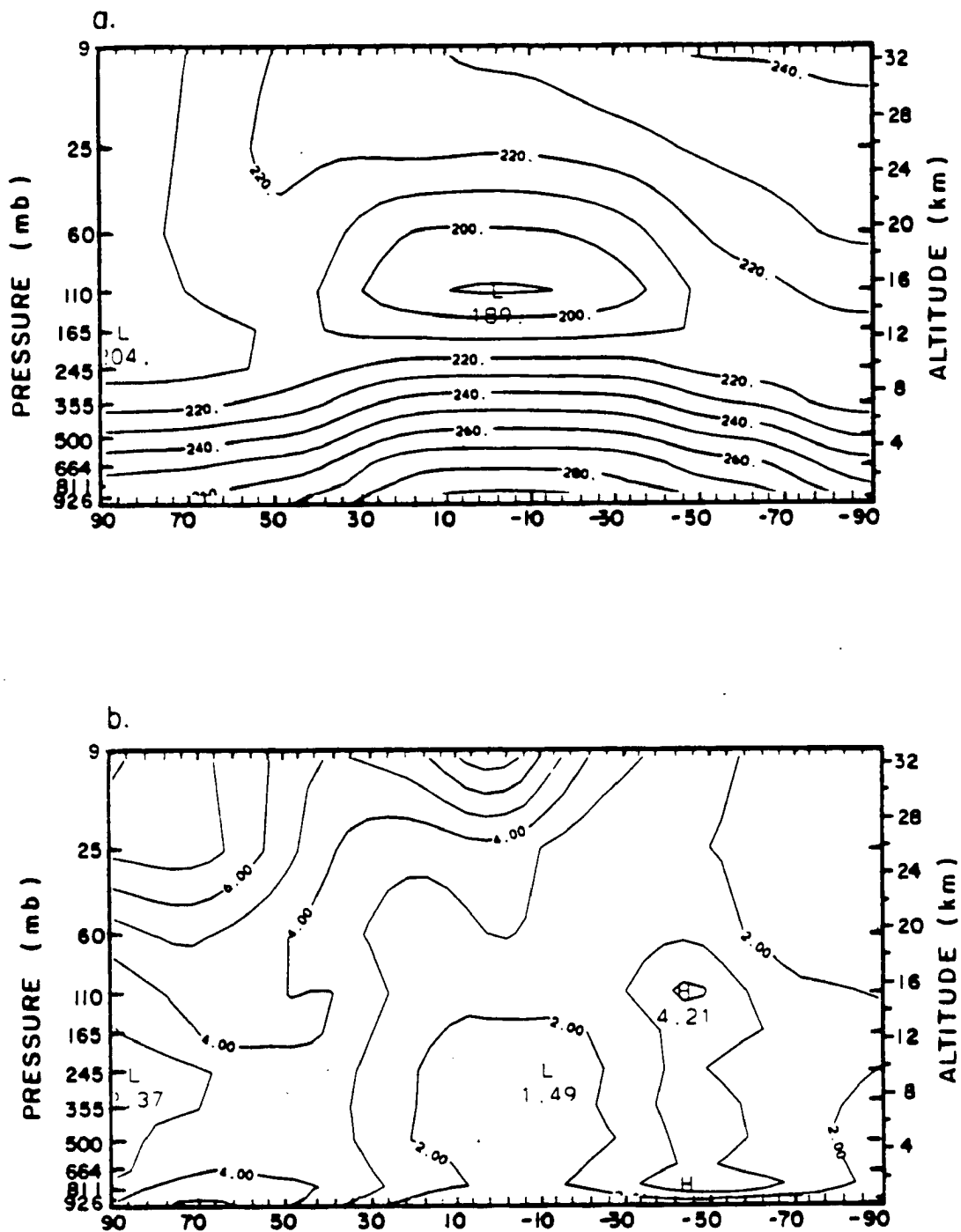


Figure 6.16: Latitude-height distribution of the temperature obtained from the CONTROL simulation (K): (a) monthly average, and (b) standard deviation.

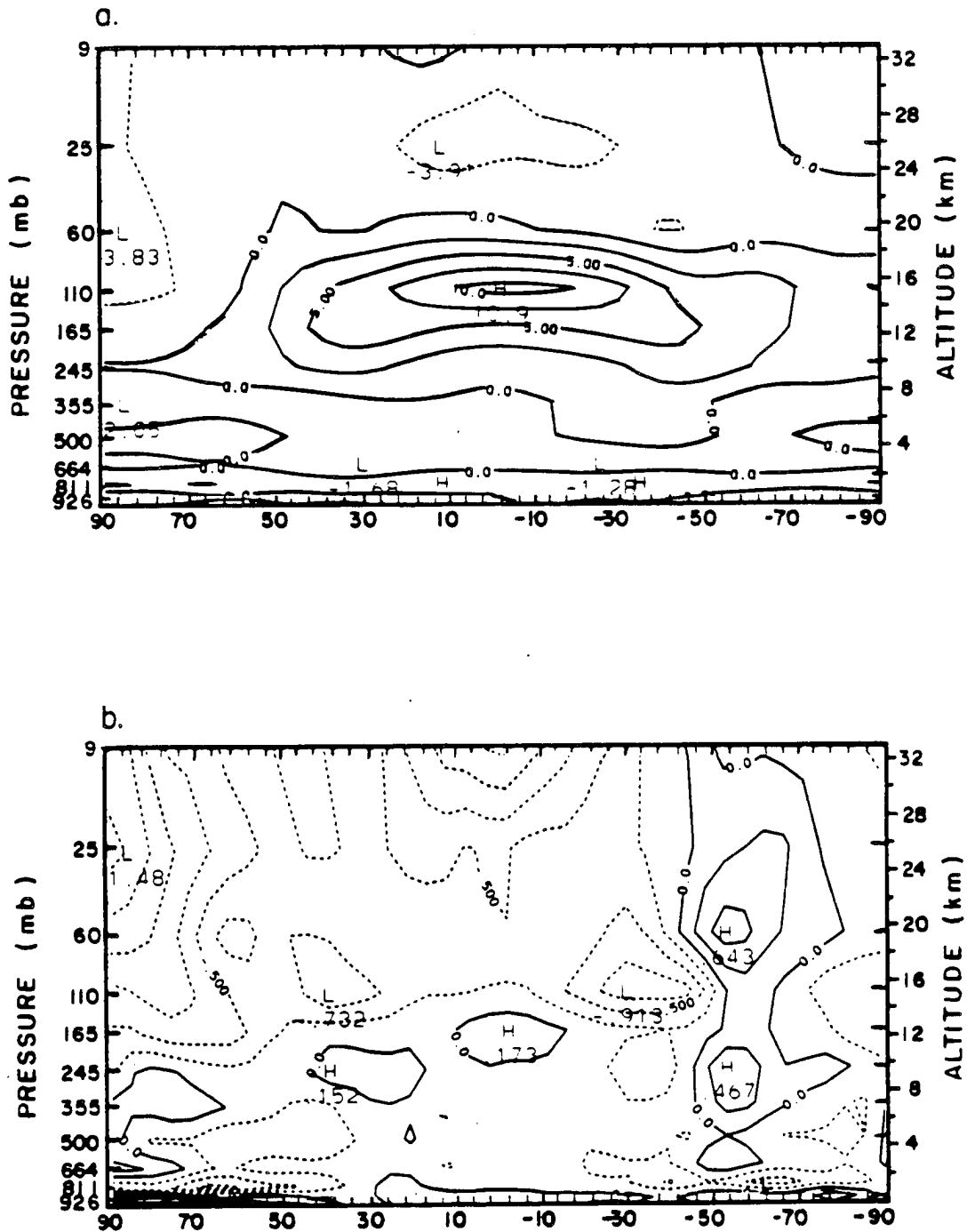


Figure 6.17: Latitude-height distribution of the difference in the temperature between the ECMWF and CONTROL simulations (K): (a) monthly average, and (b) standard deviation.

field above the continents is greater in the ECMWF simulation whereas that computed from the CONTROL simulation does not show any contrast between land and oceans. In comparing the distributions for the successive time-lags, it is clear that the autocorrelation is reduced with increasing lags in both simulations, but that its reduction is not spatially uniform. In the Southern Hemisphere, the the reduction with increasing time-lags is fairly small on the western sides of the continents whereas is quite pronounced above the ITCZ and the oceanic cyclonic activity regions. After 3 days, negative correlations dominate over the whole globe for both simulations, except above the desert regions and the continents influenced by cold air masses in the winter hemisphere. Finally, for that specific σ -level and especially above the ITCZ and the middle latitude storm track regions, there are no significant differences in the speed at which the atmospheric temperature becomes decorrelated.

6.6 ECMWF versus CONTROL relative humidity field

Figure 6.21 shows the latitude-height distribution of the monthly average and standard deviation of the relative humidity field obtained from the CONTROL simulation. As expected, there is a direct correspondence with the distribution of the cloud cover shown in Figure 6.12. In the vertical, the moisture is concentrated in the very first layers of the model below $\sigma = .811$ with a second maximum below the tropopause above the local position of the ITCZ and the storm track regions in the middle latitudes. The atmosphere also becomes drier towards the poles. The relative humidity is minimum around $\sigma = .500$ which corresponds also to a minimum in the cloud cover. The largest variability in the relative humidity field is observed below the tropopause, i.e., above the local position of its second maximum, and mainly results from variations in the intensity of the convection. The standard deviation of the relative humidity below $\sigma = .811$ is minimum because the atmosphere stays most of the time supersaturated. Map of the cloudiness at and below this σ -level shows that, in the CONTROL simulation, the earth is actually completely overcast.

The latitude-height distribution of the difference in the monthly average and standard deviation of the relative humidity between the ECMWF and CONTROL runs is shown in

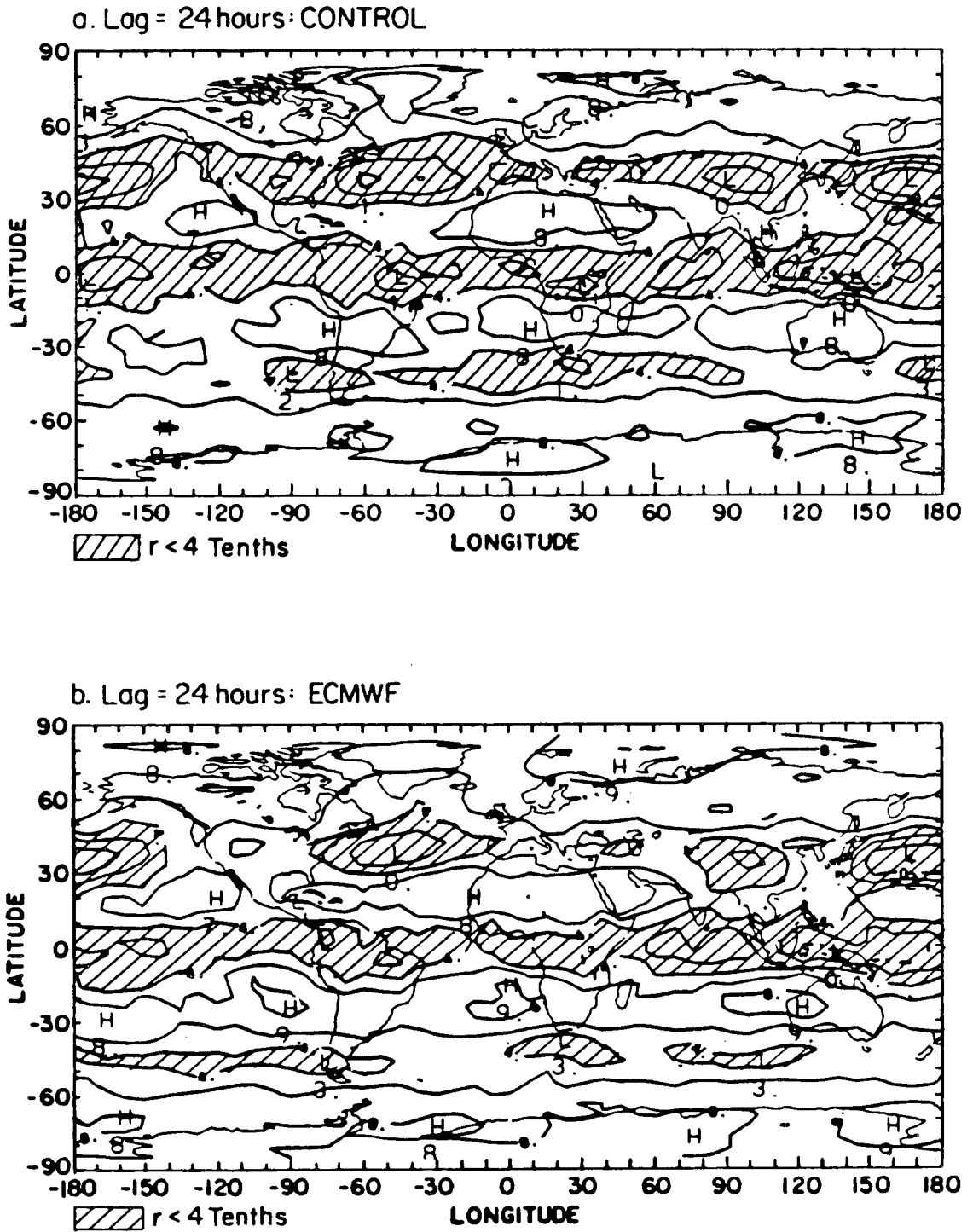


Figure 6.18: Map of the 1-day lag autocorrelation coefficient of the temperature at $\sigma = .811$ (tenths): (a) CONTROL simulation, and (b) ECMWF simulation.

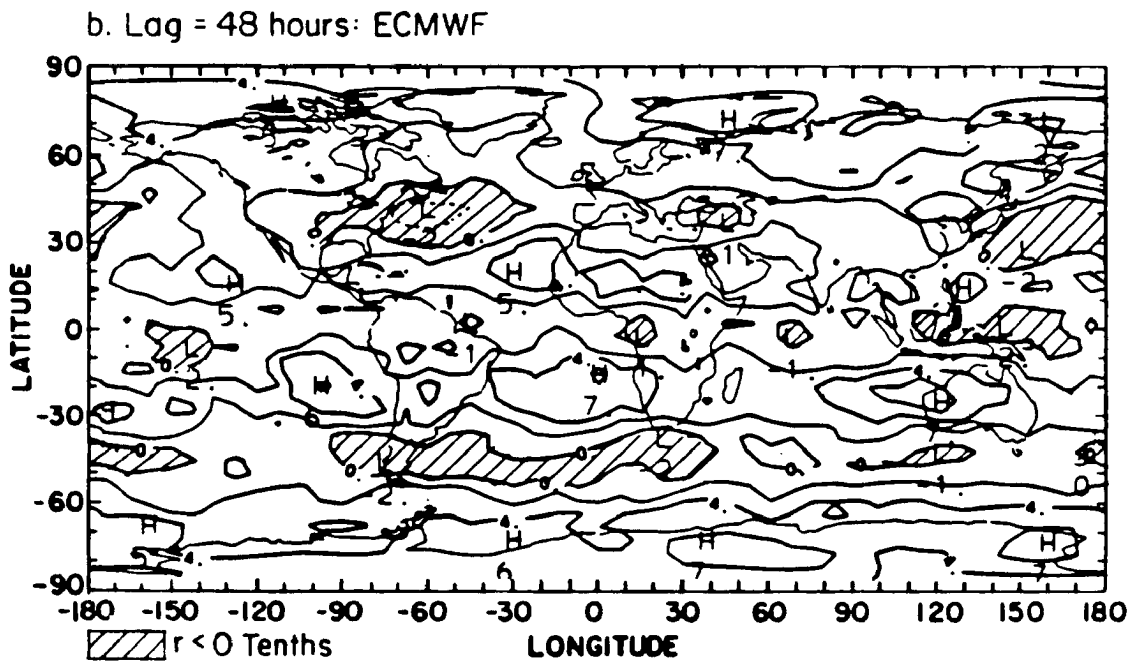
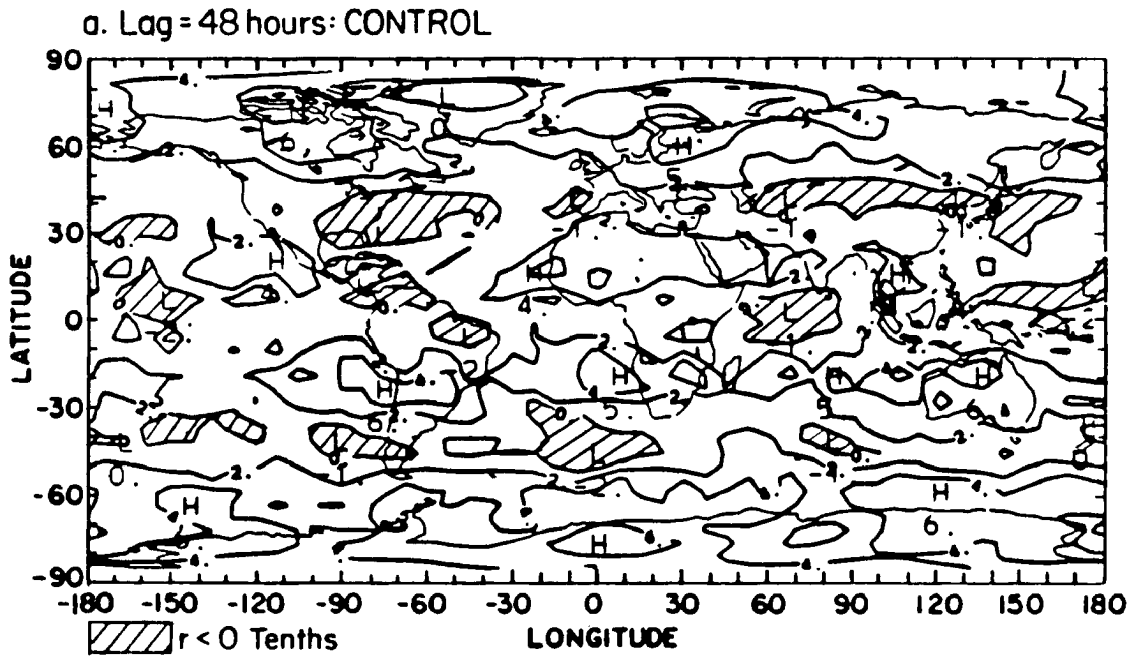


Figure 6.19: Map of the 2-day lag autocorrelation coefficient of the temperature at $\sigma = .811$ (tenths): (a) CONTROL simulation, and (b) ECMWF simulation.

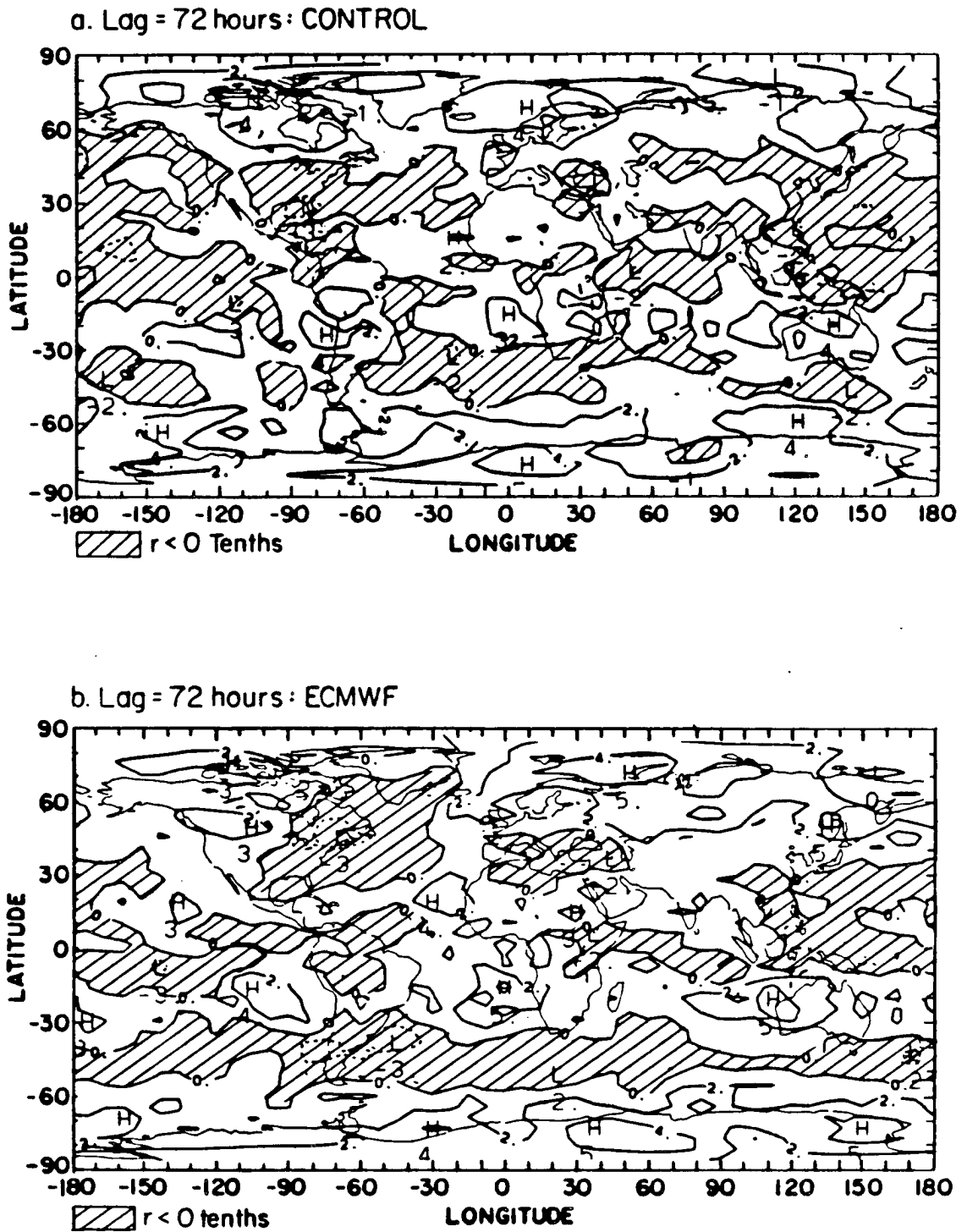


Figure 6.20: Map of the 3-day lag autocorrelation coefficient of the temperature at $\sigma = .811$ (tenths): (a) CONTROL simulation, and (b) ECMWF simulation.

Figure 6.22. Between 50°N and 50°S, the atmosphere in the ECMWF simulation is drier around $\sigma = .811$ and in the upper atmosphere (above $\sigma = .245$), wetter in the middle troposphere between $\sigma = .664$ and $\sigma = .245$. The humidity content is higher than in the CONTROL simulation in the middle latitudes, where increased cloudiness is actually observed, especially in the winter hemisphere. The change in the vertical distribution of the monthly-averaged relative humidity is accompanied by a slight increase in its standard deviation, except in the layer adjacent to the ground and in the upper troposphere at low latitudes. The decreased relative humidity in the upper tropospheric layers in the ECMWF simulation, indicates that the convection does not penetrate the atmosphere as high as in the CONTROL run, which, in turn, results in less high-level clouds, especially cirrus clouds associated with outflow from deep convection at low latitudes.

It is important to compare the dissipation in time of the relative humidity between the two simulations. As the temperature field, it provides the typical time-scale at which the model atmosphere would lose its memory in a cloudless atmosphere. In addition, as the formation of clouds depends upon an arbitrary supersaturation threshold of the relative humidity for both cloud schemes, the evolution of the cloud field is directly linked to the decorrelation in time of the moisture field. Figures 6.23, 6.24, and 6.25 present the global distribution of the autocorrelation coefficients of the relative humidity at lags 1, 2, and 3-days at the σ -level .811. Maps of the autocorrelation coefficient at a 1-day lag show that the humidity field changes the most rapidly in time above the wintertime cyclogenetic areas in the northern Pacific and Atlantic oceans. The moisture field maintains a greater correlation in the tropics because of the higher humidity content and the continuous convective activity whereas the change in the mid-latitude humidity field is driven by fast-moving frontal systems. The correlation in time is the largest above the dry subtropical regions. The agreement in the distribution of the autocorrelation of the moisture field at a 1-day lag between the ECMWF and CONTROL simulations is better than that of the temperature in the middle latitudes for the winter hemisphere. However, in the tropics, the ECMWF simulation shows a slightly stronger correlation than the CONTROL run. At increasing time lags, and as for the temperature field, the time-correlation of the relative

humidity rapidly decreases with increasing time-lags, and becomes mostly negative over the whole globe after three days.

For both simulations, and for both the temperature and humidity fields, negative correlations are found over most of the globe after 3 days, especially for regions dominated by convective and cyclogenetic activities. In addition, the global distribution of the autocorrelation coefficients at successive time-lags agree very well between the two simulations, in particular for the moisture field. It is also important to remember that the uncertainty in the computation of the correlation coefficients quickly increases with increasing time-lags. Therefore, the difference in the distribution of cloudiness between the ECMWF and CONTROL simulations does not strongly impact upon the speed at which both synoptic fields vary, and the difference in the planetary radiation balance, including its temporal variability, can be mainly be attributed to the direct radiative effect of clouds.

6.7 ECMWF versus CONTROL cloud radiative forcing

The global distribution of the seasonal average and standard deviation of the cloud radiative forcing at short and long wavelengths was discussed in Chapter Five. The net effect of clouds on the surface-atmosphere radiative heating is defined as the difference between the clear-sky fluxes and those obtained for overcast conditions for identical vertical profiles of temperature and humidity. In this section, we focus our discussion on the difference in the longwave and shortwave radiative forcings of clouds between the ECMWF and CONTROL climate simulations.

6.7.1 Longwave forcing

Figure 6.26 shows the global distribution of the difference in the monthly-averaged cloud longwave radiative forcing, C_L , between the ECMWF and CONTROL simulations, and the zonally-averaged profile of the radiative field for both simulations. In the ECMWF simulation, the increased total cloudiness above the continents and the convective activity regions over the oceans in the summer hemisphere yields an increase of C_L . The difference in the greenhouse effect of clouds between the two simulations reaches regionally values

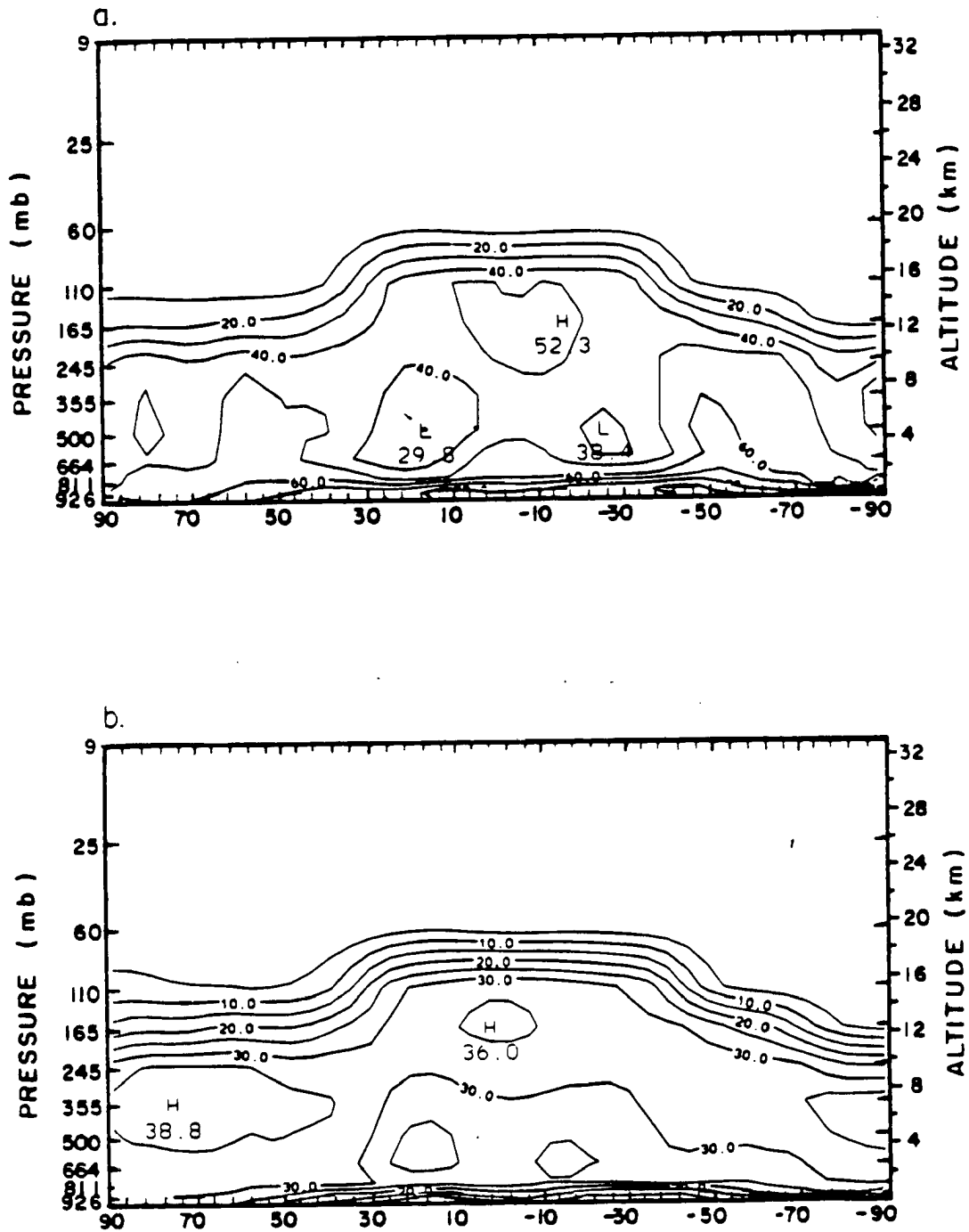


Figure 6.21: Latitude-height distribution of the relative humidity obtained from the CONTROL simulation (%): (a) monthly average, and (b) standard deviation.

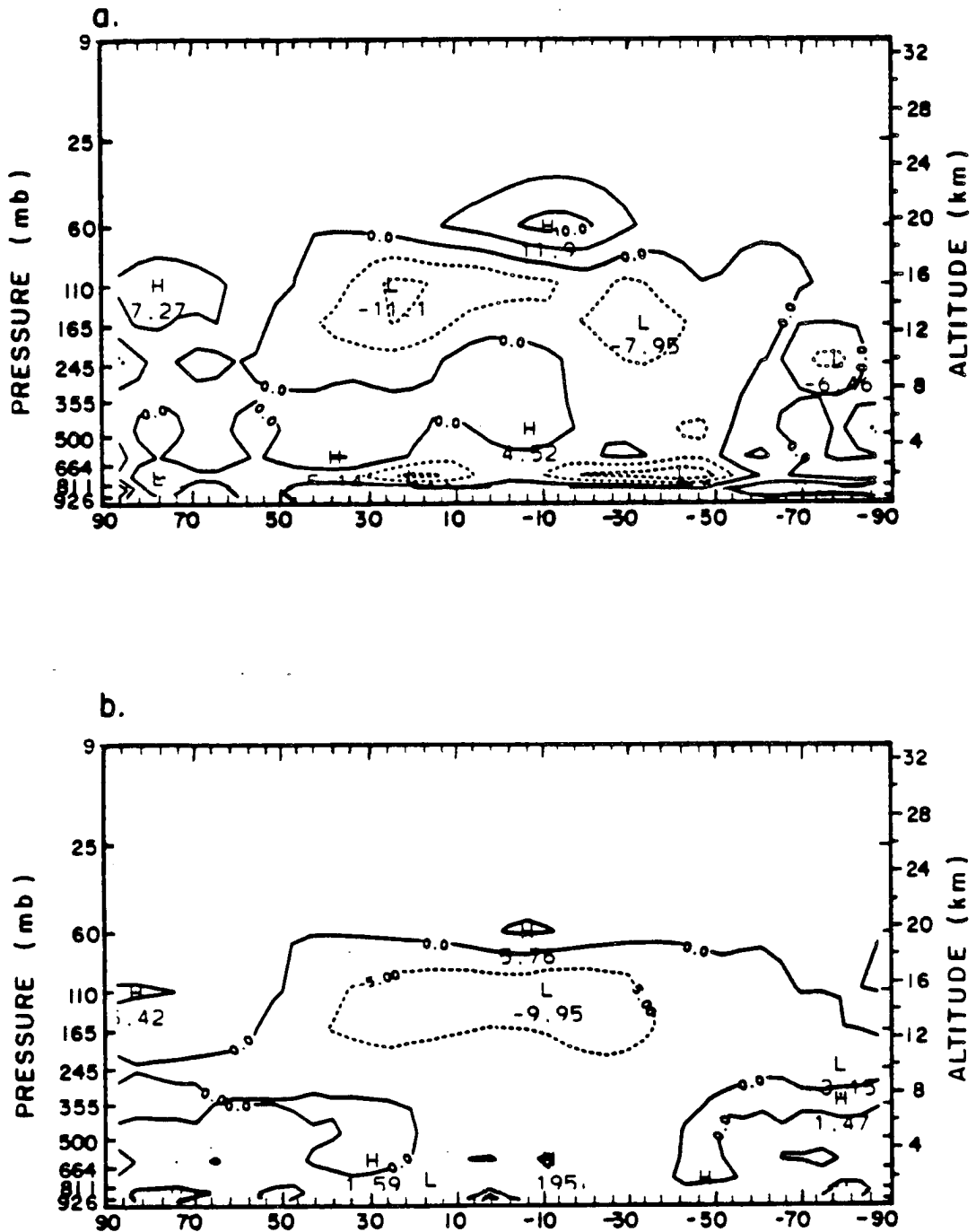


Figure 6.22: Latitude-height distribution of the difference in the relative humidity between the ECMWF and CONTROL simulations (%): (a) monthly average, and (b) standard deviation.

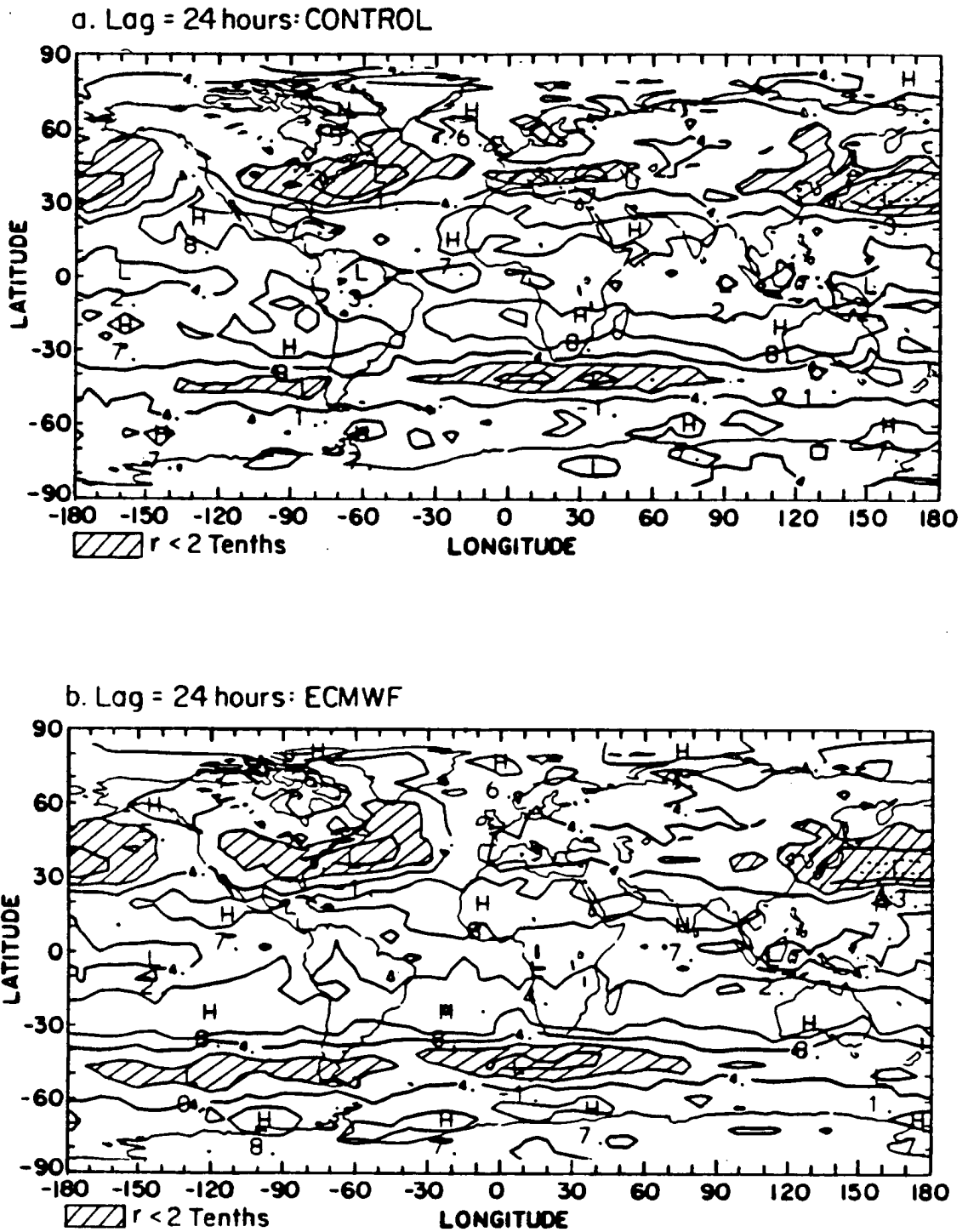


Figure 6.23: Map of the 1-day lag autocorrelation coefficient of the relative humidity at $\sigma = .811$ (tenths): (a) CONTROL simulation, and (b) ECMWF simulation.

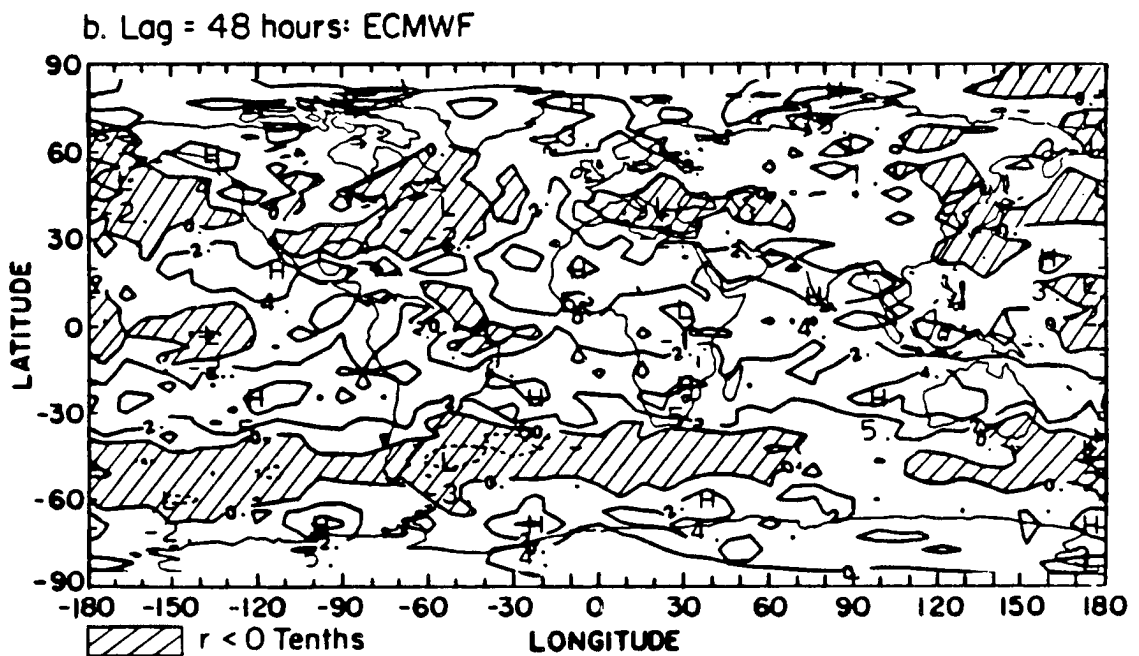
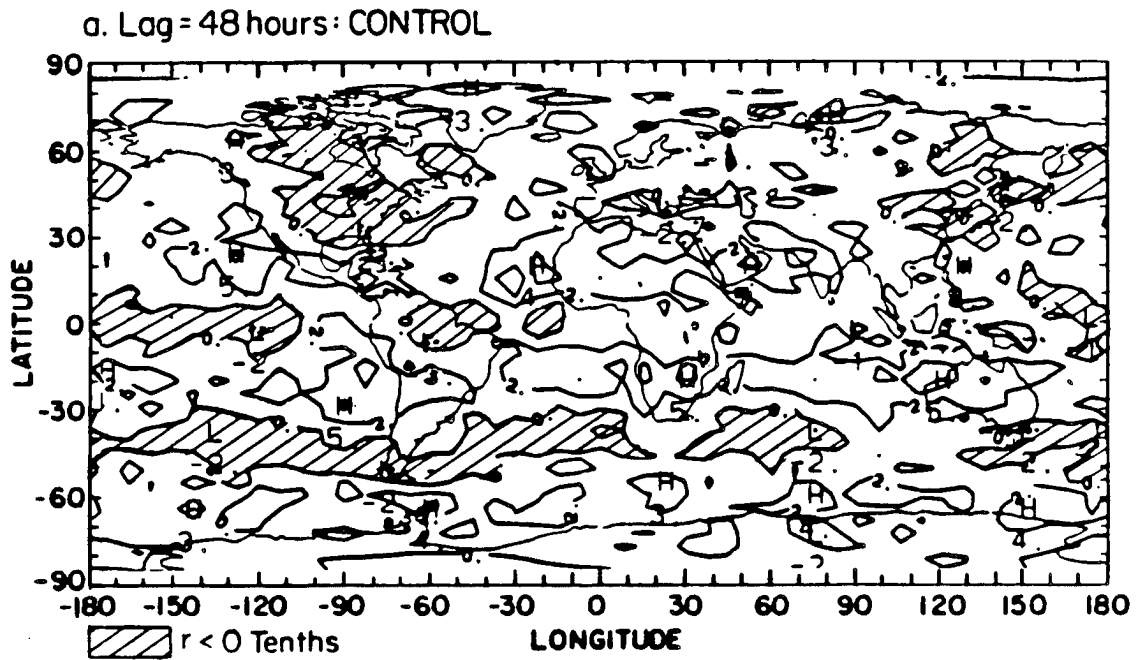


Figure 6.24: Map of the 2-day lag autocorrelation coefficient of the relative humidity at $\sigma = .811$ (tenths): (a) CONTROL simulation, and (b) ECMWF simulation.

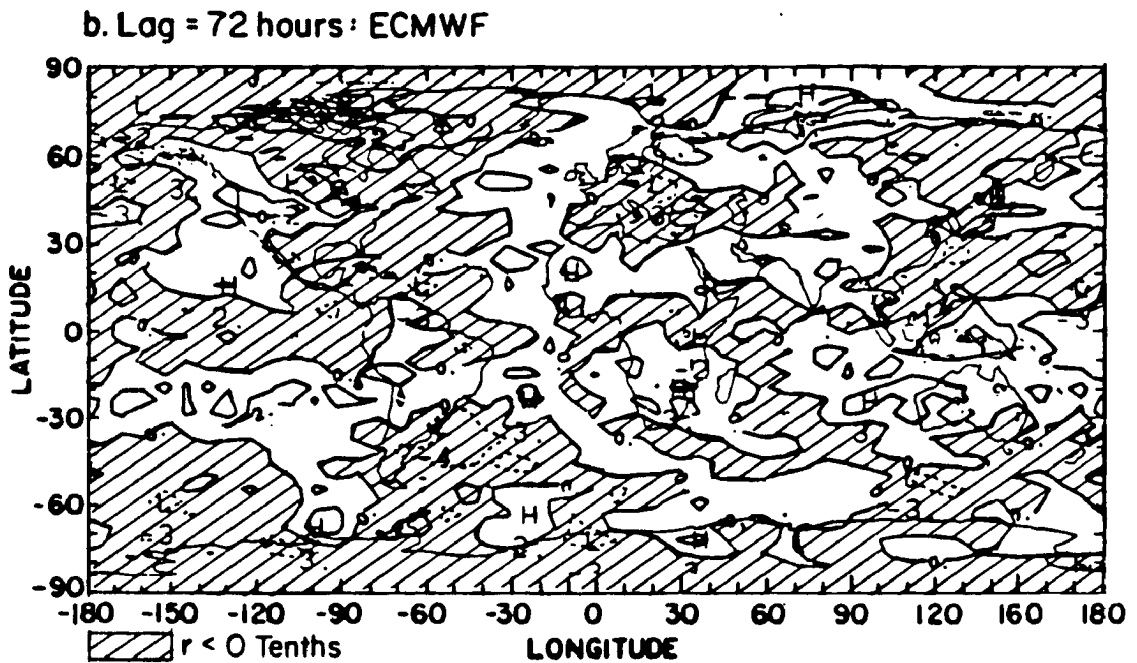
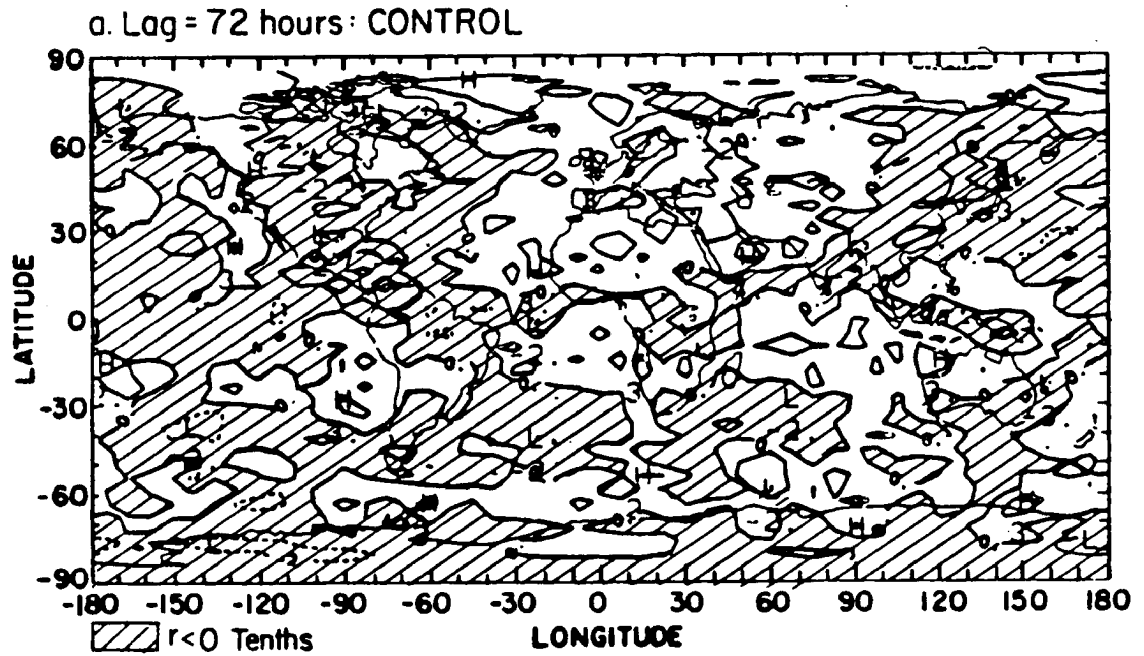


Figure 6.25: Map of the 3-day lag autocorrelation coefficient of the relative humidity at $\sigma = .811$ (tenths): (a) CONTROL simulation, and (b) ECMWF simulation.

greater than 45 Wm^{-2} above South America and 35 Wm^{-2} above southern Africa and the winter monsoon region. Although the ECMWF cloud scheme predicts more planetary boundary-layer clouds along the western coast of the continents than the CONTROL simulation, their radiative effect is less than that of higher-level clouds because of their warmer cloud-top temperatures. The decreased total cloud cover over the subtropical oceans leads to a reduced cloud forcing. The zonally-averaged profile of C_L shows that the greenhouse effect of clouds is greater in the ECMWF simulation at all latitudes. On a zonal average, the increased cloudiness has the same magnitude in the tropics and the middle latitudes, and produces a 15 Wm^{-2} atmospheric warming. In the real atmosphere, high-level clouds produce the largest greenhouse warming and we should have expected a decrease in C_L above the convective activity regions because of the lower height of the cloud cover in the ECMWF simulation. However, the radiative effect of the increased cloud cover at lower levels overcomes that of the decreased height of the cloud column, so that the net effect is an actual augmentation of C_L .

Figure 6.27 shows the global distribution of the difference in the standard deviation of the cloud longwave radiative forcing, $\sigma(C_L)$, and the zonally-averaged profile of $\sigma(C_L)$ for both simulations. The difference in $\sigma(C_L)$ not only depends on the difference in the cloud distribution but also varies with the cloud type, as discussed in Section 6.3. First, the decrease in the cloud cover above the subtropical oceans in the ECMWF simulation leads to a reduction in C_L , and therefore, in $\sigma(C_L)$. In the winter hemisphere and at high latitudes in the summer hemisphere, the increased variability of the total cloud cover in several areas yields an increase of $\sigma(C_L)$. Along the longwave radiative forcing of the planetary boundary-layer clouds along the western coasts of the continents is small, the increased cloudiness is also accompanied by a significant increase in $\sigma(C_L)$ when compared against the CONTROL run. Finally, the most interesting information from the map of $\sigma(C_L)$ is the 25 Wm^{-2} decrease in the variability of the cloud forcing above the deep tropical convective activity regions. In the ECMWF simulation these regions are characterized by greater cloud cover and greenhouse warming while the variability of the total cloud

cover is less than in the CONTROL run. This feature is also very well seen in the zonally-averaged profile of $\sigma(C_L)$. The variability of the cloud radiative forcing computed from the ECMWF simulation is greater than that obtained from the CONTROL simulation in the middle latitudes because of the increased cloudiness and its variability, except between 20°S and 50°S because of the decreased variability of the convective and associated cirrus clouds. As this feature is also seen at short wavelengths, it will be discussed later in a separate section.

6.7.2 Shortwave forcing

Figure 6.28 shows the global distribution of the difference in the monthly-averaged shortwave radiative forcing of clouds, C_S , between the ECMWF and CONTROL simulations, and the zonally-averaged profile of C_S for both simulations. The optical properties of clouds are identically prescribed in both experiments, so that differences in C_S can only result from differences in the distribution of the cloudiness. The global map of C_S obtained from the CONTROL run resembles closely that for Northern Hemisphere winter conditions discussed in Chapter Five. In the winter hemisphere, the radiative forcing of clouds, defined as the clear-sky minus cloudy absorbed solar fluxes, is small because of the predominant effect of the poleward decrease of absorbed solar radiation. In the CONTROL simulation, C_S is maximum above the convective activity areas, i.e., the South Pacific Convergence Zone, the eastern coasts of South America and southern Africa, and the monsoon region. It also exceeds 80 W m^{-2} between 30°S and 60°S which is the latitude band of maximum solar absorption and cloud cover greater than 40 % in the model. Map of the difference in C_S shows that the cloud shortwave radiative forcing is the largest over the oceans in the CONTROL simulation whereas is the largest over the continents in the ECMWF run. As already observed at long wavelengths, this is a direct consequence of the increased cloudiness above land in the ECMWF simulation. In particular, the decrease in the cloud cover over the oceans between 30°S and 60°S yields a strong reduction in C_S , except in a few areas. This is very well seen in the zonally-averaged profile of C_S . It is also important to note the strong radiative effect of the low-level clouds predicted along the western coasts of South America and southern Africa.

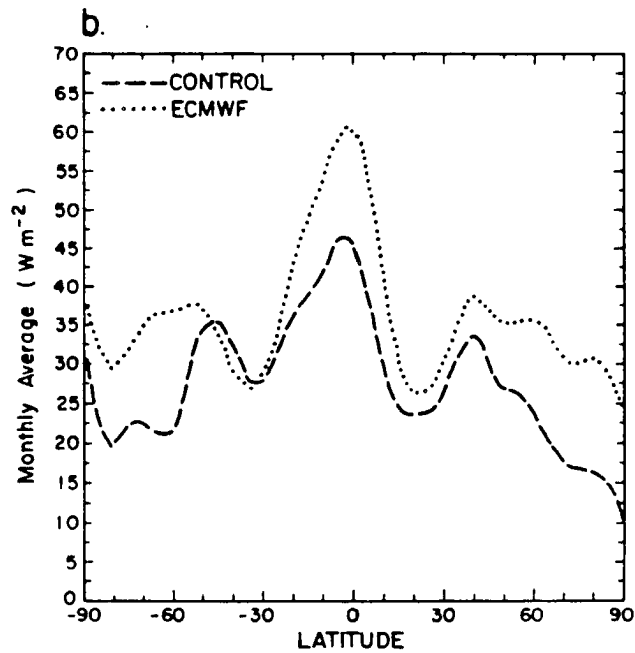
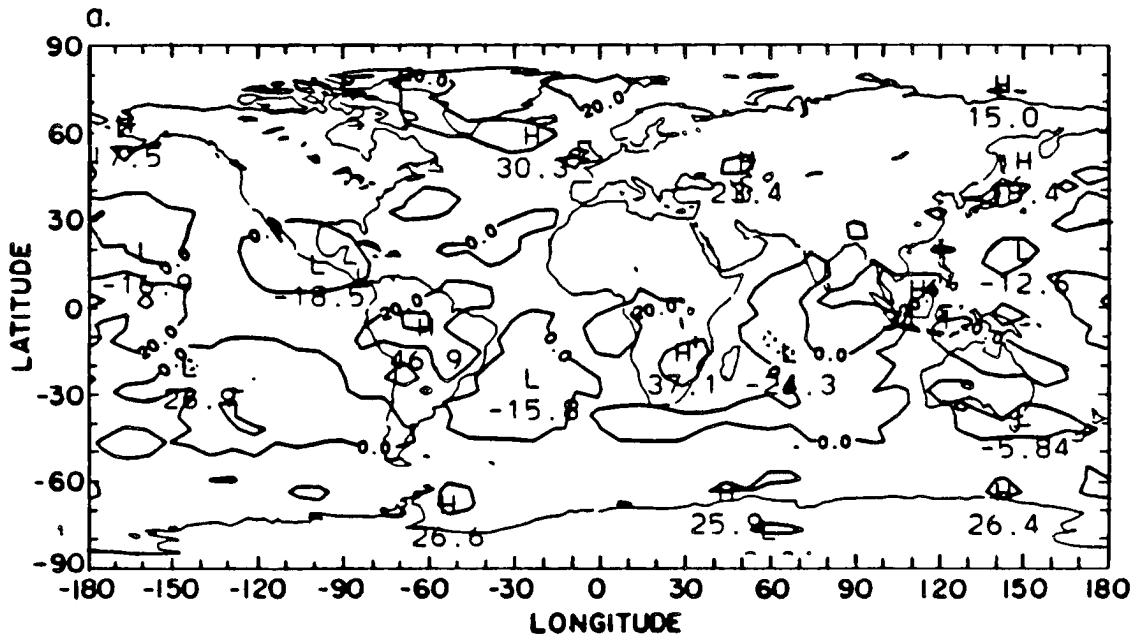


Figure 6.26: Monthly average of the cloud longwave radiative forcing (W m^{-2}): (a) global distribution of the difference between the ECMWF and CONTROL simulations, and (b) zonally-averaged distribution.

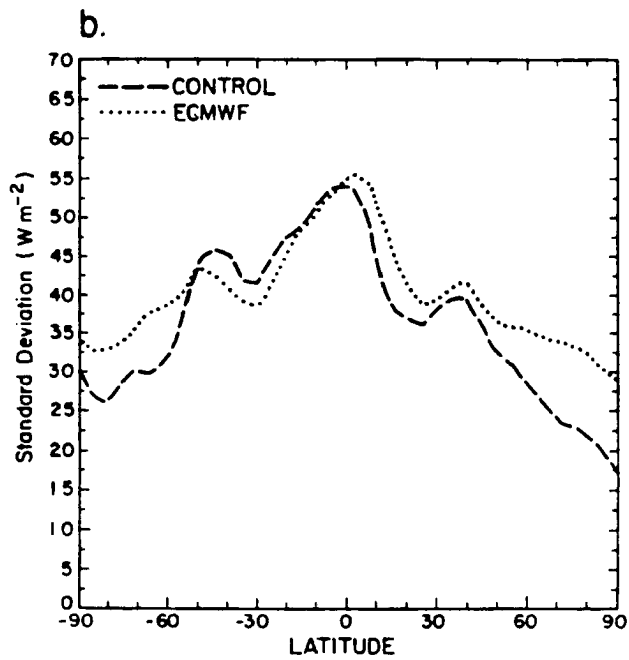
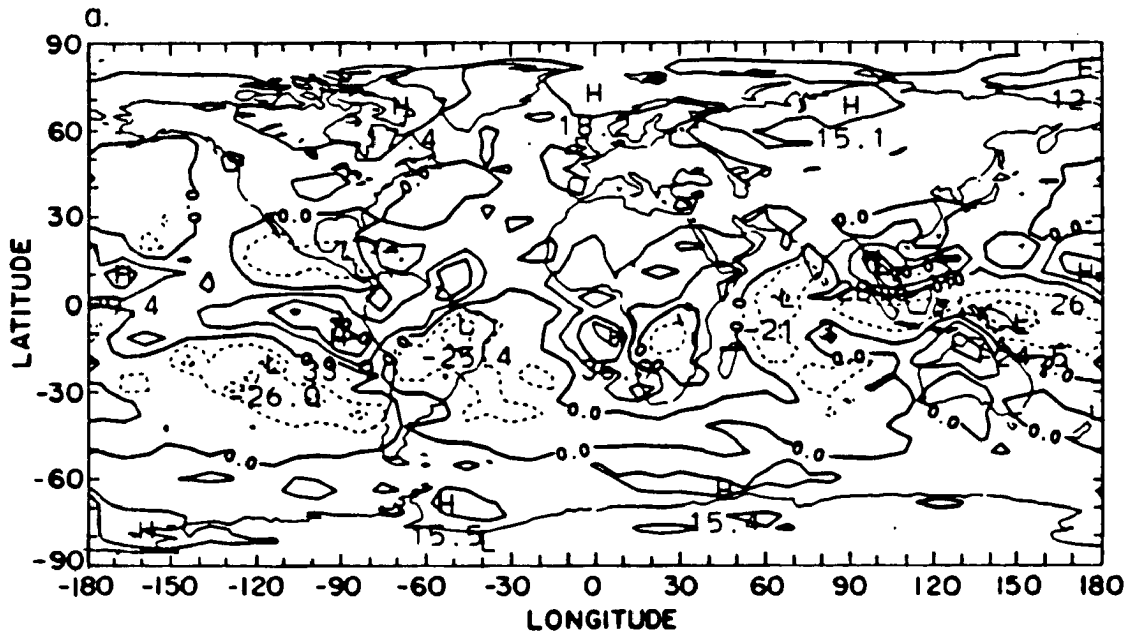


Figure 6.27: Standard deviation of the cloud longwave radiative forcing (Wm^{-2}): (a) global distribution of the difference between the ECMWF and CONTROL simulations, and (b) zonally-averaged distribution.

Figure 6.29 shows the global map of the difference in the standard deviation of the shortwave radiative forcing of clouds, $\sigma(C_S)$, and the zonally-averaged profile of $\sigma(C_S)$ for both simulations. In the CONTROL simulation, the global distribution of $\sigma(C_S)$ resembles closely that of C_S , with areas of high 12-hour variability coinciding exactly with areas of high values of the monthly-averaged cloud forcing. Above those regions, $\sigma(C_S)$ is actually as large as C_S . The global map of $\sigma(C_S)$ obtained from the ECMWF simulation is similar to that of the CONTROL run, except that the magnitude of $\sigma(C_S)$ is systematically 20 Wm^{-2} lower. This is particularly well observed in the latitude band between 30°S and 60°S . As a result, the difference in $\sigma(C_S)$ between the two simulations is mostly negative, especially in the summer hemisphere. Areas where $\sigma(C_S)$ is actually greater in the ECMWF simulation correspond to areas which undergo a strong increase in cloudiness, except, and as already observed at long wavelengths, above regions of deep tropical convection over the continents. The zonally-averaged profile of $\sigma(C_S)$ shows that the variability of the shortwave radiative effect of clouds is strongly reduced in the ECMWF simulation between 60°S and 30°N . This is the combined result of a decreased variability of the total cloud cover over the convective activity regions and the decreased cloudiness over the oceans which is the predominant effect.

6.8 ECMWF versus CONTROL planetary radiation balance

The differences in the radiative forcings of clouds between the ECMWF and CONTROL simulations explain most of the differences in the model-generated longwave and shortwave radiation budget components. The troposphere is practically transparent to solar radiation, and the optical properties of clouds and the surface albedo are identically prescribed. Therefore, variations in the absorbed solar radiation and the planetary albedo result from variations in the total cloud cover. In addition to clouds, the outgoing longwave radiation is sensitive to changes in the vertical profiles of the temperature and humidity fields. Despite some differences in the monthly average and standard deviation above overcast areas, the distributions of the time-lagged autocorrelation coefficients of the temperature and relative humidity fields are in very good agreement. This was expected because the treatment of the interactions between clouds and the thermodynamic

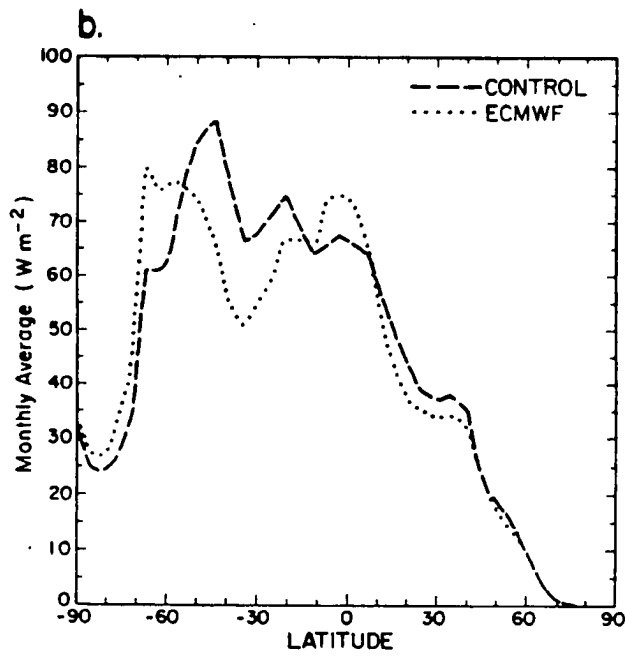
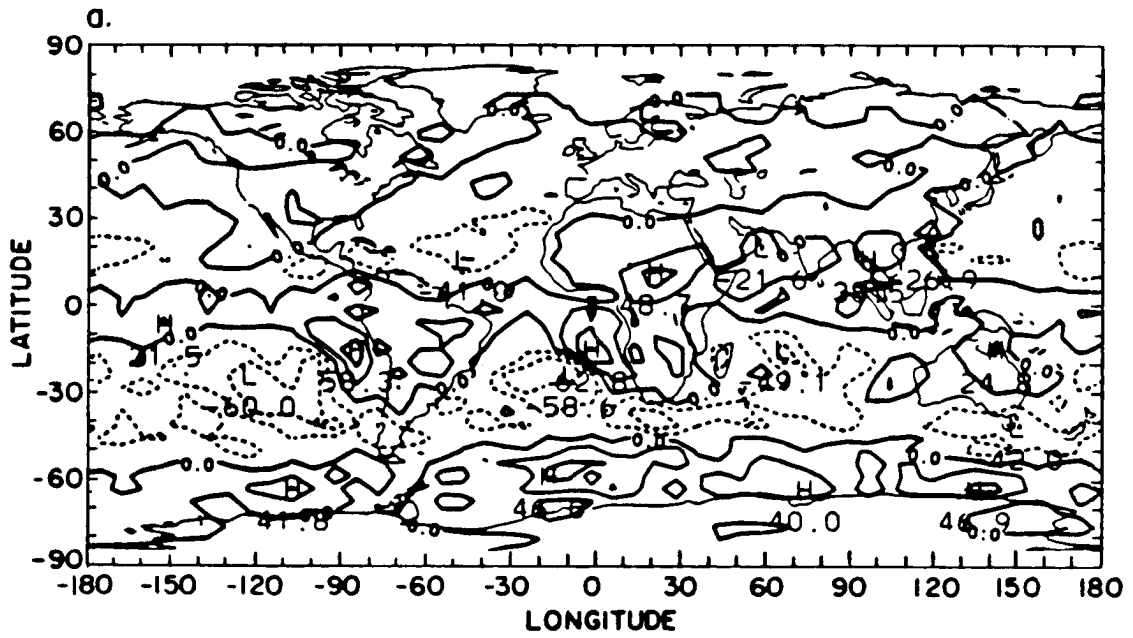


Figure 6.28: Monthly average of the cloud shortwave radiative forcing (W m^{-2}): (a) global distribution of the difference between the ECMWF and CONTROL simulations, and (b) zonally-averaged distribution.

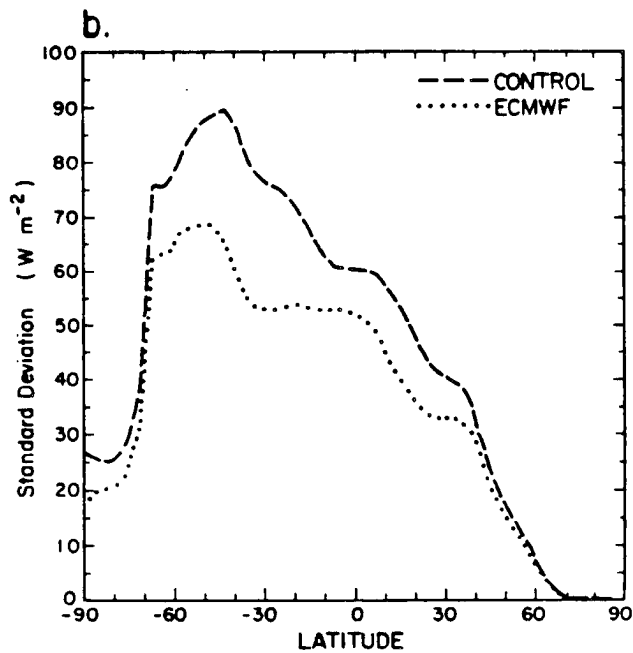
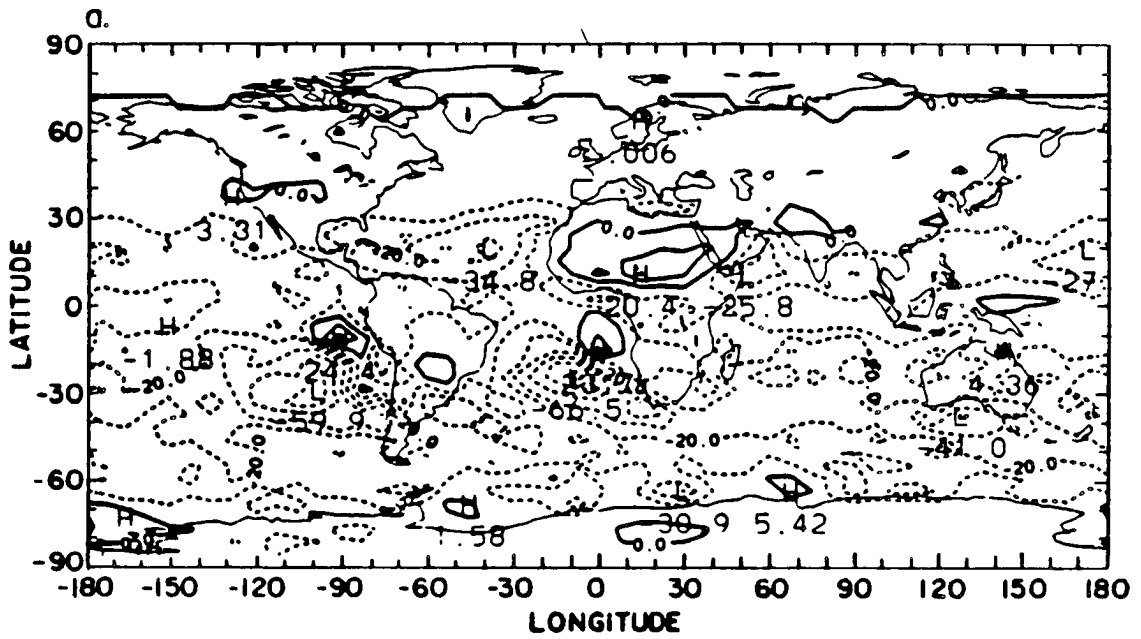


Figure 6.29: Standard deviation of the cloud shortwave radiative forcing (Wm^{-2}): (a) global distribution of the difference between the ECMWF and CONTROL simulations, and (b) zonally-averaged distribution.

processes remain unchanged in the ECMWF simulation. In particular, the correlation becomes mostly negative at a 3-day lag in both simulations. In addition, the variability of the clear-sky longwave flux is small compared to that of the cloud radiative forcing, as shown in Chapter Five. Therefore, and as at short wavelengths, variations in the outgoing infrared radiation between the ECMWF and CONTROL simulations mostly arise from variations in the total cloud cover.

6.8.1 Outgoing infrared radiation

Figure 6.30 shows the global distribution of the difference in the monthly-averaged outgoing infrared radiation between the ECMWF and CONTROL simulations, and the zonally-averaged profile of the radiation field for both simulations. As for C_L , the change in the distribution of the outgoing infrared radiation follows the change in the total cloud cover. In the ECMWF simulation, the increased cloudiness above the convective activity regions reduces the loss of terrestrial radiation to space while decreased cloudiness above the subtropical oceans increases the surface emission. The model zonal averages are compared against these computed from Nimbus-7 NFOV infrared data for January 1980. The ECMWF prediction scheme reproduces more successfully the minimum of outgoing infrared radiation at equatorial latitudes because of the greater cloud amount above the convective activity regions. The agreement between model and satellite-derived observations would be further improved if a smaller spatial resolution was used in the model. It is the best in the middle latitudes, especially in the winter hemisphere.

Figure 6.31 shows the global distribution of the difference in the standard deviation of the outgoing infrared radiation, and the zonally-averaged profile of $\sigma(\text{IR})$ for both simulations. The difference in $\sigma(\text{IR})$ has the same global distribution as the difference in $\sigma(C_L)$ but its magnitude also accounts for additional variability in the temperature and moisture fields. As for $\sigma(C_L)$, the most interesting information is the decrease in $\sigma(\text{IR})$ above the convective activity regions. The zonally-averaged profiles of $\sigma(\text{IR})$ obtained from the model are compared to that computed from daily mean satellite observations for January 1980. The zonal averages of $\sigma(\text{IR})$ are identical as those of C_L for both simulations

but are two times greater than that obtained from observations. Therefore, although there are significant differences in the monthly average and standard deviation of the total cloud cover between the ECMWF and CONTROL experiments, the implementation of the ECMWF cloud prediction scheme into CCM1 does not produce any substantial improvements in the simulation of the variability of the outgoing infrared radiation.

6.8.2 Planetary albedo

Figure 6.32 shows the global distribution of the difference in the monthly-averaged planetary albedo between the ECMWF and CONTROL simulations, and the zonally-averaged profile of α for both simulations. As for C_S , the difference in α is positive over the whole globe because of the increased cloudiness, except above the subtropical oceans. It is important to note the change in α along the western coasts of the continents which results from the inclusion of a separate parameterization of the planetary boundary-layer clouds in the ECMWF prediction scheme. The zonally-averaged distribution of α shows that both simulations similarly underestimate its magnitude along the ITCZ and in the middle latitudes because of the prescribed cloud optical thickness in the model.

Figure 6.29 shows that the reduction in the variability of the total cloud cover above the convective activity regions and the decreased cloudiness over the oceans yield a strong decrease in the standard deviation of the radiative forcing of clouds at short wavelengths. The global distribution of the difference in the standard deviation of the planetary albedo between the ECMWF and CONTROL simulations is shown in Figure 6.33, along with the zonally-averaged profile of $\sigma(\alpha)$ for both simulations. As for $\sigma(C_S)$, the difference in $\sigma(\alpha)$ is mostly negative above the oceans because of the decreased cloud cover in the ECMWF simulation. Above the convective activity regions, the impact of the decreased variability of the total cloud cover is not as large as the impact of the decreased cloud amount over the oceans. This was also observed in Figure 6.29 and actually seems less important than at infrared wavelengths. The zonally-averaged profile of $\sigma(\alpha)$ shows that the variability of the planetary albedo is strongly reduced at all latitudes when the ECMWF prediction scheme is used in CCM1. However, the comparison against the zonal distribution of $\sigma(\alpha)$

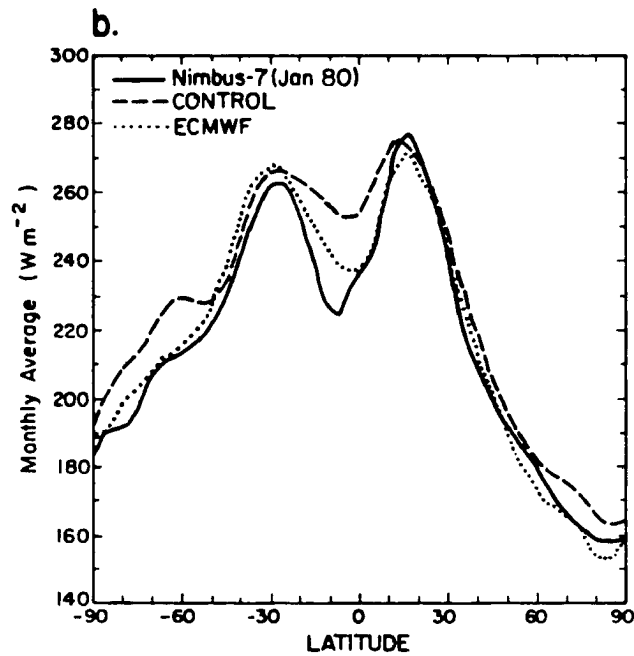
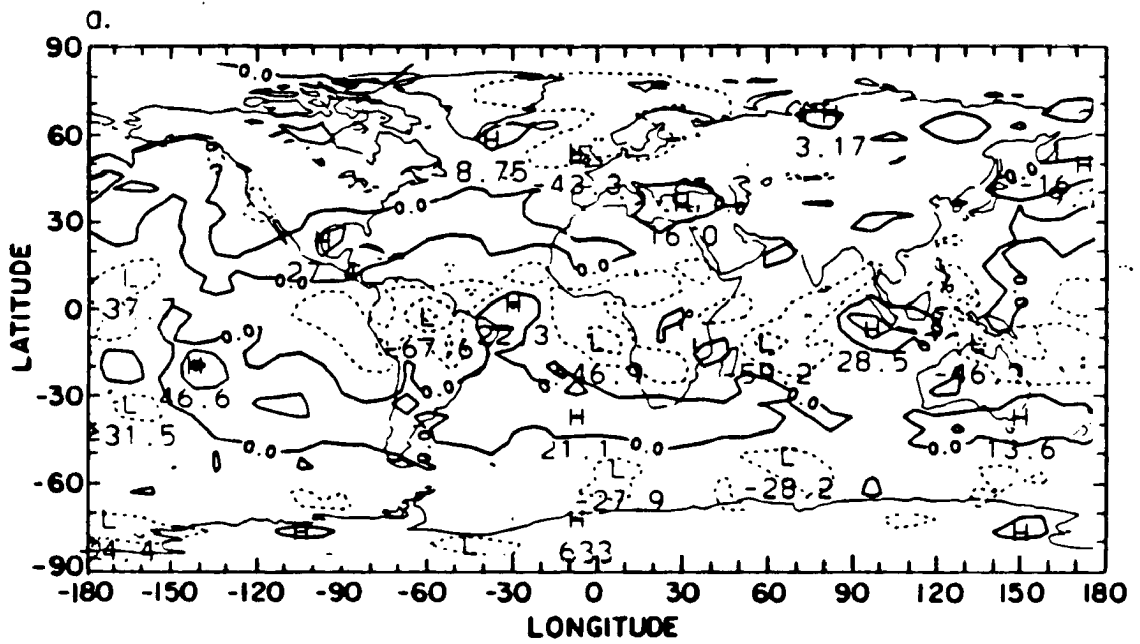


Figure 6.30: Monthly average of the outgoing infrared radiation (W m^{-2}): (a) global distribution of the difference between the ECMWF and CONTROL simulations, and (b) zonally-averaged distribution.

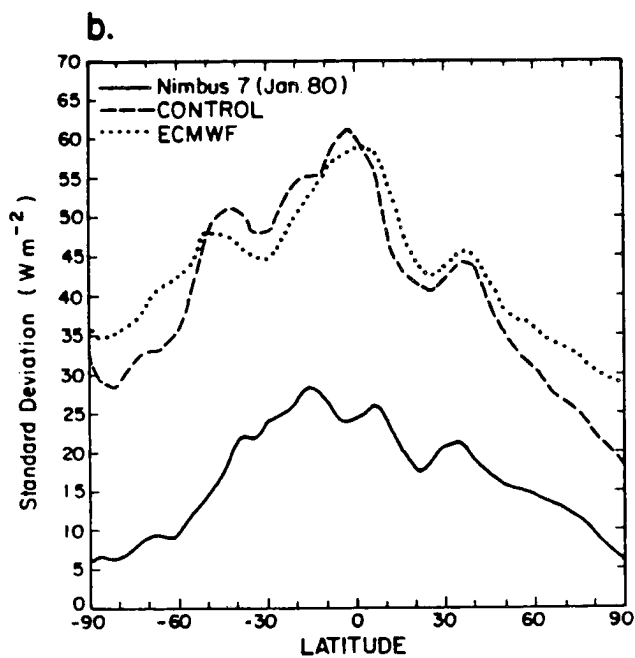
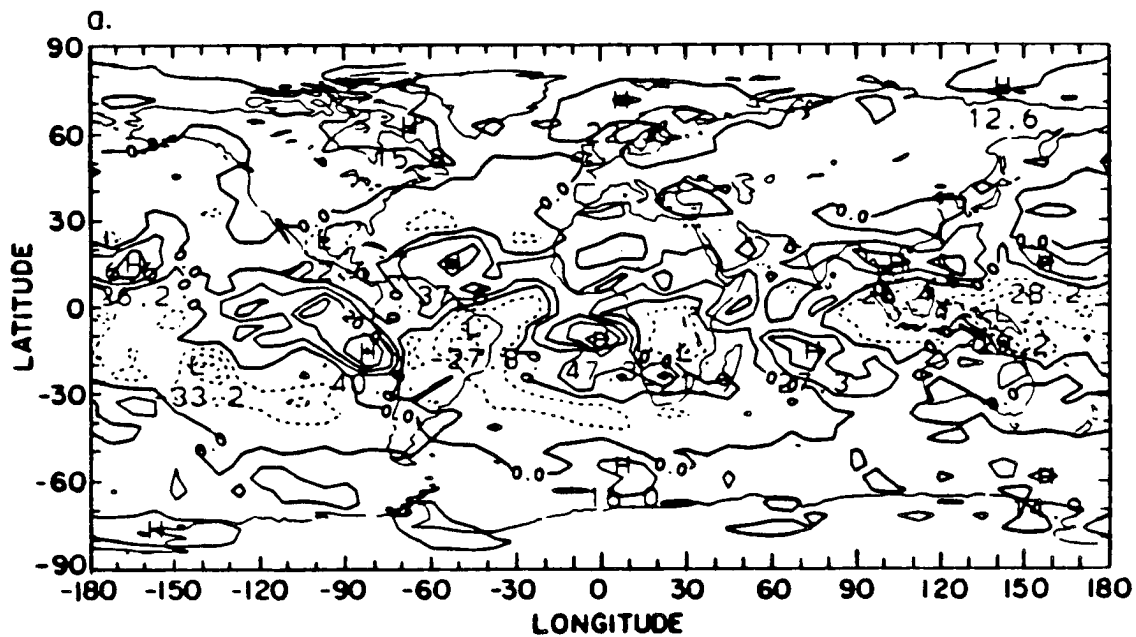


Figure 6.31: Standard deviation of the outgoing infrared radiation (Wm^{-2}): (a) global distribution of the difference between the ECMWF and CONTROL simulations, and (b) zonally-averaged distribution.

computed from satellite observations for January 1980 shows that its reduction actually results from a decrease in the total cloudiness rather than a decrease in its variability. The agreement between model and observations is very good in the subtropics, particularly in the summer hemisphere, while it strongly decreases along the ITCZ and in the middle latitudes. In addition, because of the discrepancies between the model-simulated and satellite-observed means, it is less reliable to discuss the changes that the ECWMF cloud prediction scheme produces on the temporal variability of the radiation field at short than at long wavelengths.

6.9 Discussion

In Section 6.3, it is argued that the parameterization of the convective clouds and cirrus anvils as functions of the time-averaged precipitation rate contributes to decreased fluctuations in the total cloud cover. This hypothesis is strongly supported by the fact that an increased total cloudiness above the convective activity regions does not produce an increase in its variability, as in the CONTROL simulation. This is not the case in the middle latitudes where an increased cloudiness results in higher values of the standard deviation, as in the CONTROL run. Therefore, the quadratic relationship between the cloud amount and the supersaturated relative humidity for clouds non-associated with convection does not make much difference in the fluctuations of the cloud cover. The comparison between the cloudiness generated by the ECMWF and CONTROL prediction schemes is not straightforward because clouds are not computed by cloud types but by layers in the CONTROL simulation. Therefore, it is only possible to discuss the difference in the vertical distribution of clouds in term of cloud fraction instead of cloud type. However, the differences in the distribution of the cloud longwave and shortwave radiative forcings, and the radiation balance components are completely explained using this hypothesis. It is especially supported from regional analyses of the model-generated radiation fields. In the CONTROL simulation, the standard deviation of the cloud radiative forcing at infrared and solar wavelengths increases with increasing values of the monthly average. Areas of high (respectively low) values of $\sigma(C_L)$ and $\sigma(C_S)$ superimpose very

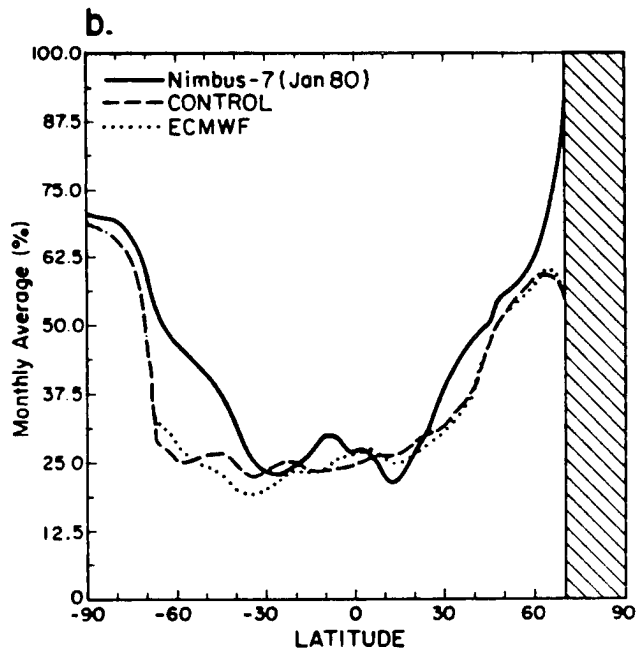
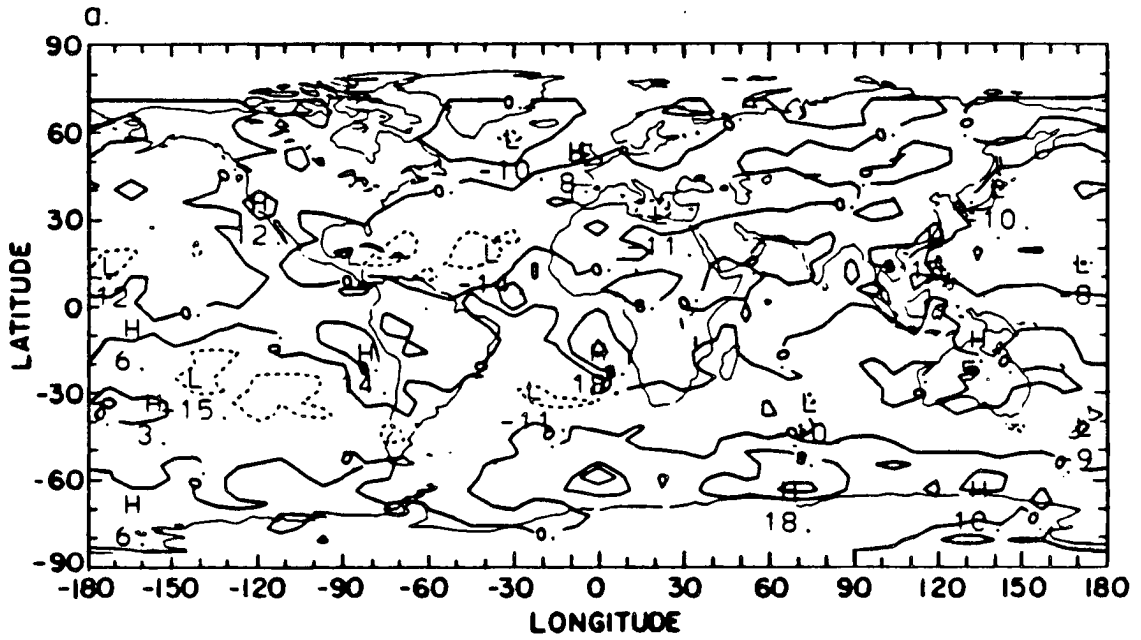


Figure 6.32: Monthly average of the planetary albedo (%): (a) global distribution of the difference between the ECMWF and CONTROL simulations, and (b) zonally-averaged distribution.

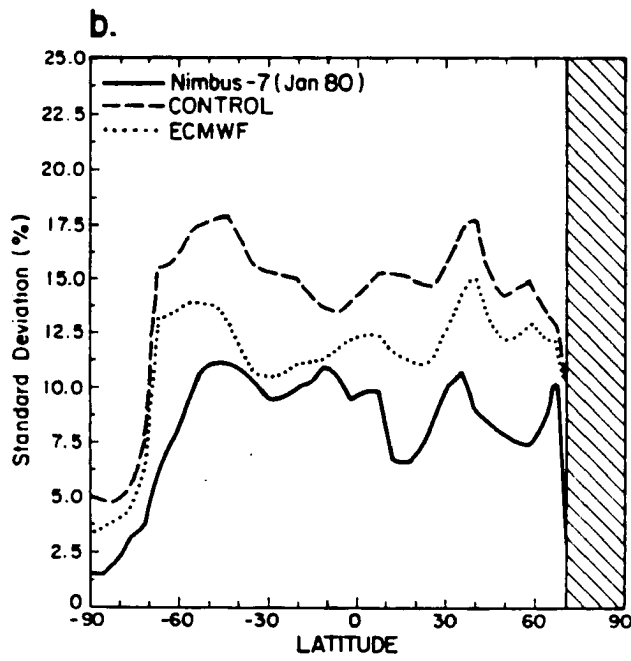
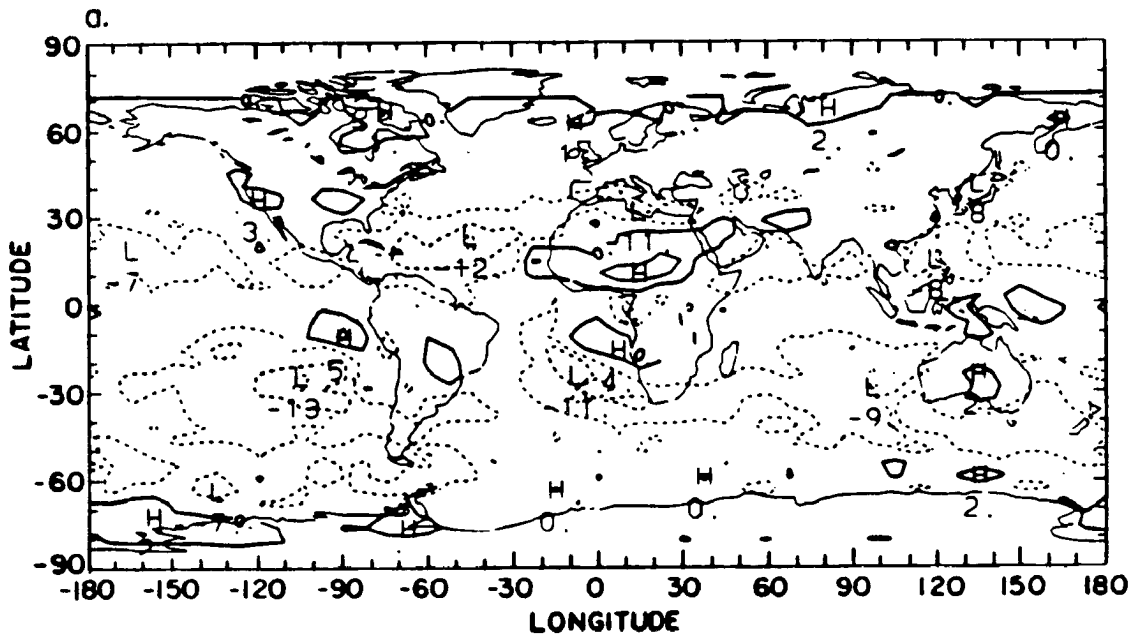


Figure 6.33: Standard deviation of the planetary albedo (%): (a) global distribution of the difference between the ECMWF and CONTROL simulations, and (b) zonally-averaged distribution.

well with areas of high (respectively low) values of C_L and C_S . The variability of the cloud radiative forcings increases with the variability of the total cloud cover, except in a very few areas. In the ECMWF simulation, there are not the same ratios $\frac{\sigma(C_L)}{C_L}$ and $\frac{\sigma(C_S)}{C_S}$ than in the CONTROL run. Increased values of C_L and C_S above the convective activity regions should produce greater values of $\sigma(C_L)$ and $\sigma(C_S)$ than those obtained in the CONTROL run, which is not the case. For instance, C_L is respectively equal to 90.5 and 115 Wm^{-2} above South America in the ECMWF and CONTROL runs for respective values of 75.2 and 62.3 Wm^{-2} for $\sigma(C_L)$. The greater cloud longwave and shortwave radiative forcings in the ECMWF simulation results from an increased cloudiness while their decreased variability results from reduced fluctuations of the total cloud cover.

Finally, Table 6.2 summarizes the globally-averaged impact of the ECMWF and CONTROL cloud prediction schemes on the model-generated radiation fields. On a global average, the net radiative forcing of clouds is respectively equal to -20.7 and -10.6 Wm^{-2} in the CONTROL and ECMWF simulations while the ECMWF total cloud cover is .8 % greater. This results from the simultaneous 7.6 Wm^{-2} increase at long wavelengths and 2.5 Wm^{-2} decrease at short wavelengths between the ECMWF and CONTROL cloud radiative forcings. The impact of the change in the spatial redistribution of clouds overcomes that of the change in the total cloudiness. In particular, it would be interesting to analyze separately the change in the cloud longwave and shortwave radiative forcings between land and oceans, especially for ECMWF and CONTROL experiments including a seasonal cycle instead of perpetual January conditions. The impact of the decreased variability of the total cloud cover in the ECMWF simulation is to decrease the globally-averaged standard deviation of the absorbed solar radiation by about 11.5 Wm^{-2} while that at long wavelengths is 1.5 Wm^{-2} greater than in the CONTROL run. On a global average, the increased cloud longwave and decreased cloud shortwave radiative forcings are respectively coupled with greater and smaller temporal fluctuations which was not true on regional scales.

6.10 Summary

In this chapter, the sensitivity of the model-generated radiation fields to the cloud cover distribution was studied by replacing the original code with an adapted version of the cloud prediction scheme of the ECMWF forecast model. The primary objective of this chapter was to analyze the change in the variability of the radiation balance components to the change in cloudiness while keeping the treatment of the interactions between clouds, radiation, and the other physical processes unchanged.

1. The ECMWF prediction scheme produces different temporal and spatial distributions of the cloud cover. The total cloudiness is greater over the continents and smaller over the oceans than in the CONTROL run while, in the vertical, there are more mid-tropospheric and less high-level clouds.
2. The radiative effect of the change in cloudiness between the ECMWF and CONTROL simulation is to increase the greenhouse effect and to decrease the albedo effect of clouds. On a global average, the net radiative effect of clouds is reduced by about a factor of two while keeping about the total cloud cover in both simulations.
3. The most interesting information is the decreased variability of the cloud radiative forcing at short and long wavelengths above the convective activity regions. We believe that the parameterization of the convective clouds and cirrus anvils developing with them as functions of the time-averaged precipitation rate yields smaller fluctuations in the total cloud cover and introduces some additional feedback between clouds and the hydrologic cycle.
4. Finally, despite significant differences in the radiative effect of clouds, including its temporal variability, the ECMWF and CONTROL simulations produce the same factor of two difference in the standard deviation between the model-generated and satellite-observed outgoing infrared radiation.

From this detailed comparison, it can be concluded that, in CCM1, any prediction scheme in which the cloud cover depends exclusively upon the large-scale synoptic fields

is likely to produce the same bias in the variability of the model-generated radiation fields. This study points the importance of a more physically-based representation of the interactions between clouds, radiation, and the hydrologic cycle. Analyses of the temporal variability of the cloud cover above convective activity regions is encouraging and strengthens the necessity to include a prognostic equation of the liquid water to correctly simulate the life-cycle of clouds. Finally, no attempts were made in this chapter to validate the simulated longwave and shortwave radiative impacts of clouds against observations. An extension of this work would be to compare the cloud radiative forcings obtained with CCM1 for both simulations against those, derived at the present time, from the Earth Radiation Budget Experiment.

Table 6.1

Table 6.1: List of time-span realizations used for comparison between the CONTROL and ECMWF climate simulations, for perpetual January conditions.

Days	History tapes	
	CONTROL	ECMWF
	/CSM/CCM1/223/	/CSM/SLINGOJ/
150.0-179.5	X22311-X223312	SLXD11-SLXD12
195.0-224.5	X22314-X223315	SLXD14-SLXD15
240.0-269.5	X22317-X223318	SLXD17-SLXD18
285.0-314.5	X22320-X223321	SLXD20-SLXD21
330.0-359.5	X22323-X223324	SLXD23-SLXD24

Table 6.2

Table 6.2: Globally-averaged values of the monthly average and standard deviation of the model-generated radiation fields. All the fields are given in $W m^{-2}$, except the planetary albedo and the total cloud cloudiness which are in %.

January conditions	CONTROL	ECMWF
<u>Monthly average:</u>		
Outgoing infrared radiation	239.6	232.6
Cloud longwave forcing	30.4	38.0
Absorbed solar radiation	248.6	251.1
Cloud shortwave forcing	51.1	48.6
Planetary albedo	31.3	30.7
Total cloud cover	47.5	48.3
<u>Standard deviation:</u>		
Outgoing infrared radiation	44.9	46.3
Cloud longwave forcing	40.3	42.6
Absorbed solar radiation	52.6	41.1
Cloud shortwave forcing	52.8	41.4
Planetary albedo	14.4	11.5
Total cloud cover	45.8	40.9

Chapter 7

INFLUENCE OF THE LARGE-SCALE PRECIPITATION RATE ON THE MODEL-GENERATED CLIMATE

7.1 Introduction

In the previous chapters, we stressed the importance of the interactions between clouds and the dynamic-hydrologic processes to the large-scale circulation of the atmosphere. In particular, clouds modify the heat budget of the surrounding environment through latent heat release and indirectly affect the large-scale motions. We listed the limitations in the treatment of those interactions in the NCAR CCM, which result from that no explicit prognostic equation of the liquid water content of clouds is included and that micro-physical processes involved in the formation of clouds and precipitation are neglected. We particularly emphasized the importance of a physically-based relationship between cloud amount and cloud liquid water for an improved representation of the cloud life-cycles in GCM climate simulations. In CCM1, the convective and large-scale condensation adjustments of Manabe *et al.* (1965) require condensation to be treated as a complete rainout process (or a 100 % precipitation efficiency) which forces clouds to precipitate more often than actually observed in the real atmosphere. In view of the impact of clouds on the vertical distribution of the radiative and condensational heating rates, it is legitimate to suspect that the on and off blinking of clouds may affect the total diabatic heating and general circulation of the model-simulated atmosphere. In addition, and because of the non-linear atmospheric response to climate forcings, the neglect of an additional feedback mechanism, as that produced by an interactive cloud liquid water content, may strongly affect the sensitivity of GCM-based climate simulations.

In this chapter, we attempt to reduce the temporal variability of the total cloud cover, at least regionally, by allowing only a fraction of the condensed water produced by the

large-scale condensation scheme to fall to the ground, while reevaporating the remaining fraction back into the atmosphere. Our primary objectives are to estimate the impact of an increased persistence of clouds, especially large-scale condensation clouds formed on the top of the convection, on the radiation and moisture budgets, and on the atmospheric circulation, and to infer the importance of reproducing more accurately the life-cycles of clouds in climate simulations made with CCM1. The water budget of individual tropical cloud clusters and mid-latitude convective complexes, as well as the impact of clouds upon the distribution of the diabatic heating rate, have been widely analyzed from observations and conceptual models (Houze and Betts, 1981; Gamache and Houze, 1982; Hartmann *et al.*, 1984). However, the ratio between precipitation and evaporation of large-scale cloud systems, as those simulated in GCMs, is unknown. In two similar experiments with CCM1, we arbitrarily choose a fraction of 50 % and 75 % between evaporation and precipitation of the condensed water resulting from large-scale adjustment. Only results from the second simulation are discussed. Starting at day 150 of the CONTROL run for perpetual January conditions, a 60-day run (later referred as HYDRO) was made in which we reduced the large-scale precipitation rate by 75 %. During the whole simulation, 25 % of the moisture condensed in the atmosphere was allowed to turn into rain while the remaining 75 % was added back into the moisture field and the temperature field corrected accordingly. In addition to the fact that the precipitation efficiency of large-scale cloud systems is mostly unknown, the choice of a 25 % large-scale precipitation efficiency was made to ensure a strong model response and, considering the length of the experiment, that the difference between the HYDRO and CONTROL simulations was greater than the model noise. The last 30 model-days are used in our comparison between the HYDRO and CONTROL simulations.

In the following section, we describe the large-scale condensation scheme of Manabe *et al.* (1965). Changes in the hydrologic and radiative budgets are respectively analyzed in Sections 7.3 and 7.4. The impact of the reduced rain efficiency and increased cloudiness on the vertical distribution of the diabatic heating rates and the induced variations in the temperature and wind fields are discussed in Sections 7.5 and 7.6. In Section 7.7 and

in view of our results, we address the importance of an improved representation of the temporal variability of the cloudiness and the radiation budget components in climate-related studies.

7.2 Description of the large-scale condensation adjustment scheme

The large-scale condensation adjustment scheme of Manabe *et al.* (1965) is applied after the dry and moist convective adjustments are made. The dry convective adjustment is called first and takes place in the stratosphere of the model only. If the predicted atmosphere is non-saturated and the lapse rate exceeds the dry adiabatic lapse rate, temperatures are reset to respect the dry adiabatic lapse rate. The moist convective adjustment is then applied when the atmosphere is supersaturated and unstable. In that case, the moisture and temperature fields are simultaneously adjusted so that the atmosphere becomes just saturated and satisfies the moist adiabatic lapse rate. Finally, the large-scale condensation adjustment scheme is called when the atmosphere is supersaturated but stable. The moisture field is adjusted to be just saturated and the temperature field is corrected to reflect the heating due to latent heat release. The equations of the large-scale condensation scheme are described below:

If for a grid-point at a given σ -level, the temperature lapse rate is stable but the moisture is supersaturated, or:

$$\frac{\hat{q}}{\hat{q}_s} > 1.0, \quad (7.1)$$

the temperature and moisture fields are simultaneously adjusted so that the grid-point becomes just saturated. The new specific humidity is given by the relation:

$$q = \hat{q}_s + \frac{d\hat{q}_s}{dT}(T - \hat{T}), \quad (7.2)$$

in which \hat{T} and \hat{q} (respectively T and q) are the temperature and specific humidity before (respectively after) adjustment, and \hat{q}_s is the saturation specific humidity. \hat{q} and $\frac{d\hat{q}_s}{dT}$ are computed by the expressions:

$$\hat{q} = \frac{\epsilon \hat{e}_s}{p - (1 - \epsilon) \hat{e}_s}, \quad (7.3)$$

and

$$\frac{d\hat{q}_s}{dT} = \left[\frac{\sigma p_s}{\sigma p_s - (1 - \epsilon)\hat{e}_s} \right] \frac{L\hat{q}_s}{R_{H_2O}\hat{T}^2}. \quad (7.4)$$

In equations 7.3 and 7.4, $\epsilon = 0.622$. e_s and p_s are the saturation vapor pressure and the surface pressure. L is the latent heat of evaporation and R_{H_2O} is the gas constant for water vapor. The temperature change due to the release of latent heat during condensation is:

$$(T - \hat{T}) = \frac{L}{C_p}(\hat{q} - q), \quad (7.5)$$

which yields Equation 7.3 to

$$q = \hat{q} - \frac{(\hat{q} - \hat{q}_s)}{\left(1 + \frac{L}{C_p} \frac{d\hat{q}_s}{dT}\right)}. \quad (7.6)$$

C_p is the specific heat at constant pressure. Equations 7.5 and 7.6 are iterated twice. The rate of large-scale precipitation at that σ -level is expressed by the relation:

$$q_{cs} = p_s(\hat{q} - q) \frac{\Delta\sigma}{g}. \quad (7.7)$$

The rate of stable precipitation ($q_{cs}/(2\Delta t)$) is added to that from the moist convective adjustment ($q_{cu}/(2\Delta t)$) to give the total rate of precipitation at each level for later use in the cloud scheme:

$$q_{ct} = \frac{q_{cs}}{2\Delta t} + \frac{q_{cu}}{2\Delta t}. \quad (7.8)$$

In both the HYDRO and CONTROL experiments, the convective and large-scale precipitation rates are computed every 30 mn while a full computation of the cloudiness, and the longwave and shortwave radiative heating rates is made every 12 hours. A partial computation of the surface radiative fluxes is made every 30 mn, to derive the surface temperature from the surface energy balance equation and to compute the latent and sensible heat turbulent fluxes. Clouds form if the total precipitation rate, accumulated over every time-step between full computation of the cloudiness and radiation, is positive. q_{ct} is reset to zero after the call to the cloud and radiation routines, and evaporation has completely compensated precipitation at the ground after 12 hours.

7.3 HYDRO versus CONTROL hydrologic cycle

In the HYDRO experiment, a reduced large-scale precipitation rate yields an increased moisture content in the atmosphere and a decreased total precipitation rate at the ground. As a result, the atmosphere stays closer to unstable conditions, and condensation and cloudiness are likely to form more often than in the CONTROL experiment.

7.3.1 Difference in the frequency of condensation

Figures 7.1 and 7.2 show time series of the condensation rate at single grid-points located both in the Pacific ocean, in the tropics and the middle latitudes. It results from the moist convective and large-scale condensation adjustments, and is shown at the three highest σ -levels of the troposphere. Although negative specific humidities are removed by taking moisture from neighboring grid-points, negative values of the total condensation rate may still occur, but their effect is very small. As expected, condensation forms more often in the HYDRO than the CONTROL experiment because increased moisture is held in the atmosphere, and the adiabatic lapse rate stays closer to unstable conditions than when condensation is treated as a complete rainout process. In addition, as the total condensed water is accumulated over the 12 hours preceding full computation of the vertical distribution of cloudiness and radiative heating rates, the higher frequency of large-scale adjustment every 30 mn time-step yields increased values of the total condensation rate in the HYDRO simulation.

Figure 7.3 shows time series of the total cloud cover at the same grid-points than the total condensation rate while Figure 7.4 shows the zonally-averaged distribution of the mostly cloudy-sky frequency obtained from both simulations. As the prediction of clouds depends upon a positive value of the accumulated condensed water, there is a strong difference in the distribution of the total cloud cover between the HYDRO and CONTROL simulations. Both grid-points stay overcast over a longer time period in the HYDRO than in the CONTROL simulation, as indicated by decreased 12-hour fluctuations in the total cloud amount. The higher occurrence of clouds in the HYDRO simulation is very well seen in Figure 7.4. A 75 % reduction of the large-scale precipitation efficiency yields a 15 % increase of the globally-averaged cloud frequency.

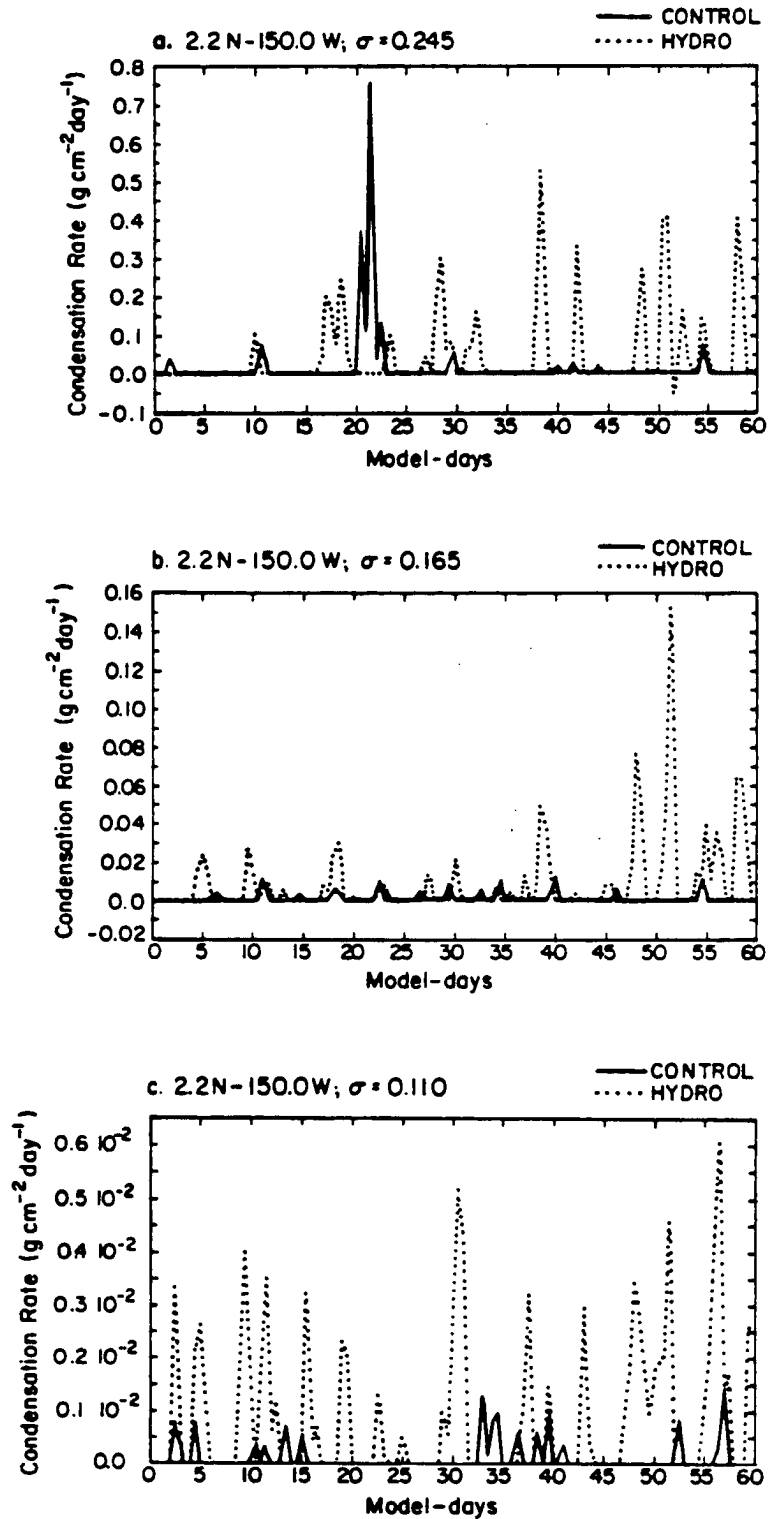


Figure 7.1: Time series of the total condensation rate obtained from the HYDRO and CONTROL simulations at a single grid-point located at 2.2°N-150.0°W ($10^2 \text{ g cm}^{-2} \text{ day}^{-1}$): (a) $\sigma = .245$, (b) $\sigma = .165$, and (c) $\sigma = .110$

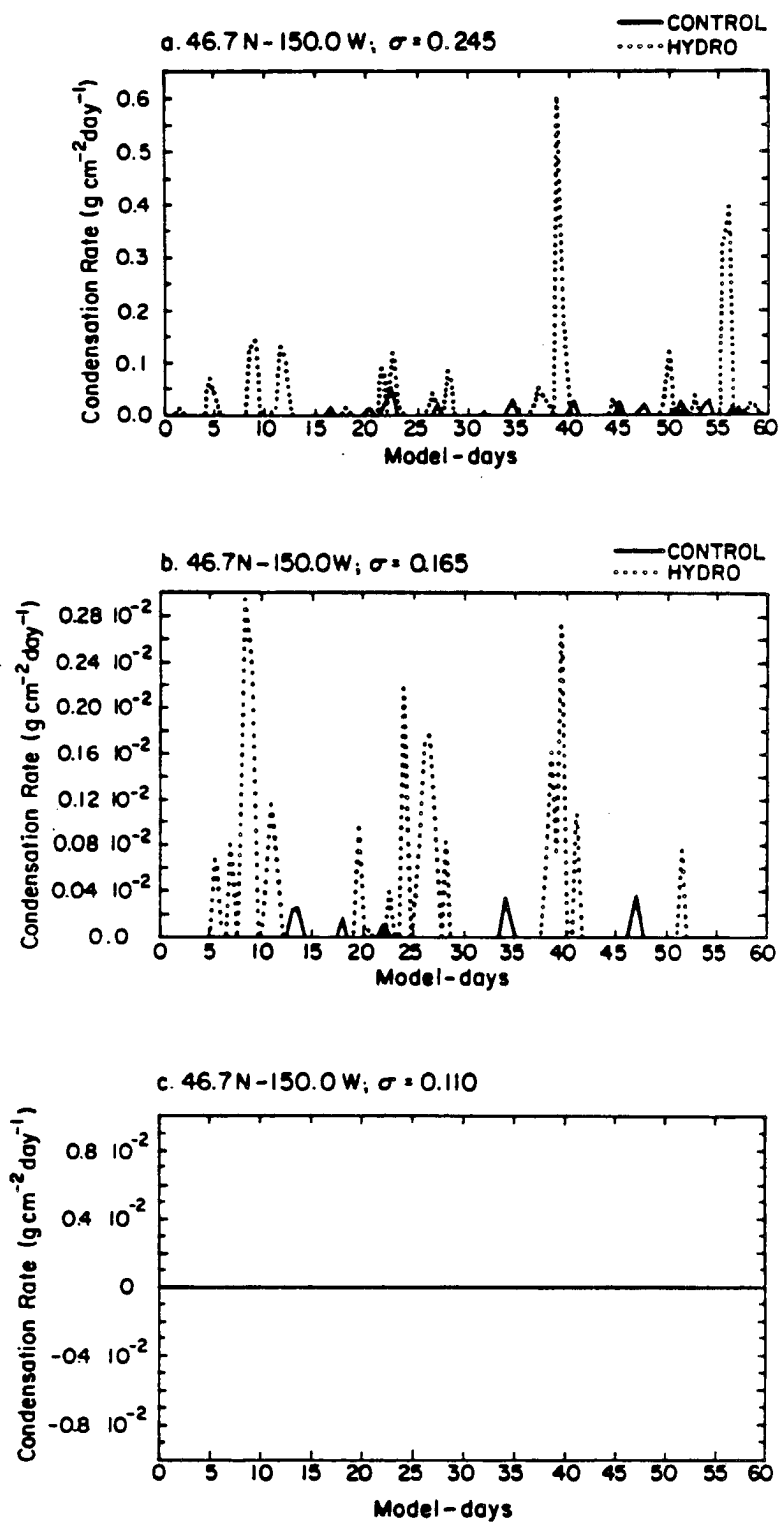


Figure 7.2: Time series of the total condensation rate obtained from the HYDRO and CONTROL simulations at a single grid-point located at 46.7°N-150.0°W ($10^2 \text{ g cm}^{-2} \text{ day}^{-1}$): (a) $\sigma = .245$, (b) $\sigma = .165$, and (c) $\sigma = .110$

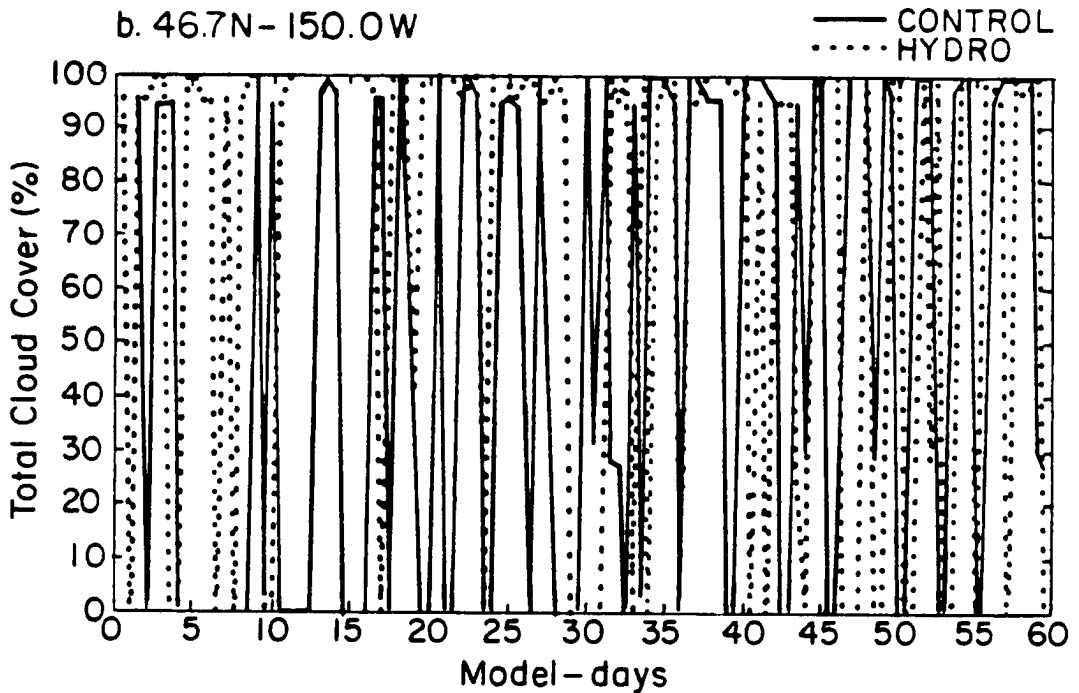
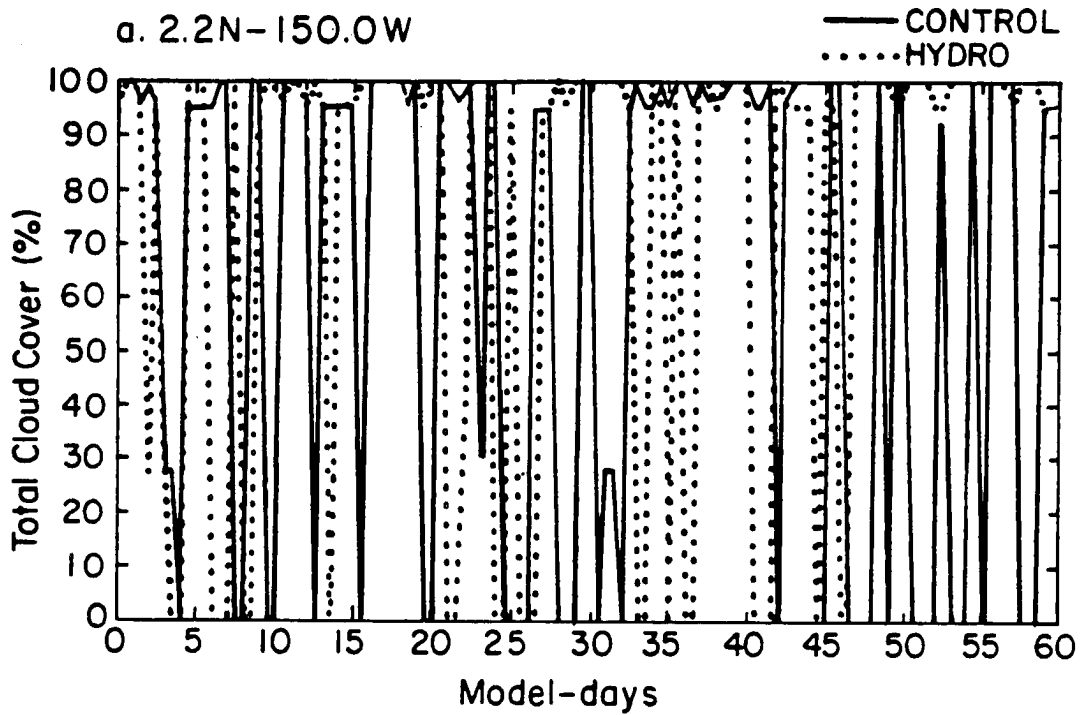


Figure 7.3: Time series of the total cloud cover (%) predicted with the HYDRO and CONTROL simulations at a single grid-point located at: (a) 2.2°N-150.0°W, and (b) 46.7°N-150.0°W.

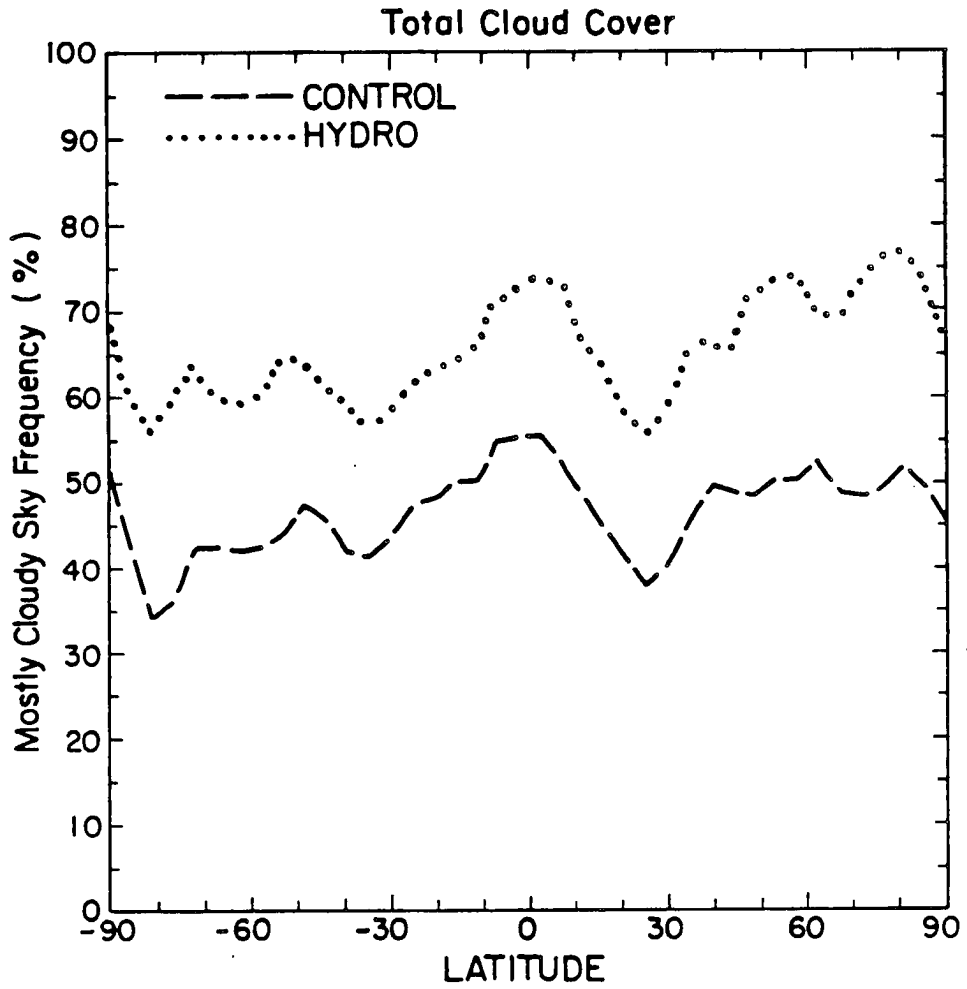


Figure 7.4: Zonally-averaged distribution of the mostly cloudy sky frequency (total cloud cover greater than 80 %) for the HYDRO and CONTROL simulations (%).

7.3.2 Difference in the moisture budget

1. Precipitation rates

In the CONTROL simulation, the vertically-averaged condensed water, after moist convective and large-scale adjustments are made, is equal to the total precipitation reaching the ground. Figures 7.5, 7.6, and 7.7 represent global maps of the large-scale, moist convective, and total precipitation rates obtained with the CONTROL run, and the zonally-averaged distribution of all three quantities for both simulations. As already discussed in Section 4.2, CCM1 reproduces successfully the regions of large-scale and convective precipitation for January-averaged conditions. These regions are: the tropical rainfall regions over the continents and the convective activity regions along the ITCZ over the oceans in the summer hemisphere, and the storm track regions above the North Pacific and North Atlantic oceans in the winter hemisphere. On a global average, the large-scale (respectively moist convective) precipitation rate contributes for about one third (respectively two third) to the total precipitation rate. However, the magnitude of the total precipitation rate is too large by about a factor of two when compared against observations, especially above regions of heavy tropical rainfall. This excess rainfall has to be attributed to the complete removal of all condensed water from the atmosphere to the ground. A 75 % reduction in the large-scale condensation efficiency yields a decreased large-scale precipitation rate at all latitudes while the convective precipitation rate slightly increases, especially in the summer hemisphere. It is also interesting to note the shift in the maximum convective rainfall rate between the HYDRO and CONTROL simulations. The compensating effect between the reduced large-scale and increased convective precipitation rates, and the smaller contribution of large-scale condensation to the total rainfall lead to a small difference in the total precipitation rate between the HYDRO and CONTROL simulations. In particular, the change in the large-scale precipitation rate does not help reduce the excess model-generated rainfall rates in the tropics.

Conservation of the total moisture requires that the evaporation rate equals the precipitation rate after 12 hours. Figure 7.8 shows the global distribution of the evaporation

rate computed from the CONTROL simulation, and its zonally-averaged distribution for both simulations. The decrease in the evaporation rate balances the decrease of the total precipitation rate and is the largest between 30°N and 30°S.

2. Humidity field

In the HYDRO simulation, 75% of the large-scale condensed water is assumed to be reevaporated and mixed back into the humidity field, and the temperature field is corrected accordingly. As less liquid water is removed from the atmosphere, the correction of the temperature field for latent heat release is smaller in the HYDRO than the CONTROL simulation. The decreased total precipitation rate at the ground yields an increased moisture content in the troposphere. Figure 7.9 shows the latitude-height distribution of the 30-day averaged specific humidity for the CONTROL run and of its difference between the HYDRO and CONTROL simulations. The largest increase in the moisture field takes place mostly in the low troposphere below $\sigma = 0.664$, with a maximum increase in the tropics. Figure 7.10 shows the latitude-height distribution of the difference in the relative humidity between the HYDRO and CONTROL simulations. On the one hand, as the atmosphere close to the surface is mostly saturated, the difference in the relative humidity is small below $\sigma = .811$. On the other hand, the increased moisture content is the largest in the upper troposphere which remains close to supersaturation in the middle latitudes, especially in the winter hemisphere. At high altitudes, the increase in the relative humidity results primarily from the change in the temperature field since the change in the specific humidity itself remains small. Therefore, the change in the moisture content which compensates the change in the total condensation rate produces a thick envelop of moisture below the tropopause height. Its effect upon the radiation fields is twofold: (1) To increase the opacity of the atmosphere and saturate the water vapor absorption bands; and (2) To indirectly create a high-level cloud shield and increase the greenhouse warming of the atmosphere.

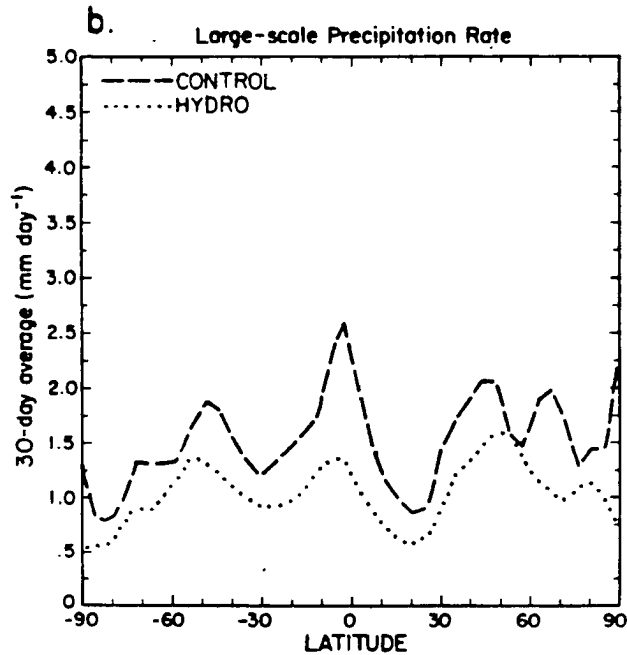
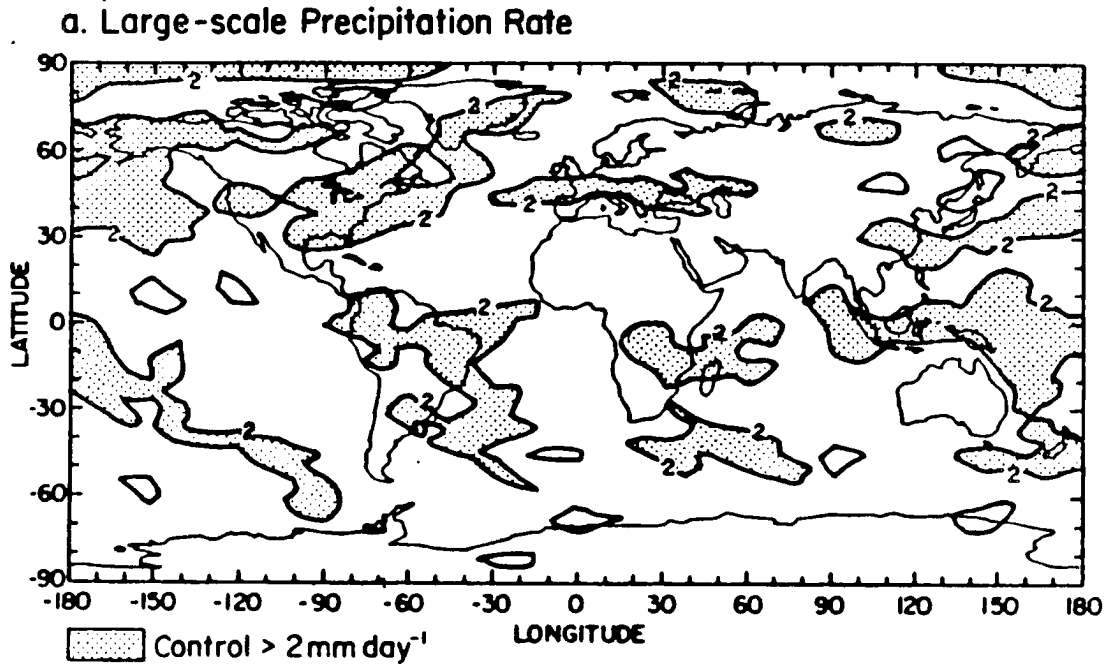


Figure 7.5: 30-day average of the large-scale precipitation rate (mm day^{-1}): (a) global distribution computed from the CONTROL simulation, and (b) zonally-averaged distribution.

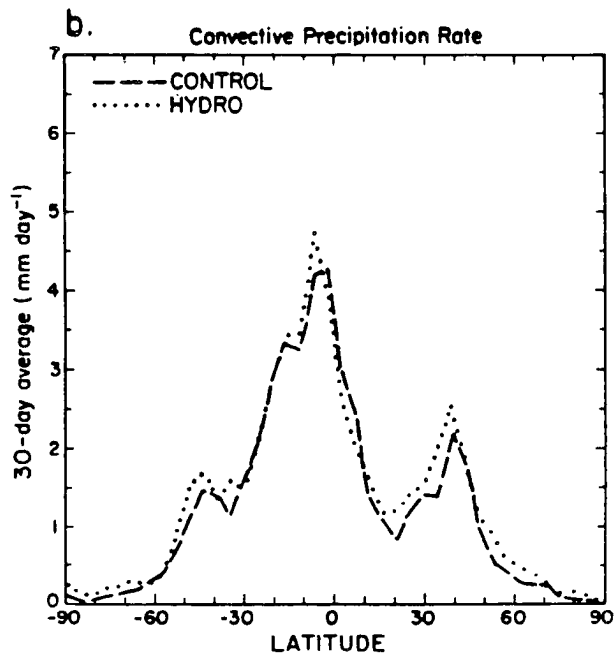
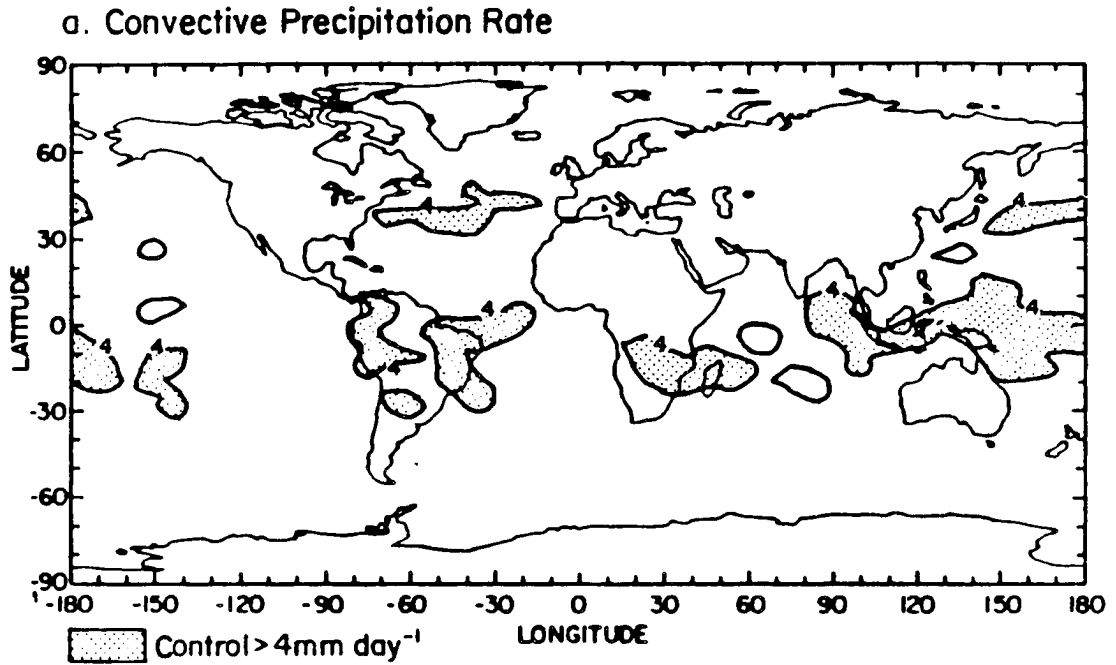


Figure 7.6: 30-day average of the convective precipitation rate (mm day^{-1}): (a) global distribution computed from the CONTROL simulation, and (b) zonally-averaged distribution.

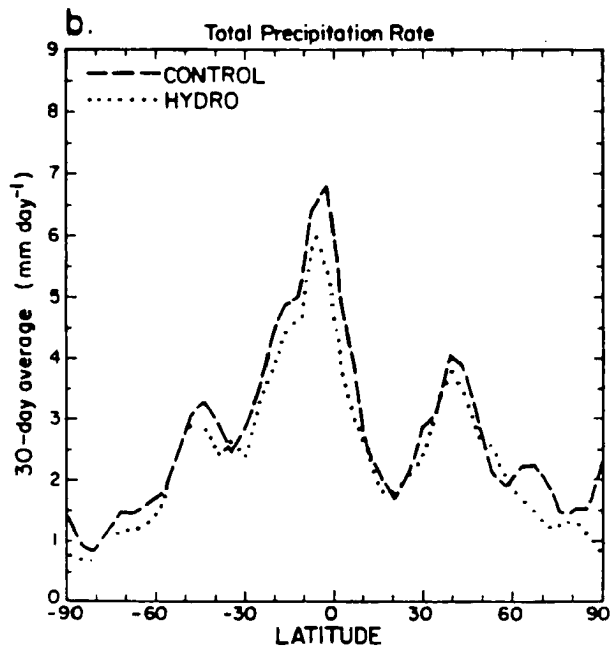
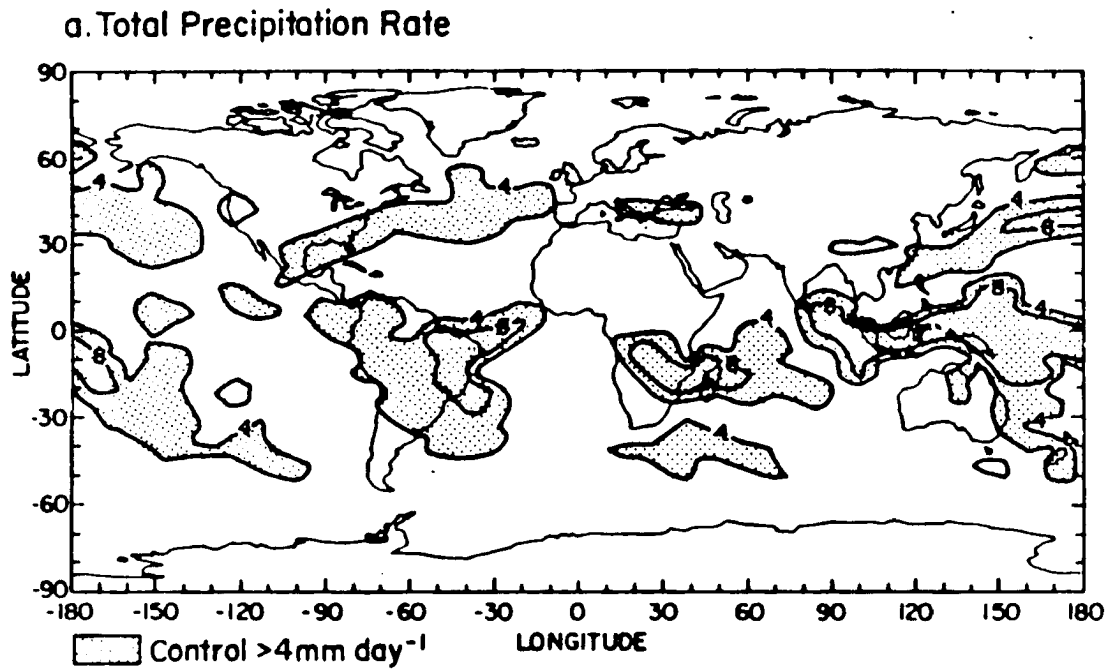


Figure 7.7: 30-day average of the total precipitation rate (mm day^{-1}): (a) global distribution computed from the CONTROL simulation, and (b) zonally-averaged distribution.

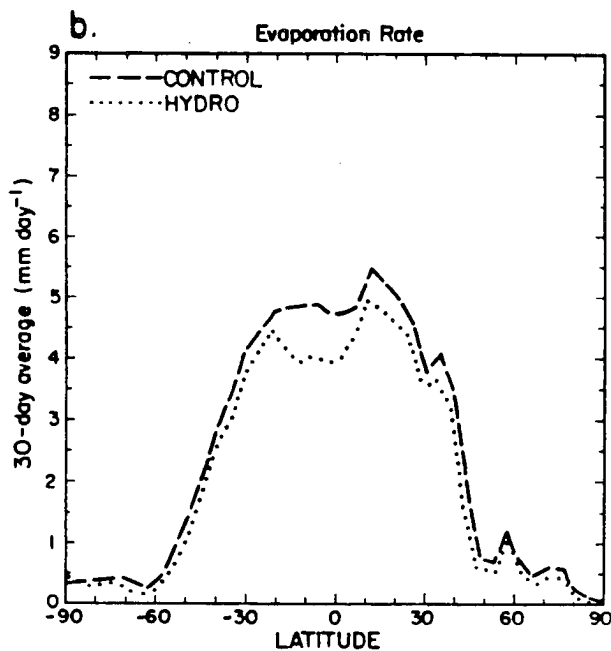
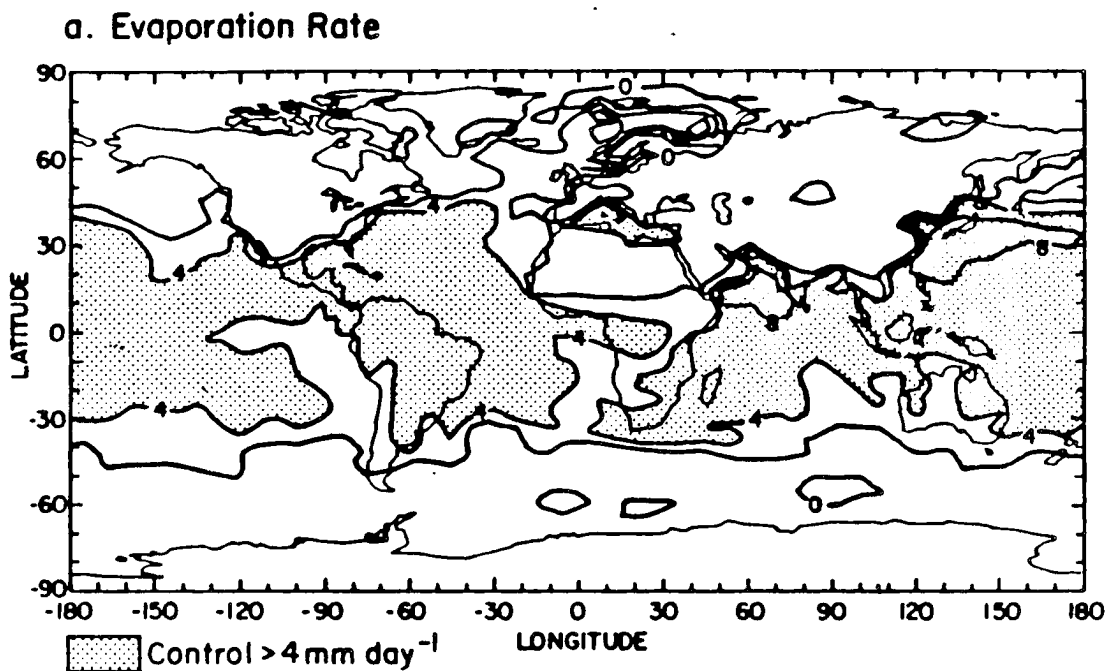


Figure 7.8: 30-day average of the evaporation rate (mm day^{-1}): (a) global distribution computed from the CONTROL simulation, and (b) zonally-averaged distribution.

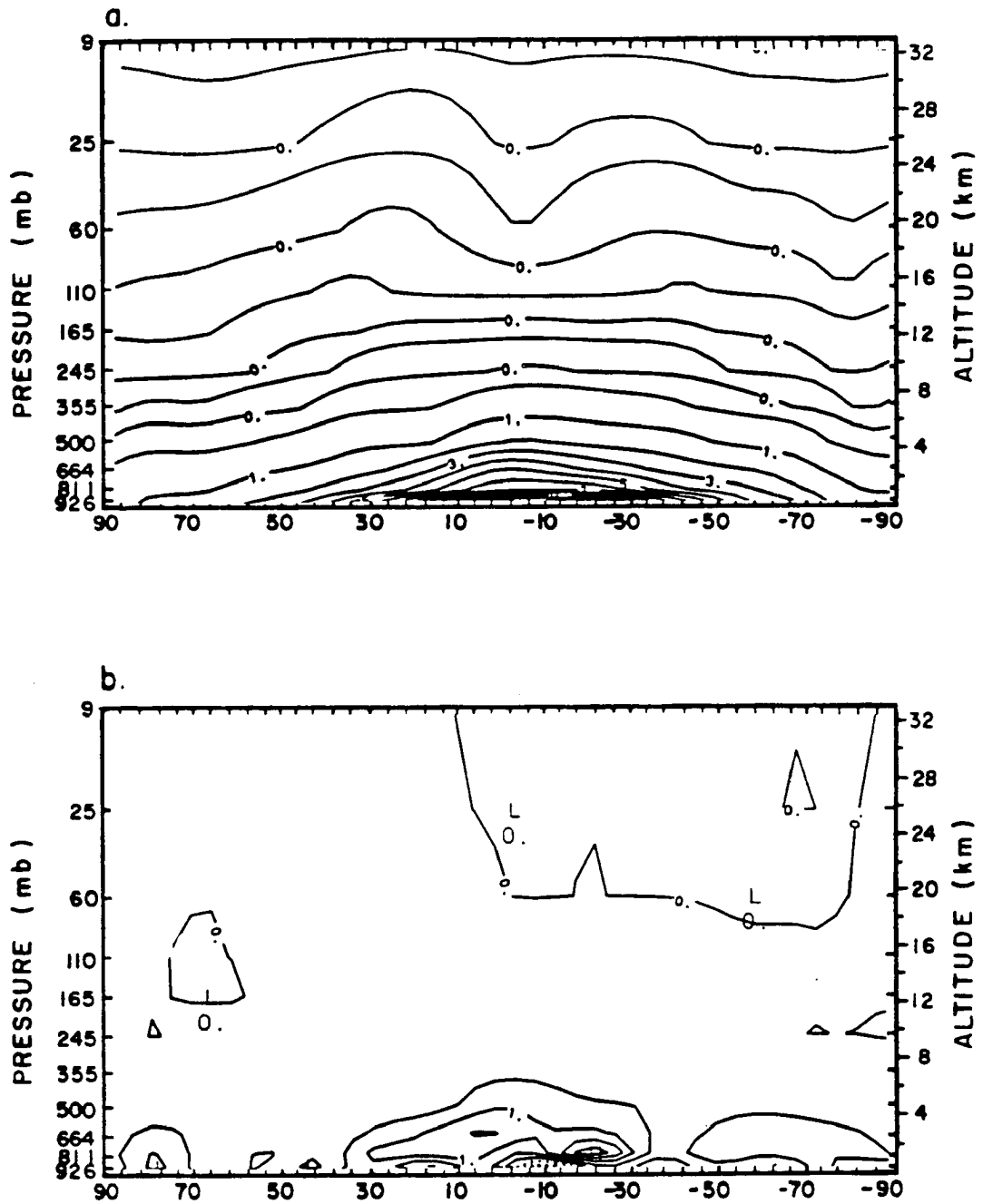


Figure 7.9: Latitude-height distribution of the 30-day average of the specific humidity (10^3 Kg Kg^{-1}): (a) distribution computed from the CONTROL simulation, and (b) difference between the HYDRO and CONTROL simulations.

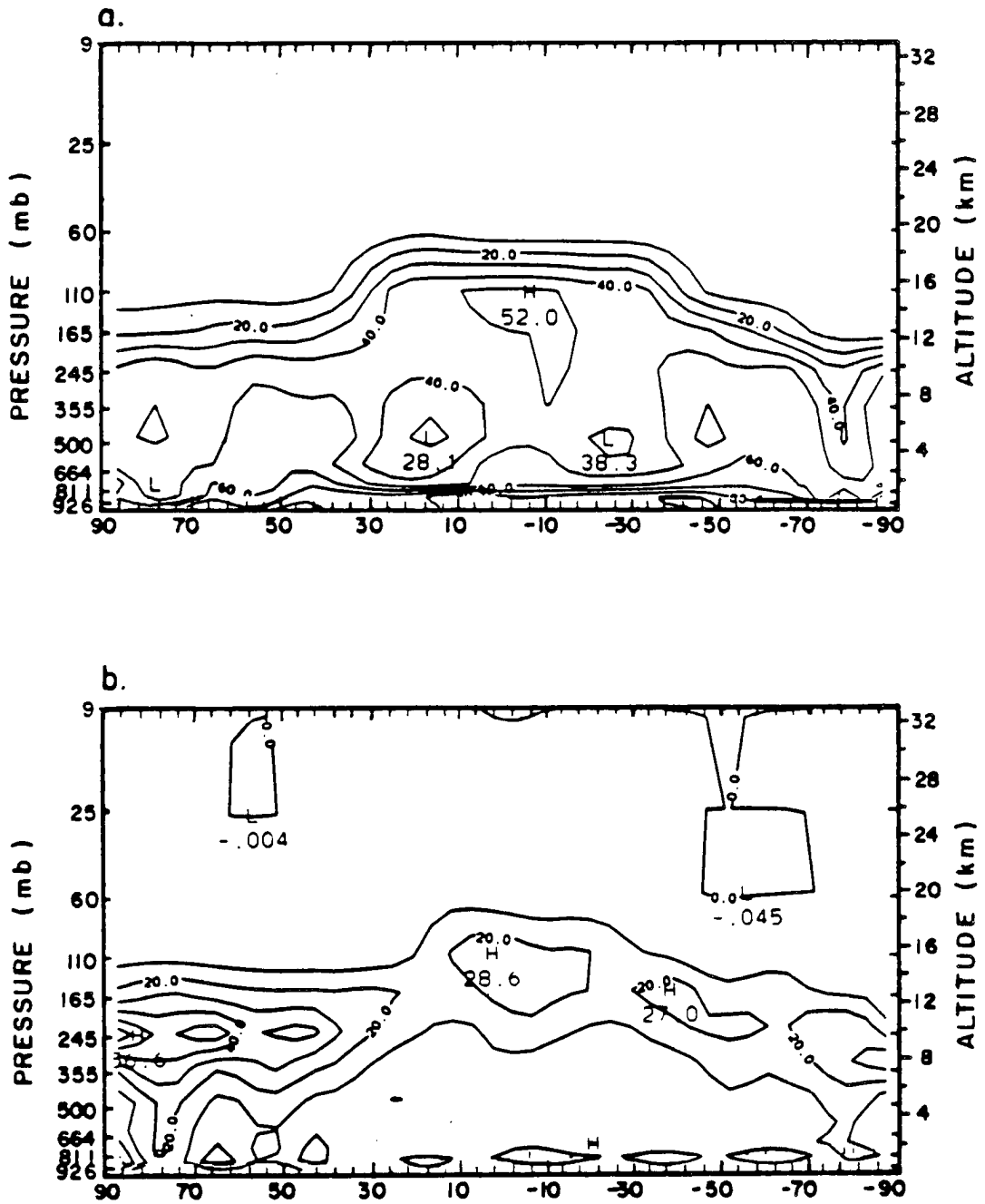


Figure 7.10: Latitude-height distribution of the 30-day average of the relative humidity (%): (a) distribution computed from the CONTROL simulation, and (b) difference between the HYDRO and CONTROL simulations.

7.3.3 Difference in the cloud cover

Figure 7.11 shows the global distribution of the difference in the 30-day average and standard deviation of the total cloud cover between the HYDRO and CONTROL simulations. The higher occurrence of clouds, induced by the higher frequency of condensation, yields a global increase in the time-averaged total cloud cover and decrease in its standard deviation, especially above mostly overcast regions. This effect is particularly well seen in the tropics, above the winter monsoon and tropical rainfall regions, as well as in the polar latitudes. However, the forcing of increased moisture in the atmosphere has a negative effect above the clear-sky desert regions which become partially cloudy in the HYDRO simulation. This is one drawback of the HYDRO simulation. In view of those two maps, the HYDRO experiment is successful to reduce the temporal variability of the total cloud cover in some regions, especially the tropical convective activity regions which radiation budget undergoes significant day-to-day fluctuations.

The difference in the distribution of cloudiness is the largest in the upper troposphere, which is in accordance with the difference in the moisture distribution between the HYDRO and CONTROL simulations. Figures 7.12 and 7.13 show the latitude-height distribution of the 30-day average of the cloud cover and effective cloud cover ¹ for the CONTROL run, and their difference between the HYDRO and CONTROL simulations. The inclusion of the cloud emissivity as a function of the condensed water produces an additional feedback mechanism in the change of the effective cloud cover between the two simulations. In the model, the emissivity is equal to one for all clouds, except for high-level large-scale condensation clouds for which it is less than unity. The latitude-height distribution of the cloud emissivity would show that lowest emissivity values correspond to highest cloud cover amounts. As a result, the position of highest effective cloud amounts is located below that of highest cloud amounts, i.e. at levels which show larger emissivity values. The increase of the upper-level cloud deck between the HYDRO and CONTROL

¹The effective cloud cover is equal to the cloud cover times the cloud emissivity

simulations is the largest, especially at very high latitudes, but its magnitude is strongly damped when the cloud emissivity feedback is included. The top figures show that the effect of an interactive emissivity is to lower the height of the cloud column and, therefore, to reduce the greenhouse warming of the atmosphere. In the CONTROL simulation, the standard deviation of clouds increases with increasing cloud amounts, so that the impact of emissivities less than one is to actually decrease the variability of the total cloud cover at long wavelengths.

Figure 7.14 shows the difference in the standard deviation of the cloud cover and effective cloud cover between the HYDRO and CONTROL simulations. In the CONTROL simulation, there is a strong correspondence between the zonally-averaged distribution of the 30-day average and standard deviation of the cloud cover, and high-level clouds are associated with large values of the standard deviation. Because of important contrasts in the longitudinal distribution of clouds and their variability, and in contrast to the decreased variability of the total cloud amount at regional scales, the increased cloud cover yields increased values of the standard deviation on a zonal mean, in the HYDRO simulation.

7.3.4 Conclusion

The reduction in the large-scale precipitation efficiency and the compensating increased atmospheric moisture content of the atmosphere yield significant differences in the distribution of the hydrologic budget between the HYDRO and CONTROL simulations, in particular the relative humidity field. In the HYDRO case, the higher frequency of condensation arising from the greater moisture content leads to increased accumulated values of the total condensed water. As a result, clouds form more often than in the CONTROL run. Analyses of the distribution of the total cloud amount show that we were partially successful at interactively producing mostly overcast conditions over limited areas, especially over the tropical convective activity regions. Over those regions, the temporal variability of the total cloud cover decreases in the HYDRO simulation. Therefore, the reduction of the large-scale precipitation efficiency produces the correct mechanism to enhance the stability of the regional-scale cloud cover. It is shown that increased upper-level clouds are mostly responsible for the change in the total cloudiness

between the HYDRO and CONTROL runs. Because of their strong potential for greenhouse warming, we can expect to see significant modifications in the distribution of the tropospheric radiative heating and the model-generated general circulation. Finally, Table 7.1 provides a summary of the globally-averaged components of the hydrologic budget for both simulations.

7.4 HYDRO versus CONTROL planetary radiation balance

One of the objectives of the HYDRO simulation was to attempt to reduce the temporal variability of the radiation balance components and to come up with an improved agreement between the standard deviation of the model-generated and observed radiation fields. In this section, we analyze the impact of the increased cloudiness upon the distribution of the outgoing infrared radiation and planetary albedo, including their temporal variability.

7.4.1 Outgoing infrared radiation

Figure 7.15 shows the global distribution of the difference in the 30-day average of the outgoing infrared radiation between the HYDRO and CONTROL simulations, and its zonally-averaged distribution for both simulations. The global increase of the total cloud cover, in particular of the high-level clouds, leads to a decrease of the outgoing infrared radiation at the top of the model atmosphere. The largest increase in the cloud longwave radiative forcing takes place in most of the tropical convective activity regions, so that the HYDRO simulation produces the minimum outgoing infrared radiation observed from the Nimbus-7 scanners. On the other hand, the increased total cloud cover in the subtropics and the middle latitudes yields systematically lower values of the outgoing infrared radiation than from Nimbus-7 observations.

Figure 7.16 shows the global distribution of the difference in the standard deviation of the outgoing infrared radiation between the HYDRO and CONTROL simulations, and its zonally-averaged distribution for both simulations. Except in a few areas, the largest being the winter monsoon region, the HYDRO experiment fails to significantly reduce the

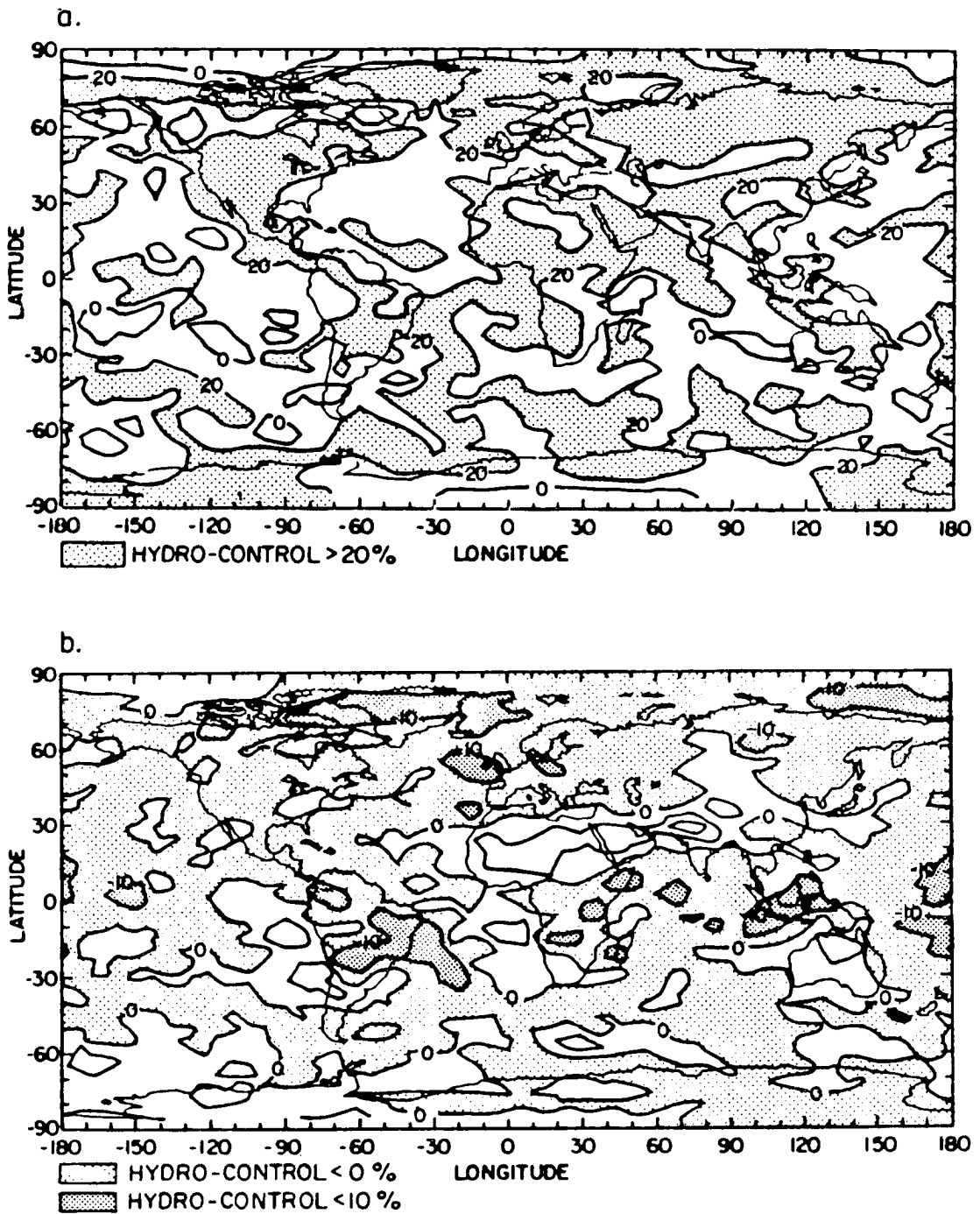


Figure 7.11: Map of the difference in the total cloud cover between the HYDRO and CONTROL simulations (%): (a) distribution of the 30-day average, and (b) distribution of the standard deviation.

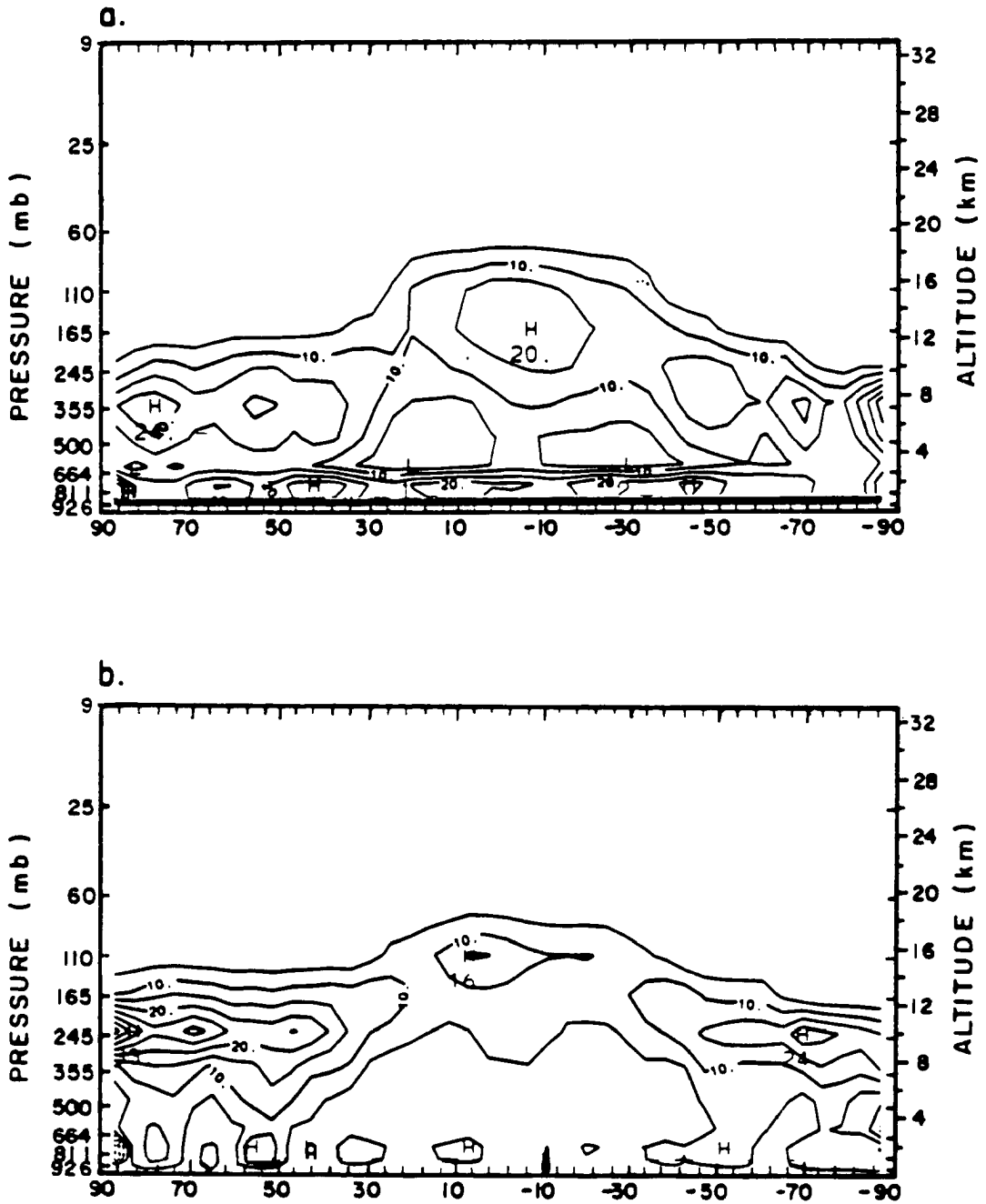


Figure 7.12: Latitude-height distribution of the 30-day average of the cloud cover: (a) computed from the CONTROL simulation, and (b) difference between the HYDRO and CONTROL simulations.

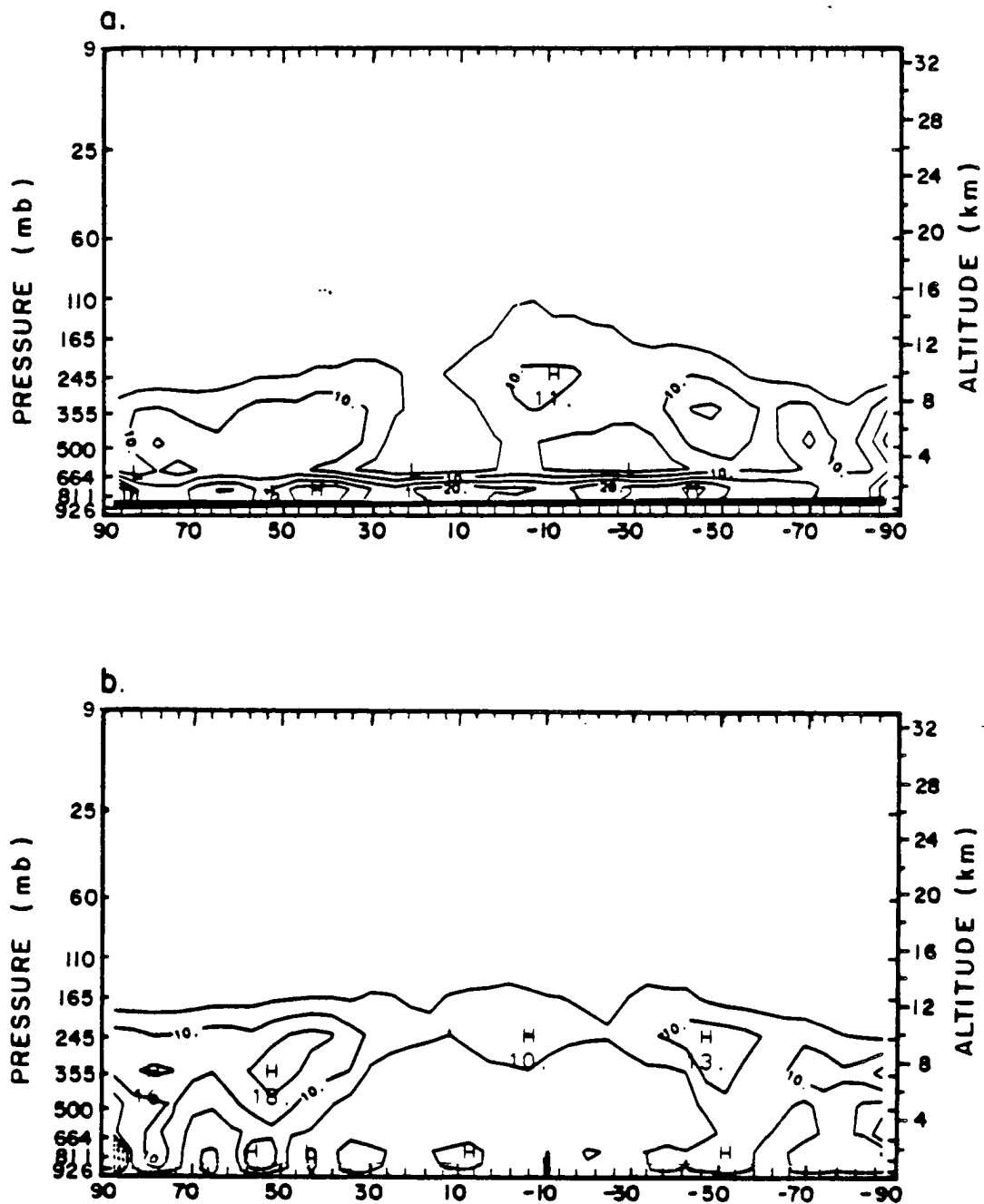


Figure 7.13: Latitude-height distribution of the 30-day average of the effective cloud cover (%): (a) computed from the CONTROL simulation, and (b) difference between the HYDRO and CONTROL simulations.

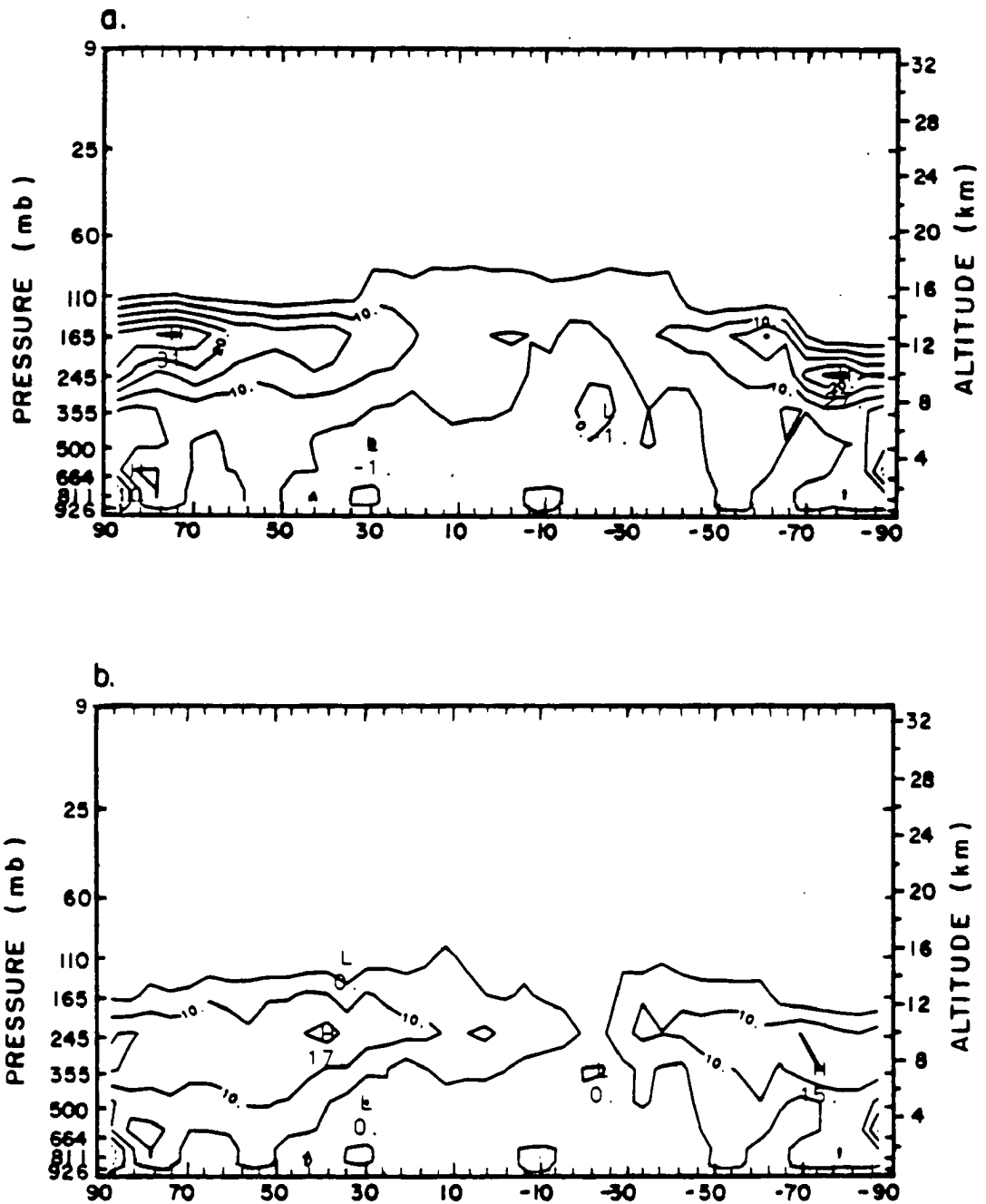


Figure 7.14: Latitude-height distribution of the difference in the standard deviation of the cloudiness between the HYDRO and CONTROL simulations (%): (a) cloud cover, and (b) effective cloud cover.

variability of the outgoing infrared radiation. On a zonal average, the standard deviation computed from the HYDRO simulation is actually systematically greater than that in the CONTROL run. We see, at least, two possible reasons which may explain this negative result. First, although we significantly increased the frequency of occurrence of the high-level cloud amount, we did not succeed at maintaining overcast conditions over time periods as long as those inferred from satellite-derived clouds, especially above the deep tropical convective activity regions. The second reason may be the dampening impact of the interactive cloud emissivity. Because of the increased frequency of condensation in the HYDRO simulation, the variability of the total effective cloud cover is greater than that which would be obtained if high-level clouds had the same life-cycles as in the CONTROL run and were assigned fixed emissivities. Additional complications from variations in the temperature and humidity fields may also have to be considered.

7.4.2 Planetary albedo

Figures 7.17 and 7.18 show the global distribution of the 30-day average and standard deviation of the planetary albedo obtained from the CONTROL simulation, and their zonally-averaged profiles for both simulations. In the HYDRO simulation, the higher total cloud cover yields a 4.0 % increase of the globally-averaged planetary albedo. As at infrared wavelengths, the HYDRO simulation fails to significantly reduce the variability of the planetary albedo. Its standard deviation is slightly decreased between 30°N and 30°S which may not be statistically significant.

7.4.3 Conclusion

Our comparison between the outgoing infrared radiation and planetary albedo fields generated by the HYDRO and CONTROL simulations shows that the impact of a reduced large-scale precipitation efficiency on the persistence of the total cloud cover is not sufficient to significantly reduce the temporal variability of the radiation fields, except in a few selected regions. It produces the correct mechanism to reduce $\sigma(\text{IR})$ (by as much as 30 Wm^{-2} in selected grid-points), but does not solely contribute to the too large fluctuations

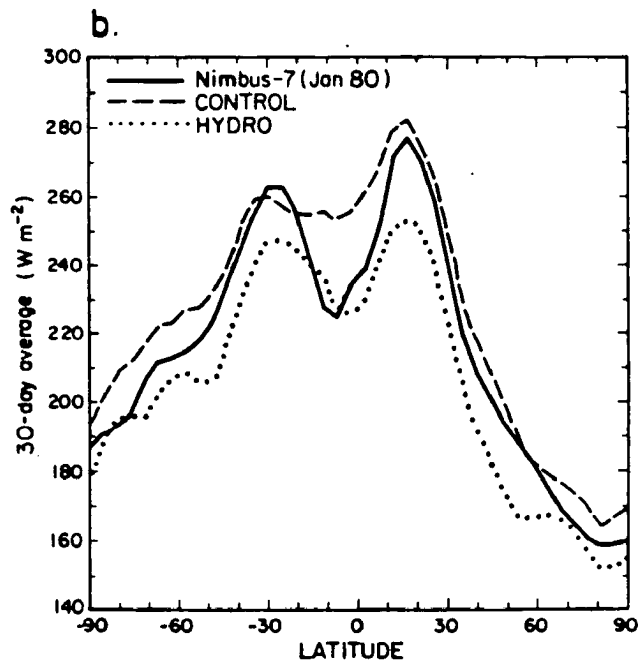
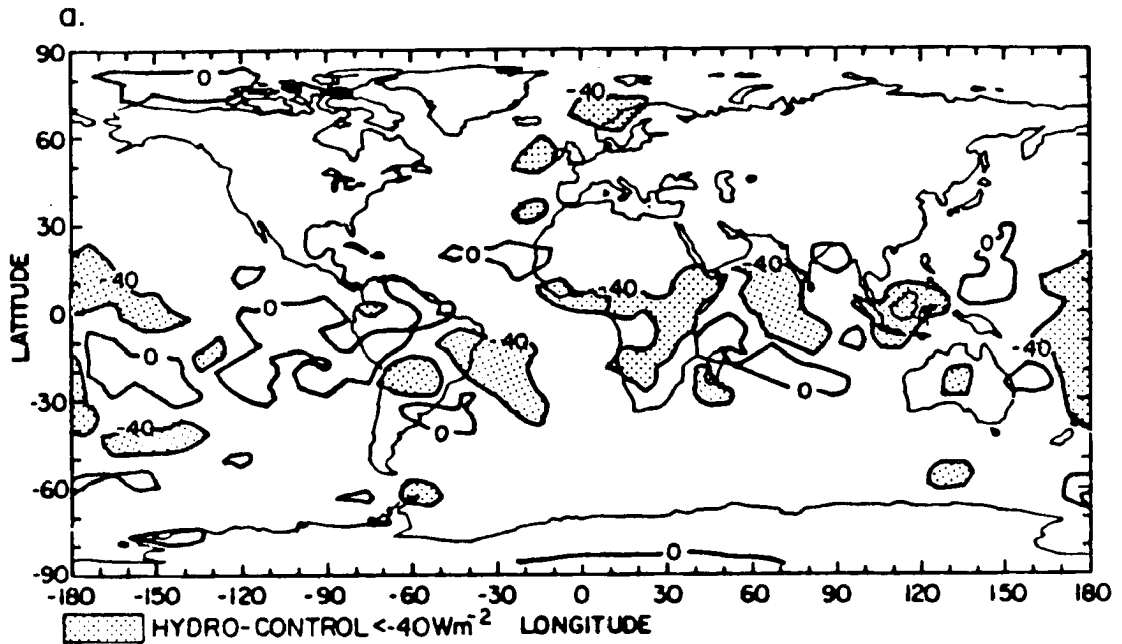


Figure 7.15: 30-day average of the outgoing infrared radiation (W m^{-2}): (a) global distribution of the difference between the HYDRO and CONTROL simulations, and (b) zonally-averaged distribution.

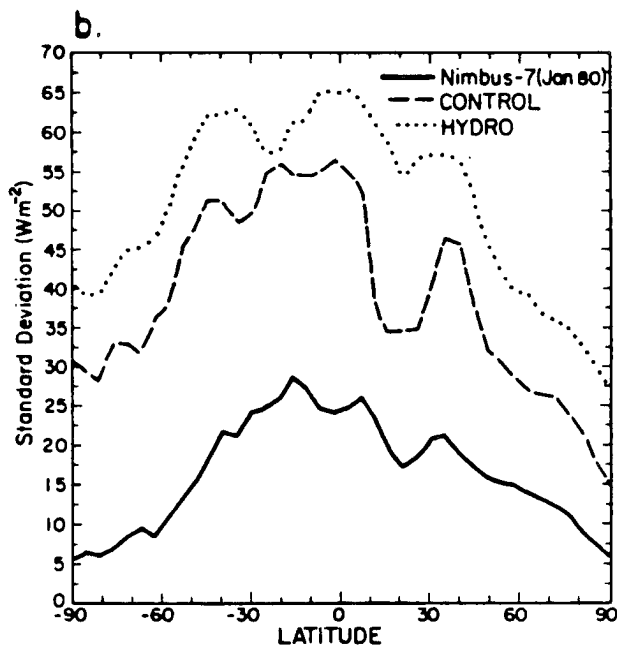
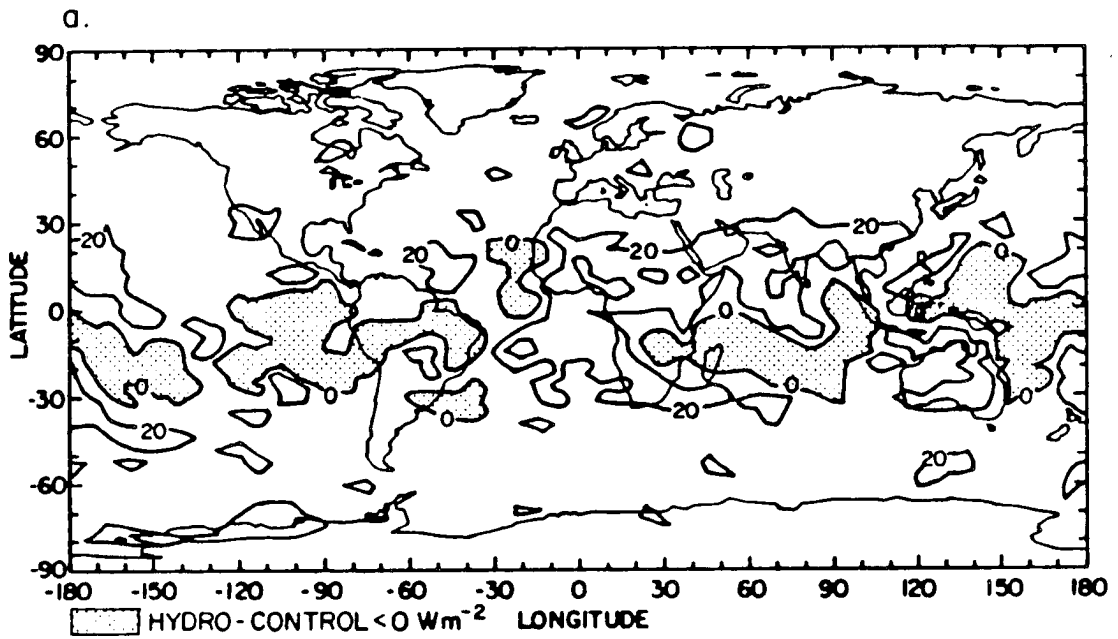


Figure 7.16: Standard deviation of the outgoing infrared radiation (Wm^{-2}): (a) global distribution of the difference between the HYDRO and CONTROL simulations, and (b) zonally-averaged distribution.

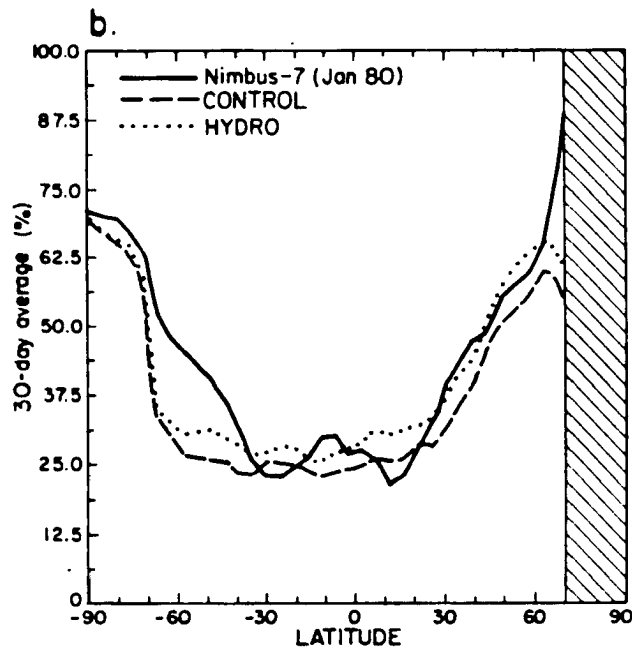
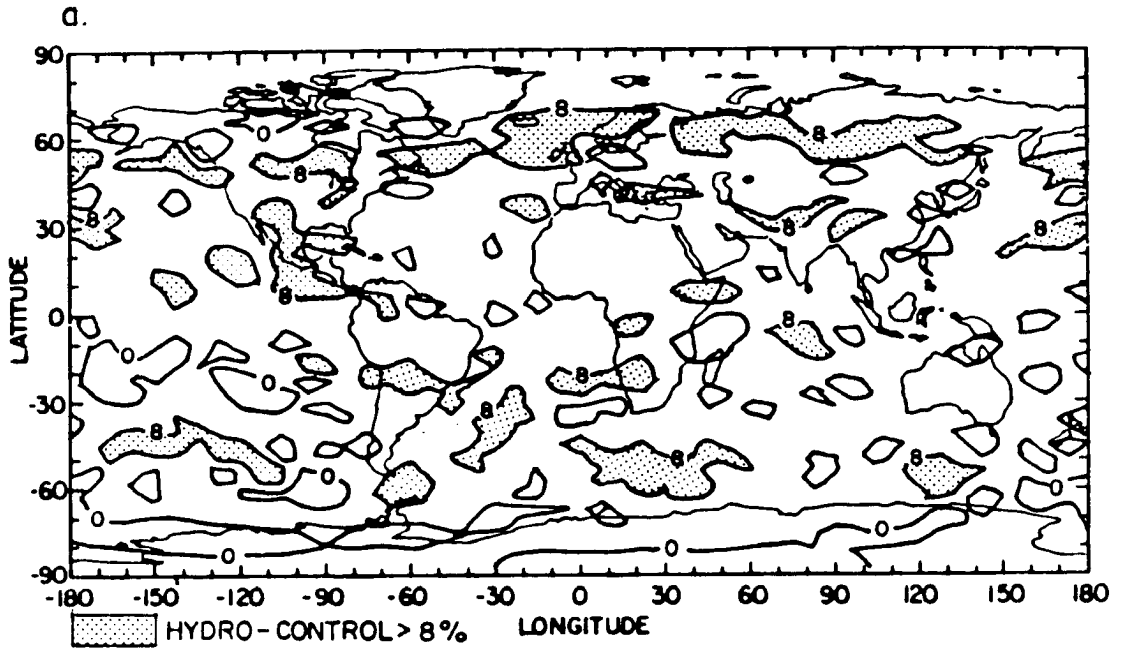


Figure 7.17: 30-day average of the planetary albedo (%): (a) global distribution of the difference between the HYDRO and CONTROL simulations, and (b) zonally-averaged distribution.

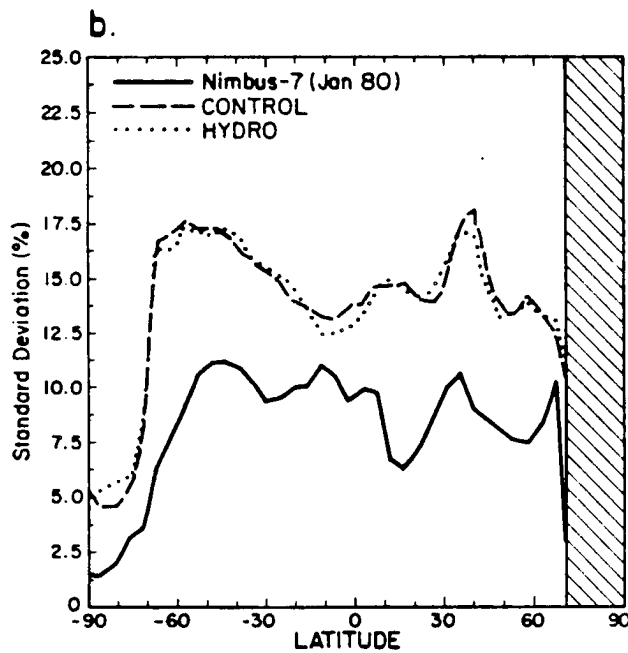
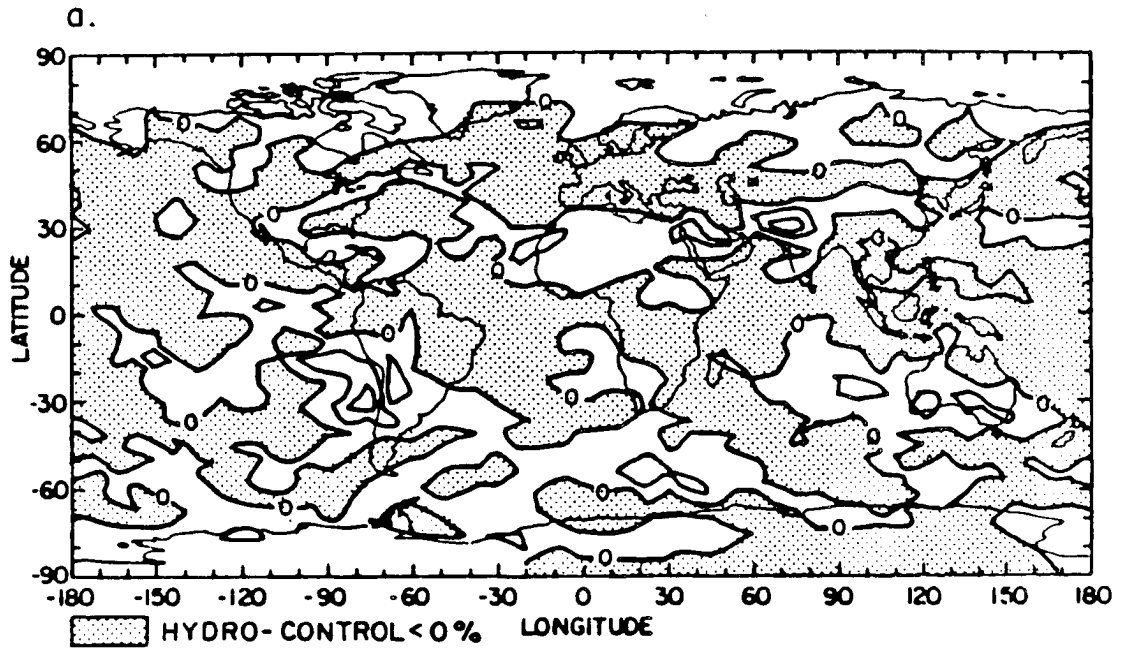


Figure 7.18: Standard deviation of the planetary albedo (%): (a) global distribution of the difference between the HYDRO and CONTROL simulations, and (b) zonally-averaged distribution.

in the model-generated radiation fields. Table 7.2 provides a summary of the globally-averaged components of the model-generated radiation components for both simulations. The global average of the net radiation increases in the HYDRO simulation which results from that the optical properties of clouds are identically prescribed in both simulations. In view of the 20 % increase in the total cloud cover and the reduced sensitivity of the radiation fields between the HYDRO and CONTROL experiments, it is obvious that a larger reduction of the large-scale precipitation efficiency will not produce a significant reduction of the temporal variability of the radiation budget.

7.5 HYDRO versus CONTROL atmospheric diabatic heating

The primary objective of this section does not concern the validation of the atmospheric diabatic heating generated with CCM1, but to estimate the impact of the reduced large-scale precipitation efficiency and increased cloudiness, upon its radiative and condensational heating components. The ability of the NCAR CCM to reproduce the distribution of the diabatic heating is partially addressed in Boville (1985) who examines the thermal balance of the model from long-term January and July climate simulations, with the aim to determine the relative importance of the dynamical and diabatic terms, and understand the maintenance of the temperature structure.

Atmospheric diabatic heating is the driving energy source of the atmospheric general circulation and is strongly sensitive to the distribution of cloudiness. Changes in the diabatic components mainly result from interactions between clouds and radiation, and between clouds and the hydrologic cycle via latent heat release during precipitation. In view of our results described in Section 7.3, we can expect significant changes in the distribution of the total diabatic heating between the HYDRO and CONTROL simulations.

The total diabatic heating can be defined as:

$$Q_T = Q_C + Q_L + Q_R + Q_B, \quad (7.9)$$

where Q_C is heating associated with cumulus precipitation; Q_L , heating associated with large-scale precipitation; Q_R , radiative heating; and Q_B is boundary layer heating (Weare,

1988). Q_B is proportional to the sensible heat flux at the surface and is assumed to affect only the planetary boundary layer. The sum $Q_C + Q_L$ represents the total latent heating. Both latent and radiative heatings contribute a major part to the total diabatic heating and their distributions are separately discussed in the following paragraphs. Finally, Equation 7.9 neglects any frictional heating.

7.5.1 Difference in the radiative heating

Figure 7.19 shows the latitude-height distribution of the longwave radiative cooling rate obtained from the CONTROL simulation, and of its difference between the HYDRO and CONTROL simulations. The difference in the vertical profile of the cooling rate results from the difference in the longwave radiative forcing of the effective cloud cover. In the CONTROL run, tropical high-level clouds produce a net warming of the cloud layer which results from that the cloud-base warming exceeds the cloud-top cooling, as commonly observed in tropical anvils (Ackerman *et al.*, 1988). For extratropical high-level clouds, the cloud-top cooling dominates which produces a net cooling of the cloud layer. In the HYDRO simulation, the increased cloud cover (in particular, of the cirrus shield) amplifies the difference in the net radiative effect between tropical and extratropical clouds, and yields an enhanced warming of the tropical atmosphere, in particular at the location of maximum high-level cloud increase, and an enhanced cooling in the middle latitudes above $\sigma = 0.245$. In addition, the radiative cooling of the low troposphere is reduced because of the increased greenhouse effect of the upper-level cloud shield.

Figure 7.20 shows the latitude-height distribution of the shortwave heating rate obtained from the CONTROL simulation and of its difference between the HYDRO and CONTROL simulations. Optically thick, low-level clouds have the largest potential to decrease the shortwave tropospheric warming. The decrease in the shortwave heating rate is the largest below $\sigma = 0.500$, in the tropics and the middle latitudes in the summer hemisphere, where both insolation and cloudiness are large. In the HYDRO simulation, the impact of the cloud shortwave radiative forcing is reduced because the optical thickness of clouds is prescribed. In case of internally-generated cloud optics, the albedo of

clouds would have increased because of the increased accumulated condensed water, producing a negative feedback mechanism and an enhanced contrast between the HYDRO and CONTROL simulations. The latitude-height distribution of the net radiative heating rate would show that changes in the longwave cooling rate dominate: The HYDRO simulation produces an increased net radiative warming below $\sigma = 0.355$ and at higher σ -levels in the tropics whereas it yields a net radiative cooling above $\sigma=0.355$ in the middle latitudes.

7.5.2 Difference in the condensational heating

The second major component of the atmospheric diabatic heating is the latent heating from convective plus large-scale precipitation. Unfortunately, the individual contribution from the cumulus and large-scale condensation rates of precipitation to the total latent heating were not saved separately on the History Tapes. However, having shown in Section 7.3 that there is no substantial difference in the amount of convective precipitation between the HYDRO and CONTROL simulations, variations in the latent heating can be mostly attributed to variations in the large-scale precipitation amount. Figure 7.21 shows the latitude-height distribution of the total latent heating, and of its difference between the HYDRO and CONTROL simulations. In the CONTROL simulation, the latent heating is the largest in the tropics, via latent heat release from cumulus towers and associated cloud anvils, and in the winter storm track regions in the middle latitudes, via latent heat release from frontal cloud systems. At both latitudes, the peak of latent heat release is located at $\sigma = 0.811$, which corresponds to the base of the convection.

In accordance with the decreased total precipitation rate between the HYDRO and CONTROL simulations, the condensational heating rate decreases at the latitudes of maximum latent heat release, i.e. above the equator and the middle latitudes in the Northern Hemisphere. On the other hand, the latent heating rate slightly increases at the latitudes of minimum condensation in the CONTROL simulation, i.e. above the subtropics. The excess condensation and formation of clouds above dry and mostly clear-sky regions is one drawback of the HYDRO experiment, which may result from an inefficient transport of moisture.

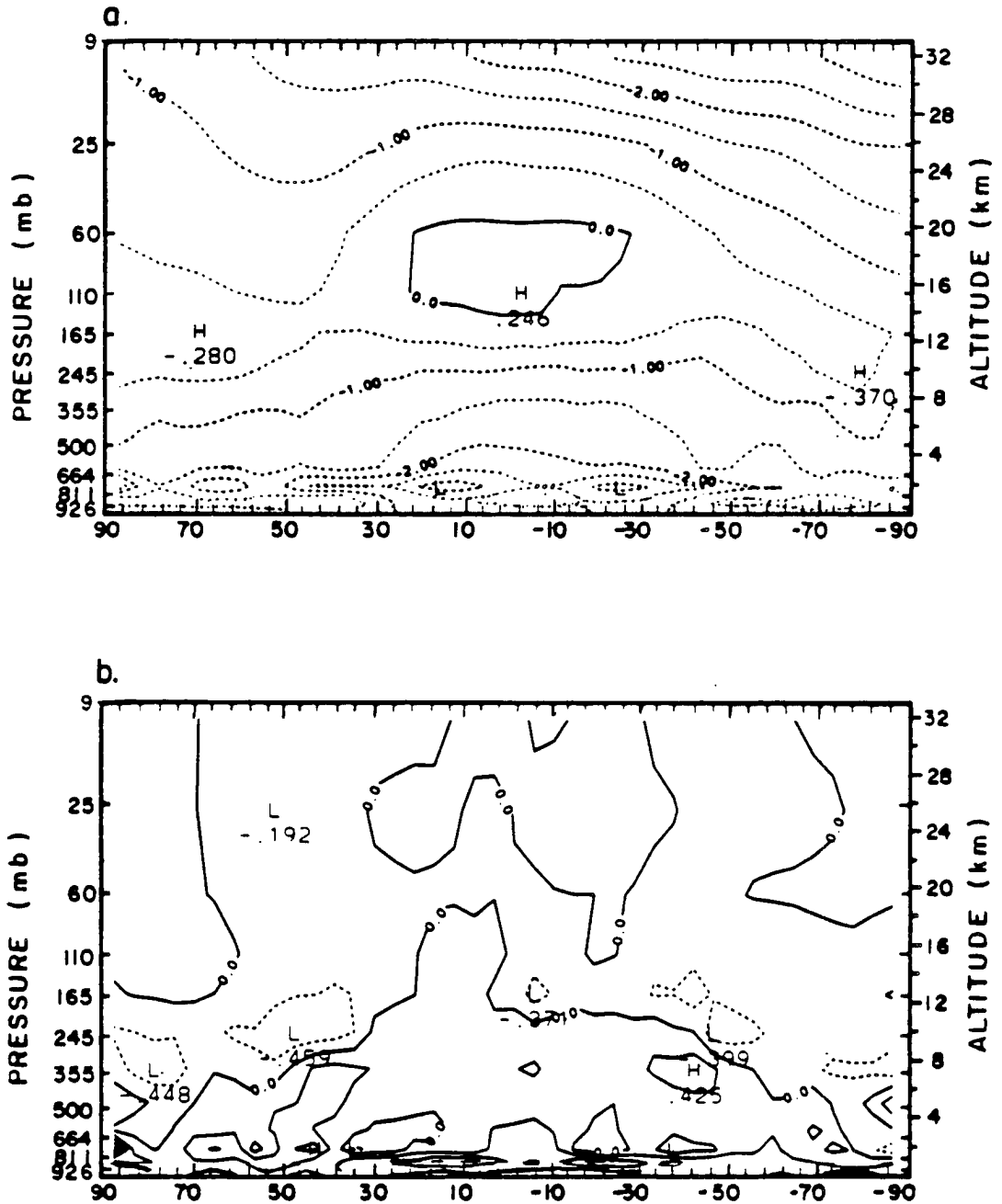


Figure 7.19: Latitude-height distribution of the longwave radiative heating rate (K day^{-1}): (a) 30-day average computed from the CONTROL simulation, and (b) difference between the HYDRO and CONTROL simulations.

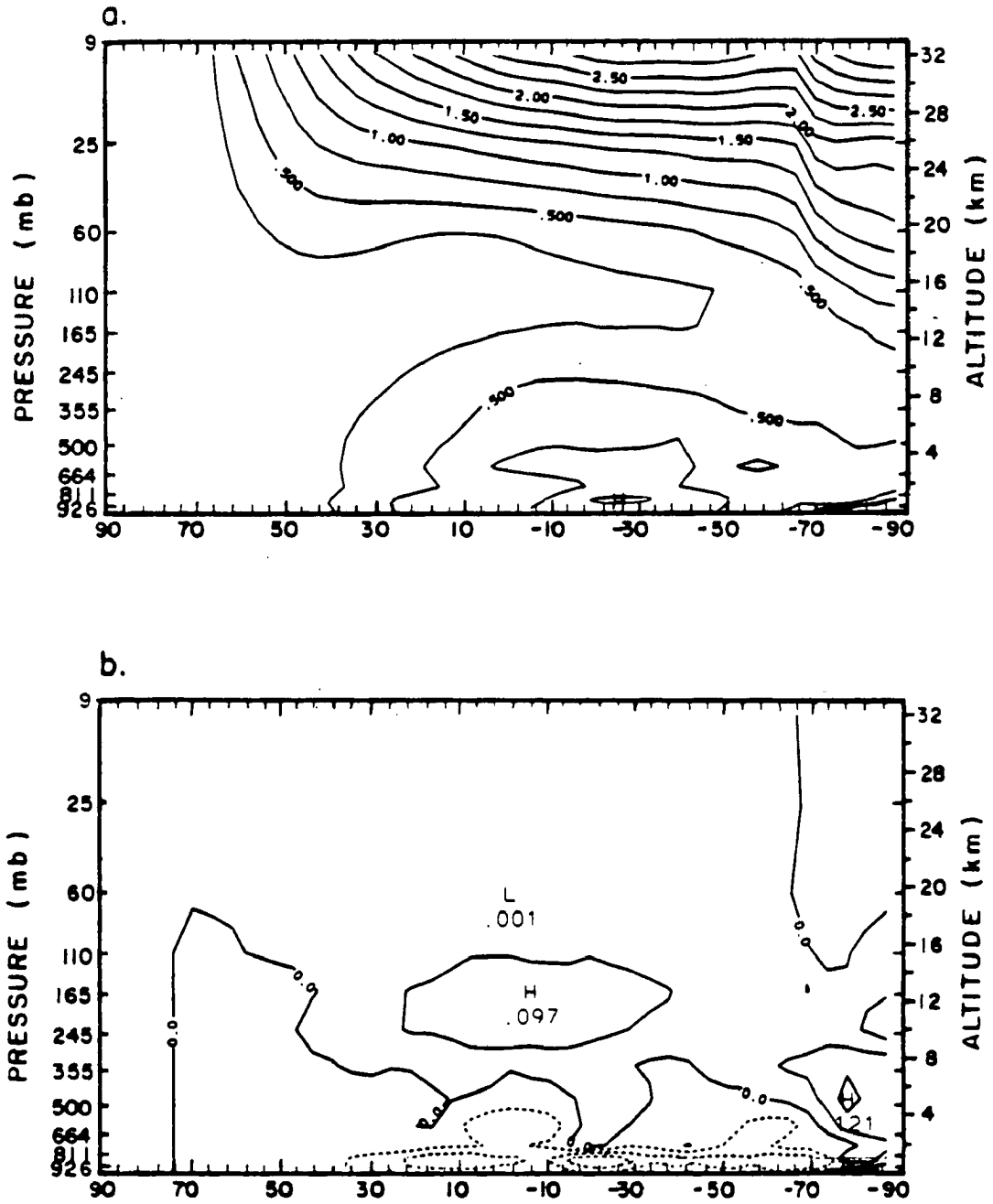


Figure 7.20: Latitude-height distribution of the shortwave radiative heating rate (K day^{-1}): (a) 30-day average computed from the CONTROL simulation, and (b) difference between the HYDRO and CONTROL simulations.

7.5.3 Difference in the diabatic heating

Separate analyses of the distribution of the radiative and latent heating rates showed, in the middle and low troposphere below the high-level cloud shield, the competing effect between the increased net radiative warming produced by larger high-level cloud amounts and decreased condensational heating produced by the decreased precipitation rate. In the upper troposphere, the radiative effect dominates. In the HYDRO simulation, the simultaneous radiative and condensational heating rate changes across the whole troposphere helps maintain the total energy balance, as in the CONTROL experiment. Figure 7.22 shows the latitude-height distribution of the total diabatic heating obtained from the CONTROL simulation, and of its difference between the HYDRO and CONTROL simulations. Figure 7.23 shows the global distribution of the vertically-averaged (between $\sigma=0.991$ and $\sigma = 0.110$) diabatic heating rate obtained with the CONTROL simulation, and of its difference between the HYDRO and CONTROL simulations. The comparison between Figures 7.19(a), 7.21(a), and 7.22(a), indicates that below the upper-level cloud base, latent heating is the dominant component of the diabatic heating equation in the tropics and the middle latitude storm track regions in the winter hemisphere, while radiative cooling prevails in the subtropics and at polar latitudes. Above $\sigma = 0.355$, the radiative heating term dominates the diabatic heating equation, except at low latitudes. The partition between the latent and radiative heatings is, therefore, strongly driven by the global distribution of the moisture field. In contrast to Figure 7.22 which provides a picture of the global-scale vertical structure of the diabatic heating, Figure 7.23 shows that the atmospheric diabatic heating takes place in specific regions of the globe. For mean January conditions, they are: (1) The convective activity regions at low latitudes, mainly, the South Pacific Convergence Zone, the winter monsoon region, the rainfall region over South America and its extension eastward into the South Atlantic ocean, and the rainfall region of southern Africa and its extension eastward into the Indian ocean; (2) The middle latitude cyclogenetic regions in the winter hemisphere, mainly, the North Pacific and North Atlantic oceans. In addition to significant meridional variations, this strong longitudinal contrast in the distribution of the diabatic heating is important to the

maintenance of regional circulation between regions dominated by radiative cooling and condensational heating.

Figure 7.22(b) indicates that just above and below the high-level cloud shield, the change in the diabatic heating is dominated by the change in the net radiative heating rate. In the HYDRO simulation, the increased total cloud cover produces an increased cooling above the cloud-top and an increased warming below the cloud base. In the low troposphere, the change in diabatic heating depends upon the magnitude of the decreased condensational heating rate, since the radiative term produces a positive difference between the HYDRO and CONTROL simulations. In particular, the diabatic heating decreases above the tropical convective activity regions, as also showed on the vertically-averaged map (Figure 7.23(b)).

7.5.4 Conclusion

In the HYDRO simulation, the simultaneous decreased condensation rate and increased upper-level clouds produce competing changes between the latent heating rate and the net radiative heating rate, so that the globally-averaged energy input is maintained close to zero, as in the CONTROL simulation. As the atmospheric diabatic heating contributes the ultimate energy source for all atmospheric motions, we can foresee significant changes in the distribution of the temperature and wind fields between the HYDRO and CONTROL simulations.

7.6 HYDRO versus CONTROL atmospheric general circulation

The impact of the change in the distribution of the total diabatic heating on the model-generated atmospheric general circulation is discussed from analyses of the variations in the temperature and wind fields between the HYDRO and CONTROL simulations. Validation of the model-generated atmospheric temperature and wind fields against observations was made at the beginning of Chapter Four. It was shown that the NCAR CCM reproduces successfully the chief characteristic features of the observed general circulation for the Northern Hemisphere winter season.

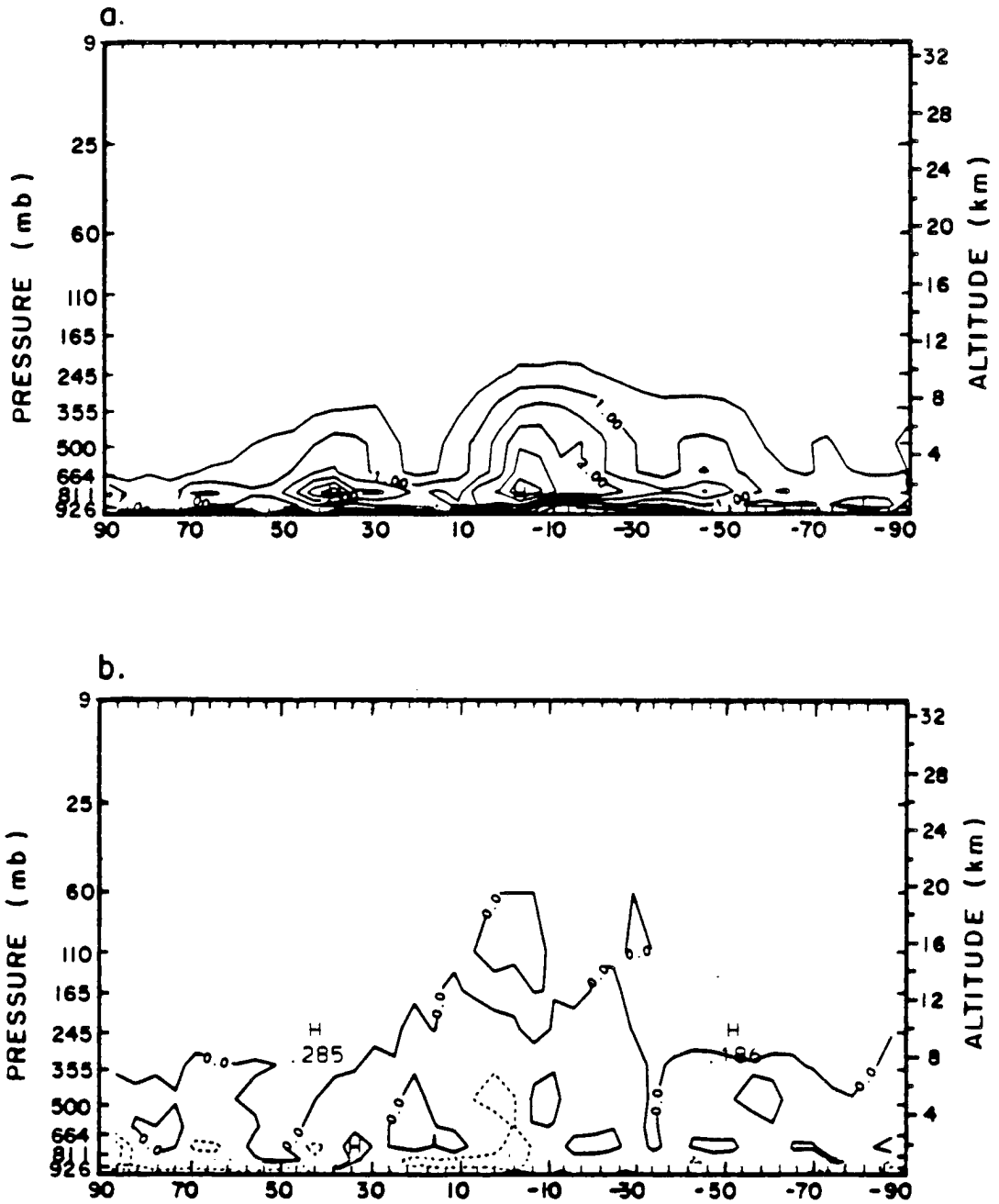


Figure 7.21: Latitude-height distribution of the latent heating (K day^{-1}): (a) 30-day average computed from the CONTROL simulation, and (b) difference between the HYDRO and CONTROL simulations.

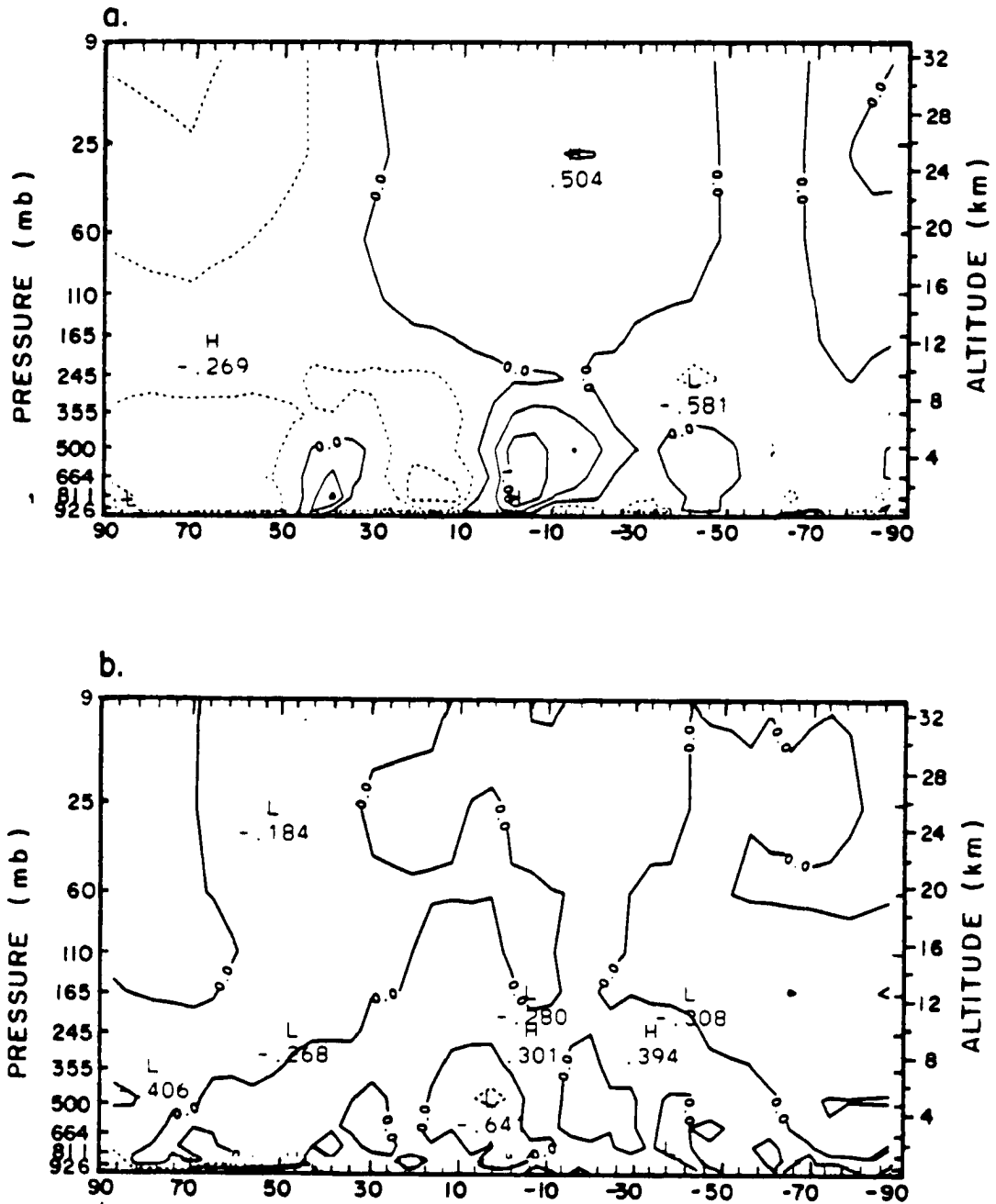


Figure 7.22: Latitude-height distribution of the sum of the net radiative and latent heating rates (K day^{-1}): (a) 30-day average computed from the CONTROL simulation, and (b) difference between the HYDRO and CONTROL simulations.

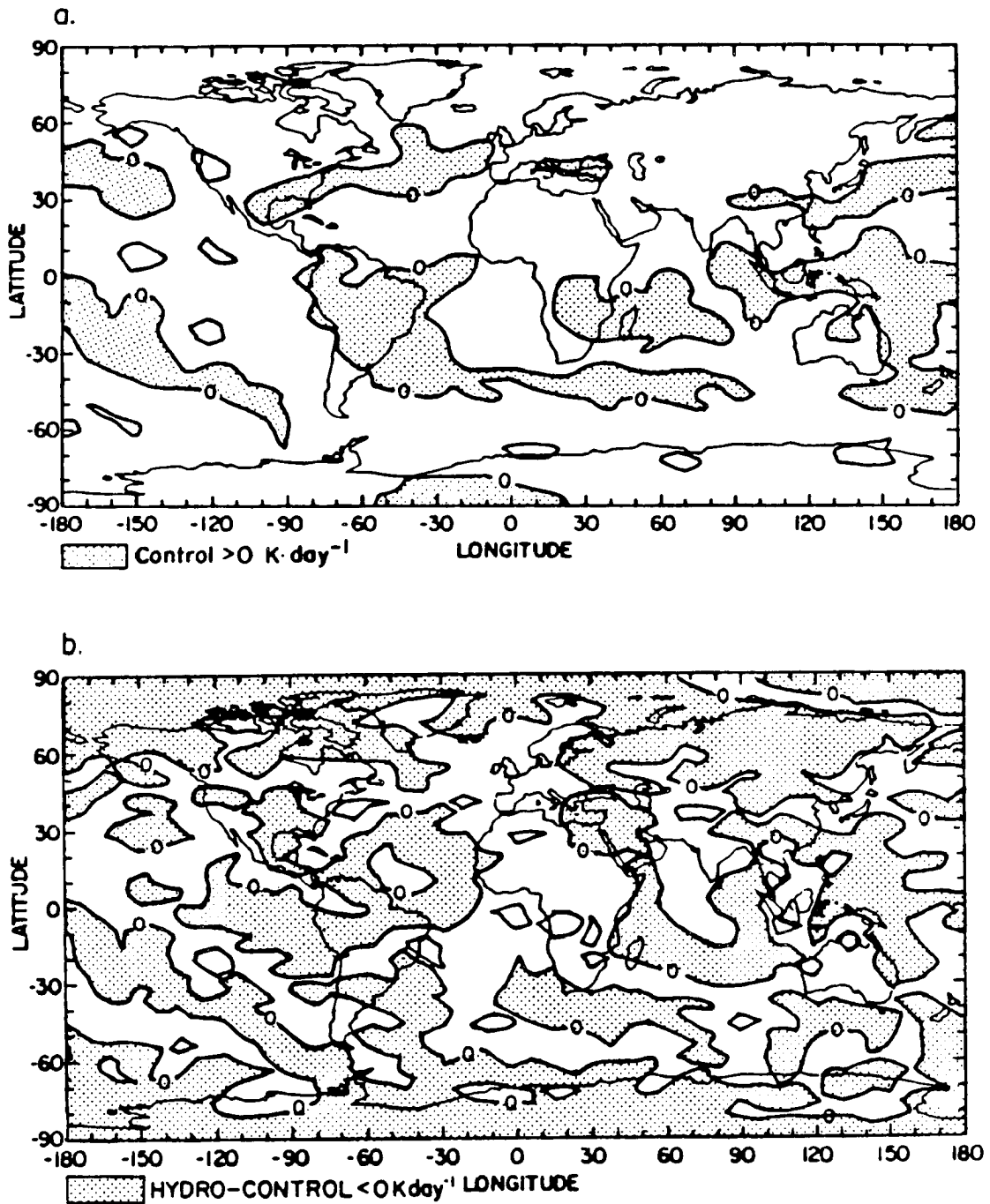


Figure 7.23: Vertically-integrated global distribution of the sum of the net radiative and latent heating rates ($\text{K} \cdot \text{day}^{-1}$): (a) 30-day average computed from the CONTROL simulation, and (b) difference between the HYDRO and CONTROL simulations.

7.6.1 Difference in the temperature field

Figure 7.24 shows the latitude-height distribution of the difference in the temperature field between the HYDRO and CONTROL simulations. The impact of the increased upper-level cloud shield at $\sigma = 0.245$ changes sign between the tropical and extratropical latitudes, in accordance with the difference in the net radiative heating rate between the HYDRO and CONTROL simulations. On the one hand, the enhanced cloud longwave radiative forcing produces an increased warming of the tropical upper troposphere which is larger than 3 K at $\sigma = 0.165$. On the other hand, the cooling of the upper troposphere reaches as much as 7.5 K at high latitudes, especially over the poles which stay mostly overcast in the HYDRO simulation. The troposphere, below the upper-level cloud deck undergoes an overall warming because of the enhanced longwave forcing of clouds in the HYDRO simulation.

7.6.2 Difference in the vertical velocity

The latitude-height distribution of the mean cloud cover shows that the altitude of the highest cloud layer decreases between the equator and the poles, in a manner similar as the tropopause-height. This indicates that the tropopause acts as a lid to the upward motion which is responsible for the formation of clouds in the upper model troposphere. In the HYDRO simulation, the thickening of the upper-level cloud shield is very likely to modify the vertical stability of the atmosphere, and therefore, the vertical velocity. Figure 7.26 shows the latitude-height difference in the vertical velocity field ($\Delta\omega$) between the HYDRO and CONTROL simulations. The comparison of $\Delta\omega$ against the 30-day averaged vertical velocity shows that $\Delta\omega$ is positive above the latitudes of upward vertical motion ($\omega < 0$), i.e. the tropics and the middle latitudes, and that $\Delta\omega$ is negative above the latitudes of downward vertical motions ($\omega > 0$), i.e. the subtropics. In both cases, this implies that the impact of the increased upper-level cloud shield is to decrease the vertical motion or increase the vertical stability of the atmosphere. Above the convective activity regions, the enhancement of the atmospheric diabatic heating due to the increase latent heat release occurs with a decrease in the intensity of the convection upward, and

saturated air tends to spread horizontally. This is a positive feedback mechanism to the formation of cirrus anvils associated with convection.

7.6.3 Difference in the zonal wind

Changes in the zonal wind are related to changes in the temperature field via the thermal wind equation. Figure 7.25 shows the latitude-height distribution of the 30-day average of the zonal wind for the CONTROL simulation and its difference between the HYDRO and CONTROL simulations. The increase in the meridional temperature gradient above $\sigma = 0.245$ produces a significant acceleration of the subtropical jets in both hemispheres. In contrast to the summer hemisphere, the strengthening of the zonal wind occurs with a southward shift of its position of maximum intensity in the winter hemisphere. Outside those latitudes, the zonal wind intensity decreases in the HYDRO simulation.

7.6.4 Conclusion

In this section, we analysed the impact of the change in the distribution and amount of the cloud cover on the model-simulated general circulation. In addition to significant variations in the diabatic heating of the atmosphere, the increased upper-level cloud shield produced significant variations in the temperature and zonal wind fields, as well as an enhanced vertical stability of the atmosphere. A fundamental issue in studying the nature of the interactions between clouds and the dynamics of the atmosphere is concerned with the impact of clouds on the poleward transport of heat flux and angular momentum, in particular by the eddies. In view of our results, it would be interested to undertake this kind of analysis from longer runs of the HYDRO and CONTROL simulations.

7.7 Discussion

The HYDRO experiment is partially successful at reaching our goals outlined in the introduction. Our arbitrary partition between large-scale precipitating and non-precipitating condensed water produces the correct mechanism to enhance the stability of

the total cloud cover, at least at regional scales. However, its impact on the on and off blinking of the model atmosphere remains limited.

Our first objective was to reduce the temporal variability of the model-generated radiation fields which the HYDRO experiment failed to achieve, except in very limited areas. One of such area is the winter monsoon region above the Indonesian peninsula for which the convective clouds are capped by a greater amount and more stable large-scale condensation clouds. Above those specific regions, and in contrast to the CONTROL experiment in which a high cloud amount is characterized by high values of its standard deviation, the HYDRO experiment is able to build mostly overcast conditions with decreased cloud fluctuations. In that regard, the atmospheric response is qualitatively similar as that produced with the ECMWF experiment. There are numerous embedded reasons to explain the relative insensitivity of the radiation fields to the increased cloudy-sky frequency. First, the HYDRO experiment does not modify the convective precipitation rate and, therefore, does not produce any improvement of the total precipitation rates above the deep convective activity regions. Second, the HYDRO experiment produces more clouds over the whole globe instead of above selected regions. As a result, regions which are mostly clear in the CONTROL run, as the subtropical oceans and the desert areas, are becoming more cloudy in the HYDRO run. As a result, the standard deviation of the total cloud cover increases above those regions. On a zonal average, the greater variability of the less cloudy regions overcomes the lesser variability of the mostly cloudy regions. This effect arises from that there is no advection of the condensed water and would be corrected if evaporation and precipitation of clouds were correctly parameterized in CCM1.

Our second objective was to analyze the importance of an increased stability of the total cloud cover, or improved cloud life-cycles on the circulation of the model atmosphere. Despite the fact that the HYDRO experiment did not succeed at significantly decreasing the temporal variability of the planetary radiation budget, we showed that an increased frequency of occurrence of clouds does have a profound impact upon the distribution of the total diabatic heating, and the temperature and wind fields. In particular, the increase of

the upper-level cloud amount yields an increased vertical stability of the model atmosphere and acceleration of the subtropical jets in both hemispheres. If the evaporation, precipitation, and advection of clouds were more realistically represented in CCM1, we would obtain the same dynamic response than in the HYDRO simulation. Therefore, assuming that the parameterization of all the physical processes in the model does not change, it is very likely that the inclusion of the liquid water as a prognostic variable would modify the mean steady state of the model-generated climate. Because of the non-linear response of the atmosphere to climate forcings, it is reasonable to think that the additional feedback mechanism produced by interactive liquid water may significantly amplify or tamper the model sensitivity.

7.8 Summary

In this chapter, our primary objective was to quantify the impact of treating condensation as a complete rainout process on the temporal variability of the cloud cover, in climate simulations made with CCM1. Starting from the assumption that reduced interactions between clouds and the hydrologic cycle lead to unrealistic cloud life-cycles, we decided to test the sensitivity of the interactions between clouds, and the radiative, thermodynamic, and dynamic processes when only a fraction of the condensed water is allowed to fall to the ground. During the HYDRO simulation, 25 % of the moisture from large-scale condensation turned into precipitation while the remaining 75 % was added back into the moisture field and mixed through horizontal motions. After several attempts, this arbitrary partition between precipitating and non-precipitating rain was chosen because it provided a significant atmospheric response in a short-term climate experiment.

Computations of the time standard deviation of the outgoing infrared radiation and planetary albedo showed the insensitivity, on a global scale, of the radiation fields to an increased stability of the total cloud cover. Therefore, the HYDRO experiment was not successful in reducing the on and off blinking of the model atmosphere. On the other hand, the HYDRO experiment produced important results on the treatment of the interactions

between clouds and the hydrologic cycle, to the diabatic heating budget and general circulation of the model-simulated atmosphere. As in most GCM-simulated climates, the upper troposphere produced with CCM1 is too cold and too dry, whereas the rainfall rate is too large at the surface. Although the HYDRO experiment did not reduce significantly the total precipitation rate, it produced the correct mechanism to simultaneously warm and moisten the upper troposphere below the high-level cloud shield. Therefore, our results emphasize the importance of an improved advection scheme of moisture, in addition to increased clouds-hydrologic cycle interactions. Finally, our results strongly support the necessity to include, in the near future, a physically-based relationship between the time evolution of clouds and the cloud liquid water in GCM-simulated climate.

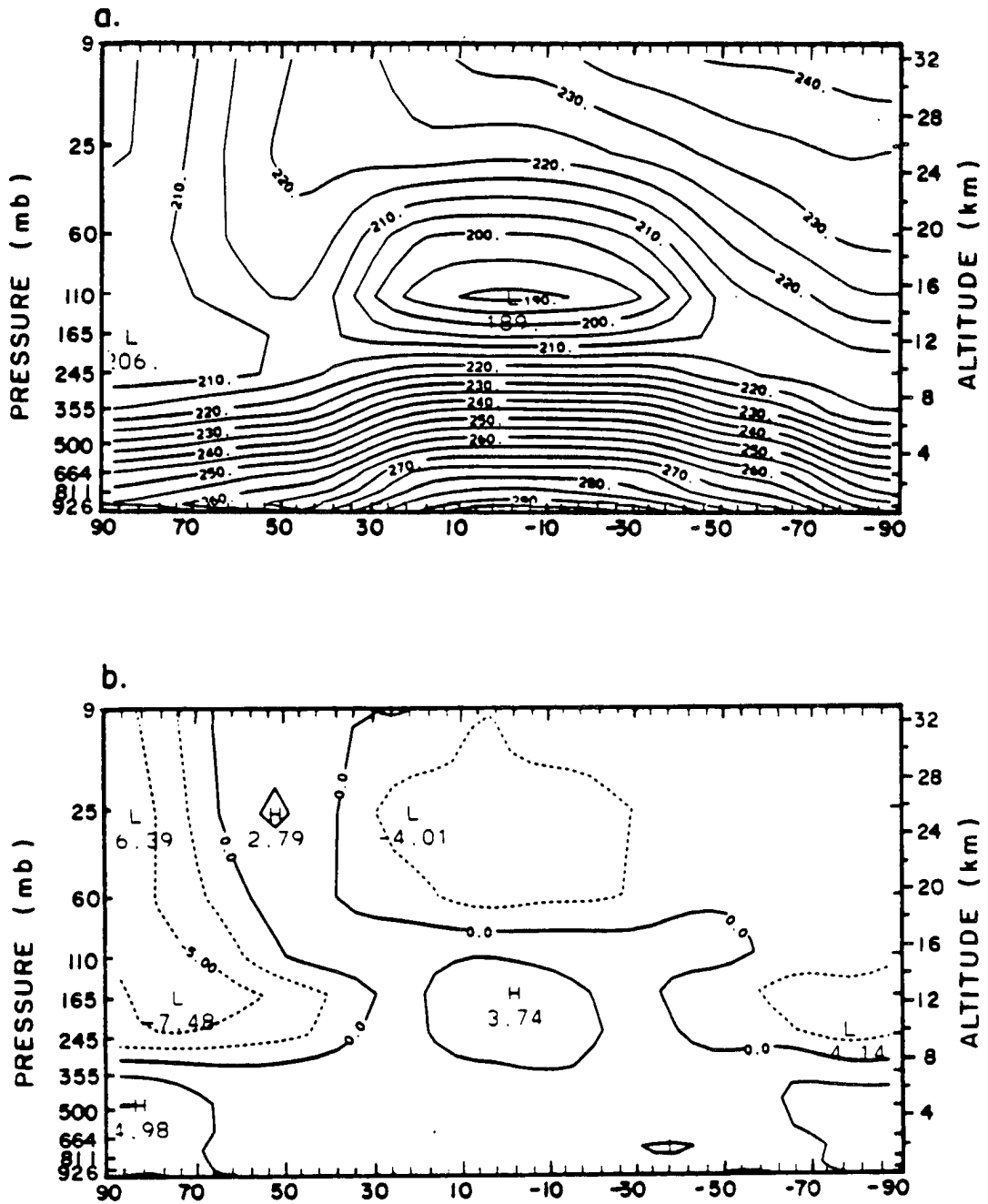


Figure 7.24: Latitude-height distribution of the atmospheric temperature (K): (a) 30-day average computed from the CONTROL simulation, and (b) difference between the HYDRO and CONTROL simulations.

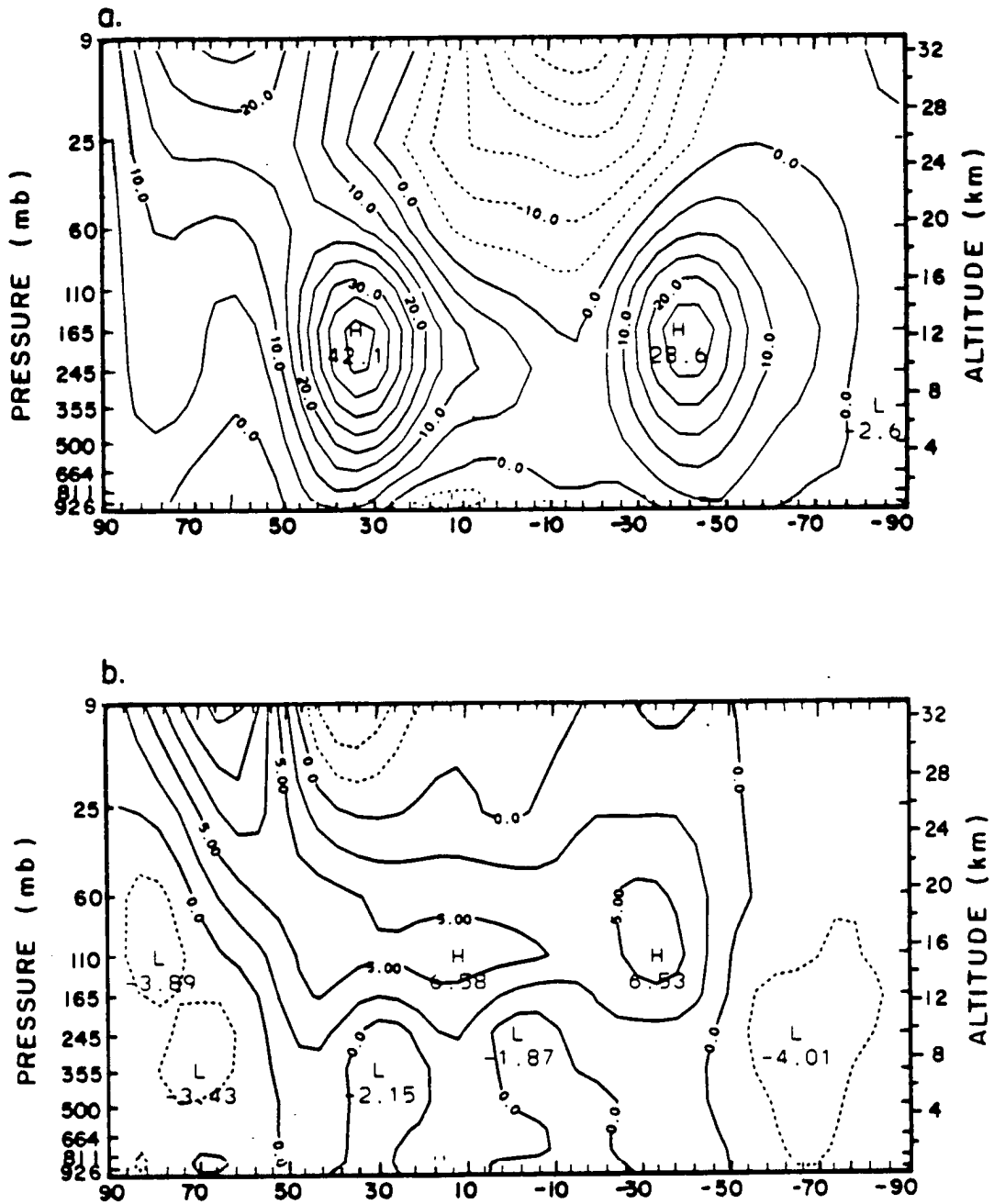


Figure 7.25: Latitude-height distribution of the zonal wind (ms^{-1}): (a) 30-day average computed from the CONTROL simulation, and (b) difference between the HYDRO and CONTROL simulations.

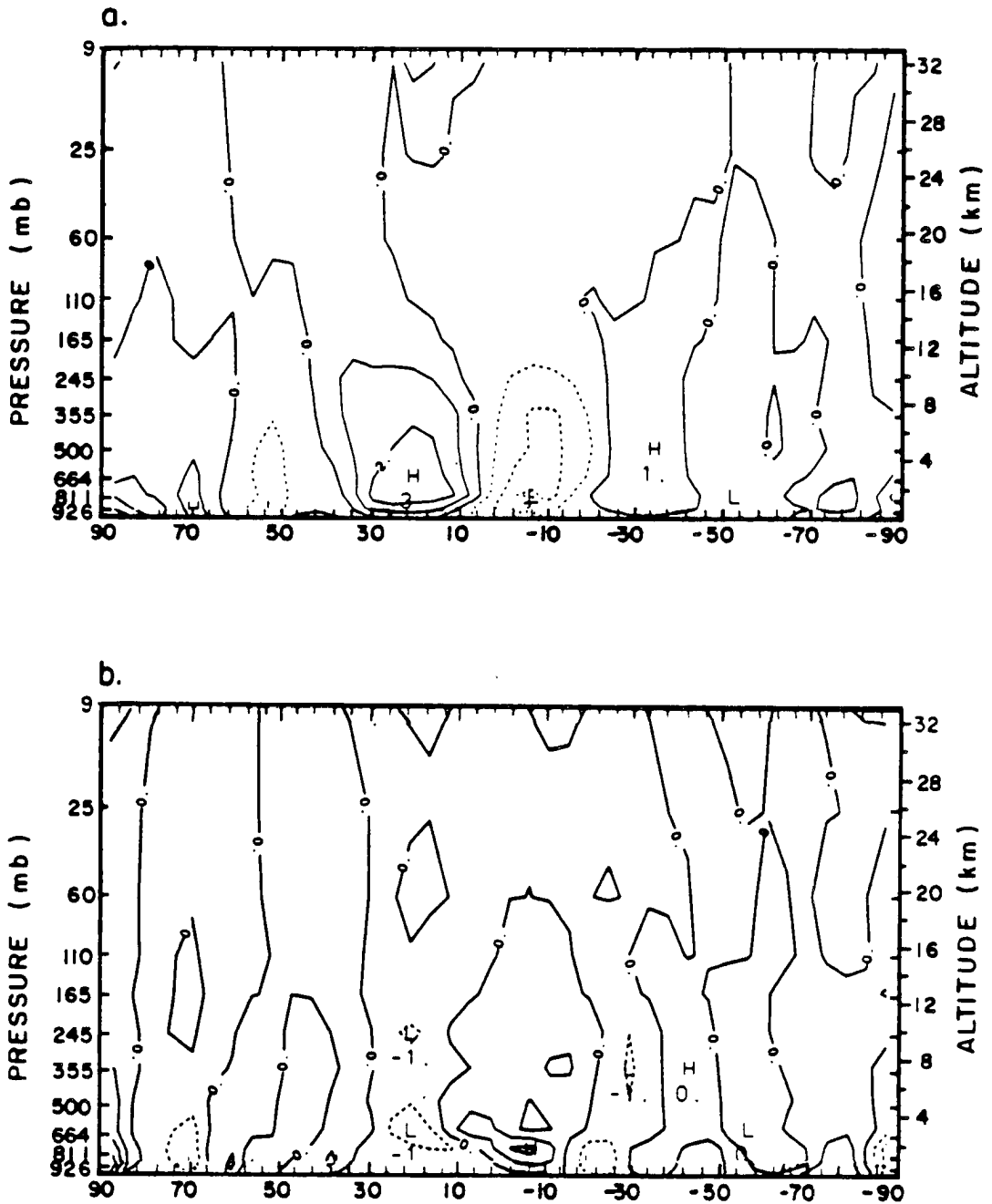


Figure 7.26: Latitude-height distribution of the vertical velocity (10^4 mb s^{-1}): (a) 30-day average computed from the CONTROL simulation, and (b) difference between the HYDRO and CONTROL simulations.

Table 7.1

Table 7.1: Globally-averaged values of the 30-day averaged components of the hydrologic budget. All the fields are in mm day^{-1} , except the total cloud cover which is %.

January conditions	CONTROL	HYDRO
Large-scale precipitation rate	1.551	1.053
Convective precipitation rate	1.637	1.784
Total precipitation rate	3.188	2.837
Total evaporation rate	3.186	2.830
Total cloud cover (%)	47.4	64.9

Table 7.2

Table 7.2: Globally-averaged values of the 30-day average and standard deviation of the planetary radiation budget components. All the fields are in Wm^{-2} , except the planetary albedo which is in %.

January conditions	CONTROL	HYDRO
<u>Monthly average</u>		
Outgoing infrared radiation	239.4	218.3
Absorbed solar radiation	248.3	234.8
Planetary albedo	31.4	35.4
<u>Standard deviation</u>		
Outgoing infrared radiation	44.9	55.3
Absorbed solar radiation	52.3	51.1
Planetary albedo	14.3	14.0

Chapter 8

SUMMARY AND CONCLUSION

Measurements of the earth-atmosphere radiation balance from satellites and long-term climate simulations made with GCMs make complementary contributions to an increased understanding of the interactions between clouds, radiation, and climate, and the role of clouds in the atmospheric general circulation. Due to the complexity of the interactions between the various components of the climate system, GCMs can only produce a simplified representation of the mean observed climate. The first step towards an increased use of three dimensional climate models to study the sensitivity of climate to a change in cloudiness, or to any climate forcings is, therefore, the validation of GCM-simulated climates against observations, including their temporal and spatial variability. Observations of the earth's radiation budget from space-borne instruments constitute one of the most suitable means for objective and easy comparison with model outputs. In particular, they provide the necessary conditions that GCMs have to conform to.

The chief objectives of this dissertation were:

1. To compare the top-of-atmosphere radiation fields obtained from long-term climate simulations with the NCAR Community Climate Model (NCAR CCM) against ERB satellite observations.
2. In view of the impact of clouds on the distribution of the mean outgoing infrared radiation and planetary albedo, and their temporal variability, to explain the discrepancies between the model-generated and satellite-observed radiation fields in term of the parameterization of clouds and their interactions with the other physical processes in CCM1.

3. To demonstrate the importance of correctly simulating the life-cycles of clouds and the temporal variability of the radiation budget components.
4. To propose strategies towards an improved treatment of the interactions between clouds and the radiative, thermodynamic, and dynamic processes in simulations of climate made with CCM1. In that regard, we did not attempt to modify the model code with the aim to improve the model performance.

ERB measurements were taken by the relatively NFOV scanner radiometers on-board the satellite Nimbus-7 during the time period between May 1979 and June 1980. They were broad-spectral-band observations which covered daily (twice daily at infrared wavelengths) the entire globe. The Northern Hemisphere summer and winter seasons referred respectively to June-July-August 1979 and December 79-January-February 1980. At the present time, this data set is the only multi-month set of archived broad-spectral-band observations while waiting for the next generation of NFOV data from the ongoing multi-satellite Earth Radiation Budget Experiment (ERBE) which started in November 1984. Estimates of cloud amounts derived from satellite radiances taken by the THIR and TOMS instruments, both on-board Nimbus-7, and NFOV measurements of the outgoing infrared radiation taken by scanner radiometers on board the NOAA satellites complete our set of observations.

The different long-term simulations of climate were obtained from the newest version of the NCAR CCM (version CCM1) and archived on History Tapes. Part of our research contributed, therefore, to the validation of the improvements brought into the model code and helped outline the future modifications which should be implemented to increase the model performance to simulate the present climate. The model-generated radiation fields were obtained from a 15-year run including a seasonal cycle (Case 239) and a 1500-day run corresponding to perpetual January conditions (Case 223). Ensemble averages of the time average, standard deviation about the time average, and time-lagged autocorrelation coefficients were computed from five independent realizations of climate. They were

considered to be representative of the mean GCM-climate and of its temporal variability. Our comparison between model-generated and satellite-observed shortwave and longwave components of the planetary radiation balance made use, therefore, of the best quality data sets, available at present, to assess the performance of a GCM to reproduce the mean climate and its temporal variability.

8.1 Summary

8.1.1 Observed radiation balance

The global distribution of the seasonal average and standard deviation, computed from the seasonal average, of the outgoing infrared radiation, absorbed solar radiation, and planetary albedo fields obtained from the Nimbus-7 ERB Experiment was discussed in Chapter Two. It was shown that temporal variations of the radiation budget components were primarily driven by variations in the distribution of cloudiness through evaporation, precipitation, and advection processes. At low latitudes, there was a particularly good correspondence between areas of high (respectively low) values of the seasonal average and areas of low (respectively high) values of the standard deviation for both infrared and solar radiation fields. The computation of the covariance between the outgoing infrared radiation and the absorbed solar radiation helped identify regions of the globe which are influenced by simultaneous high and low variability at long and short wavelengths. The convectively active regions were clearly delineated from those which were mostly cloud-free and influenced by the presence of low-level cloud regimes. In addition, global maps of the covariance showed the seasonal shift of the ITCZ over the oceans and the tropical rainfall regions over the continents between the winter and summer seasons. Maps of the cloud factor showed that the sensitivity of the net radiation balance to a change in cloudiness undergoes large geographical variations for both seasons. Negative globally-averaged values of the cloud factor indicated that an increase of the cloud cover would yield an overall cooling of the earth climate, in accordance with earlier observations. Finally, limited comparisons between our results and those obtained from other satellite data sets

confirmed that scanner observations from the Nimbus-7 ERB Experiment do produce accurate and reliable estimates of the temporal variability of the planetary radiation balance for validation of GCMs' simulations of climate.

8.1.2 Simulated radiation balance

In Chapter Four, comparisons of the shortwave and longwave radiation fields generated with CCM1 against satellite observations showed that the NCAR CCM reproduced more successfully the global distribution of the mean outgoing infrared radiation than that of the absorbed solar radiation and planetary albedo fields. This had to be attributed mainly to the prescribed distribution of the surface albedo and cloud optical thickness. The geographical distribution of the standard deviation of the model-generated radiation fields resembled fairly well that obtained from satellite observations, especially at long radiative wavelengths. However, its magnitude was found to be systematically about two times larger than that computed from satellite observations. Global distribution of the time-lagged autocorrelation coefficients of the outgoing infrared radiation showed dramatic decreases in the correlation of the model-simulated radiation fields with increasing time-lags, in accordance with its high temporal variability. In summary, our comparison between the model-simulated and satellite-observed radiation fields revealed a major deficiency in the representation of the temporal variability of climate with CCM1: The model atmosphere loses its memory faster than the actual atmosphere. Charlock *et al.* (1988) compares the outgoing infrared radiation field obtained from a 120-day simulation for perpetual January conditions against Nimbus-7 and NOAA AVHRR satellite observations. Our results, based on improved simulations of climate made with CCM1, corroborate Charlock's comparison at both long and short wavelengths.

8.1.3 Impact of cloudiness

In view of the impact of clouds on the radiation and hydrologic budgets, it was suspected that the cloud prediction scheme, or the treatment of the interactions between clouds and the radiative, thermodynamic, and dynamic processes had to be held responsible for the on and off blinking of the model-simulated atmosphere. Analyses of the seasonal

average and standard deviation of the predicted total cloud cover against satellite-derived cloud estimates, and of the cloud longwave and shortwave radiative forcings demonstrated the model inability to correctly simulate the life-cycles of clouds. Therefore, it was concluded, in Chapter Five, that the high frequency of occurrence of clouds in CCM1 explained the factor of two difference between the temporal variability of the model-generated and satellite-observed radiation fields.

In Chapter Six, we discussed the influence of the cloud prediction scheme on the model-generated radiation fields in CCM1, including their temporal variability. Analyses of a January climate simulation, in which the CONTROL cloud prediction scheme had been replaced by an adapted version of the scheme routinely used at ECMWF, showed the reduced sensitivity of the temporal variability of the radiation fields to the distribution of cloudiness. Although the CONTROL and ECMWF cloud prediction schemes produced different distributions of clouds and cloud amounts, the temporal variability of both longwave and shortwave radiation was found to be about the same in both climate simulations. In view of our results, it was concluded that any parameterization of cloudiness in which cloud amounts were predicted only in term of some synoptic fields and their large-scale tendencies would yield identical discrepancies between CCM1 and satellite observations. This resulted from that both simulations maintained the same decoupling between cloudiness, and the radiation and hydrologic budgets.

In Chapter Seven, we discussed the influence of treating condensation as a complete rainout process on the frequency of occurrence of clouds in climate simulations made with CCM1. We showed that a 75 % reduction of the large-scale precipitation efficiency produced a 20 % increase of the cloudy-sky frequency, especially of the high-level large-scale condensation clouds. As a result, we were partially successful at reducing the standard deviation of the radiation fields, especially above the deep convective activity regions in the summer hemisphere. In addition, our arbitrary partition between non-precipitating and precipitating condensed water led significant differences in the distribution of the diabatic heating and general circulation in the troposphere. In view of the strong sensitivity of the

model climate to variations in the distribution of the hydrologic budget, we emphasized the importance of including an increased coupling between the time evolution of clouds and cloud liquid water in CCM1.

8.2 Contributions and future research

This dissertation made, at least, three significant contributions in climate research using the NCAR Community Climate Model. First, it helped isolate a major deficiency in the representation of the variability of the longwave and shortwave radiation fields when compared against that computed from satellite observations. Second, it clearly demonstrated that clouds were responsible for the on and off blinking of the model-simulated atmosphere. Finally, it stressed out the importance of an improved coupling between cloudiness, and the radiation and hydrologic budgets in order to reduce the discrepancy between model outputs and satellite observations. In view of the importance of the partition between evaporation, precipitation, and advection of clouds to the atmospheric general circulation in CCM1, we recommended the inclusion of the cloud liquid water as an additional prognostic variable, or the inclusion of a relationship between the life-cycles of clouds and the temporal evolution of liquid water.

Our work showed the need for additional and new research using satellite observations with the aim to improve climate simulations made with GCMs. Two ongoing satellite experiments, the Earth Radiation Budget Experiment and the International Satellite Cloud Climatology Project are providing new and exciting estimates of the earth radiation budget and cloud amounts from multiple space-borne instruments. The combination of those two data sets offers the unique opportunity of studying the temporal and spatial scales of interactions between cloudiness and the radiation budget components from satellite-derived observations only. In particular, we would like to carry forward our research on the determination of cloud life-cycles for various cloud types and their impact upon the time and space correlation of the radiation fields.

Going back to the Nimbus-7 Experiment, estimates of the precipitable water over the oceans, computed from brightness temperature measurements taken by the Scanning

Multichannel Microwave Radiometer (SMMR), are available on an identical gridded map and over the same time period as the ERB and cloud measurements. We plan to investigate the possibilities of combining all three data sets with the aim to obtain a deeper understanding of the characteristic relationships between clouds, and the radiation and hydrologic budgets, at least on a monthly scale.

Finally, in view of the importance of observations to validate simulations of climate made with GCMs, and of the fundamental role of climate models to an increased knowledge of climate and its sensitivity to different climate forcings, we want our future research to include both observations and modeling, with an emphasis on the use of satellite-based observations to help validate and improve modeling of climate with GCMs.

REFERENCES

- Ackerman, T. P., K. N., F. P. J. Valero, and L. Pfister, 1987: Heating rates in tropical anvils. Submitted to *J. Atmos. Sci.*
- Arakawa, A., 1975: Modelling clouds and cloud processes for use in climate models. GARP Publications series no. 16, ICSU/WMO, pp183-197.
- Ardanuy, P. E., and H. L. Kyle, 1986: El Niño and outgoing longwave radiation: Observations from Nimbus-7 ERB. *Mon. Wea. Rev.*, **114**, 415-433.
- Barkstrom, B. R., and G. L. Smith, 1986: The Earth Radiation Budget Experiment: Science and implementation. *J. Geophys. Res.*, **24**, 379-390.
- Bourke, W., B. Mc Avaney, K. Puri, and R. Thurling, 1977: Global modeling of atmospheric flow by spectral methods. *Methods in Computational Physics*, Vol. 17: *General Circulation Models of the Atmosphere*, J. Chang, Ed., Academic Press, 267-324.
- Boville, B. A., 1985: The thermal balance of the NCAR Community Climate Model. *J. Atmos. Sci.*, **42**, 695-709.
- Briegleb, B. P., P. Minnis, V. Ramanathan, and E. Harrison, 1986: Comparison of regional clear-sky albedos inferred from satellite observations and model computations. *J. Clim. Appl. Meteor.*, **25**, 214-226.
- Cahalan, R. F., D. A. Short, and G. R. North, 1982: Cloud fluctuation statistics. *Mon. Wea. Rev.*, **110**, 26-43.
- Campbell, G. G., and T. H. Vonder Haar, 1980: An analysis of two years of NIMBUS-6 Earth Radiation Budget observations. *Atmos. Sci. Pap. 320*, Dept. of Atmospheric Sciences, Colorado State Univ., Fort Collins, Colorado.
- , and T. H. Vonder Haar, 1980: Climatology of radiation budget measurements from satellites. *Atmos. Sci. Pap. 323*, Dept. of Atmospheric Sciences, Colorado State Univ., Fort Collins, Colorado.
- Carissimo, B. C., A. H. Oort, and T. H. Vonder Haar, 1985: Estimating the meridional energy transport in the atmosphere and in the oceans. *J. Phys. Oceanogr.*, **15**, 82-92.
- Cess, R. D., 1976: Climate change: An appraisal of atmospheric feedback mechanisms employing zonal climatology. *J. Atmos. Sci.*, **33**, 1831-1843.

- , B. P. Briegleb, and M. S. Lian, 1982: Low latitude cloudiness and climate feedback: comparative estimates from satellite data. *J. Atmos. Sci.*, **39**, 53–59.
- Charlock, T. P., K. M. Cattany-Carnes, and F. Rose, 1988: Fluctuation statistics of outgoing longwave radiation in a general circulation model and in satellite data. *Mon. Wea. Rev.*, **116**, 1540–1554.
- Charlock, T. P., and V. Ramanathan, 1985: The albedo field and cloud radiative forcing produced by a general circulation model with internally generated cloud optics. *J. Atmos. Sci.*, **42**, 1408–1429.
- Charney, J. G., and N. A. Phillips, 1953: Numerical integration of the quasi-geostrophic equations for barotropic and simple baroclinic flows. *J. Meteor.*, **10**, 71–99.
- Chervin, R. M., 1980a: Estimates of first- and second-moment climate statistics in GCM simulated climate ensembles. *J. Atmos. Sci.*, **37**, 1889–1902.
- , 1980b: On the simulation of climate and climate change with general circulation models. *J. Atmos. Sci.*, **37**, 1903–1913.
- , 1981: On the comparison between observed and GCM simulated climate ensembles. *J. Atmos. Sci.*, **38**, 885–901.
- , and S. H. Schneider, 1976: On determining the statistical significance of climate experiments with general circulation models. *J. Atmos. Sci.*, **33**, 405–412.
- Coakley, J. A., 1977: Feedbacks in vertical column energy balance models. *J. Atmos. Sci.*, **34**, 465–470.
- Ellis, J. S., 1978: Cloudiness, the planetary radiation budget and climate. *PhD Thesis*, Dept. of Atmospheric Sciences, Colorado State Univ., Fort Collins, Colorado, 129 pp.
- Ellis, J. S., and T. H. Vonder Haar, 1976: Zonal average earth radiation budget measurements from satellites for climate studies. *Atmos. Sci. Pap.* 240, Dept. of Atmospheric Sciences, Colorado State Univ., Fort Collins, Colorado.
- Fye, F. K., 1978: AFGWC automated cloud analysis, T.M. 78-002, Global Weather Central, Offutt AFB, 97pp.
- Gamache, J. F., and R. A. Houze, Jr., 1983: Water Budget of a mesoscale convective system in the tropics. *J. Atmos. Sci.*, **40**, 1835–1850.
- Geleyn, J. F., A. Hense, and H. J. Preuss, 1982: A comparison of model generated radiation fields with satellite measurements. *Contrib. Atmos. Phys.*, **55**, 253–286.
- Griffith, K. T., S. K. Cox, and R. G. Knollberg, 1980: Infrared radiative properties of tropical cirrus clouds inferred from aircraft measurements. *J. Atmos. Sci.*, **37**, 1077–1087.
- Gruber, A., 1985: The status of NOAA/NESDIS radiation budget data set. *Proceedings of the 9th Climate diagnostics workshop*, Climate Analysis Center, National Oceanic and Atmospheric Administration, Washington, D.C.

- , and H. Jacobowitz, 1985: The longwave radiation estimated from NOAA polar orbiting satellites: An update and comparison with Nimbus-7 ERB results. *Adv. Space Res.*, **5**, 111-120.
- Hansen, J., G. Russell, D. Rind, P. Stone, A. Lacis, S. Lebedeff, R. Ruedy, and L. Travis, 1983: Efficient three-dimensional global models for climate studies: Models I and II. *Mon. Wea. Rev.*, **111**, 609-662.
- Harshvardhan, D. A. Randall, T. G. Corsetti, and D. A. Dazlich, 1988: Earth radiation budget and cloudiness simulations with a general circulation model. Submitted to *J. Atmos. Sci.*
- Hartmann, D. L., V. Ramanathan, A. Berroir, and G. E. Hunt, 1986: Earth Radiation Budget data and climate research. *Rev. Geophys.*, **24**, no.2, 439-468.
- , and E. E. Recker, 1986: Diurnal variation of outgoing longwave radiation in the tropics. *J. Clim. Appl. Meteor.*, **25**, 800-812.
- , H. H. Hendon, and R. A. Houze, 1984: Some implications of the mesoscale circulations in tropical cloud clusters for large-scale dynamics and climate. *J. Atmos. Sci.*, **41**, 113-121.
- , and D. A. Short, 1980: On the use of Earth Radiation Budget statistics for studies of clouds and climate. *J. Atmos. Sci.*, **37**, 1233-1250.
- Heath, D., A. J. Krueger, and H. Park, 1978: The solar backscatter ultraviolet (SBUV) and total ozone mapping spectrometer (TOMS) experiment. *The Nimbus-7 User's Guide*, C.R. Madrid, Ed., NASA, Goddard Space Flight Center, 175-211.
- Hense, A., and E. Heise, 1984: A sensitivity study of cloud parameterizations in general circulation models. *Contr. Atmos. Phys.*, **57**, 240-258.
- House, F. B., A. Gruber, G. E. Hunt, and A. T. Mecherikunnel, 1984: History of satellite missions and measurements of the Earth Radiation Budget (1957-1984). *Rev. Geophys.*, **24**, 357-377.
- Houze, R. A., Jr., 1982: Cloud clusters and large-scale vertical motions in the tropics. *J. Meteor. Soc. Japan*, **60**, 396-410.
- Houze, R. A., and A. K. Betts, 1981: Convection in Gate. *Rev. Geophys. Space Phys.*, **16**, 541-576.
- Hunt, B. G., 1978: On the general circulation of the atmosphere without clouds. *Quart. J. R. Meteorol. Soc.*, **104**, 91-102.
- Hunt, G. E., V. Ramanathan, and R. M. Chervin, 1980: On the role of clouds in the general circulation model of the atmosphere. *Quart. J. R. Meteorol. Soc.*, **106**, 213-215.
- Hwang, P. H., Ed., 1982: Nimbus-7 temperature humidity infrared radiometer (THIR) data user's guide. NASA/Goddard Space Flight Center. 52 pp.

- Jacobowitz, H., N. L. Smith, H. B. Howell, F. W. Nagle, and J. R. Hickey, 1979: The first 18 months of planetary radiation budget measurements from the Nimbus-6 ERB experiment. *J. Atmos. Sci.*, **36**, 501-507.
- , H. V. Soule, H. L. Kyle, F. B. House, and the Nimbus-7 ERB Experiment Team, 1984: The Earth Radiation Budget Experiment: An overview. *J. Geophys. Res.*, **89**, 5021-5038.
- , R. J. Tighe, and the Nimbus-7 ERB Experiment Team, 1984: The earth radiation budget derived from the Nimbus-7 experiment. *J. Geophys. Res.*, **89**, 4997-5010.
- Kiehl, J. T., and B. P. Briegleb, 1988: A new parameterization of CO_2 absorption for use in climate models. In preparation.
- , R. J. Wolski, B. P. Briegleb, and V. Ramanathan, 1987: *Documentation of Radiation and Cloud routines in the NCAR Community Climate Model (CCM1)*. NCAR Technical Note NCAR/TN-288+IA, Boulder, Colorado.
- , and T. Yamanouchi, 1985: A parameterization for absorption due to the A, B, and γ oxygen bands. *Tellus*, **37B**, 1-6.
- Kratz, D. P., and R. D. Cess, 1985: Solar absorption by atmospheric water vapor: A comparison of radiation models. *Tellus*, **37B**, 53-63.
- Kyle, H. L., P. E. Ardanuy, and E. J. Hurley, 1985: The status of Nimbus-7 earth radiation budget data set. *Bull. Am. Meteorol. Soc.*, **66**, 1378-1388.
- , and K. L. Vasanth, 1986: Some characteristic differences in the earth's radiation budget over land and ocean derived from the Nimbus-7 ERB experiment. *J. Climate Appl. Meteor.*, **25**, 958-981.
- Lacis, A. A., and J. E. Hansen, 1974: A parameterization for the absorption of solar radiation in the earth's atmosphere. *J. Atmos. Sci.*, **31**, 118-133.
- Lau, N. C., 1981: A diagnostic study of recurrent meteorological anomalies appearing in a 15-year simulation with a GFDL general circulation model. *Mon. Wea. Rev.*, **109**, 2287-2311.
- Leary, C. A., and R. A. Houze, Jr., 1979a: The structure and evolution of convection in a tropical cloud cluster. *J. Atmos. Sci.*, **36**, 437-457.
- Manabe, S., 1969: Climate and the ocean circulation: I. The atmosphere circulation and the hydrology of the earth's surface. *Mon. Wea. Rev.*, **97**, 739-774.
- , and D. G. Hahn, 1981: Simulation of atmospheric variability. *Mon. Wea. Rev.*, **109**, 2260-2286.
- , J. Smagorinsky, and R. F. Strickler, 1965: Simulated climatology of a general circulation model with a hydrologic cycle. *Mon. Wea. Rev.*, **93**, 769-798.
- McAvaney, B. J., W. Bourke, and K. Puri, 1978: A global spectral model for simulation of the general circulation. *J. Atmos. Sci.*, **35**, 1557-1583.

- Meleshko, V.P., and R. T. Wetherald, 1981: The effect of a geographical cloud distribution in climate: A numerical experiment with an atmospheric general circulation model. *J. Geophys. Res.*, **86**, 11995–12014.
- Newell, R. E., J. W. Kidson, D. G. Vincent, and G. J. Boer, 1972: *The general circulation of the tropical atmosphere and interactions with extratropical latitudes*, Vol. 1. The MIT Press, 258pp.
- Ohring, G., and P. Clapp, 1980: The effect of changes in cloud amount on the net radiation at the top of the atmosphere. *J. Atmos. Sci.*, **37**, 447–454.
- , and A. Gruber, 1983: Satellite observations and climate theory. *Adv. Geophys.*, **25**, 237–304.
- , A. Gruber, and R. Ellingson, 1984: Satellite determination of the relationship between total longwave radiation flux and infrared window radiance. *J. Clim. Appl. Meteor.*, **22**, 416–425.
- Oort, A. H., and T. H. Vonder Haar, 1976: On the observed annual cycle in the ocean-atmosphere heat balance over the Northern Hemisphere. *J. Phys. Oceanogr.*, **6**, 781–800.
- Phillips, N. A., 1956: The general circulation of the atmosphere: a numerical experiment. *Quart. J. Roy. Met. Soc.*, **82**, 123–164.
- Pitcher, E. J., R. C. Malone, V. Ramanathan, M. L. Blackmon, K. Puri, and W. Bourke, 1983: January and July simulations with a spectral general circulation model. *J. Atmos. Sci.*, **40**, 580–604.
- Ramanathan, V. 1987: The role of Earth Radiation Budget studies in climate and general circulation research. *J. Geophys.*, **92**, 4075–4094.
- , and R. E. Dickinson, 1979: The role of stratospheric ozone in the zonal and seasonal radiative energy balance of the earth-troposphere system. *J. Atmos. Sci.*, **36**, 1084–1104.
- , and P. Downey, 1986: A non-isothermal emissivity and absorptivity formulation for water vapor. *J. Geophys. Res.*, **22**, 474–487.
- , E. J. Pitcher, R. C. Malone, and M. L. Blackmon, 1983: The response of a spectral general circulation model to refinements in radiative processes. *J. Atmos. Sci.*, **40**, 605–630.
- Randall, D. A., Harshvardhan, D. A. Dazlich, and T. G. Corsetti, 1988: Interactions among radiation, convection, and large-scale dynamics in a general circulation model. Submitted to *J. Atmos. Sci.*
- Raschke, E., and W. R. Bandeen, 1970: The radiation balance of the planet earth from radiation measurements of the satellite Nimbus-II. *J. Appl. Meteor.*, **9**, 215–238.

- , T. H. Vonder Haar, W. R. Bandeen, and M. Pasternak, 1973: The annual balance of the earth-atmosphere system during 1969-1970 from Nimbus-3 measurements. *NASA Tech. Note 7249*.
- Rind, D., R. Suozzo, N. K. Balachandran, A. Lacis, and G. Russell, 1988: The GISS global climate-middle atmosphere model. Part I: Model structure and climatology. *J. Atmos. Sci.*, **45**, 329-370.
- , R. Suozzo, and N. K. Balachandran, 1988: The GISS global climate-middle atmosphere model. Part II: Model variability due to interactions between planetary waves, the mean circulation and gravity wave drag. *J. Atmos. Sci.*, **45**, 371-386.
- Rutledge, S. A., and M. E. Schlesinger, 1985: The treatment of clouds in general circulation models: Current status and more physically-based parameterizations. Report No. 63. 50 pp. Climatic Research Institute and Dept. of Atmospheric Sciences. Oregon State Univ., Corvallis, Oregon.
- Sasamori, T., J. London, and D. V. Hoyt, 1972: Radiation budget of the Southern Hemisphere. *Meteor. Mag.*, **13**, 9-23.
- Schiffer, R. A., and W. B. Rossow, 1983: The International Cloud Climatology Project (ISCCP): The first project of the World Climate Research Programme. *Bull. Am. Meteorol. Soc.*, **64**, 779-784.
- Schlesinger, M. E., and W. L. Gates, 1980: The January and July performance of the OSU two-level atmospheric general circulation model. *J. Atmos. Sci.*, **37**, 1914-1943.
- Schneider, S. H., 1972: Cloudiness as a global climate feedback mechanism: The effects on the radiation balance and surface temperature of variations in cloudiness. *J. Atmos. Sci.*, **29**, 1413-1422.
- Schutz, C., and W. L. Gates, 1971: Global climatic data for surface, 800 mb, 400 mb: January. Advanced Research Projects Agency, Rep. R-915-ARPA, Rand Corporation, Santa Monica, 173pp. [NTIS AD-736204].
- , and W. L. Gates, 1972a: Supplemental global climatic data for surface, 800 mb, 400 mb: January. Advanced Research Projects Agency, Rep. R-915/1-ARPA, Rand Corporation, Santa Monica, 41pp. [NTIS AD-744633].
- , and W. L. Gates, 1972b: Supplemental global climatic data for surface, 800 mb, 400 mb: July. Advanced Research Projects Agency, Rep. R-1029-ARPA, Rand Corporation, Santa Monica, 180pp. [NTIS AD-760283].
- Short, D. A., and J. M. Wallace, 1980: Satellite-inferred morning to evening cloudiness changes. *Mon. Wea. Rev.*, **108**, 1160-1169.
- Shukla, J., and Y. Sud, 1981: Effect of cloud-radiation feedback on the climate of a general circulation model. *J. Atmos. Sci.*, **38**, 2337-2353.
- Simmons, A. J., and L. Bengtsson, 1984: Atmospheric general circulation models: Their design and use for climate studies. The global climate. Cambridge University Press. 38-62.

- Slingo, A., 1985: Simulation of the earth's radiation budget with the 11-layer general circulation model. *Meteorol. Mag.*, **114**, 121-141.
- , and J. M. Slingo, 1988: The response of a general circulation model to cloud longwave radiative forcing. I: Introduction and initial experiments. *Quart. J. R. Meteorol. Soc.*, **114**, 1027-1061.
- Slingo, J. M., 1980: A cloud parameterization scheme derived from GATE data for use with a numerical model. *Q. J. R. Meteorol. Soc.*, **106**, 747-770.
- , 1987: The development and verification of a cloud prediction scheme for the ECMWF model. *Q. J. R. Meteorol. Soc.*, **113**, 899-927.
- , and A. Slingo, 1988: The response of a general circulation model to cloud longwave radiative forcing. II: Sensitivity to cloud-prediction and convection schemes. In preparation.
- Smagorinsky, J., 1960: On the dynamical prediction of large-scale condensation by numerical methods. *Physics of precipitation, Geophys. Monogr.*, **5**, 727-768.
- , 1963: General circulation experiments with the primitive equations: I. The basic experiment. *Mon. Wea. Rev.*, **93**, 99-164.
- , S. Manabe, and J. L. Holloway Jr., 1965: Numerical results from a 9-level general circulation model of the atmosphere. *Mon. Wea. Rev.*, **93**, 727-768.
- Smith, L. D., T. H. Vonder Haar, and D. L. Randel, 1986: Interannual variability study of the earth radiation budget from Nimbus-7 monthly data. Sixth Conference on Atmospheric Radiation, Williamsburg, Va. *Extended Abstracts*, 211-214.
- , and T. H. Vonder Haar, 1988: Temporal variability of the outgoing infrared flux from NFOV daily data: Comparison between NOAA and Nimbus-7 polar orbiting satellites. Third Conference on satellite meteorology and oceanography, Anaheim, Ca. *Extended Abstracts*, 142-147.
- Stephens, G. L., 1978: Radiation profiles in extended water clouds. II: Parameterization schemes. *J. Atmos. Sci.*, **35**, 2123-2132.
- , G. G. Campbell, and T. H. Vonder Haar, 1981: Earth radiation budgets. *J. Geophys.*, **86**, 9739-9760.
- Stowe, L. L., C. G. Wellemeyer, T. F. Eck, H. Y. M. Yeh, and the Nimbus-7 Cloud data processing Team, 1988: Nimbus-7 global cloud climatology. Part I: Algorithms and validation. *J. Clim.* **1**, 445-470.
- Sundqvist, H., 1978: A parameterization scheme for non-convective condensation including prediction of cloud water content. *Quart. J. R. Met. Soc.*, **104**, 677-690.
- Taylor, V. R., and L. L. Stowe, 1984: Reflectance characteristics of uniform earth and cloud surfaces derived from Nimbus-7 ERB. *J. Geophys. Res.*, **89**, 4987-4996.

- Thiele, O., and R. A. Schiffer, 1985: Understanding climate: A strategy for climate modeling and predictability research. *NASA Reference Publication 1158*, NASA Goddard Space Flight Center, Greenbelt, Maryland.
- Vonder Haar, T. H., and V. E. Suomi, 1971: Measurements of the earth's radiation budget from satellites during a five-year period. I. Extended time and space means. *J. Atmos. Sci.*, **28**, 305-314.
- Washington, W. M., and D. L. Williamson, 1977: A description of the NCAR global circulation models. *Computational Physics*, Vol. 17, Academic Press, New York, 111-172.
- Weare, B. C., 1988: Diabatic heating in the UCLA general circulation model. *J. Clim.*, **1**, 704-714.
- Wetherald, R. T., and S. Manabe, 1975: The effects of changing the solar constant on the climate of a general circulation model. *J. Atmos. Sci.*, **32**, 2044-2059.
- , and S. Manabe, 1975: The effects of doubling the CO_2 concentration on the climate of a general circulation model. *J. Atmos. Sci.*, **32**, 3-15.
- , and S. Manabe, 1980: Cloud cover and climate sensitivity. *J. Atmos. Sci.*, **37**, 1485-1510.
- , and S. Manabe, 1988: Cloud feedback processes in a general circulation model. *J. Atmos. Sci.*, **45**, 1397-1415.
- Williamson, D. L., J. T. Kiehl, V. Ramanathan, R. E. Dickinson, and J. J. Hack, 1987: *Description of NCAR Community Climate Model (CCM1)*. NCAR Technical Note NCAR/TN-285+STR, Boulder, Colorado.
- Wolski, R., 1987: *CCM Modular Processor Users' Guide (Version PROC02)*. NCAR Technical Report, NCAR/TN-290+IA, Boulder, Colorado.

Appendix A

BASIC RADIOMETRIC CONVERSION ALGORITHMS

A.1 Introduction

This appendix summarizes the scientific processing which converts input radiances taken by the NFOV channels into fluxes and which is completely described in Jacobowitz *et al.* (1984). The computation of the NFOV shortwave fluxes is based upon a procedure developed by Raschke *et al.* (1973). First, the input radiances are corrected for anisotropy in reflectance dependent upon the surface type of the source target area (land, water, snow/ice, clouds). This represents the application of an angular dependence model (Taylor and Stowe, 1984). Next, the NFOV shortwave processing applies a correction for the directional reflectance characteristics of the source target area. In addition, this processing converts the instantaneous fluxes into mean daily NFOV shortwave fluxes. Averages over 1-day and monthly periods are computed for all the ERB scientific parameters. In addition, the net radiation is averaged over a 6-day period, which is the approximate repeat cycle of the satellite suborbits.

A.2 Albedo derived from the NFOV channels

Input: N_S , shortwave radiance; θ , satellite zenith angle; ξ , solar zenith angle; ψ , relative azimuth angle; ϕ , latitude of target area; λ , longitude of target area; S_o , solar constant; t , day of the year.

Output: $\bar{A}(\phi, \lambda, t)$, mean daily albedo.

Process:

1. Compute reflectances $\pi\rho$, assuming that the surface reflects diffusively:

$$\pi\rho(\theta, \psi, \xi, \lambda, t, \phi) = \frac{\pi N_S(\theta, \psi, \xi, \lambda, t, \phi)}{S_o L(t) \cos \xi}, \quad (\text{A.1})$$

where $L(t) = (\bar{d}/d(t))^2$, $d(t)$ is the earth-sun distance, and \bar{d} is the annual mean earth-sun distance.

2. Determine the target scene type M (land, water, snow/ice, cloud) from the values of $\pi\rho$ and N_S .
3. Obtain the anisotropic factor $R(\theta, \psi, \xi, M)$ from the angular model corresponding to the scene type M for the solar angle ξ and viewing angles θ and ψ .
4. Compute the directional reflectances r corrected for anisotropy.

$$r(\xi, \phi, \lambda, t, M) = \pi\rho(\theta, \psi, \xi, \phi, \lambda, t) \cdot R(\theta, \psi, \xi, M). \quad (\text{A.2})$$

5. Compute the daily average reflected flux W_R :

$$W_R(\phi, \lambda, t) = S_o \cdot L(t) \cdot r(0, \phi, \lambda, t, M) \cdot \frac{1}{12} \int_{t_{SR}}^{t_n} \frac{r(\xi)}{r(0)}_M \cos \xi \, d\tau, \quad (\text{A.3})$$

where

$$r(0, \phi, \lambda, t, M) = \frac{r(\xi, \phi, \lambda, t, M)}{(r(\xi)/r(0))_M}. \quad (\text{A.4})$$

$(r(\xi)/r(0))_M$ are normalized reflectance models, and t_{SR} and t_n are the time of the local sunrise and noon, respectively.

6. Compute the daily average reflected flux averaged over all observations, \overline{W}_R .

7. Compute the daily averaged insolation \overline{H}_S :

$$\overline{H}_S(\phi, \lambda, t) = S_o L(t) \cdot \frac{1}{12} \int_{t_{SR}}^{t_n} \cos \xi \, d\tau. \quad (\text{A.5})$$

8. Compute the daily mean albedo \overline{A} :

$$\overline{A}(\phi, \lambda, t) = \frac{\overline{W}_R(\phi, \lambda, t)}{\overline{H}_S(\phi, \lambda, t)}. \quad (\text{A.6})$$

A.3 Outgoing longwave flux for the NFOV channels

Input: N_L , longwave radiance; θ , satellite zenith angle; ϕ , latitude of target area; t , day of the year.

Output: $\overline{W}_L(\phi, \lambda, t)$, mean daily outgoing longwave flux.

Process:

1. Determine whether the field of view (FOV) was during the daytime D or during the nighttime N.
2. Compute the emitted flux W_L corresponding to a given observation.

$$W_L^{(D,N)}(\phi, \lambda, t) = N_L^{(D,N)}(0, \phi, \lambda, t) \cdot 2\pi \cdot \int_0^{\frac{\pi}{2}} \left(\frac{N_L(\theta, \phi)}{N_L(0, \phi)} \right)_M \cos\theta \sin\theta \, d\theta, \quad (\text{A.7})$$

where

$$N_L^{(D,N)}(0, \phi, \lambda, t) = \frac{N_L^{(D,N)}(\theta, \phi, \lambda, t)}{\left(\frac{N_L(\theta, \phi)}{N_L(0, \phi)} \right)_M}. \quad (\text{A.8})$$

$\left(\frac{N_L}{N_L(0, \phi)} \right)_M$ is a model of the limb-darkening.

3. Compute daytime and nighttime fluxes \overline{W}_L^D and \overline{W}_L^N averaged over all observations of the target areas.
4. Compute the daily averaged emitted flux \overline{W}_L :

$$\overline{W}_L(\phi, \lambda, t) = \frac{T_D \overline{W}_L^D(\phi, \lambda, t) + T_N \overline{W}_L^N(\phi, \lambda, t)}{24}. \quad (\text{A.9})$$

where T_D and T_N are the number of hours the target area is in daylight and night-light, respectively.

A.4 Net radiation derived from the NFOV channels

Input: \bar{A} , daily averaged albedo; \bar{W}_L , daily averaged longwave flux; \bar{H}_S , daily averaged insolation; ϕ , latitude of the target area; λ , longitude of the target area; t , day of the year.

Output: $\bar{N}(\phi, \lambda, t)$, mean daily net radiation.

Process:

$$\bar{N}(\phi, \lambda, t) = (1.0 - \bar{A}(\phi, \lambda, t)) \cdot \bar{H}_S(\phi, t) - \bar{W}_L(\phi, \lambda, t). \quad (\text{A.10})$$

A.5 Computation of the monthly mean values

$\tilde{X}(\dots)$ is the monthly average of $\bar{X}(\dots, t)$ over all observation days of the month.

1. Albedo: $\tilde{A}(\phi, \lambda) = \tilde{W}_R(\phi, \lambda) / \tilde{H}_S(\phi)$
2. Outgoing longwave flux: $\tilde{W}_L(\phi, \lambda)$
3. Net radiation flux: $\tilde{N}(\phi, \lambda)$